Proceedings of the 5th Conference

18th September 2014

All contributions in this book have been reviewed. However, the authors take responsibility for the content and for the correctness of their texts, the quality of the tables, graphs and figures. The editors therefore cannot accept responsibility for the final appearance of the manuscripts.

Edited by:

Tomáš Plachý, Pavel Padevět, Pavel Tesárek, Jan Stránský, Ondřej Zobal

Published by:

Department of Mechanics, Faculty of Civil Engineering, Czech Technical University in Prague, Thákurova 7, 166 29 Praha 6

Printed by:

Česká technika - nakladatelství ČVUT, Thákurova 1, 160 41 Praha 6, pages 231, 1st Edition

Acknowledgement:

SVK 07/14/F1

ISBN 978-80-01-05570-0

Table of Contents

RECONSTRUCTION OF DATA FROM CREEP MEASUREMENTS

Petr BITTNAR[1], **Pavel PADEVĚT**[2]

***Abstract**: The paper is focused on the describing of data reconstruction from creep measurements. The raw data were damaged by power outages. The repaired measurements were used for the creep evaluation of the cement paste with sand. Evaluation of creep measurements of the reconstructed data was carried out and is presented. The measurement was performed on the dried and saturated specimens prepared from the cement paste [1]. Creep and shrinkage were measured.*

***Keywords**: Cement paste, Shrinkage, Creep, Water saturated specimens,*

INTRODUCTION

Measuring the creep of a cement paste is a long process. The measurement that is presented in the paper has run for one month. During the time of measurement, the unpredictable events can occur that may degrade the measurement. The most common cause is an unexpected power outage. This is left to prevent that the measurement system is preceded by battery backup. This allows writing the last read data to the computer memory and from there they are no longer deleted. In the case of long-term measurements, the reading and writing of data is performed with a longer time lag, this event is not destructive for measurements. During the read time, a service outage and re-start of the measurement system can occur. The data record is not violated in this case.

The second possibility of damage of the record is accumulation of errors in the records. This may be due to errors in data transmission between the measuring probe and the storage or inappropriate composition program in the processor that controls data recording. The elimination of complications from the second group of data corruption is a complicated process. Faulty measurements or data recording interruption can occur at any time during the measurement. The occurrence of these

[1] Ing. Petr Bittnar, Department of Mechanics, Faculty of Civil Engineering, Czech Technical University in Prague, petr.bittnar@fsv.cvut.cz

[2] Ing. Pavel Padevět, Ph.D., Department of Mechanics, Faculty of Civil Engineering, Czech Technical University in Prague, pavel.padevet@fsv.cvut.cz

complications affects the quality of the power supply and noise disturbances on the cable between the probe and the computer.

SYSTEM OF MEASUREMENT

The measuring principle is simple, based on a long-term stable system loading. The loading of the sample is performed in the lever mechanism. The specimen is loaded by properly chosen force that does not change during a measurement. The probes are placed around the specimen parallel to its longitudinal axis [2]. Total three optoelectronic probes are used. During the test, the change of the length of the specimen is measured. The usual length of the specimen is 70 mm.

The values of the deformation - the lengths are written to a file that is created during measurement. Writing in this case was conducted with an interval of 5 minutes. A longer interval between records is possible because the measurement of creep and shrinkage does not rank of rapid processes, in which the frequent reading is necessity. The time step of writing of the selected data from measurement is controlled by processor placed between the probe and the computer. If there is an error in the measurement, it is usually due to faults in the processor during the measurement.

This was a case of damage measurement, which is described in the article. The recorded measurement is shown in Figure 1. The horizontal axis describes the time in days. The vertical axis represents the average deformation of the body. This value is calculated as an average of three sensors.

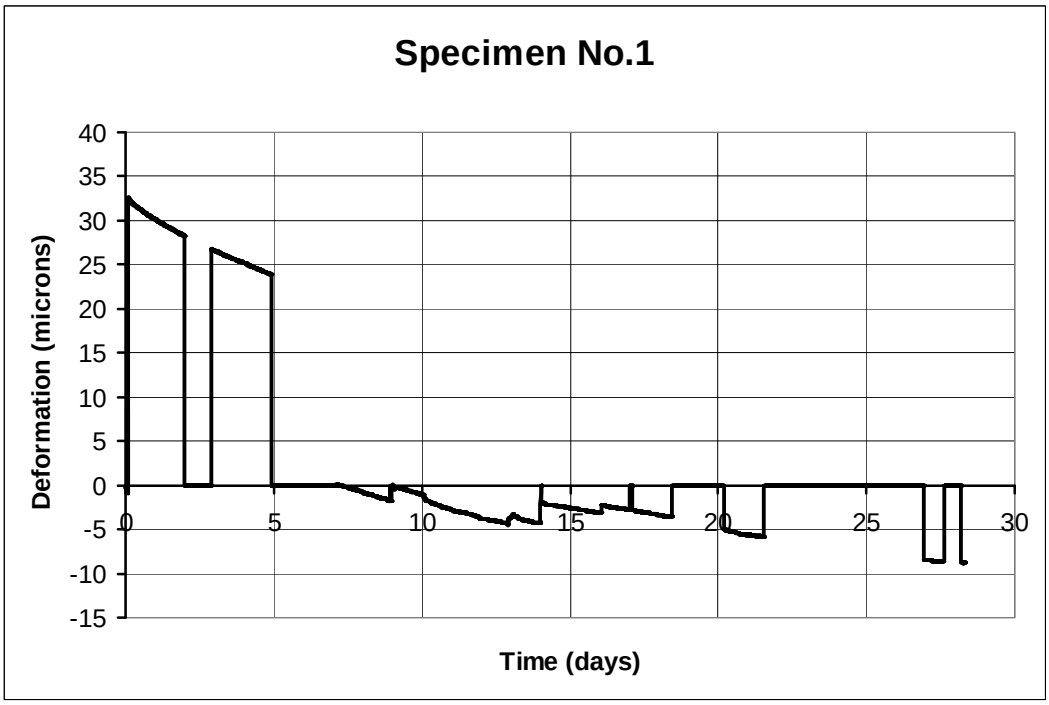

Fig. 1 The original recording of measurements.

Random measurement shutdowns are shown in the graph (Fig. 1). There is discontinued deformation measurement and values are not recorded. However, the time recording in the central processor remained unchanged. Re-starting the measurements were carried out by restarting the whole measurement system.

DESCRIBING OF RECONSTRUCTION

The shape of the creep and shrinkage curves of the materials with the cement matrix remains continuous in the case of continuous measurements. Therefore in this case, deformation curves should be continuous, too. The reconstruction was carried out in two steps. The first step is to ensure the continuity of deformation changes. The second step is the elimination of erroneous measurements so as to maintain the correct time axis.

Continuity changes of deformation is performed by prediction of deformation in time at the time of the disturbed measurements. In this case, it is necessary to proceed from the errors incurred at the beginning to the errors of measurement at the end of the record.

Then it is possible to remove incorrect measurements on the horizontal time axis. The corrected entry is shown in Figure 2.

RESULTS OF MEASUREMENT

Resulting reconstruction of damaged data is shown in Fig. 2 to 7.

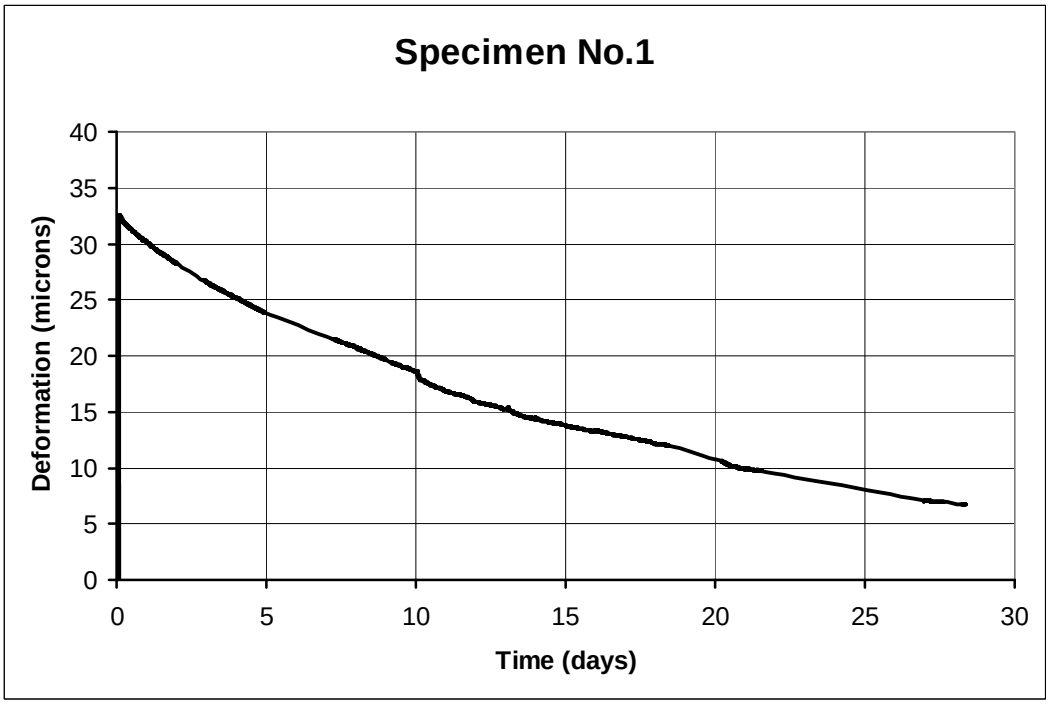

Fig. 2 Reconstructed creep measurements on the specimen No.1.

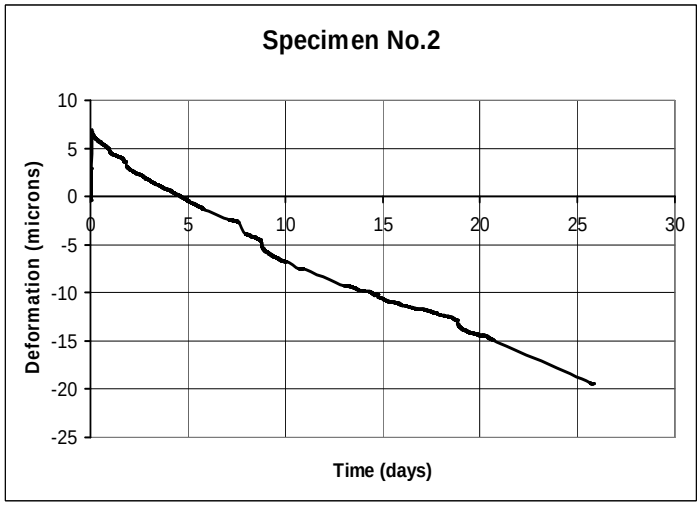

Fig. 3 Reconstructed creep measurements on the specimen No.2, in drying condition.

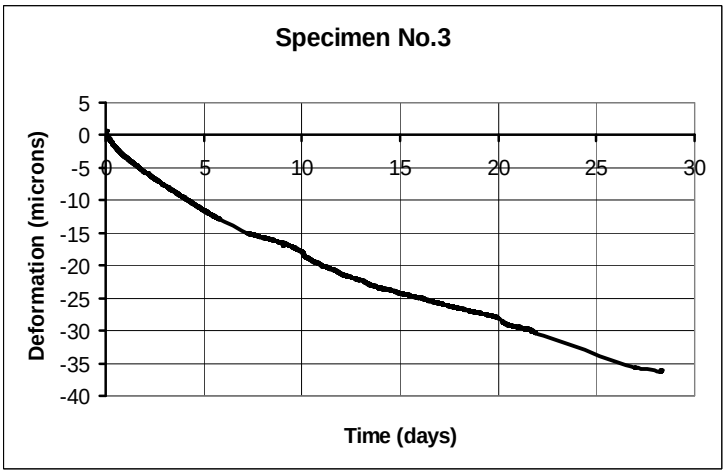

Fig. 4 Reconstructed shrinkage measurements on the specimen No.3, in drying condition.

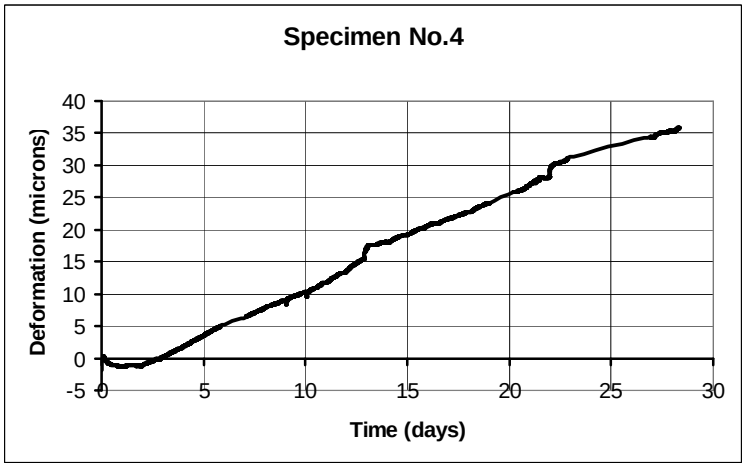

Fig. 5 Reconstructed shrinkage measurements on the specimen No.4, water saturated.

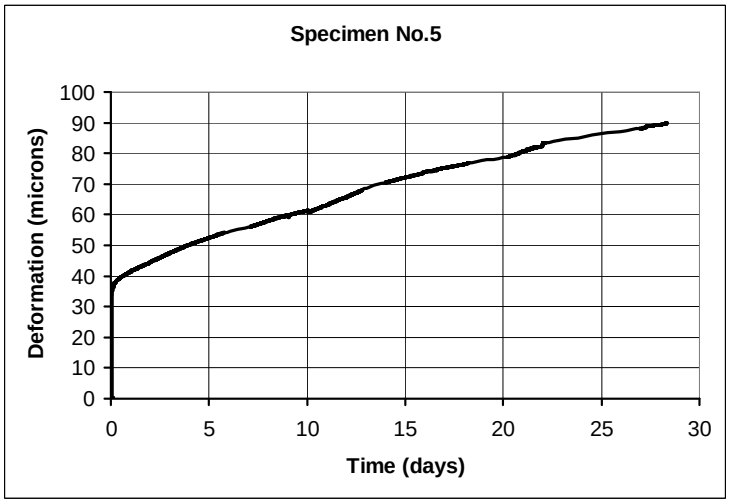

Fig. 6 Reconstructed creep measurements on the specimen No.5, water saturated.

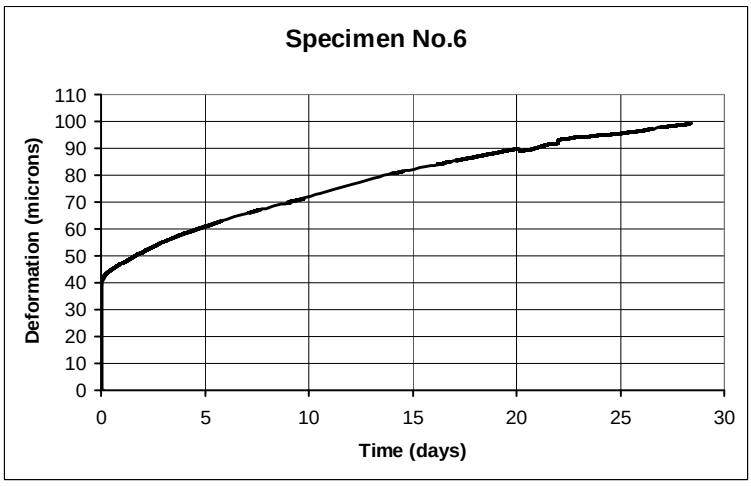

Fig. 7 Reconstructed creep measurements on the specimen No.6, water saturated.

The measurements must be divided into two groups. The first group consists of specimens 1-3 that have been dried before the test. The second group consists of the specimens 4, 5 and 6. The samples were saturated with water before the beginning of the test. Each group can be divided into specimens which were loaded and specimens without loading. Loaded specimens were 1, 2, 5 and 6 and the result of measuring was the creep. Unloaded specimens had No. 3 and 4, and the shrinkage was measured on them.

The cement paste was prepared from the Portland cement CEM I 42.5R and using the water-cement ratio of 0.4 [3]. The cement paste contains sand. The weight of sand to cement weight was 1: 1. The sand was applied to a grain size of 1 mm. The percentage representation of the sand in its overall amount was: 4.5 % fraction of 0 - 0.125; fraction from 0.125 to 0.25 9.18 %; fraction of 0.25 to 0.5 48.2 % and fraction of 0.5 - 1 38 %. The specimens were made in cylindrical molds with a diameter of 10 mm. The specimens were placed into a water bath after concreting and their pressure surfaces

were adjusted by cutting [4] at the age of 1 month. Overall length was reduced to 70 mm. Creep tests were performed at the age of 1 year.

CONCLUSION

The size of creep of dried specimens was 24 and 25 microns after 25 days. The size of shrinkage of the dried specimen No.3 was 24 microns after 25 days. The creep of saturated water specimens was 53 and 57 microns. The shrinkage of the specimen No.4 reached the value of 32 microns. The results are related to the 25 day testing.

Very interesting results would be achieved by removal of the shrinkage from the creep measurements. The name for these results on the dried specimens is basic creep. The same process can be done with water-saturated specimens. The name for the results is the creep of water saturated specimens.

ACKNOWLEDGEMENT

The financial support of this experiment by the Faculty of Civil Engineering, Czech Technical University in Prague SGS project No. 14/122/OHK1/2T/11 is gratefully acknowledged.

REFERENCES

[1] PADEVĚT, P. Mechanical Properties of Cement Pastes. in: *Proceedings of the International Conference 70 years of FCE ST, Slovak University of Technology,* Faculty of Civil Engineering, Bratislava, 2008, pp. 1-4. ISBN 978-80-227-2979-6

[2] PADEVĚT, P. and BITTNAR, P:, Measuring of Creep of Cement Paste Specimen, *Proceedings of the 2nd WSEAS International Conference on Applied Mathematics, Simulation, Modeling (ASM'09),* Athens, Greece, 2009, pp. 33-39. ISBN 978-960-474-147-2.

[3] PADEVĚT, P. and ZOBAL, O., Change of Material Properties of the Cement Paste CEM I, in *Proceedings of the 48th International Scientific Conference on Experimental Stress Analysis,* Velké Losiny, May – June 2010, pp. 307-310, ISBN 978-80-244-2533-7.

[4] NEVILLE, A. M. *Properties of Concrete*, John Wiley & Sons, (1997), ISBN 0-470-23527-6.

NUMERICAL SIMULATION AND ANALYSIS OF KINETIC PROCESSES OF CALLUS TISSUE FORMATION AND OSSIFICATION DURING DISTRACTION OSTEOGENESIS TREATMENT IN STAGE OF ACTIVE ELONGATION AND NEUTRAL FIXATION

František DENK[1], Miroslav PETRTÝL[2]

***Abstract**: Biomechanical stimulations during long bones lengthening by distraction osteogenesis method have key influence on the development and formation acceleration of bone regenerate tissue in interfragmental gap of interrupted diaphysis. These physiological or artificially applied external effects with regard to their direction and size by different ways regulate the extracellular matrix synthesis of intefragmental tissue, resulting in the genesis of the relevant characteristic phenotypes of tissue structures. The study of kinetic processes of callus tissue formation and ossification with dependency on stress and strain distribution changes is performed according to various and inhomogeneous course of bone tissue formation in the callus sub-volume locations within individual characteristic phases of the healing process.*

***Keywords**: distraction osteogenesis, bone regenerate, kinetics of callus ossification, external fixation, controlled biomechanical stimulations*

INTRODUCTION

Currently there are available numerous methods allowing analysis of quality, structure and density development of bone tissue (RTG, CT, densitometry, histology, exact mathematical models) during long bones lengthening, however, most of these methods are imprecise, in clinical practice inapplicable, financially or time demanding. Affordable and efficient tool based on the fundamental principles of mechanics, which would take into account the simultaneous effects of a number of very important factors affecting the formation and consolidation process of bone regenerate (e.g.

[1] Ing. arch. et Ing. František Denk; Laboratory of Biomechanics and Biomaterial Engineering, Department of Mechanics, Faculty of Civil Engineering, CTU in Prague; Thákurova 7, 160 00, Prague, Czech republic; frantisek.denk@fsv.cvut.cz

[2] Prof. Ing. Miroslav Petrtýl, DrSc.; Laboratory of Biomechanics and Biomaterial Engineering, Department of Mechanics, Faculty of Civil Engineering, CTU in Prague; Thákurova 7, 160 00, Prague, Czech republic; petrtyl@fsv.cvut.cz

inhomogeneous and nonlinear temporal changes of material properties, real shape and volume changes, load changes during the treatment program, mechanical properties of the applied fixator, etc.), continuously serve sufficiently realistic picture of the bone regenerate behavior in macro, micro a mezo levels, export information useful for clinical practice and provide feedback to specific clinical outcomes (homogeneous Young´s modulus of tissue, homogeneous stiffness of bone regenerate, ossification degree, etc.), has still not been developed. Presented work deals with a detailed X-ray evaluation of specific bone regenerate and numerical analysis simulating kinetic processes of formation and ossification during the whole period of the lower limb shaft lengthening by distraction osteogenesis method. All initial and final boundary conditions for the theoretical calculation are derived from the experimental results of X-ray analysis of clinical practice. Simulation process of bone tissue formation and regeneration is based on available theories of tissue differentiation [1], relations between mechanical stimulation and tissue differentiation [2], and dependency of bone tissue modeling, remodeling and resorption dependency on mechanical stress and strain [3]. For calculation is compiled basic biomechanical model, which defines the basic components influencing external force effects transmission and determines their role in different stages of treatment program.

RADIOGRAPHIC ANALYSIS OF BONE REGENERATE

The case of successful 65 mm extension of the left tibia in a patient without achondroplasia with total treatment time of 214 days (sex: female, age: 6 years, height: 124 cm, weight: 25 kg, BMI: 15,9) was selected for detailed X-ray analysis of interfragmental regenerate formation, consolidation and ossification during entire period of distraction osteogenesis method treatment. Total observation time is 969 days (2,6 years). Stabilization of the shaft was ensured with Kirschner wires attached in external circular fixation system with three supporting helixes (Ilizarov system). Radiographic evaluation of callus development process from the elongation beginning is performed by treatment plan analysis with corresponding detailed study of 2D images of A/P and L projections in various stages of healing, i.e. determination of callus length, CDR (Callus Diameter Ratio) [4] and evaluation of macroscopic appearance (Fig. 1) [5]. The evaluation also includes a detailed analysis of the morphology and structure in bone regenerate characteristic development phases.

Active elongation process ran from 14th day (since osteotomy) to 74th day of treatment (Fig. 1, A, B), i.e. total 60 days. Until 39th day the extension is executing symmetrically on all 3 helixes with distraction velocity of 1 mm/day, after that the speed of extension was on one of supporting helixes reduced to 3/4 mm/day. From the 25th day of treatment the diaphysis was gradually fully loaded by walking with underarm crutches. During elongation process the K-wires and supporting helixes of fixation apparatus were irreversible deformed. Neutral fixation period lasted 90 days, removal of external fixator was done 164 days after osteotomy. 214th day is considered the end of treatment. The course of treatment was uneventful, the 115th day the patient was in home care.

Fig. 1 RTG A/P projection, bone tissue formation in gap of interrupted diaphysis, day of treatment no.: 39(A), 67(B), 102(C), 164(D), 501(E), 969(F)

The relatively advanced stage of the extension process (Fig. 1, A) shows a slight hypotrophy of the callus. Due to elongation process, i.e. thanks to the action of tensile stress, the interfragmental space mainly consists of highly oriented fibrous tissue. As a result of the full loading are in regenerate already formed the localities of pressure stress. Due to this effect the beginnings of early maturation is already observable (osteoid formation and beginning of the ossification process) around the bone fragments of interrupted diaphysis. Length of the regenerate is in this state 30 mm, CDR ratio is indefinable because medial zone still entirely consists of fibrous tissue.

Final stage of elongation process (Fig. 1, B) is in volume of medial zone characterized by a slight hypotrophic drift, which is caused by tissue maturation and early ossification in proximal and distal part of interfragmental volume. Due to the elongation process the medial zone is still made up of fibrous tissue. Length of the regenerate is 55 mm, CDR ratio is 0,85.

In the early stage of neutral fixation (Fig. 1, C) bone regenerate is still slightly hypotrophic, length of callus is 65 mm, CDR ratio is 0,80. Exterior biomechanical effects are entirely in pressure zones and it leads to very intensive consolidation and formation of mainly imature bone tissue. In medial zone there is apparent the narrow sawtooth line, where the ossified tissue is gradually and continuously interconnected.

At the time of fixation apparatus removal (Fig. 1, D) the bone regenerate is fully ossified, slight hypertrophic drift is caused by the very rapid stiffness increase thanks to full interconnection of proximal and distal ossified tissue pillars of interfragmental volume, CDR ratio is 0,90. Tissue of the bone regenerate is homogeneous and formed by mature bone tissue of very high quality or by corticalis. Around the longitudinal axis of diaphysis the intramedullar cavity recovery is also apparent.

Other radiographic documentation (Fig. 1, E, F) presents the influence of fully physiological load of the lower limb on the modeling and remodeling processes and consolidation of completely cortical bone and part of tibial diaphysis with its characteristic architecture.

NUMERICAL SIMULATION OF BONE REGENERATE FORMATION

General biomechanical model

Compilation of biomechanical model and its response is given particularly by the definition and basic characteristic of partial components participating in the transmission of external force and deformation effects in various stages of healing by distraction osteogenesis method. This basic biomechanical model is formed as a system of linear springs representing the components of entire scheme fixed to deformation-resistant shoulders with only vertical possibility of shift (Fig. 2, A, B).

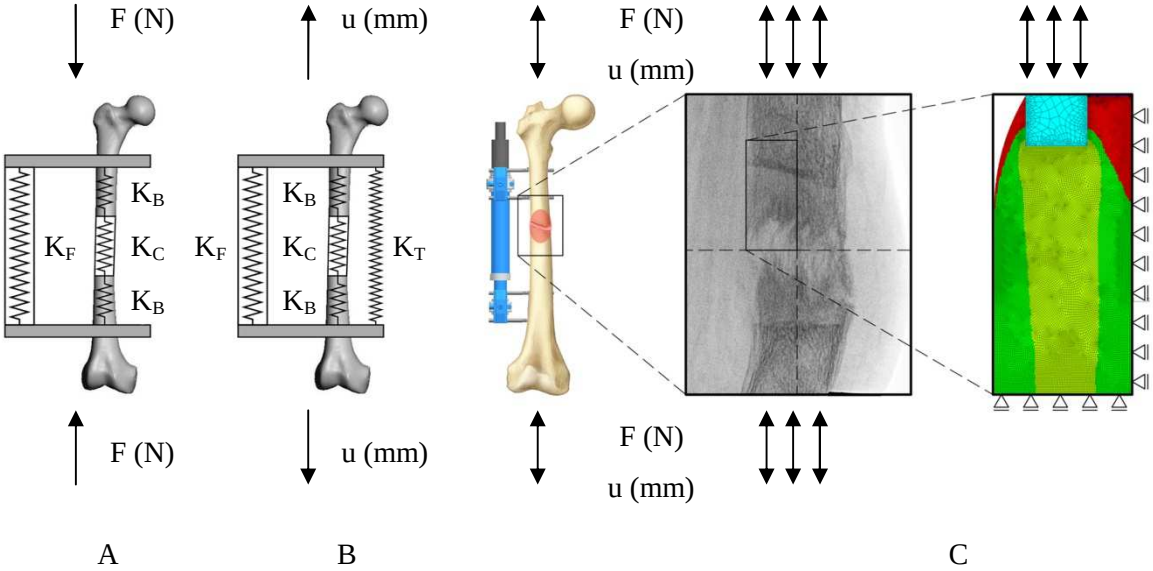

Fig. 2 Biomechanical spring model of external fixation for neutral fixation stage (A) and for active elongation (B), detail FE model for bone regenerate numerical analysis (C)

The overall basic stiffness of the spring system $\boldsymbol{K_P}$ is given by the equation:

$$K_P = K_F + \left(\frac{1}{\sum K_B} + \frac{1}{K_C}\right)^{-1} + \sum K_T \qquad (N.mm^{-1}), \tag{1}$$

where the individual components are defined as follows:

K_F external fixation apparatus stiffness, K_F = 286 N/mm [6] [7] [8]

K_B stiffness of femur corticalis, represented by value E_B = 17200 MPa

K_C bone regenerate stiffness, contemplated the time dependence of E_C value development in the range of 0 - 17200 MPa defined by curve on the basis of numerical verification

K_T stiffness of surrounding tissues - unknown, as a general rule $E_T > 0$ MPa

In phases of active elongation the system is loaded with static vertical displacement, typically 1 mm/day. Inasmuch as the distraction speed corresponds to the velocity of growth and regeneration capability of tissues [9], it can be assumed their relaxation and creep, and due to these effects time disappearance of stiffness of some components, i.e. $\boldsymbol{K_C}$ a $\boldsymbol{K_T} \rightarrow 0$. In this stage during physiological loading (compressive stress) the contribution of components $\boldsymbol{K_C}$ a $\boldsymbol{K_T}$ is not applied because $\boldsymbol{K_C} \sim 0$ a $\boldsymbol{K_T} > 0$. Inasmuch as $\boldsymbol{K_B} >> \boldsymbol{K_C}$, equation describing the overall resistance of the system *(1)* in case of physiological loading can be for **active elongation (AE)** phase formulated:

$$K_{P,AE,c}(t) = K_F + K_{C,c}(t) \qquad (N.mm^{-1}), \tag{2}$$

where $\boldsymbol{K_{C,c}(t)}$ is a function of development of the bone regenerate pressure stiffness due to its early maturation. Simultaneously it is applied $\boldsymbol{K_{C,c}} << \boldsymbol{K_F}$. For the case of distraction process is valid the modification of relation *(1)* which represents the resistance rate of tissue components to the fixator:

$$K_{P,AE,t}(t) = K_{C,t}(t) + \sum K_T\,(t) \qquad (N.mm^{-1}), \tag{3}$$

where $\boldsymbol{K_{C,t}(t)}$ and $\boldsymbol{K_T(t)} \rightarrow 0$, and $\boldsymbol{K_{C,t}(t)}$ is function of inhomogeneous development of callus tension stiffness. In phases of **neutral fixation (NF)** the equation *(1)* can be accordingly adjusted to form:

$$K_{P,NF}(t) = K_F + \left(\frac{1}{\sum K_B} + \frac{1}{K_C(t)}\right)^{-1} \qquad (N.mm^{-1}) \tag{4}$$

inasmuch as $\boldsymbol{K_C} < \boldsymbol{K_B}$. In later phases of neutral fixation the fixation apparatus performs only stabilizing function and can be applied relation $\left(\frac{1}{\sum \mathrm{K_B}} + \frac{1}{\mathrm{K_C}}\right)^{-1} >> K_F$, it can be written:

$$K_{P,NF}(t) = \left(\frac{1}{\sum K_B} + \frac{1}{K_C(t)}\right)^{-1} \qquad (N.mm^{-1}) \tag{5}$$

Numerical FEM analysis

Numerical simulation of bone tissue formation in interfragmental space was performed through iterative computational algorithm separately for the stage of active elongation and neutral fixation. Optimization of various parameters of computational process is carried out with regard to results of a particular case X-ray evaluation of 65 mm tibia extension with the aim of achieving the maximum conformity during the course of interfragmental regenerate development for the characteristic sub-phases of bone tissue formation within the treatment program.

Computing process was performed in the form of 2D FE model in ANSYS APDL environment. The problem is with regard to the time consumption in this phase solved by plane strain and biaxial symmetry. The model mesh is composed of quadratic planar elements of Plane183 type. Time unit is an iteration step. Evaluation of the deformation fields distribution in sagittal section during loading of

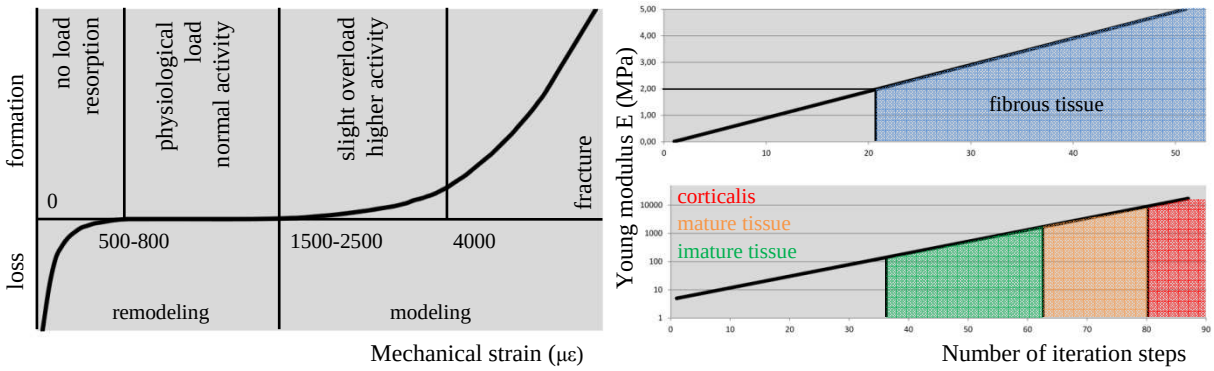

Fig. 3 Dependency of bone tissue remodeling on mechanical strain [3] (left), evolution of Young modulus E in time (right)

diaphysis bone fragments by tensile displacement or physiological force effect in one iteration step is the basis for the temporal changes calculation of the biomechanical properties of callus tissue internal structure to next computational step of the algorithm. Criteria for average strain evaluation on elements are controlled by the modeling processes dependence on the degree of biomechanical stimulation (Fig. 3) [3]. Calculation expects predetermined time evolution of Young´s modulus E (MPa) for fibrous tissue and corticalis (Fig. 3). Numerical simulation doesn´t take account the regenerate volume changes as a result of elongation process and combination of different load cases during advanced part of active elongation stage and during early time of neutral fixation. Simultaneous formation of oriented fibrous tissue and early mature tissue in callus volume isn´t also taken into account in the simulation. Fields of Young´s modulus $\boldsymbol{E}$ (MPa) distribution, total deformation of the bone regenerate and fields of principal stresses $\boldsymbol{\sigma_1}$, $\boldsymbol{\sigma_3}$ (MPa) are within iterative process evaluated (Obr. 4,5). It was carried out and evaluated total of 6 sets of 102 - 159 steps for active elongation stage

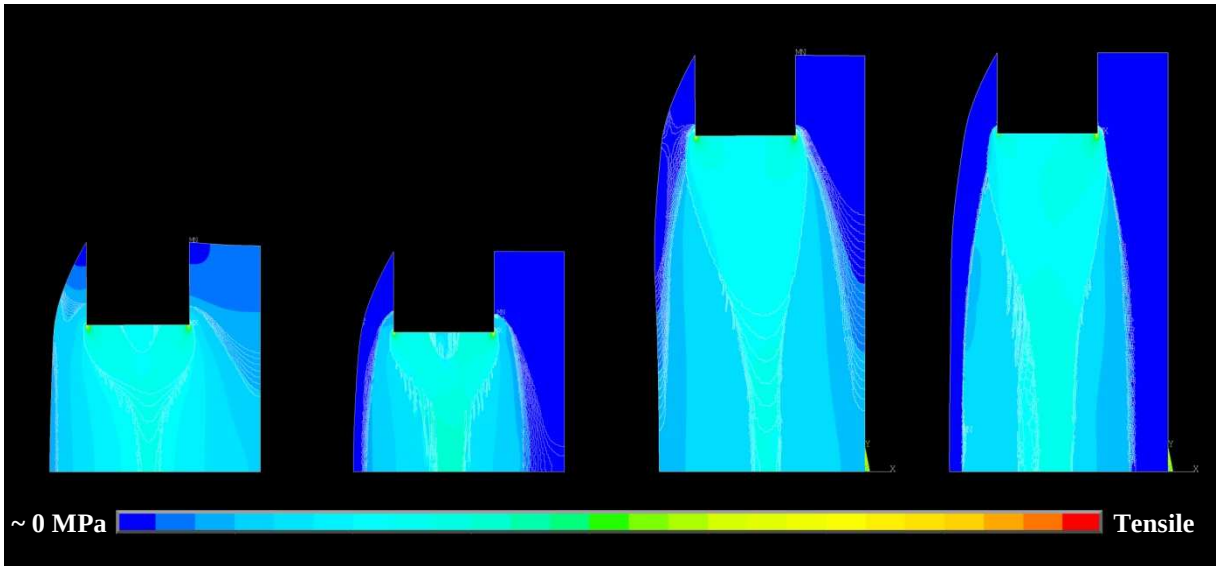

Fig. 4 Numerical analysis of kinetics of callus fibrous tissue formation, active elongation, from left step no. 2/9 and 2/45, 5/38 and 5/90, stress $\boldsymbol{\sigma_1}$ (MPa)

and 2 sets of 402 a 265 iteration steps. Iteration process was terminated after the creation of equilibrium state of bone regenerate volume.

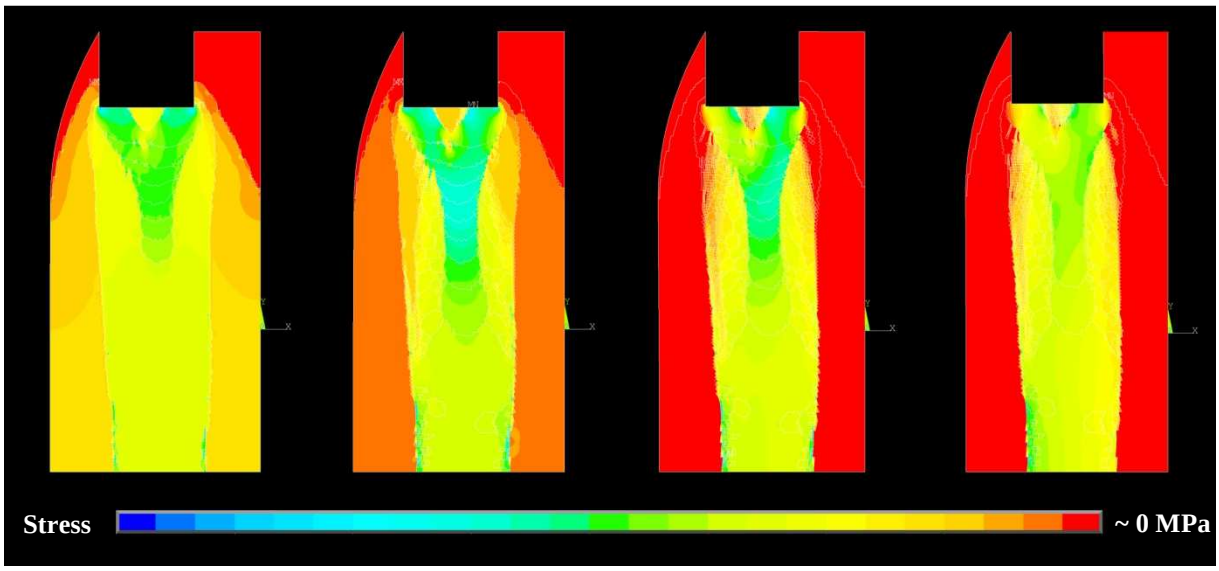

Fig. 5 Numerical analysis of kinetics of callus bone tissue formation, neutral fixation, from left step no. 2/9, 2/21, 2/67, 2/111, stress σ_3 (MPa)

CONCLUSION

Based on the performed numerical simulation of bone tissue formation in interfragmental gap of interrupted diaphysis during treatment by distraction osteogenesis method the time dependence of bone regenerate homogeneous stiffness course can be compiled (Fig. 6). Detailed verification of radiographic analysis in combination with bone regenerate numerical simulations presents a very real picture of characteristic phenotypes of tissue structures production in different locations in various stages of treatment and concurrently allows the absolute location of each iteration step in the treatment process time schedule.

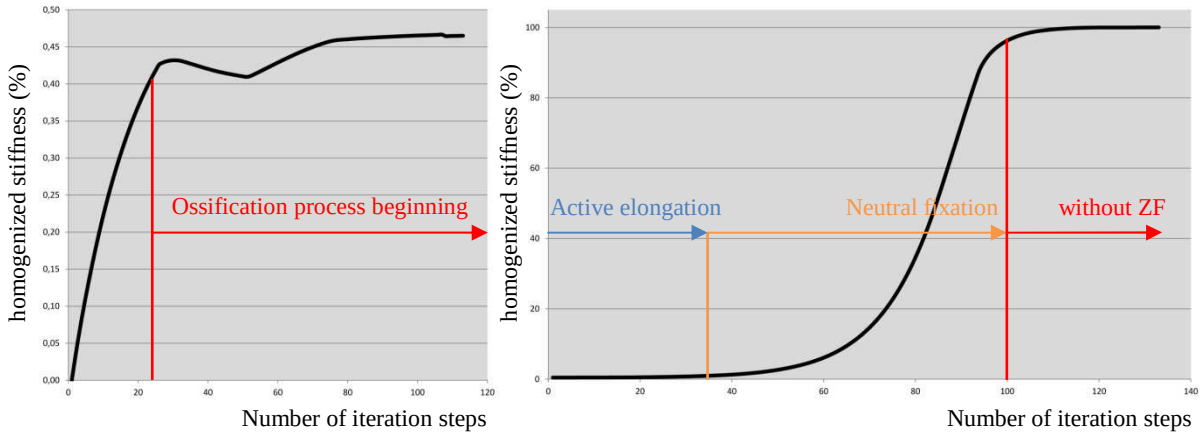

Fig. 6 Time dependence of bone regenerate homogeneous stiffness course during active elongation (left) and neutral fixation stage (right)

Presented results of submitted study forms the basis for recursive optimization of input parameters (e.g. functional time dependencies of homogenized Young´s modulus E fields evolution on macro/mezo structural levels), for preparing detailed analysis of bone regenerate behavior (formation, consolidation, ossification) throughout the treatment period and subsequently for the creation an effective tool of classification and continuous optimization of the treatment process in relation to a new electronically controlled fixation apparatus [6] [7].

ACKNOWLEDGEMENT

The financial support of this experiment by the Faculty of Civil Engineering, Czech Technical University in Prague (SGS project No. SGS14/122/OHK1/2T/11) is gratefully acknowledged.

REFERENCES

[1] PAUWELS, F. Eine neue theorie über den einflub mechanischer reize auf die differenzierung der stützgewebe. *Zeitschrift für Anatomie und Entwicklungsgeschichte.* 1960. **121**(6). 478-515. ISSN 1432-0568.

[2] CARTER, D.R., BEAUPRÉ, G.S., GARY, S., GIORI, N.J., NICHOLAS, J., HELMS, J.A., JILL, A. Mechanobiology of Skeletal Regeneration. *Clinical Orthopaedics & Related Research.* 1998, **355**. S41-S55. ISSN 1941-7551.

[3] FROST, H.M. Wolff´s Law and bone´s structural adaptations to mechanical usage: an overview for clinicians. *The angle Orthodontist*. 1994. **64**. 175-188. ISSN 0003-3219.

[4] MAMADA, K., NAKAMURA, K., MATSUSHITA, T., OKAZAKI, H., SHIRO, R., OU, W., TANAKA, K., KUKOKAWA, T. The diameter of callus in leg lengthening, 28 tibial lengthening in 14 patients with achondroplasia. *Acta Orthopaedica Scandinavica.* 1998. **69**(3). 306-310. ISSN 0001-6470.

[5] LI, R., SALEH, M., YANG, L., COULTON, L. Radiographic classification of osteogenesis during bone distraction. *Journal of Orthopaedic Research.* 2006. **24**. 339-347, ISSN 1554-527X

[6] CZECH TECHNICAL UNIVERSITY IN PRAGUE FACULTY OF CIVIL ENGINEERING, PETRTÝL, M., MAŘÍK, I., LÍSAL, J., DENK, F. Equipment for long bones lengthening. Czech patent application. Industrial property office. 303910. 9.5.2013.

[7] CZECH TECHNICAL UNIVERSITY IN PRAGUE FACULTY OF CIVIL ENGINEERING, LERACH, A., VÍTEK, T., PETRTÝL, M., LÍSAL, J., MAŘÍK, I., DENK, F. External monolateral fixation apparatus. Utility design. Industrial property office. 24421. 15.10.2012.

[8] PETRTÝL, M., DENK, F., LERACH, A., PADEVĚT, P. Experimental verification of the external fixator for legthening of long bones. In: *Nano & Macro Mechanics 2011.* Praha. ČVUT v Praze. 2011. pp 21-28. ISBN 978-80-01-04892-4.

[9] ILIZAROV, G.A. The principles of the Ilizarov method. *Bulletin of the Hospital for Joint Diseases Orthopaedic Institute*. 1988. **48**(1). 1-11. ISSN 0883-9344

WANG TILINGS IN HOMOGENIZATION TASKS

Martin DOŠKÁŘ[1], Jan NOVÁK[2]

Abstract: *An efficient representation of microstructure of real materials based on Wang tiling is presented in brief. Once the microstructure is compressed reconstructed domains of arbitrary size can be efficiently generated. This makes the tiling concept appealing from the viewpoint of numerical homogenization. Computational enhancement based on the method of Schur complement is investigated.*

Keywords: *microstructure compression, numerical homogenization, Wang tilings*

INTRODUCTION

All materials exhibit heterogeneous structure from certain scale. Besides physical properties of material constituents, the microstructural composition influences the overall response as well. Inspired by Nature one of current trends in Materials Engineering is to actively design materials to suit intended applications. With growing computational power *in silico* testing along with optimization strategies seem to be an appealing alternative to the classical approach to material design based on manufacturing and physical testing of various microstructural compositions, which is rather time-consuming and costly [1]. Therefore a suitable framework that links a material microstructure and properties of constituents with the macroscopic behaviour is desired. Such problem, referred to as homogenization, has been studied since the end of nineteenth century, e.g. [2], and is currently well established especially in the case of linear problems [3]. However, we believe that in the perspective of the recently introduced concept of Wang tilings [4] the homogenization procedures may be enhanced with concepts of domain decomposition leading to reduced computational overhead. Thus, the objective of this work is to develop a numerical homogenization framework that would benefit from the repetitive nature of Wang tilings.

WANG TILINGS

To keep the paper self-contained fundamentals of Wang tiling concept are introduced next, for further readings on applications of Wang tilings see e.g. [5].

[1] Ing. Martin Doškář, Department of Mechanics, Faculty of Civil Engineering, Czech Technical University in Prague, martin.doskar@fsv.cvut.cz

[2] Ing. Jan Novák, Ph.D., Department of Mechanics, Faculty of Civil Engineering, Czech Technical University in Prague, novakj@cml.fsv.cvut.cz

The basic element of the concept is a Wang tile, a square tetraminoe-like piece with codes assigned to its edges. Tiling is understood as a mapping from a regular grid of points to a set of distinct tiles. The edge codes play the role of a constrain such that only the tiles with the same codes on the adjacent edges can be placed side by side. Moreover, tiles can be neither rotated nor reflected during the tiling. It means that two identical tiles mutually rotated by $k\pi/2$ with $k \in \{1, 2, 3\}$ are considered as different.

The concept of Wang tilings was introduced by Hao Wang in 1961. In Wang's work [6] the decision problem of certain class of logical statements was converted into a question whether the related tile set is capable of tiling the infinite plane. Since there is no general rule how to decide the tiling problem, Wang conjecture was that if a periodic portion of plane (patch) can be tiled by the given tile set, then the set is solvable and the statement holds true. Later, Berger came up with the first set which can cover up the infinite plane without a periodically repeating patch. His findings initiated research on other aperiodic tile sets that resulted in discovery of the aperiodic set containing only 13 tiles reported by Culik in [7]. However, from the perspective of Materials Engineering the stochastic tile sets introduced by Cohen [8] are more appealing as they correspond better with the aim of modelling of materials with random microstructure [5]. Henceforward by the notion *tile set* the *stochastic tile set* is understood.

By making use of either optimization techniques [4] or the automatic design of tiles [8, 5] a microstructural information can be compressed within a tile set such that a tiled portion of plane resembles the reference microstructure in sense of statistical descriptors with desired level of accuracy. From this point of view the tiling concept can be understood as a generalization to the widely accepted Periodic Unit Cell (PUC) approach but instead of a single cell a microstructure information is attributed to multiple tiles. By employing the stochastic tiling algorithm [8] arbitrarily large representations of the compressed microstructure can be obtained in a very efficient way. This characteristic makes the concept suitable for numerical investigation of homogenized properties as explained in the following section.

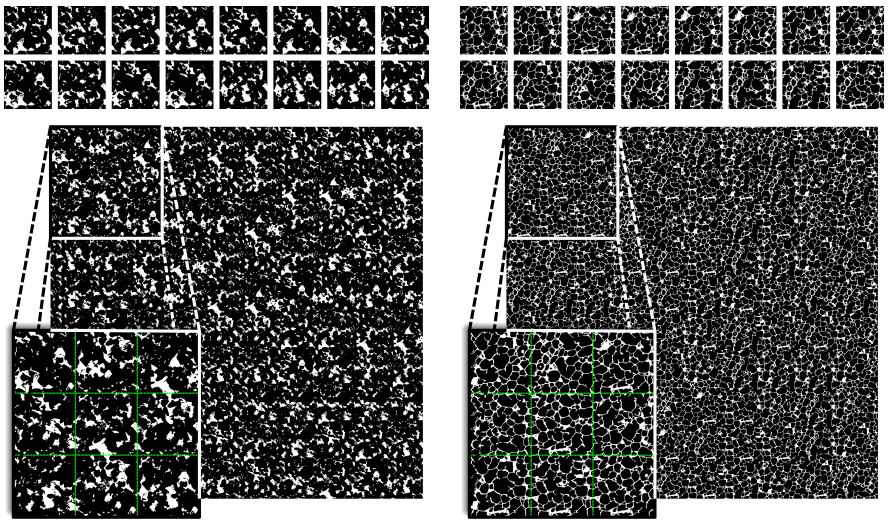

Fig. 1 Examples of compressed microstructures and one reconstructed microstructure realization: (a) sandstone, (b) Alporas foam.

REPRESENTATIVE VOLUME ELEMENT

In numerical homogenization the question of representativeness of a computational domain is of a primary concern. Such a domain is usually referred to as the Representative Volume Element (RVE) [9]. In general, RVE should incorporate all characteristic features of the microstructure under investigation, which leads to the requirement of statistical homogeneity and ergodicity of treated microstructure. According to Hill [10], the overall response of RVE should be invariant to uniform boundary load. It is widely accepted, e.g. [11], that this requirement usually leads to very large RVEs. Thus it can be relaxed to the condition that the wave length of physical filed fluctuations caused by the presence of inhomogeneities should be significantly smaller in comparison to the RVE dimension, i.e. the coefficient of variation of effective properties of different microstructure realizations under the same load is below a certain threshold. On the other hand, RVE must be small enough such that it can be considered as a single material point in a macro scale analysis. This results in known condition of separation of scales.

The particular size of an RVE is the function of the microstructural geometry, the contrast between material constituent properties and physical phenomenon under investigation [12]. In the case of complex microstructures and high contrasts RVE dimensions can reach large numbers [13]. To avoid the excessive computing a solution based on Representative Volume Element Sets (RVE Set) was proposed in [11]. In this paper, we follow the standard asymptotic homogenization procedure in order to meet the aforementioned Hill's criterion. In addition, we adopt Niezgoda's premise that the microstructure represented to a high degree of accuracy automatically provides us with a broad range of effective properties [11].

The ability of the tiling concept to produce a microstructure realization of arbitrary size implies that the asymptotic analysis of various physical phenomena can be performed effectively. Note that from the perspective of Niezgoda's nomenclature a tile set represents an RVE Set in terms of the microstructural information providing that the average is taken over a tiling than each tile separately. That is because the information associated with tile edges is accurately revealed only when assembled into tilings. For other quantities a tiling, one microstructure realization, of dimensions smaller than RVE stands for Statistical Volume Element (SVE). Averages over SVEs arising from uniform Dirichlet and Neumann boundary conditions give upper and lower bounds on effective properties, respectively, refining the arithmetic and harmonic bounds (also called Voight-Reuss-Hill bounds for linear elasticity problem and Weiner bounds for heat transport problem) [12, 14]. With increasing tiling size the apparent properties, i.e. macroscopic properties of SVEs, converge to the sought effective properties.

NUMERICAL HOMOGENIZATION

As mentioned in the previous section the tiling-based compression of microstructural information is appealing especially in the case of complex random microstructures and high contrast in material properties. For such microstructures standard analytical bounds such as Hashin-Shtrikman are far apart,

hence, employing strategies that take into account the real geometries is needed. In this paper we omit the analytical approaches and focus solely on numerical homogenization.

The profound overview of numerical homogenization of linear properties can be found e.g. in Kanit [12]. In the developed framework both heat transport and linear elasticity problems are covered. However, we illustrate the methodology with heat transport problem. In brief, a computational domain, SVE, is subjected to Uniform Gradient of Temperature – $\boldsymbol{\Theta}$ (Dirichlet) , and Uniform Heat Flux – $\boldsymbol{Q}$ (Neumann), respectively, with prescribed boundary conditions in the form

$$T(\boldsymbol{x}) = \boldsymbol{\Theta} \cdot \boldsymbol{x}\,, \quad \text{or} \quad \boldsymbol{q}(\boldsymbol{x}) \cdot n(\boldsymbol{x}) = \boldsymbol{Q}\,, \quad \forall \boldsymbol{x} \in \Gamma\,. \tag{1}$$

Spatial averages of local temperature gradient and heat flux are computed as

$$\langle \boldsymbol{\nabla} T \rangle = \frac{1}{|\Omega|} \int_\Omega \boldsymbol{\nabla} T(\boldsymbol{x})\, \mathrm{d}\boldsymbol{x}\,, \quad \langle \boldsymbol{q} \rangle = \frac{1}{|\Omega|} \int_\Omega \boldsymbol{q}(\boldsymbol{x})\, \mathrm{d}\boldsymbol{x}\,. \tag{2}$$

If the macroscopic quantity is prescribed such that it induces unit excitation in one direction, the dual averaged quantity directly yields the corresponding components of thermal conductivity or resistivity matrix. For instance, if $\boldsymbol{\Theta} = \{1, 0, 0\}^T$ is prescribed, the spatial average $\langle \boldsymbol{q} \rangle$ yields components $\lambda_{11}^{\text{app}}$, $\lambda_{21}^{\text{app}}$, and $\lambda_{31}^{\text{app}}$ of the apparent/macroscopic conductivity tensor $\boldsymbol{\lambda}^{\text{app}}$. The remaining members can be obtained analogically by Θ_2 or $\Theta_3 = 1$ while the other components vanish.

The governing partial differential equation of heat conduction arising from Fourier's law is solved using standard finite element method. Discretization of computational domain is chosen as voxel-based, i.e. each voxel represents a single finite element, since outputs of microstructure compression are usually in form of digital images. This assumption leads to substantial reduction in computational cost since an analytical expression for the element conductivity matrix can be derived as a function of material properties and voxel size. The matrix values are pre-calculated for each of material constituents and are added to the appropriate position during localization avoiding integration at a level of each element. The simple geometry of voxel-based elements also allows for an analytical relation between element volume average of gradient and flux, respectively, and element nodal values.

To further address the RVE size issue, various models are obtained from tilings of increasing size. Moreover, for each size a number of realization is generated to get insight in variation of results. Such an approach leads to numerous computations for repetitive geometries. Thus incorporation of elements of domain decomposition may reduce the computational overhead.

First, each tile is treated as a separate finite-element task. Without introducing any boundary conditions a global tile-level conductivity matrix K is assembled. No load R^Ω is assumed to be prescribed for

the internal degrees of freedom r^{Ω}, therefore the system of equations can be recast as

$$\begin{bmatrix} \mathsf{K}_{11} & \mathsf{K}_{12} \\ \mathsf{K}_{21} & \mathsf{K}_{22} \end{bmatrix} \begin{Bmatrix} \mathsf{r}^{\Omega} \\ \mathsf{r}^{\Gamma} \end{Bmatrix} = \begin{Bmatrix} 0 \\ \mathsf{R}^{\Gamma} \end{Bmatrix}, \tag{3}$$

where r^{Γ} denotes the boundary degrees of freedom and K_{ij} are corresponding parts of tile global conductivity matrix.

Condensation of the internal degrees of freedom, also called Schur complement method, results in

$$(\mathsf{K}_{22} - \mathsf{K}_{21}\mathsf{K}_{11}^{-1}\mathsf{K}_{12})\mathsf{r}^{\Gamma} = \mathsf{R}^{\Gamma}, \tag{4}$$

where $\hat{\mathsf{K}} = (\mathsf{K}_{22} - \mathsf{K}_{21}\mathsf{K}_{11}^{-1}\mathsf{K}_{12})$ defines the tile conductivity matrix. Hence, at the tiling level number of unknowns is reduced to number of tile boundary nodes resulting in significant reduction in number of degrees of freedom (DOFs), see Fig. 2. The global conductivity matrix of a tiling is assembled by localization of corresponding tile conductivity matrices.

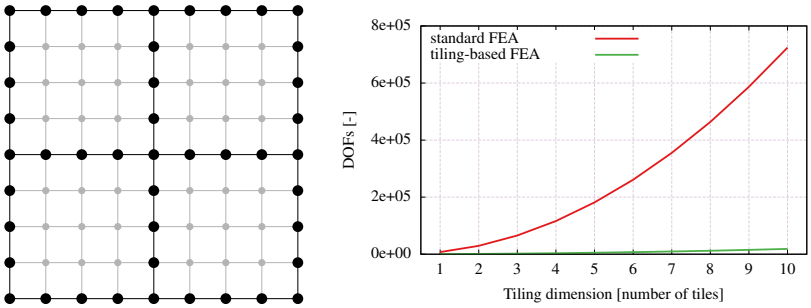

(a) (b)

Fig. 2 (a) Mesh of 2×2 *tiling with condensed internal DOFs shown in grey and (b) graph of number of DOFs with respect to tile edge size.*

Moreover, matrices that relates the tile boundary nodal values with tile volume averages of temperature gradient and heat flux, such that

$$\langle \nabla \mathsf{T} \rangle_{\Omega_t} = \tilde{\mathsf{B}}_{\nabla T}\mathsf{r}^{\Gamma} \quad \text{and} \quad \langle \mathsf{q} \rangle_{\Omega_t} = \tilde{\mathsf{B}}_{q}\mathsf{r}^{\Gamma}, \tag{5}$$

can be constructed along with the tile conductivity matrix in the pre-processing part and saved for later use.

COMPUTATIONAL PERFORMANCE

A study on computational efficiency was performed, resulting graphs in Fig. 3 and Fig. 4, comparing the proposed tiling aided homogenization to the standard FEM analysis in terms of computational time and memory cost. Homogenization of thermal conductivity was chosen as a benchmark problem. The

reference microstructure was compressed into 16 tiles each consisting of 85×85 px. The apparent properties were computed for 1×1 up to 10×10 tiling, ten realizations of each tiling size were generated.

In Fig. 3a, the assembly phase consists of tiling generation, discretization and localization, the post-processing covers averaging given by *((2))*. As can be seen the major time saving is achieved in

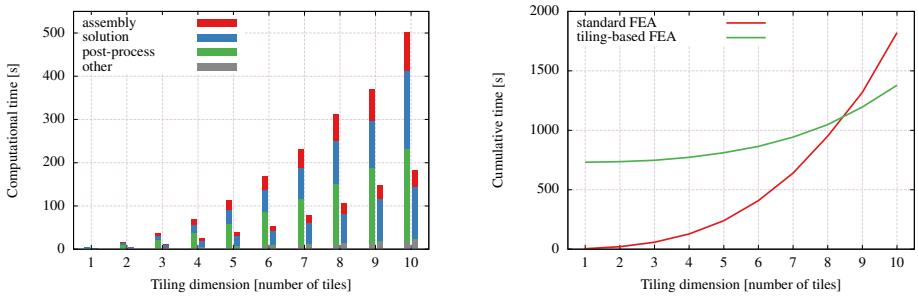

(a) (b)

Fig. 3 Comparison of (a) computational time for standard FEM homogenization (left columns) and macro-element FEM (right columns) for each tiling size, and (b) cumulative time including the pre-calculation part. Computational time for Intel(R) Core(TM)2 Duo CPU T5870@2,00GHz, 4,00GB RAM, Windows 7 64bit, Matlab R2012b.

the averaging part. The time needed for condensation is excluded from the graph Fig. 3a, however, it took 730 s to construct the tile conductivity matrices and the matrices which couple boundary nodal values with the gradient and flux averages in this case. In Fig. 3b the cumulative time including the pre-calculation is plotted. The tiling approach outperforms the standard analysis when larger domains are to be computed. With more realizations of each tiling size the tiling approach would perform even better.

However, there is a trade-off between reduction in computational time and memory. Despite a significant reduction in number of DOFs in the tiling approach the tile conductivity matrices are fully populated so the global matrix is less sparse, see Fig. 4a, resulting in more data to be stored, Fig. 4b. This feature limits the application of the described methodology in three dimensions, where memory demands are even more pronounced.

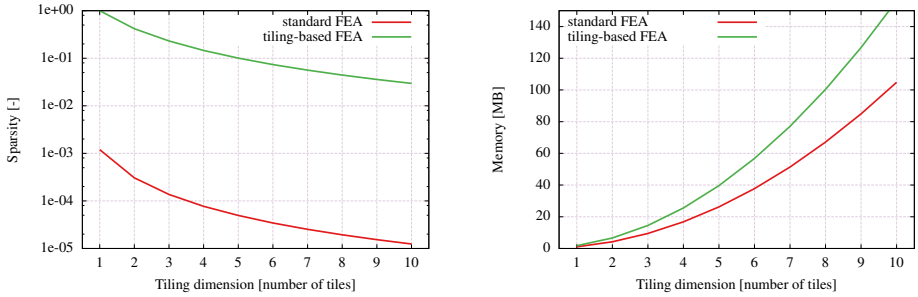

(a) (b)

Fig. 4 Comparison of (a) sparsity, the ratio of number of non-zero members to all matrix members, of the global stiffness matrices, and (b) memory required to store the global conductivity matrix.

SUMMARY

The concept of Wang tilings has been examined from the perspective of homogenization theory. Once a microstructure is compressed into a set of Wang tiles a convergence analysis of apparent properties may be easily performed. The repetitive nature of tilings may be further utilized to improve computational performance. The presented framework is substantially general and as demonstrated can be applied effectively to any linear problem. In three dimensional analyses, however, the associated memory costs may quickly exceed available resources. In such a case more sophisticated approach of domain decomposition techniques should be used and will be in focus of our future work.

ACKNOWLEDGEMENT

The support by the Czech Science Foundation through project No. 1324027S is gratefully acknowledged. We would also like to thank the Grant Agency of the Czech Technical University in Prague, grant No. SGS14/028/OHK1/1T/11.

REFERENCES

[1] FULLWOOD, D. T., NIEZGODA, S. R., ADAMS, B. L. and KALIDINDI, S. R. Microstructure sensitive design for performance optimization. *Progress in Materials Science* [online]. August 2010, **55**(6), pp. 477-562 [cited 2014-07-14]. ISSN 00796425. Available from: doi:10.1016/j.pmatsci.2009.08.002

[2] VOIGHT, W. Theoretische Studien über die Elasticitätsverhältnisse der Krystalle. *Abhandlungen der Königlichen Gesellschaft der Wissenschaften in Göttingen.* 1887, **34**, pp. 53-100.

[3] GEERS, M. G. D., KOUZNETSOVA, V. G., BREKELMANS, W. A. M. Multi-scale computational homogenization: Trends and challenges. *Journal of Computational and Applied Mathematics* [online]. August 2010, **234**(7), pp. 2175-2182 [cited 2014-07-14]. ISSN 03770427. Available from: doi:10.1016/j.cam.2009.08.077

[4] NOVÁK, J., KUČEROVÁ, A. and ZEMAN, J. Compressing random microstructures via stochastic Wang tilings. *Physical Review E* [online]. October 2012, **86**(4) [cited 2014-07-14]. ISSN 1550-2376. Available from: doi:10.1103/PhysRevE.86.040104

[5] DOŠKÁŘ, M. *Wang Tilings for Real World Material Systems.* Praha, 2014. Master Thesis. České Vysoké Učení Technické v Praze. Fakulta stavební.

[6] WANG, H. Proving Theorems by Pattern Recognition - II. *Bell System Technical Journal* [online]. January 1961, **40**(1), pp. 1-41 [cited 2014-07-14]. ISSN 00058580. Available from: doi:10.1002/j.1538-7305.1961.tb03975.x

[7] CULIK II, K. An aperiodic set of 13 Wang tiles. *Discrete Mathematics* [online]. November 1996, **160**(1-3), pp. 245-251 [cited 2014-07-14]. ISSN 0012365X. Available from: doi:10.1016/S0012-365X(96)00118-5

[8] COHEN, M. F., SHADE, J., HILLER, S. and DEUSSEN, O. Wang Tiles for image and texture generation. *ACM Transactions on Graphics* [online]. July 2003, **22**(3), pp. 287-294 [cited 2014-07-14]. ISSN 07300301. Available from: doi:10.1145/882262.882265

[9] ZEMAN, J. *Analysis of Composite Materials with Random Microstructure.* Praha, 2003. Doctoral Thesis. České Vysoké Učení Technické v Praze. Kloknerův ústav.

[10] HILL, R. Elastic properties of reinforced solids: Some theoretical principles. *Journal of the Mechanics and Physics of Solids* [online]. September 1963, **11**(5), pp. 357-372 [cited 2014-07-14]. ISSN 00225096. Available from: doi:10.1016/0022-5096(63)90036-X

[11] NIEZGODA, S. R., TURNER, D. M., FULLWOOD, D. T., KALIDINDI, S. R. Optimized structure based representative volume element sets reflecting the ensemble-averaged 2-point statistics. *Acta Materialia* [online]. August 2010, **58**(13), pp. 4432-4445 [cited 2014-07-14]. ISSN 13596454. Available from: doi:10.1016/j.actamat.2010.04.041

[12] KANIT, T., FOREST, S., GALLIET, I., MOUNOURY, V., JEULIN, D. Determination of the size of the representative volume element for random composites: statistical and numerical approach. *International Journal of Solids and Structures* [online]. June 2003, **40**(13-14), pp. 3647-3679 [cited 2014-07-14]. ISSN 00207683. Available from: doi:10.1016/S0020-7683(03)00143-4

[13] DIRRENBERGER, J., FOREST, S., JEULIN, D. Towards gigantic RVE sizes for 3D stochastic fibrous networks. *International Journal of Solids and Structures* [online]. June 2014, **51**(2), pp. 359-376 [cited 2014-07-14]. ISSN 00207683. Available from: doi:10.1016/j.ijsolstr.2013.10.011

[14] HUET, C. Application of variational concepts to size effects in elastic heterogeneous bodies. *Journal of the Mechanics and Physics of Solids* [online]. January 1990, **38**(6), pp. 813-841 [cited 2014-07-14]. ISSN 00225096. Available from: doi:10.1016/0022-5096(90)90041-2

DOUBLE DRUCKER-PRAGER CRITERION OF PLASTICITY FOR CONCRETE

Josef FIEDLER[1], **Tomáš KOUDELKA**[2]

***Abstract**: Two Drucker-Prager yield functions are used to define a nonlinear material model for concrete that is used for tri-axial analysis of plasticity. One function is to approximate tensile stress area the other compression area. Both functions are connected with a first derivative singularity that is solved on the level of the stress invariants by using imaginary tangent as a local yield function. Computation is performed by SIFEL (Simple Finite Element) solver using the Finite Element Method (FEM).*

***Keywords**: Double Drucker-Prager, Concrete Plasticity Model, Finite Element Method*

INTRODUCTION

Given that behavior of concrete in tension and compression is very different, creation of proper material model needs a special treatment. By joining two Drucker-Prager (DP) yield conditions [1] one can obtain two different approaches in a single material model that can solve tri-axial stress states. The first condition shall be set to describe tension and the other compression. In the paper, there will be a description of the parameter setting to properly cover the stress areas and basic principles of stress return including the solution to singularities of the model. There will be also described basic principles of plasticity in Finite Element Method (FEM) and also an essence of the Cutting Plane Method. Eventually, all findings will be implemented into the FEM solver SIFEL [2] and results will be presented afterwards.

AN ELEMENTARY CHARACTERISTICS OF DP CRITERION

DP yield function [3] is defined as follows

$$f(\boldsymbol{\sigma}) = \alpha_{\phi} I_1(\boldsymbol{\sigma}) + \sqrt{J_2(\boldsymbol{\sigma})} - \tau_0, \qquad (1)$$

[1]Bc. Josef Fiedler, Department of Mechanics, Faculty of Civil Engineering, Czech Technical University in Prague, josef.fiedler@fsv.cvut.cz

[2]Ing. Tomáš Koudelka, Ph.D., Department of Mechanics, Faculty of Civil Engineering, Czech Technical University in Prague, koudelka@cml.fsv.cvut.cz

where α_ϕ and τ_0 are the parameters of the model. τ_0 represents the yield strength in shear and α_ϕ friction angle**.** I_1 is the first invariant of the stress tensor and J_2 is the second invariant of the deviatoric stress tensor. This yield condition creates a cone, if displayed in the principle stress space.

A DOUBLE DP CRITERION, PARAMETERS OF THE MODEL

Each yield condition shall be set by using parameters α_ϕ and τ_0 according to which stress area it is supposed to describe. DP condition intended for compression is obtained by the following adjustment of parameters [4]

$$\alpha_\phi = \frac{\sqrt{3}}{3}\frac{f_b - f_c}{2f_b - f_c}, \quad \tau_0 = f_c \frac{\sqrt{3} - 3\alpha_\phi}{3}, \tag{2}$$

where f_c represents the strength in axial compression and f_b in biaxial compression.

For approximation of tensile stress area, following set of parameters is used

$$\alpha_\phi = \frac{\sqrt{3}}{3}\frac{f_c - f_t}{f_c + f_t}, \quad \tau_0 = f_c \frac{\sqrt{3} - 3\alpha_\phi}{3}, \tag{3}$$

where f_t is the tensile strength..

Resulting double DP criterion dependent on stress invariant is displayed as follows

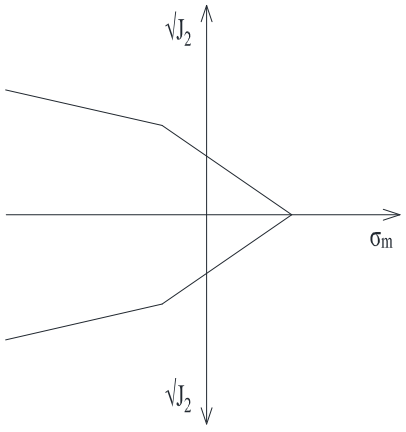

Fig. 1 Double DP in axial system of stress invariants

For better understanding, the model is presented in case of plane stress Fig. 2 (for values f_c = 30MPa, f_t =3MPa, f_b = 1,2 f_c). Its approximations of areas of axial tension and compression and biaxial compression are very satisfactory but it is inaccurate in biaxial tension. Nevertheless, a reduction of number of first derivative discontinuities is the biggest advantage (compared to the combination of DP and Rankine criterion [5]), thus it represents significant simplification of numerical computation.

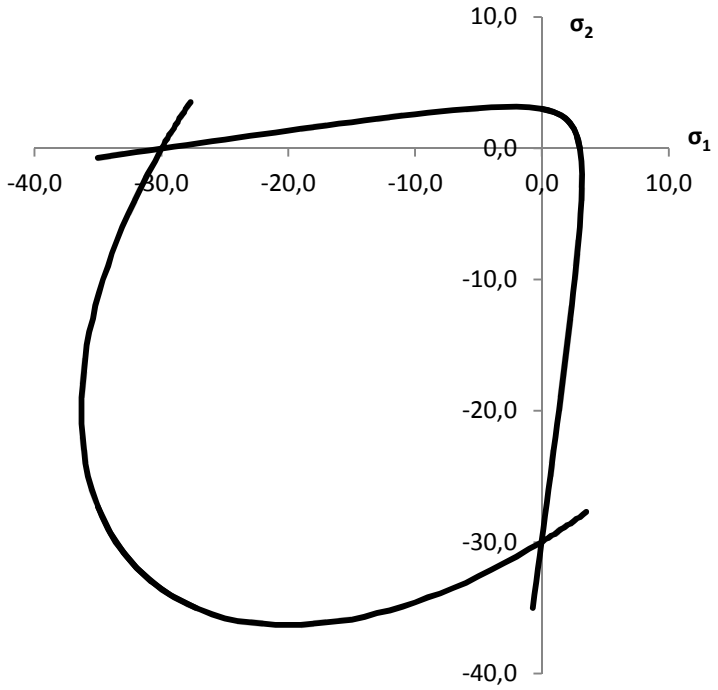

Fig 2. Double DP model in plane stress

PLASTICITY IN FINITE ELEMENT METHOD

A yield condition for material models considering plasticity [3] [6] is generally expressed as

$$f(\boldsymbol{\sigma}, \boldsymbol{q}) = 0\,, \tag{4}$$

where $\boldsymbol{\sigma}$ is the stress tensor, $\boldsymbol{q}$ is the vector of internal variables and f is the yield function. The stress state expressed by Eq. 4 means that the material exhibits plastic flow. If values of the yield function are negative $f < 0$, the material is located in elastic stress state. Stress states where yield function $f > 0$ are not admissible.

Assuming the elastoplastic behaviour of the material, the total strain tensor can be decomposed as follows

$$\boldsymbol{\varepsilon} = \boldsymbol{\varepsilon}_e + \boldsymbol{\varepsilon}_p \tag{5}$$

where $\boldsymbol{\varepsilon}$ is the total strain, $\boldsymbol{\varepsilon}_e$ is the elastic strain and $\boldsymbol{\varepsilon}_p$ is the plastic strain. The stress is directed by the elastic strain and it is defined by

$$\boldsymbol{\sigma} = \boldsymbol{D}_e \boldsymbol{\varepsilon}_e \tag{6}$$

where $\boldsymbol{D}_e$ is the initial elastic stiffness tensor.

The evolution of plastic flow can be firstly expressed as associated flow rule

$$\dot{\boldsymbol{\varepsilon}}_p = \dot{\gamma}\frac{\partial f}{\partial \boldsymbol{\sigma}} \tag{7}$$

and secondly as nonassociated flow rule

$$\dot{\boldsymbol{\varepsilon}}_p = \dot{\gamma}\frac{\partial g}{\partial \boldsymbol{\sigma}} \tag{8}$$

where $\dot{\gamma}$ is the rate of plastic multiplier, which indicates the magnitude of the plastic strain and the gradients give the direction of plastic strains. Functionality of above mentioned equations is conditioned by following expressions

$$\dot{\gamma} \geq 0, \;\; f \leq 0, \;\; \dot{\gamma} f = 0. \tag{9}$$

The last expression states that if increment of plastic multiplier $\dot{\gamma} > 0$ yield condition has to be fulfilled by $f = 0$. Otherwise material is found in elastic stress state $f < 0$ and plastic multiplier has to be $\dot{\gamma} = 0$.

The rate of plastic multiplier can be expressed as

$$\dot{\gamma} = \frac{\left(\frac{\partial f}{\partial \boldsymbol{\sigma}}\right)^T \boldsymbol{D}_e \dot{\boldsymbol{\varepsilon}}}{\left(\frac{\partial f}{\partial \boldsymbol{\sigma}}\right)^T \boldsymbol{D}_e \frac{\partial g}{\partial \boldsymbol{\sigma}} - \left(\frac{\partial f}{\partial \boldsymbol{q}}\right)^T \frac{\partial \boldsymbol{q}}{\partial \gamma}} \tag{10}$$

The increment of plastic strains is obtained by substituting Eq. 10 into Eq. 8

$$\dot{\boldsymbol{\varepsilon}}_p = \frac{\partial g}{\partial \boldsymbol{\sigma}}\dot{\gamma} = \frac{\frac{\partial g}{\partial \boldsymbol{\sigma}}\left(\frac{\partial f}{\partial \boldsymbol{\sigma}}\right)^T \boldsymbol{D}_e}{\left(\frac{\partial f}{\partial \boldsymbol{\sigma}}\right)^T \boldsymbol{D}_e \frac{\partial g}{\partial \boldsymbol{\sigma}} + H}\dot{\boldsymbol{\varepsilon}} \tag{11}$$

where

$$H = -\left(\frac{\partial f}{\partial \boldsymbol{q}}\right)^T \frac{\partial \boldsymbol{q}}{\partial \gamma} \tag{12}$$

is the hardening modulus.

CUTTING PLANE ALGORITHM

The cutting plane algorithm [3] is used for the returning trial stresses to admissible yield surface. It requires first derivatives of the yield function and plastic potential function and the yield function itself.

In the very first step it is necessary to determine the trial stresses $\boldsymbol{\sigma}_{tr}$

$$\boldsymbol{\sigma}_{tr} = \boldsymbol{D}_e\left(\boldsymbol{\varepsilon}^{(n)} - \boldsymbol{\varepsilon}_p^{(n-1)}\right) \tag{13}$$

The superscript *n* indicates the iteration step in the global iterative procedure. Assuming that the current trial stresses need to be revised, the evaluation of the correct stresses can be written

$$\boldsymbol{\sigma}^{(n)} = \boldsymbol{\sigma}^{tr} - \boldsymbol{D}_e \Delta\boldsymbol{\varepsilon}_p^{(n)} \tag{14}$$

$$\Delta\boldsymbol{\varepsilon}_p^{(n)} = \Delta\gamma^{(n)} \frac{\partial g^{(n-1)}}{\partial \boldsymbol{\sigma}} \tag{15}$$

$$\boldsymbol{\sigma}^{(n)} = \boldsymbol{\sigma}^{tr} - \boldsymbol{D}_e \Delta\gamma^{(n)} \frac{\partial g^{(n-1)}}{\partial \boldsymbol{\sigma}} \tag{16}$$

Combining Eq. (16) and the discrete consistency condition

$$f\left(\boldsymbol{\sigma}^{(n)}, \boldsymbol{q}^{(n)}\right) = 0 \tag{17}$$

leads to

$$f\left(\boldsymbol{\sigma}^{tr} - \boldsymbol{D}_e \Delta\gamma^{(n)} \frac{\partial g^{(n-1)}}{\partial \boldsymbol{\sigma}}, \boldsymbol{q}^{(n)}\right) = 0\,. \tag{18}$$

The Eq. (18) is solved by the Newton method

$$\Delta\gamma^{(n,k+1)} = \Delta\gamma^{(n,k)} + \delta\gamma^{(n,k)} \tag{19}$$

$$\boldsymbol{\sigma}^{(n,k+1)} = \boldsymbol{\sigma}^{(n,k)} - \delta\gamma^{(n,k)} \boldsymbol{D}_e \frac{\partial g}{\partial \boldsymbol{\sigma}^{(n-1)}} \tag{20}$$

$$\boldsymbol{q}^{(n,k+1)} = \boldsymbol{q}^{(n,k)} - \delta\gamma^{(n,k)} \frac{\partial \boldsymbol{q}^{(n,k)}}{\partial \gamma} \tag{21}$$

where the superscript *k* indicates the inner iteration step in the stress return algorithm. The increment of the parameter $\delta\gamma$ is evaluated every step by the following expression

$$\delta\gamma^{(n,k)} = \frac{f^{(n,k)}}{\left(\dfrac{\partial f^{(n,k)}}{\partial \boldsymbol{\sigma}}\right)^T \boldsymbol{D}_e \left(\dfrac{\partial g^{(n,k)}}{\partial \boldsymbol{\sigma}}\right) + H^{(n,k)}} \tag{22}$$

A PRINCIPLE OF NUMERICAL COMPUTATION

As mentioned above the cutting plane algorithm requires a yield function and derivatives of the yield function and a plastic potential function. The elementary issue of the model is to determine which surface one shall return to, in other words, which yield function and derivatives shall be used in the iterative process. The first derivative singularities have to be treated separately.

The whole problem is solved on the level of the stress invariants. The area of the inadmissible stress states is divided into different sections. To every section a corresponding yield function, which shall be returned to, is assigned. In case of the section that is connected to the point of first derivative discontinuity (there are 2 all together), there has to be set up an imaginary tangent. This tangent is created as the normal from the connecting line between the point of discontinuity and the point of trial stress state. Afterwards, it is considered as a local yield function and with its derivatives can be used in the cutting plane algorithm. The whole problem and all sections are displayed on the following diagram Fig. 3

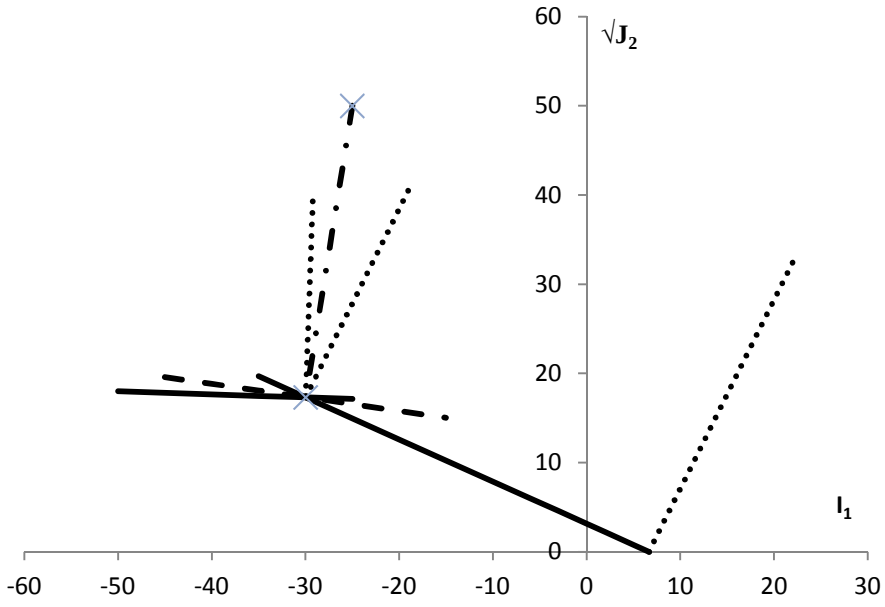

Fig. 3 Diagram of possible returns

The dashed line represents the tangent, the dash-dot line is the connecting line, the continuous lines are boundaries of admissible stress states and the dot lines define returning sections.

IMPLEMENTATION

The material model using double DP criterion has been implemented into computational package SIFEL [2] and tested on simple example shown in Fig. 4 (dimensions: 0,9m height, 1,8m length, 0,5m depth; material: concrete C30/37 f_c = 30MPa, f_t =3MPa, f_b = 1,2 f_c - double DP plasticity model)

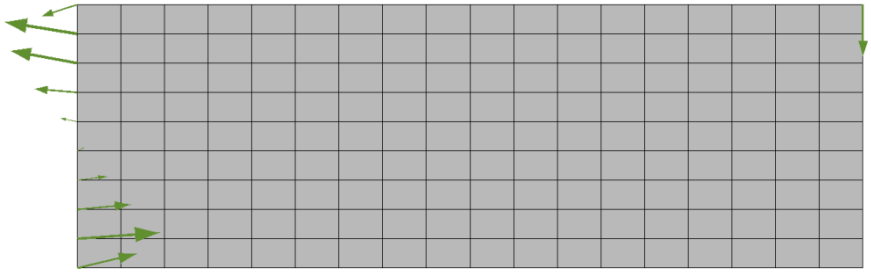

Fig. 4 Input topology + reactions

This concrete girder has been loaded by the vertical force that can be seen in the upper right corner and has been supported alongside the left edge, where the proper reactions are displayed. Calculation has been controlled by increments of the loading force and reached the maximum value 123,0kN. Tensile strength of concrete has been reached and developing plastic strains can be seen on the Fig. 5 below.

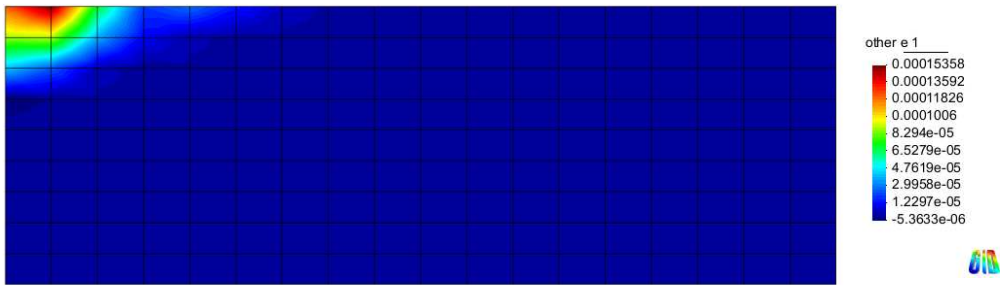

Fig. 5 Plastic strains

The development of the plastic strains has an effect of the stress distribution on the height of the cross-section, which is displayed on the Fig. 6. One can clearly observe that the values in compression are higher than in tension and the stress distribution on the height is no longer linear.

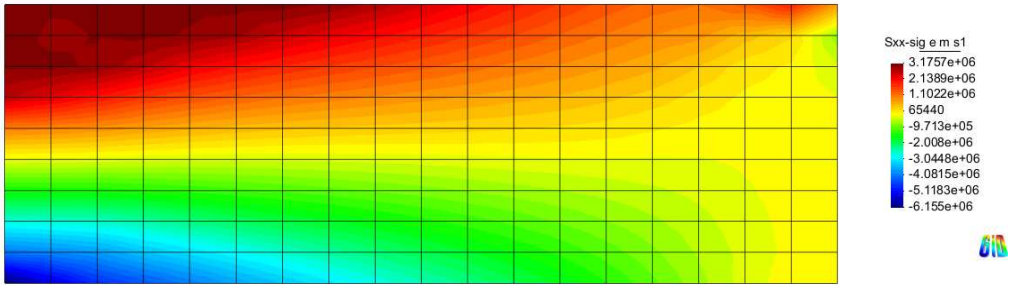

Fig. 6 Distribution of the normal stress σ_x

CONCLUSION

In the paper, there were a solution of difficulties in the double DP plasticity model such as setting parameters and solution of singularities, elementary explanation of numerical computation of the material model and plasticity and results from the implementation of the model into FEM solver SIFEL.

On the note of prospects, it is currently being worked on adding a hardening parameter to the model, which could enable a post-peak analysis.

ACKNOWLEDGEMENT

The financial support of this experiment by the Faculty of Civil Engineering, Czech Technical University in Prague (SGS project No. 14/029/OHK1/1T/11) is gratefully acknowledged.

REFERENCES

[1] HAMON, F., *Constitutive law BETON_DOUBLE_DP with double Drucker-Prager criterion for the cracking and the compression of the Résumé.* 2013, R7.01.03.

[2] KRUIS, J., KOUDELKA, T. and KREJČÍ T. (2001-2014). *Simple Finite Element (SIFEL).* Available from: http://ksm.fsv.cvut.cz/~sifel/.

[3] JIRÁSEK, M. and BAŽANT, Z. P., *Inelastic Analysis of Structures*. 1st ed. Wiley, Chichester, 2002, 757 p. ISBN 0-471-89716-6.

[4] JIRÁSEK, M. and ZEMAN, J., *Přetváření a porušování materiálů.* 2006, ČVUT, Praha.

[5] FEENSTRA, P. H. and BORST, R. de, A Composite Plasticity Model for Concrete, *International Journal of Solids and Structures, 1996,* 33: 707-730.

[6] de SOUZA NETO, E.A., PERIĆ, D. and OWEN, D.R.J., *Computational Methods for Plasticity – Theory and Applications.* 1st ed. Wiley, Chichester, 2008, 816 p. ISBN 978-0-470-69452-7.

DETERMINATION OF FINITE ELEMENT DISCRETIZATION BASED ON COVARIANCE FUNCTION PARAMETERS

Jan HAVELKA[1], **Jan SÝKORA**[2], **Anna KUČEROVÁ**[3]

Abstract: *Uncertainty propagation is becoming more popular approach to capture the randomness in given systems. One of substantial elements of relevance is the choice of covariance function that drives the spatial distribution of randomness. A majority of algorithms are using various prescribed covariance functions which are differently sensitive to domain discretization. This paper is focused on the determination of discretization based on given parameters.*

Keywords: *Uncertainty propagation, finite element method, covariance function, discretization error, random field*

INTRODUCTION

Current needs are driving computational mechanics to extend existing models which results in complex problems. Due to safety reasons a lot of work has been devoted to tasks involving probability and uncertainty in these models. The uncertainty could appear in various forms and may be distributed in space and/or time. By form of appearance it is meant that one can be uncertain about boundary conditions, material properties, geometry and other model parameters which comes from real measurements or assumptions [1]. The actual source of uncertainty could be accounted to lack of accuracy of measurements or lack of measurements, i.e. unfamiliarity with the environment.

This article focuses on the accuracy of representation of the input information that is characterizing randomness in the system before addressing the differential equation and gives an estimate of finite element discretization properties depending on covariance function parameter values. In other words, this paper provides an overview of the principles of discretization choice in the approximation of eigenvalues of the covariance function.

[1] Ing. Jan Havelka, Faculty of Civil Engineering, Department of Mechanics, Czech Technical University in Prague, jan.havelka.1@fsv.cvut.cz

[2] Ing. Jan Sýkora, PhD., Faculty of Civil Engineering, Department of Mechanics, Czech Technical University in Prague, jan.sykora.1@fsv.cvut.cz

[3] Ing. Anna Kučerová, PhD., Faculty of Civil Engineering, Department of Mechanics, Czech Technical University in Prague, anicka@cml.fsv.cvut.cz

Problem definition

Since the analytical formula for eigenfunctions for arbitrary domain is not generally known [2], we will consider spatially discretized eigenvalue problem which is defined by following equation

$$\mathbf{W}\phi_i = \lambda_i \mathbf{M}\phi_i, \tag{1}$$

where ϕ_i and λ_i are eigenvectors and eigenvalues respectively, $\mathbf{W} = \mathbf{MCM}$ is a symmetric positive semi-definite matrix [3, 4] with $\mathbf{M}$ being a Gram matrix defined by equation (2), matrix $\mathbf{C}$ is obtained by projection of covariance function (3) on the finite element (FE) mesh. Matrix $\mathbf{C}$ is by definition symmetric and positive semi-definite [3, 4].

$$M_{ij} = \int_D N_i(\mathbf{x}) N_j(\mathbf{x}) \, \mathrm{d}A, \quad i,j = 1,\ldots,n, \tag{2}$$

where $\mathbf{N}(\mathbf{x}) = (N_1(\mathbf{x}),\ldots,N_n(\mathbf{x}))$ are spatial basis functions and n is number of FE nodes.

Further we will consider exponential covariance function given by following equation

$$C_{\kappa}^{(exp)}(\mathbf{x}) \;=\; \widetilde{\sigma}^2 \exp\left[-\left(\frac{x-x'}{\sqrt{2}l_x}\right)^2 - \left(\frac{y-y'}{\sqrt{2}l_y}\right)^2 \right], \tag{3}$$

where l_x a l_y are correlation lengths [1] and $\widetilde{\sigma}$ is standard deviation.

Eigenvectors are then normalized by following equation

$$\hat{\phi}_i = \frac{\phi_i}{\phi_i^T \mathbf{M} \phi_i}, \quad i = 1,\ldots,n, \tag{4}$$

and the eigenvalues are sorted in descending order

$$\lambda_1 > \lambda_2 > \ldots > \lambda_n. \tag{5}$$

METHODOLOGY

For the purpose of determining the error a square domain with dimensions 20×20 [m] was chosen. The domain is uniformly discretized with linear triangular elements with element size s_e, which is defined as the length of the side of the triangle, see table 1. Example of discretization can be seen in figure 1.

As eigenvectors are normalised, only eigenvalues play a role of weight with which the eigenvectors

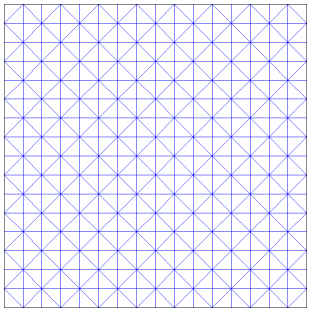

Fig. 1 Example of discretization (mesh c=3 according to table 1)

enter into the calculation. Therefore the error measure was chosen according to the following formula

$$Err_c = \frac{\sum_{i=1}^{n}(\lambda_i^{(1)} - \lambda_i^{(c)})}{\sum_{i=1}^{n}\lambda_i^{(1)}}, \quad c = 1, \cdots, 5, \tag{6}$$

where $\lambda_i^{(1)}$ is i-th eigenvalue computed using fine mesh and $\lambda_i^{(c)}$ is i-th eigenvalue computed using coarse mesh, superscript (c) indicates the mesh discretization in table 1.

Tab. 1 Mesh properties

c	Elements	Nodes	s_e
1	8192	4225	0.3125
2	2048	1089	0.625
3	512	289	1.25
4	128	81	2.5
5	32	25	5

Figure 2 shows the error threshold for the ratio of element size s_e and correlation length l_c.

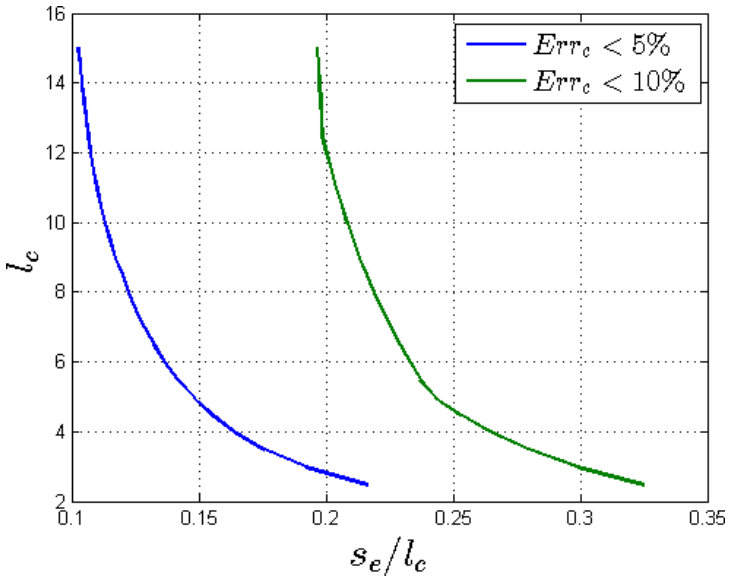

Fig. 2 Error threshold defined by equation (6)

CONCLUSION

From figure 2 it can be seen what is the dependency between element size and correlation length for given error threshold. One can also recognize the general rule that says: the greater correlation length, the greater element size can be. Although the law is not linear dependent for given covariance function, one can say that $s_e/l_c < 0.35$ is safe choice of discretization for $l_c \in \langle 1; 15 \rangle$.

ACKNOWLEDGEMENT

The financial support of this research by the SGS14/028/OHK1/1T/11 (Modelling of random heterogeneous materials) and P105/12/0331 (Efficient solvers for transport processes in saturated and unsaturated porous media) is gratefully acknowledged.

REFERENCES

[1] HAVELKA, J. *Efektivní metody pro propagování nejistot v popisu proudění podzemní vody.* Praha, 2014. Diploma Thesis. České vysoké učení technické v Praze. Fakulta stavební.

[2] XIU, D. *Numerical methods for stochastic computations: a spectral method approach.* Princeton University Press, 2010. ISBN 978-0-691-14212-8.

[3] KEESE, A. *Numerical solution of systems with stochastic uncertainties. A general purpose framework for stochastic finite elements.* Braunschweig, 2003. PhD Thesis. Department of Mathematics and Computer Science.

[4] ROSIĆ, B. *Variational Formulations and Functional Approximation Algorithms in Stochastic Plasticity of Materials* Braunschweig, 2013. PhD Thesis. Department of Mathematics and Computer Science.

CRITICAL ASSESSMENT OF THE METHODOLOGY FOR SHRINKAGE UPDATING

Petr HAVLÁSEK[1], Milan JIRÁSEK[2]

Abstract: *The methodology [1] for shrinkage updating needs to be due to the ill-posedness of the problem different from the creep updating procedure. It assumes on a similarity between the shrinkage and drying processes; both processes possess a characteristic time called shrinkage/water-loss halftime. Using the short-time shrinkage data together with the shrinkage half-time, the shrinkage development and its ultimate value can be determined uniquely. However, validation of this methodology on experimental data [2], [3] has shown that the linear relationship between the shrinkage and water loss halftimes is not realistic and together with a small error made in the estimate of the ultimate water loss can cause a big error in the prediction of the ultimate shrinkage.*

Keywords: *shrinkage, moisture loss, updating, concrete, modeling*

INTRODUCTION

The goal of the proposed methodology [1] is to improve the initial prediction of the B3 model by utilizing the short-time shrinkage and water loss measurements. The capabilities of this method are demonstrated on the experimental data of Granger [2] and Aguilar [3].

On contrary to creep, shrinkage updating based only on shrinkage measurements represents an ill-posed problem. Fig. 1a shows two functions with shrinkage halftimes 100 and 300 days and significantly different ultimate values are almost indistinguishable during the first 50 days of drying. Comparing to creep, higher initial shrinkage does not necessarily mean that its final value (or its value after a certain period) would be higher than of a different concrete which initially exhibits lower shrinkage, Fig. 1b.

The shrinkage updating procedure proposed in [1] stems from the similarity between the shrinkage and the drying process; both can be described with the function of the same form. They occur almost simultaneously and their relationship only slightly differs from linear. If the final value of the moisture loss at given humidity $\Delta w_\infty(h_{\mathrm{env}})$ is known, the drying halftime τ_w can be then fitted/optimized based

[1] Ing. Petr Havlásek, University Centre for Energy Efficient Buildings, Czech Technical University in Prague, petr.havlasek@gmail.com

[2] prof. Ing. Milan Jirásek, DrSc. Faculty of Civil Engineering, Czech Technical University in Prague, milan.jirasek@fsv.cvut.cz

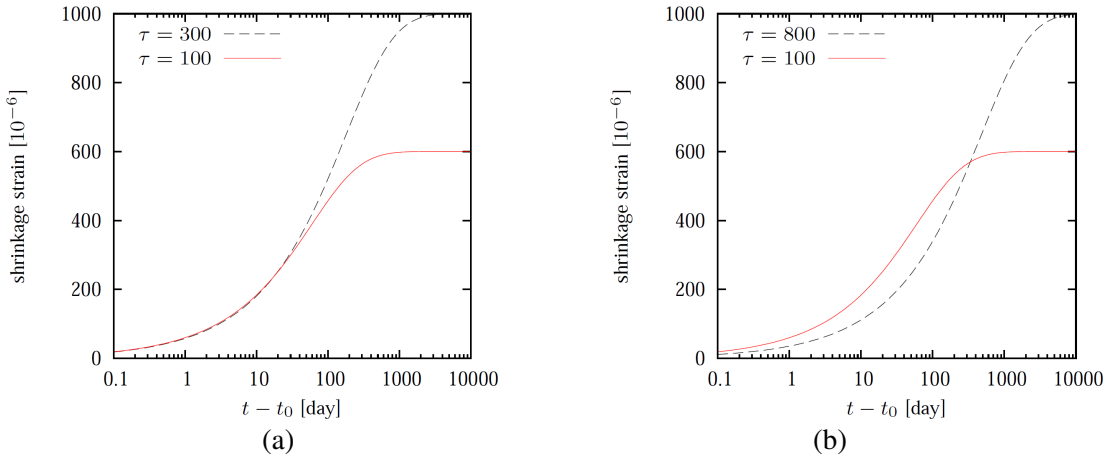

Fig. 1 Illustration of two shrinkage histories (a) with almost identical values during the first 50 days of drying but with different ultimate values, (b) giving misleading initial assumption of the ultimate value

on the short time measurements. Provided that there exists the link between the shrinkage and drying halftime, τ_{sh} can be computed in the next step. As the final step, the ultimate shrinkage is determined using least-squares fitting, keeping the previously computed value of τ_{sh} fixed.

The recommended procedure [1] can be subdivided into two parts, first it is necessary to achieve an accurate shrinkage prediction of the experimental specimen and then to update the parameters of the B3 model which will be used for the real structure.

The ultimate value of water loss is affected mainly by the relative humidity of the ambient environment, amount of water and of cementitious materials in concrete mixture, degree of hydration and the type of concrete curing. If one knows the total amount of evaporable water $\Delta w_\infty(h_{\text{env}} = 0)$, the moisture loss for a specified relative humidity $\Delta w_\infty(h_{\text{env}})$ can be computed from the (measured or assumed) desorption isotherm. In case of water/moist curing the only possibility how to determine $\Delta w_\infty(h_{\text{env}} = 0)$ is to oven-heat the specimen to 105–110 °C and to measure the weight difference. If no additional water was added during curing (specimen was sealed), then it can be roughly estimated based on concrete composition as the amount of added water from which is subtracted the chemically bound water which is usually in the range 0.18–0.26 of the cement content, the typical value is 0.25.

EXPERIMENTAL DATA

Granger's Ph.D. thesis [2] studies creep and shrinkage of concrete used in six French nuclear power plants. Experimental data are provided for basic creep, autogenous shrinkage, drying shrinkage and water loss. Experimental data for drying creep are missing; Granger presents merely the results of numerical simulations. Shrinkage was measured on concrete cylinders exposed to $h_{\text{env}} = 50\%$ after 28 days, until then the specimen was sealed. The cylinders were 1 m in height (0.5 m gauge length) and 16 cm in diameter, the top and bottom surfaces were kept sealed throughout the experiment.

Extensive study published in the Ph.D. thesis of Aguilar [3] contains a broad set of experimental data

on shrinkage and moisture loss of concrete prisms of two different sizes (ASTM and DIN standard). The main aim was to analyze the influence of concrete mixture on drying shrinkage, because the local Chilean aggregates cause larger creep than usual (600–1300$\times 10^{-6}$). Many different concrete compositions were tested from which 94 were selected for the analysis. Even though the compositions were often quite different, the intended specific strength was 30 MPa.

Weight loss and shrinkage were measured on the same specimens. Length changes (shrinkage) were measured both on the lateral surface and between the specimen bases. The specimens were cast into standardized molds from which they were removed 24 hours ($\pm$2 hours) after casting. Just before the first reading, they were submerged into water for 30-60 minutes in order to attain temperature stability. Before the measurement, the surface was wiped with a cloth to remove excessive water. After the first reading, the prisms were returned for curing into the lime water where they were kept for another 6 days. Afterwards, the specimens were again superficially wiped and measured. The specimens were stored in a room with controlled environment: 50$\pm$4% relative humidity and 23$\pm$1.7°C. No sealing was used, the specimens were drying from all sides. Finally, the specimens were oven-dried at 110°C and the final weight was recorded

RESULTS

This paper presents only the most important findings; the whole detailed study can be found in the Ph.D. thesis of the first author [5].

All computations and numerical simulations were implemented and solved in Matlab program environment and in the FE package OOFEM [6], [7], [8]. Matlab served mainly for nonlinear least-squares fitting and data processing, while program OOFEM was used for more demanding and complex tasks - particularly for coupled simulations of creep and shrinkage with nonlinear moisture diffusion. The material model for creep and shrinkage was based on the modified Microprestress-solidification theory [9], [10], [11].

- The originally proposed function describing water loss in time $\Delta w(t) = \tanh(\sqrt{t/\tau_w})$ should be modified because it gives poor agreement with the experimental data in the early period of drying. It should be extended with another term which would correspond to water loss associated with emptying of large pores filled with water. This additional term is necessary not only for concrete that was cured in water (Aguilar), but also for sealed specimens (Granger).

- Granger's data indicate that having a certain experience, it is possible to predict the final value of the moisture loss from composition of the concrete mixture. The nonlinear (cubic) isotherm $\Delta w_\infty(h_{\rm env}) \approx \eta \left[1 - (h_{\rm env}/0.98)^3\right] \Delta w_\infty(0)$ tends to overestimate the assumed ultimate value, while the linear isotherm reaches only 60% of the expected value. The best agreement is obtained with the bilinear desorption isotherm.

- Based on Aguilar's data, the prediction of the ultimate water loss of the drying concrete specimen can be computed using two different methods providing comparable accuracy. The first one uses concrete composition, the second one makes use of the results of the oven-drying experiment.

- The correct value of the shrinkage halftime and a proper form of a shrinkage function are necessary for the correct shrinkage prediction. Having these two conditions fulfilled, the shrinkage can be predicted from experiment of very limited duration. With correct shrinkage halftime and a function which does not decribe well the initial period of drying, it is better to use only the last measured point.

- Aguilar's shrinkage data indicate that the shrinkage function $\varepsilon_{sh}(t) = \tanh\sqrt{\frac{t}{\tau_{sh}}}\varepsilon_{sh}^{\infty}(h_{\mathrm{env}})$ is not suitable, the function terminates too rapidly. Considerably smaller error is reached with the function $\varepsilon_{sh}(t) = \left(\frac{t}{t+\tau_{sh}}\right)^{q_{sh}}\varepsilon_{sh}^{\infty}(h_{\mathrm{env}})$ with exponent q_{sh} bigger than 0.5.

- The shrinkage data from the first 10 days of drying should be neglected.

- The originally proposed relationship between the halftimes $\tau_{sh} = 1.25\tau_w$ was found to be unrealistic. The shrinkage and drying halftimes are very sensitive to data, especially at the later stage. It was shown that even small changes can lead to completely different ratio. The linear relationship between τ_{sh} and τ_w is in any case very simplistic and can lead to considerable errors.

  As an example consider that the final water loss at given relative humidity Δw_{∞} was estimated 10% higher than the actual value. Using least squares, the computed drying halftime τ_w is 40% higher than the actual (see Fig. 2a). Even when the shrinkage halftime τ_{sh} could be computed with 100% accuracy from τ_w, the value of the final shrinkage $\varepsilon_{sh}^{\infty}$ would be 20% overestimated (considering also that the shrinkage function correctly captures the data in the whole range, see Fig. 2b). Taking into account the error induced by assuming on the linear realtionship between τ_w and τ_{sh} the error would be comparable to (maybe even exceed) the original (blind) prediction. For the B3 model [4] coefficient of variation is 34%.

- The ratio between the drying halftime and shrinkage halftime does not exhibit a uniform trend (see Fig. 3), this makes the estimation of τ_{sh} from τ_w is literally impossible.

- The predicted shrinkage magnitude based on concrete composition should be preserved and changed only when necessary. The originally recommended methodology can improve as well as deteriorate the blind prediction.

- The dependence of shrinkage on moisture loss is far from linear, more suitable is a "S"-shaped curve having three distinct parts: 1) substantial moisture loss and minor shrinkage strain - this part corresponds to emptying of large capillary pores, 2) approximately linear relationship between shrinkage and moisture loss, and 3) very slow moisture loss leading to almost no shrinkage strain

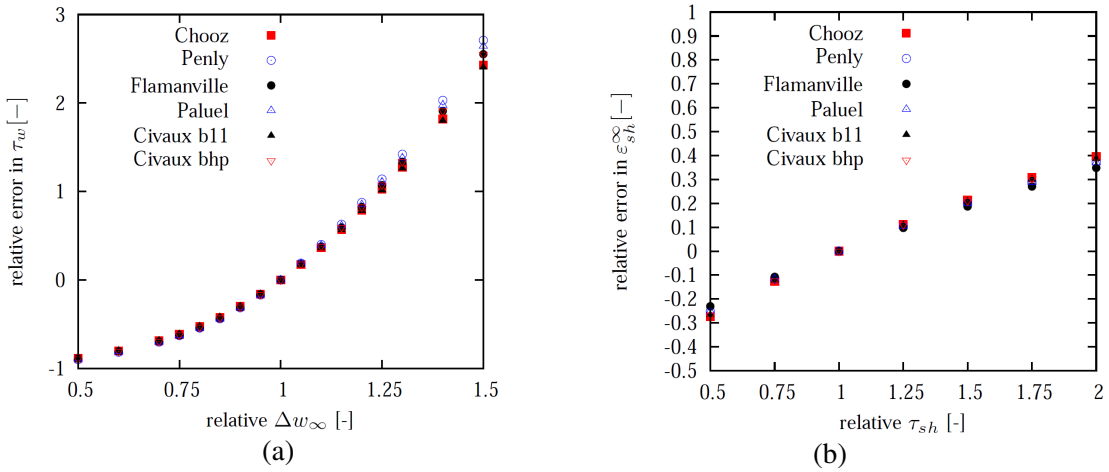

Fig. 2 (a) Influence of incorrectly assumed amount of evaporable water Δw_∞ on error in water-loss halftime τ_w, (b) influence of incorrectly assumed shrinkage halftime τ_{sh} on error in the ultimate shrinkage value

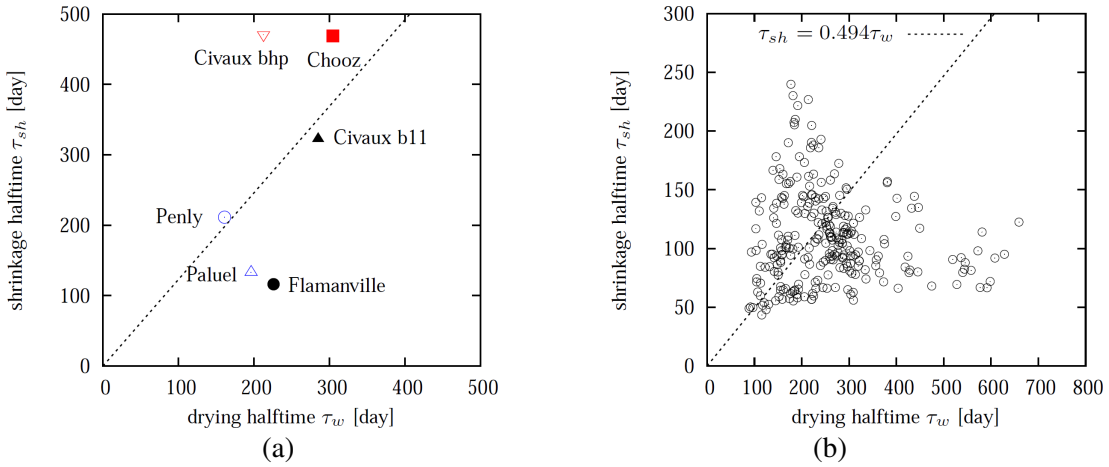

Fig. 3 Relationship between the shrinkage and drying halftimes obtained from fitting considering all measured points, (a) Granger's data, (b) Aguilar's data

- The finite element simulations in program OOFEM have revealed that the experimentally measured water loss data can be fitted with almost any isotherm provided that the difference between the moisture content at free saturation w_f and the content $w(h_{\text{env}})$ matches the asymptotic value of moisture loss. However, the shape of the desorption isotherm drastically influences the development of relative humidity which is the driving force of shrinkage. Highly nonlinear isotherms led to significant delay in the computed evolution of shrinkage compared to the experiment. In order to match the shrinkage data, the desorption isotherm had to be almost straight.

  The slope of the desorption isotherm (moisture capacity) identified in simulations of Aguilar's data is very steep; the average is 149 kg/m^3, which is far above the typical value 100 kg/m^3.

CONCLUSIONS

The methodology for shrinkage updating based on short-term measurements of water loss and shrinkage was critically assessed. It has been found that the key assumption of this approach – the linear relationship between the shrinkage halftime and water loss halftime – is not realistic. A small error made in the estimate of the ultimate water loss can lead to a big error in the prediction of the ultimate shrinkage.

ACKNOWLEDGEMENT

The financial support of this research by the Czech Technical University in Prague (SGS project No. SGS14/029/OHK1/1T/11) is gratefully acknowledged.

REFERENCES

[1] BAŽANT, Z.P. and BAWEJA, S. Justification and refinements of model B3 for concrete creep and shrinkage 2. Updating and theoretical basis. *Materials and Structures.* 1995, **28**, 488–495. ISSN 1359-5997.

[2] GRANGER, L. *Comportement differe du beton dans les enceintes de centrales nucleaires: analyse et modelisation (in French).* Paris, 1995. Doctoral Thesis. LCPC.

[3] AGUILAR, C.P. *Estudio del comportamiento y desarrollo de una metodologia de prediccion de la retraccion hidraulica de hormigones (in Spanish).* Santiago de Chile, 2005. Doctoral Thesis. Pontificia Universidad Catolica de Chile. Escuela de Ingenieria.

[4] BAŽANT, Z.P. and BAWEJA, S. Creep and shrinkage prediction model for analysis and design of concrete structures - model B3. *Materials and Structures.* 1995, **28**, 357–365. ISSN 1359-5997.

[5] HAVLÁSEK, P. *Creep and Shrinkage of Concrete Subjected to Variable Environmental Conditions.* Prague, 2014. Doctoral Thesis. Czech Technical University in Prague. Faculty of Civil Engineering.

[6] *OOFEM home page* [online]. [cited 2014-06-22]. Available from: http://www.oofem.org

[7] PATZÁK, B. and BITTNAR, Z. Design of object oriented finite element code. *Advances in Engineering Software* 2001, **32**(10-11), 759–767. ISSN 0965-9978.

[8] PATZÁK, B., RYPL, D. and BITTNAR, Z. Parallel explicit finite element dynamics with nonlocal constitutive models. *Computers & Structures* 2001, **79**(26-28), 2287-2297. ISSN 0045-7949.

[9] BAŽANT, Z.P, HAUGGAARD, A.B. and ULM, F. Microprestress-Solidification Theory of Concrete Creep: Reformulation and Improvement. *Journal of Engineering Mechanics* 1997, **123**(11), 1188–1194. ISSN 0733-9399.

[10] JIRÁSEK, M. and HAVLÁSEK, P. Microprestress-Solidification Theory of Concrete Creep: Reformulation and Improvement. *Cement and Concrete Research* 2014, **60**, 51–62. ISSN 0008-8846.

[11] BAŽANT, Z.P, HAVLÁSEK, P. and JIRÁSEK, M. Microprestress-solidification theory: Modeling of size effect on drying creep. In: *EURO-C 2014: Computational Modelling of Concrete Structures.* EH Leiden, The Netherlands: CRC Press/Balkema, 2014, pp. 749–758. ISBN 978-1-1380014-5-9.

COMPARISON OF THE LAYER SLAB MODEL WITH THE DISCRETE REINFORCEMENT MODEL

Martin HLAVAČKA[1], **Jan VOREL**[2]

Abstract: *The static behaviour of reinforced concrete structures has been an object of research for many years. In view of the complexity of the given topic and as reinforced concrete is of great importance for the building industry, this topic is attractive. A preliminary study of available approaches in finite element code OOFEM [1] are presented. The comparison of results on the layer slab model and on the discrete reinforcement model are shown in the paper.*

Keywords: *OOFEM, layer model, discrete reinforcement*

INTRODUCTION

The presented paper deals with an analysis of a reinforced concrete slab. The analysis has been carried out by means of OOFEM [1], a freeware with object-oriented architecture based on the finite element method. The behavior of the structure under static loading is discussed in this work. The archived numerical results (size and distribution of displacements and stresses) on two numerical models are shown and discussed. The former is the layer slab model, the latter is a model with discretely modelled reinforcement. Finally, the conclusions and recommendations for further development of this work are given.

THE STRUCTURE UNDER CONSIDERATION

The paper follows the foregoing work of authors [2] where a building structure loaded gradually with subsidence of the surrounding ground points was presented. The loading was caused by tunelling under the structure (see Fig. 1 and 2). An elastic model, two conditions based on damage mechanics and two conditions based on the plasticity condition were utilized to model the material of the building structure.

The achieved results clearly showed that a more precise model was necessary to capture the structural behaviour. In the paper, attention is paid to the models of slabs which highly influence the final response

[1] Ing. Martin Hlavačka, Department of Mechanics, Faculty of Civil Engineering, Czech Technical University in Prague, martin.hlavacka@fsv.cvut.cz

[2] Ing. Jan Vorel, Ph.D., Department of Mechanics, Faculty of Civil Engineering, Czech Technical University in Prague, jan.vorel@fsv.cvut.cz

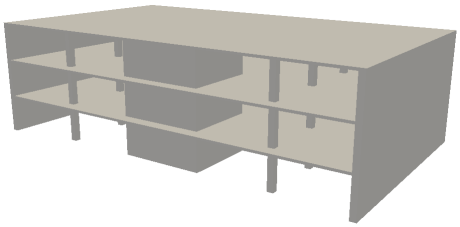

Fig. 1 Axonometric view on the building

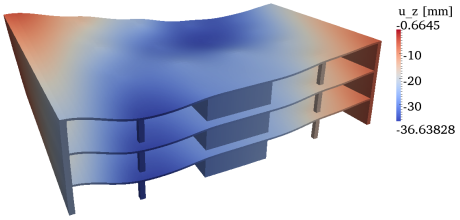

Fig. 2 Response of the building model loaded due to ground falls

as well as the computational cost.

The model based on the layered cross-section of the slab material is studied first. The layered cross section model is based on the geometrical hypothesis, that cross sections remain plane after deformation. Materials for each layer are specified separately. In this particular approach the concrete layer is defined as shown in Fig. 3. Then the reinforcement is placed in the tension part of the cross-section (see Fig. 3). The steel area is prescribed in such way that it corresponds to the common reinforcement ratio of concrete slabs, i.e.$\sim 1\%$. No secondary reinforcement or stirrups are considered.

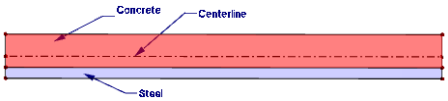

Fig. 3 Layer model of the slab

As an alternative approach the discrete reinforcement is modelled by means of reinforcing bars. Both slabs are supported at the corners and loaded in the grid points with forces representing the self-weight and imposed load. The slabs have dimensions of 2.0 $\times$ 2.0 m and a thickness of 0.2 m (see Fig. 4).

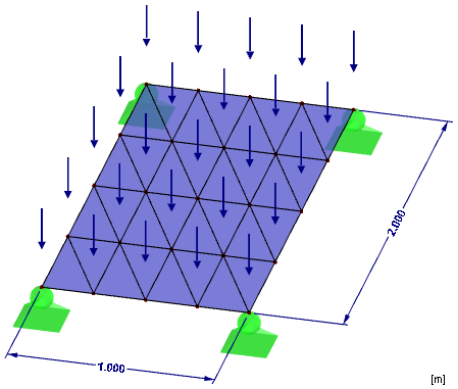

Fig. 4 Axonometric view on the slab model with the FE-grid and loading

The element RerShell has been chosen in the OOFEM library for the layered model of the slab. This is a triangular plane element based on the Mindlin hypothesis with a linear approximation of rotations, a quadratic approximation of the displacement field and six degrees of freedom at each node. The element tr_shell01 has been chosen for the model of the slab with discrete reinforcement. The properties of the element are the same as those of the element RerShell but the element tr_shell01 does not support the layered cross-section. The element truss3d with a linear approximation of the displacement field has been chosen for the reinforcement. The linear elastic isotropic material model has been chosen for both models of the slabs.

RESULTS AND DISCUSSION

As expected and evident from Figs. 5 and 6, both slabs had the same response with the given load type and chosen parameters. The maximum vertical displacement amounted to 0.12 mm. In Fig. 5 the reinforcing bars in the longitudinal direction are marked in white. When making a decision as to which slab model to use in the total structure model, time-consumption could be taken into account. The slab model with discrete reinforcement contains additional elements that define reinforcing bars, therefore time-consumption will be higher in this case. On the other hand, it can be supposed that the model response will be more accurate than in the model based only on the layer model of the slab.

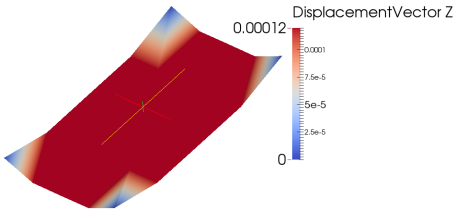

Fig. 5 Response of the layer model of the slab

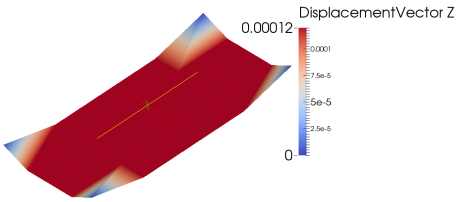

Fig. 6 Response of the model with the discrete reinforcement

In order to verify our assumption, a test was undertaken in which both models were loaded solely with a vertical force of 4 kN and the experiment was carried out on the models with a coarser grid. In Figs. 7 and 8 the response of the structure models are shown. The magnitude of the maximum displacement of 0.12 mm is the same; however, the total character of the displacements differs. It is very clear in Fig. 8 that the reinforcing bars act, due their stiffness, against the loading and assist the slab markedly to transfer the loading.

Elastic material has been used for the slabs in all cases. The option of a plastic material model with the von Mises condition for bars and the option of an isotropic damage model for concrete are not

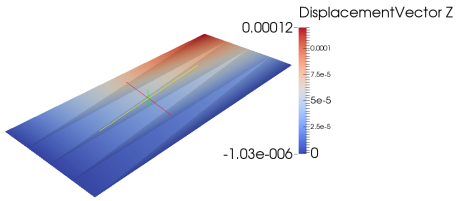

Fig. 7 Response of the layer model of the slab

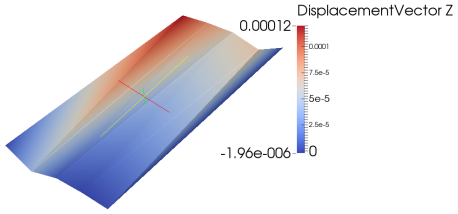

Fig. 8 Response of the model with the discrete reinforcement

implemented in the program OOFEM at present. Therefore, subsequent research will be focused on implementing these options in the interface of the program OOFEM.

CONCLUSION

The aim of the presented paper is to show the response character of two models of reinforced concrete slabs. The modelling was performed in the program OOFEM with elastic material parameters. As expected and verified it has been shown that the same response is obtained for both models for the common reinforcement ratio and the bending load of the slab. The choice of one model over the other thus results from the point of view of time-consumption of the modelling and from the point of view of calculation time, where, in the case of more complex structures, it has additionally been proven that more precise results are obtained from the model with discrete reinforcement. Subsequent research will be focused on implementing the damage material model for concrete in combination with the plastic condition for steel.

ACKNOWLEDGEMENT

The financial support of this research by the Czech Technical University in Prague (SGS project No. SGS14/028/OHK1/1T/11) is gratefully acknowledged.

REFERENCES

[1] PATZÁK, B., BITTNAR, Z. Design of object oriented finite element code. *Advances in Engineering Software,* 32(10-11):759–767, 2001. ISSN 0965-9978.

[2] HLAVAČKA, M. *Poruchy budov způsobené tunelováním* Praha, Diploma thesis, ČVUT v Praze, Fakulta stavební, 2012, 73 p.

ENHANCED TREFFTZ FINITE ELEMENT METHOD

Martin HORÁK[1], **Jan NOVÁK**[2]

Abstract: *Analysis of composite materials with inclusions is of interest in many engineering applications. Application of the standard finite element method may be computationally ineffective, since the finite element mesh must resolve all heterogeneity details. In this paper we present an alternative approach based on the Trefftz finite element formulation enhanced by micromechanical fields thereby leading to an effective method which overcomes the need of detailed discretization.*

Keywords: *Trefftz method, micromechanics, enrichment functions*

INTRODUCTION

During past decades Hybrid Trefftz Finite Element Method (HTFEM) has become very efficient tool for solving variety of boundary value problems. In contrast to the standard Finite Element Method (FEM), the Trefftz method uses two sets of displacement fields. First field is an auxiliary internal field chosen such that the homogenous part of the governing differential equation is satisfied a priory. The second field represents displacements on the element boundary and links the internal displacement fields among individual elements, i.e. ensures continuity conditions. Moreover, degrees of freedom associated with internal field are usually filtered out using static condensation and the HTFEM formulation yields the classical form that can be combined with conventional FEM. The main advantages with respect to the standard finite element method are

- Integration along the element boundaries
- Straightforward introduction of subscale phenomena such as crack or inclusion associated singularities

In this contribution we use HTFEM for description of composites materials with multiple inclusions. The strategy exploits so-called Eshelby solution to elliptical inhomogeneity in infinite media. It is used as the perturbation of the macroscopic field and is additively incorporated into the standard Trefftz finite

[1] Ing. Martin Horák, Faculty of Civil Engineering, Czech Technical University In Prague, nitramkaroh@seznam.cz

[2] Ing. Jan Novák, Ph.D, Faculty of Civil Engineering, Brno University of Technology and Czech Technical University In Prague, novakj@cml.fsv.cvut.cz

element basis. The main advantage rests upon the fact that the finite element mesh can be regular and does not need not to fully resolve the geometry of heterogeneities.

BASIC EQUATIONS

In this section we state equations for plane elasticity problem. The basic equations are (for the implementation purposes the matrix notation is used in the sequel)

- Equilibrium equation:

$$\mathbf{L}\boldsymbol{\sigma} = \mathbf{0} \tag{1}$$

- Kinematic equation:

$$\boldsymbol{\varepsilon} = \mathbf{L}^T \boldsymbol{u} \tag{2}$$

- Stress-strain law

$$\boldsymbol{\sigma} = \mathbf{D}\boldsymbol{\varepsilon} \tag{3}$$

- Boundary conditions

$$\boldsymbol{u} = \bar{\boldsymbol{u}} \quad on \quad \Gamma_u \tag{4}$$

$$\boldsymbol{A}\boldsymbol{\sigma} = \bar{\boldsymbol{t}} \quad on \quad \Gamma_t \tag{5}$$

In the equations above, $\boldsymbol{\sigma}$ denotes the stress vector

$$\boldsymbol{\sigma} = \begin{bmatrix} \sigma_x & \sigma_y & \sigma_{xy} \end{bmatrix} \tag{6}$$

$\boldsymbol{\varepsilon}$ is the strain vector

$$\boldsymbol{\varepsilon} = \begin{bmatrix} \varepsilon_x & \varepsilon_y & 2\varepsilon_{xy} \end{bmatrix} \tag{7}$$

$\boldsymbol{L}$ stands for the differential operator matrix

$$\boldsymbol{L} = \begin{bmatrix} \frac{\partial}{\partial x} & 0 & \frac{\partial}{\partial y} \\ 0 & \frac{\partial}{\partial y} & \frac{\partial}{\partial x} \end{bmatrix} \tag{8}$$

In the plane stress case, the elastic stiffness matrix $\boldsymbol{D}$ has the form

$$\boldsymbol{D} = \frac{E}{1-\nu^2} \begin{bmatrix} 1 & \nu & 0 \\ \nu & 1 & 0 \\ 0 & 0 & \frac{1-\nu}{2} \end{bmatrix} \tag{9}$$

While for the plane strain condition it reads as

$$\boldsymbol{D} = \frac{E(1-\nu)}{(1+\nu)(1-2\nu)} \begin{bmatrix} 1 & \frac{\nu}{1-\nu} & 0 \\ \frac{\nu}{1-\nu} & 1 & 0 \\ 0 & 0 & \frac{1-2\nu}{2(1-\nu)} \end{bmatrix} \tag{10}$$

Above E is the Young's modulus and ν represents the Poisson's ration. Matrix

$$\boldsymbol{A} = \begin{bmatrix} n_x & 0 & n_y \\ 0 & n_y & n_x \end{bmatrix} \tag{11}$$

resembles components of the unit normal vector to the boundary of the element domain, $\bar{\boldsymbol{u}}$and $\bar{\boldsymbol{t}}$ designate prescribed displacements and tractions, respectively. The entire boundary Γ can be decomposed such that $\Gamma = \Gamma_u \cup \Gamma_t$ and $\Gamma_u \cap \Gamma_t = 0$. In the Trefftz formulation, the traction boundary condition is rewritten in the weak sense

$$\int_{\Gamma_t} \boldsymbol{w}_1(\boldsymbol{A}\boldsymbol{\sigma} - \bar{\boldsymbol{t}})\, \mathrm{d}\Gamma \tag{12}$$

where $\boldsymbol{w}_1$ is a suitable energy consistent weighting function. The kinematic equation is also fulfilled only in the weak sense, namely

$$\int_{\Omega} \boldsymbol{w}_2(\boldsymbol{\varepsilon} - \boldsymbol{L}^T\boldsymbol{u})\, \mathrm{d}\Omega \tag{13}$$

By analogy to Equation (12), $\boldsymbol{w}_2$ in the above equation stands for a suitable weighting function. Moreover, integrating by parts, weak form of compatibility equation may be rewritten as

$$\int_{\Omega} \boldsymbol{w}_2(\boldsymbol{\varepsilon} - \boldsymbol{L}^T\boldsymbol{u})\, \mathrm{d}\Omega = \int_{\Omega} \boldsymbol{w}_2(\boldsymbol{\varepsilon} - (\boldsymbol{L}\boldsymbol{w_2})^T\boldsymbol{u})\, \mathrm{d}\Omega - \int_{\Gamma} \boldsymbol{A}\boldsymbol{w_2}^T\boldsymbol{u}\, \mathrm{d}\Gamma = \boldsymbol{0} \tag{14}$$

The last term can be decomposed as

$$\int_{\Gamma} \boldsymbol{A}\boldsymbol{w_2}^T\boldsymbol{u}\, \mathrm{d}\Gamma = \int_{\Gamma_t} \boldsymbol{A}\boldsymbol{w_2}^T\boldsymbol{u}\, \mathrm{d}\Gamma + \int_{\Gamma_u} \boldsymbol{A}\boldsymbol{w_2}^T\bar{\boldsymbol{u}}\, \mathrm{d}\Gamma \tag{15}$$

Since it is not possible to find a solution for both equations, the independent displacement field $\boldsymbol{u}_\Gamma$ on the interelement boundary is introduced. This leads to

$$\int_{\Omega} \boldsymbol{w}_2(\boldsymbol{\varepsilon} - \boldsymbol{L}^T\boldsymbol{u})\, \mathrm{d}\Omega = \int_{\Omega} \boldsymbol{w}_2(\boldsymbol{\varepsilon} - (\boldsymbol{L}\boldsymbol{w_2})^T\boldsymbol{u})\, \mathrm{d}\Omega - \int_{\Gamma_t} \boldsymbol{A}\boldsymbol{w_2}^T\boldsymbol{u}\, \mathrm{d}\Gamma - \int_{\Gamma_u} \boldsymbol{A}\boldsymbol{w_2}^T\bar{\boldsymbol{u}}\, \mathrm{d}\Gamma \tag{16}$$

HYBRID TREFFTZ FINITE ELEMENT APPROXIMATION

Within HTFEM formulation we have two independent displacement fields. The first field is related to interior of the element and is called intra-element field. The second field is related to element boundary. However, the numerical procedure is the same as in the conventional finite element approach. The intra-element displacement field is approximated as

$$\boldsymbol{u} = \boldsymbol{N}\boldsymbol{d} \tag{17}$$

where $\boldsymbol{N}$ is chosen such that the homogeneous equilibrium condition is satisfied pointwise. Thus, starting from equations (1) and (2) and making use of equation (17) we have

$$\boldsymbol{L}\boldsymbol{\sigma} = \boldsymbol{L}\boldsymbol{T}\boldsymbol{d} = \boldsymbol{L}\boldsymbol{D}\boldsymbol{L}^T\boldsymbol{N}\boldsymbol{d} = \boldsymbol{0} \tag{18}$$

where $\boldsymbol{T} = \boldsymbol{D}\boldsymbol{L}^T\boldsymbol{N}$is the matrix of stress approximation functions. Moreover $\boldsymbol{B} = \boldsymbol{L}^T\boldsymbol{N}$ we denote approximation matrix for strains. Construction of interpolation functions that satisfy the homogeneous equilibrium equation brings us to the so-called T-complete functions, which are not particularly described here, for detail see reference [1]. The boundary field enforce the continuity of the displacement fields among neighboring elements and is approximated as

$$\boldsymbol{u}_\Gamma = \boldsymbol{N}_\Gamma\boldsymbol{d}_\Gamma \tag{19}$$

where $\boldsymbol{N}_\Gamma$ is the interpolation matrix containing basis functions defined over the element boundary. For linear element it has the standard form

$$\boldsymbol{N}_\Gamma = \begin{bmatrix} \dfrac{1-\xi}{2} & \dfrac{1+\xi}{2} \end{bmatrix} \tag{20}$$

where ξ is the natural coordinate ranging from -1 to 1. Substituting of all the approximations into the weak forms in equations (12) and (16) we arrive at

$$\int_{\Gamma_t} \boldsymbol{w}_1(\boldsymbol{A}\boldsymbol{T}\boldsymbol{d} - \bar{\boldsymbol{T}})\,\mathrm{d}\Gamma = \boldsymbol{0} \tag{21}$$

and

$$\int_\Omega \boldsymbol{w}_2\boldsymbol{B}\boldsymbol{d} + (\boldsymbol{L}\boldsymbol{w}_2)^T\boldsymbol{N}\boldsymbol{d}\,\mathrm{d}\Omega - \int_{\Gamma_t} \boldsymbol{A}\boldsymbol{w}_2^T\boldsymbol{N}_\Gamma\boldsymbol{d}_\Gamma\,\mathrm{d}\Gamma = \int_{\Gamma_u} \boldsymbol{A}\boldsymbol{w}_2^T\bar{\boldsymbol{u}}\,\mathrm{d}\Gamma \tag{22}$$

Choosing weight function according suggestions made in [2] $\boldsymbol{w}_1 = \boldsymbol{N}_\Gamma$ and $\boldsymbol{w}_2 = \boldsymbol{T}$ yields

$$\int_{\Gamma_t} \boldsymbol{N}_\Gamma(\boldsymbol{A}\boldsymbol{T}\boldsymbol{d}\,\mathrm{d}\Gamma = \int_{\Gamma_t} \boldsymbol{N}_\Gamma \bar{\boldsymbol{t}}\,\mathrm{d}\Gamma \tag{23}$$

and

$$\int_\Omega \boldsymbol{T}\boldsymbol{B}\boldsymbol{d}\,\mathrm{d}\Omega - \int_{\Gamma_t} \boldsymbol{A}\boldsymbol{T}\boldsymbol{N}_\Gamma \boldsymbol{d}_\Gamma\,\mathrm{d}\Gamma = \int_{\Gamma_u} \boldsymbol{A}\boldsymbol{T}\bar{\boldsymbol{u}}\,\mathrm{d}\Gamma \tag{24}$$

Alternatively, recast in compact form

$$\begin{bmatrix} \boldsymbol{F} & -\boldsymbol{Q}^T \\ -\boldsymbol{Q} & \boldsymbol{0} \end{bmatrix} \begin{bmatrix} \boldsymbol{d} \\ \boldsymbol{d}_\Gamma \end{bmatrix} = \begin{bmatrix} \boldsymbol{p}_u \\ \boldsymbol{p}_t \end{bmatrix} \tag{25}$$

where

$$\boldsymbol{F} = \int_\Omega \boldsymbol{T}\boldsymbol{B}\,\mathrm{d}\Omega = \int_\Gamma \boldsymbol{A}\boldsymbol{T}\boldsymbol{N}\,\mathrm{d}\Gamma \tag{26}$$

$$\boldsymbol{Q} = \int_\Gamma \boldsymbol{N}_\Gamma \boldsymbol{A}\boldsymbol{T}\,\mathrm{d}\Gamma \tag{27}$$

and

$$\boldsymbol{p}_u = \int_\Gamma \boldsymbol{A}\boldsymbol{T}\bar{\boldsymbol{u}}\,\mathrm{d}\Gamma \tag{28}$$

$$\boldsymbol{p}_t = \int_\Gamma \boldsymbol{N}_\Gamma \bar{\boldsymbol{t}}\,\mathrm{d}\Gamma \tag{29}$$

Note that all the terms in equations (26)-(29) can be evaluated using boundary integration only. Using static condensation, intra-element degrees of freedom can be eliminated and the classical system of equations is achieved. This enables to couple the HTFEM with standard FEM. In particular, the global system reads as

$$\boldsymbol{K}\boldsymbol{d}_\Gamma = \boldsymbol{f} \tag{30}$$

where

$$\boldsymbol{K} = \boldsymbol{Q}\boldsymbol{F}^{-1}\boldsymbol{Q}^T \tag{31}$$

represents the stiffness matrix of the structure and

$$\boldsymbol{f} = \boldsymbol{p}_t - \boldsymbol{Q}\boldsymbol{F}^{-1}\boldsymbol{p}_u \tag{32}$$

is the right hand side load vector.

ENHANCED HTFEM

Our purpose is to describe body with heterogeneities, such as inclusions or voids. This can be done by enhancing the homogeneous approximation introduced in the previous chapter by a perturbation field. Stresses, strains and displacements can be therefore decomposed as $\boldsymbol{\sigma} = \boldsymbol{\sigma}^0 + \boldsymbol{\sigma}^*$, $\boldsymbol{\varepsilon} = \boldsymbol{\varepsilon}^0 + \boldsymbol{\varepsilon}^*$, and $\boldsymbol{u} = \boldsymbol{u}^0 + \boldsymbol{u}^*$, where superscripts ^{0} denote the macroscopic component and * indicate the perturbation part. Detailed description of derivation of the perturbation fields is not given here and readers are linked to the paper [2] for additional details. Here we only point out that the perturbation fields are derived from the well-known Eshelby solution of elliptical inhomogeneity in infinite elastic body. The total stress is thus approximated as

$$\boldsymbol{\sigma} = \left(\boldsymbol{T}^0 + \boldsymbol{T}^*\right) \boldsymbol{d} \tag{33}$$

$\boldsymbol{T}^0$ is the matrix of T-complete functions and $\boldsymbol{T}^*$ is the matrix containing the perturbation part of stress approximation function. Important property of perturbation fields is that these are self-equilibrated, so that following equation holds

$$\boldsymbol{L}\boldsymbol{\sigma} = \boldsymbol{L}\left(\boldsymbol{T}^0 + \boldsymbol{T}^*\right) \boldsymbol{d} = \boldsymbol{0} \tag{34}$$

Following the same procedure as in the previous chapter we end up with the extended system of algebraic equations

$$\begin{bmatrix} \boldsymbol{F}^* & -\boldsymbol{Q}^{*T} \\ -\boldsymbol{Q}^* & \boldsymbol{0} \end{bmatrix} \begin{bmatrix} \boldsymbol{d} \\ \boldsymbol{d}_\Gamma \end{bmatrix} = \begin{bmatrix} \boldsymbol{p}_u^* \\ \boldsymbol{p}_t^* \end{bmatrix} \tag{35}$$

where where

$$\boldsymbol{F}^* = \int_\Omega (\boldsymbol{T}^0 + \boldsymbol{T}^*)(\boldsymbol{B}^0 + \boldsymbol{B}^*)\, \mathrm{d}\Omega = \int_\Gamma \boldsymbol{A}(\boldsymbol{T}^0 + \boldsymbol{T}^*)(\boldsymbol{N}^0 + \boldsymbol{N}^*)\, \mathrm{d}\Gamma \tag{36}$$

$$\boldsymbol{Q} = \int_\Gamma \boldsymbol{N}_\Gamma \boldsymbol{A}(\boldsymbol{T}^0 + \boldsymbol{T}^*)\, \mathrm{d}\Gamma \tag{37}$$

and

$$\boldsymbol{p}_u = \int_\Gamma \boldsymbol{A}(\boldsymbol{T}^0 + \boldsymbol{T}^*)\bar{\boldsymbol{u}}\, \mathrm{d}\Gamma \tag{38}$$

The expressions for the components of the vector $\boldsymbol{p}_t$ remains the same as in the previous case.

NUMERICAL EXAMPLE

The HTFEM element has been implemented in open finite element code OOFEM, see [3]. In this section we show one numerical example of a single inclusion test. The inclusion in placed in the square piece of isotropic elastic matrix fixed at the left edge and pulled at the right edge. For the comparison purposes, we first simulated this problem using standard finite element method with 2560 elements, see Fig. 1(a).

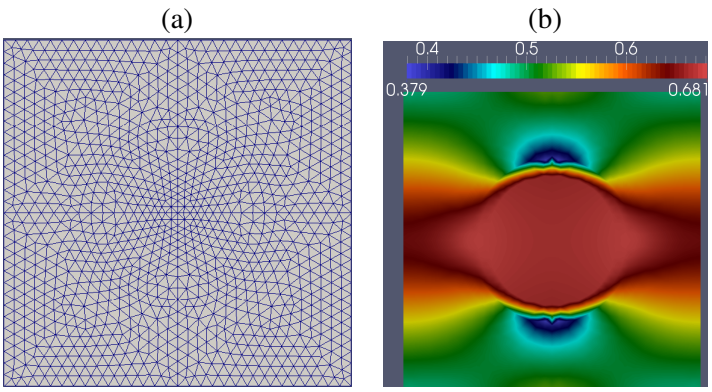

Fig. 1 Single Inclusion test: (a) FEM mesh, (b) FEM results

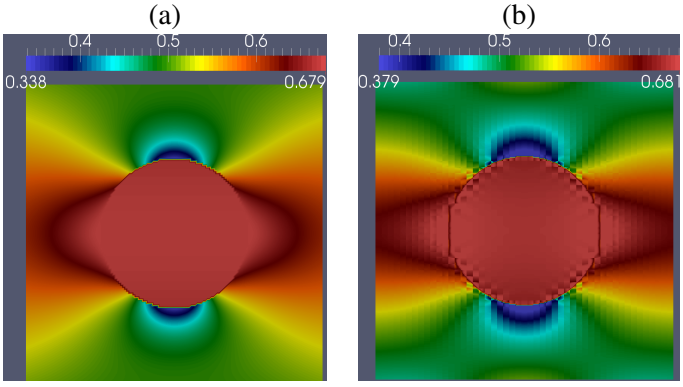

Fig. 2 Single Inclusion test: (a) HTFEM - 1 element, (b) HTFEM - 16 elements

Consequently we have compared the solution with results obtained by HTFEM with regular mesh using 1 and 16 elements. In Fig 1(b), 2(a) and 2(b) we can see the stress for conventional FEM and HTFEM using 1 and 16 elements, respectively. It can be seen that HTFEM gives very good results in comparison with FEM even if a single element is used. However, the results are polluted near boundaries since the perturbation fields are based on analytical solution that has the infinite support. Substantially better behavior near boundaries is achieved with increasing number of elements. Already for only 16 elements we obtained almost the perfect match. However, for this case, oscillations at the matrix-inclusion interface can be observed. This phenomenon will be explored in the future research.

CONCLUSION

In this paper we have presented an efficient approach for numerical modelling of composite materials containing elastic matrix with elastic inclusions or voids. In the future work we will focus on exploration of artificial oscillations at the matrix-inclusion interface and the extension of the proposed approach to the elasto-plastic setting.

ACKNOWLEDGEMENT

This outcome has been achieved with the financial support of the Czech Science Foundation under project no. 13-22230S and SGS project no. OHK1-089/14.

REFERENCES

[1] QING-HUA, Qin and HUI, Wang. *Matlab and C Programming for Trefftz Finite Element Methods.* Florida: CRC Press, 2009. 451 p. ISBN 978-1-4200-7275-4.

[2] NOVÁK et al. Micromechanics-enhanced finite element formulation for modelling heterogeneous materials. *Computer Methods in Applied Mechanics and Engineering.* 2012, **201**(204), 53-64. ISSN 0045-7825.

[3] *OOFEM Project Page.* [online]. [cited 2014-08-01]. Available from: http://www.oofem.org

FORM-FINDING OF MEMBRANE STRUCTURES - COMPARISON OF SCHEMAS OF DYNAMIC RELAXATION

Miloš HÜTTNER[1], Jiří MÁCA[2], Petr FAJMAN[3]

***Abstract**: This study is focused on the form-finding process of membrane structures using the dynamic relaxation method with kinetic damping. Eight different schemes of dynamic relaxation method are compared in the paper. The effect of mass distribution along the structure is also of interest and it is studied in the paper. The efficiency and stability of each process are compared to four selected 3D examples of membrane structures.*

***Keywords**: membrane structures, form finding, dynamic relaxation, kinetic damping, triangular element*

INTRODUCTION

Membrane structures represent an attractive way of modern roofing constructions. Ordinarily, the design of membrane structures follows a three-stage procedure:

(i) the form-finding

(ii) the pattering

(iii) the static analysis

"The form-finding is process of finding the basic static shape of the structure (under pre-tension forces only), before detailed analysis, involving imposed loads such as snow and wind, can commence. Thus, the form-finding stage addresses the question of the structure geometry of the tension membrane spanning a given boundary configuration [1]."

Mathematically, the form-finding of membrane structure represents a geometrically nonlinear problem. Dynamic relaxation method [2] is an attractive approach for solution of these structures because the stiffness matrix inversion is not required.

[1] Ing. Miloš Hüttner, Department of Mechanics, Czech Technical University in Prague - Faculty of Civil Engineering, Thákurova 7; 166 29, Prague 6 - Dejvice; CZ, e-mail: milos.huttner@fsv.cvut.cz

[2] Prof. Ing. Jiří Máca, CSc.: Department of Mechanics, Czech Technical University in Prague - Faculty of Civil Engineering, Thákurova 7; 166 29, Prague 6 - Dejvice; CZ, e-mail: maca@fsv.cvut.cz

[3] Doc. Ing. Petr Fajman, CSc.: Department of Mechanics, Czech Technical University in Prague - Faculty of Civil Engineering, Thákurova 7; 166 29, Prague 6 - Dejvice; CZ, e-mail: fajman@fsv.cvut.cz

MEMBRANE ELEMENT

"The shape of prestressed membranes may be determined using constant stress triangular elements (see Fig. 1). If the membrane stress σ is the same in each direction and the shear stress τ_{xy} is zero then this case corresponds to a minimum surface network of the type that is similar to a soap film model [3]."

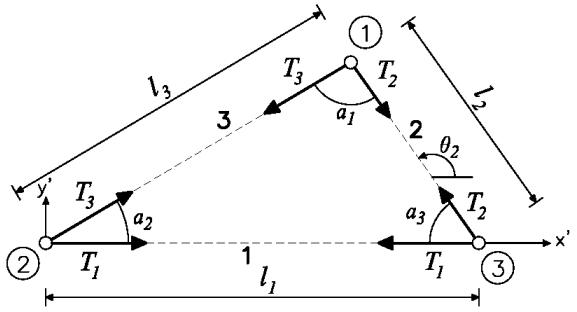

Fig. 1 Triangular element

The initial forces T_1, T_2 and T_3 of sides 1, 2 and 3 are defined for a membrane element as:

$$T_s = \frac{\sigma h L_i}{2 \tan \alpha_i} \tag{1}$$

Where: T_s is the side force in the side s, with s = 1, 2 or 3,

σ is the prescribed stress in the membrane,

h is the thickness of the membrane,

L_i is the length of the side s,

α_s is enclosed angle α_s of the side s, see Fig. 1.

"The equation (1) represents a transformation of the element surface stress into a discrete set of forces T_s acting in the sides of the element. Depending on the value of the enclosed angle α_i, the side forces can be either positive or negative. They can be resolved into x, y and z components at the nodes and included directly in the calculation of residual forces within the dynamic relaxation [1]."

DYNAMIC RELAXATION

The dynamic relaxation method (DRM) is an iterative process that is used to find static equilibrium of geometrically nonlinear problems. DRM is not used for the dynamic analysis of structures; a dynamic solution is used for a fictitious damped structure to achieve a static solution. The theory of this method was first described by Day [2]. This theory was further developed and its detailed

overview can be found in Barnes [4], Topping [3] or Lewis [1]. In this study, a technique with kinetic damping will be used.

"Kinetic damping is an alternative to viscous damping that was suggested by Cundall [5] for application to unstable rock mechanics problems. The method of kinetic damping has been found to be very stable and rapidly convergent when dealing with large displacements [3]."

Principle

The basic unknowns form nodal velocity, which are calculated from nodal displacements. The discretization from timeline with time step Δt will be performed. During the step Δt a linear change of velocity is assumed. Acceleration during the step Δt is thus considered to be constant. By substituting the above assumptions the velocity for joint i in direction j (x, y and z) can be expressed in a new time point $t + \Delta t/2$ thus:

$$v_{ij}^{(t+\Delta t/2)} = v_{ij}^{(t-\Delta t/2)} + \Delta t \frac{R_{ij}^{t}}{M_{ij}} \qquad (2)$$

Where R_{ij}^{t} is residual force (i.e. out of balance) at joint i in the direction j and at time t,

M_{ij} is the fictitious mass at joint i in the direction j,

$v_{im}^{(t+\Delta t/2)}$ is velocity at joint i in the direction j and at time $t + \Delta t/2$.

The residual forces are calculated of the sum of the side forces T_s of the membrane elements. If the sum of the side force $T_s^t < 0$ the force is compressive so T_s^t must be set equal to zero.

"With kinetic energy damping the velocities of all joints are set to zero when a fall in the level of the total kinetic energy of the structures occurs. This fall in the kinetic energy indicates that the peak has been passed [3]." Coordinates of the peak kinetic energy can be calculated using the approximation of linear [3] or parabolic approximation [1]. The coordinates are taken as the starting point for the next cycle of computation.

Algorithm

The acceptable error of residual forces $R_{\lim}$ must be defined before starting the calculation. The iteration process can be outlined as below:

Preprocessing:

a) Set initial conditions.

b) Set fictitious masses and the size of a time step.

c) Determine the initial side forces from equation (1) and residual forces for the each degree of freedom.

The general iterative steps:

d) Determine velocities for the each degree of freedom from equation (1).

f) Calculate the kinetic energy of the whole structure.

g) If the decrease in kinetic energy, then determine the peak kinetic energy and zero velocities.

h) Update the coordinates.

i) Determine the current side forces from equation (1) and residual forces for the each degree of freedom.

If $\max\left|R_{ij}\right| < R_{\lim}$ then stop the algorithm. Otherwise continue the DRM iteration from step d).

Fictitious mass

The stability and the speed of calculation depend on the appropriate choice of the fictitious mass. The stiffness of the side connection determines the value of the fictitious mass. To ensure the stability of the calculation, it is appropriate to apply the following relationship [6]:

$$M_{ij} = M_i = \frac{\Delta t}{2} S_i \qquad (3)$$

where S_i is lumped stiffness at the node i and for membrane structures in form-finding process it can be calculated as:

$$S_i = \frac{\sum T_s}{L_s} \qquad (4)$$

where $\sum T_S$ is the sum of the force in the side s of the membrane elements and L_S is current length of the side s.

Used schemas

Eight dynamic relaxation schemas are examined in this paper. Tab. 1 gives an overview of selected attributes for individual processes, “KP” indicates the calculation with kinetic damping with a parabolic approximation of the peak [1] and “KL” indicates the calculation with linear approximation of the peak [3]. The symbol “M_i” denotes the calculation of the mass using equation (3), “M” denotes that the mass is the same for all nodes and it is calculated as $M = \max(M_i)$. The symbol “Re”

denotes the fictitious masses are recalculated after each restart of the kinetic energy. The symbol "No" denotes the fictitious masses are not recalculated after restart of the kinetic energy.

Tab. 1 Outline of the schemas

Processes	1	2	3	4	5	6	7	8
Approximation	KP	KP	KP	KP	KL	KL	KL	KL
Mass	M	M_i	M	M_i	M	M_i	M	M_i
Recalculated	No	No	Re	Re	No	No	Re	Re

EXAMPLES

The efficiency of the processes was studied on four membrane structures. Moreover, each example is analyzed from two different initial positions. The time step is chosen $\Delta t = 1$ s in all calculations. The parameters of membranes are $\sigma = 100$ MPa and thickness $h = 1$ mm. The calculation is terminated when the residual forces in all joints are less than 0.01 kN. Self-created scripts in MATLAB 8.0.0.783 (2012b) was used for all calculations.

Example 1

It is a fictitious membrane structure with 48 degrees of freedom. The coordinates of nodes (in meters) are: A = [0, 0, 1], B = [6, 0, 0], C = [0, 6, 0], D = [6, 6, 1]. The first initial setting of construction is shown in Fig. 1b. The second initial setting of construction is shown in Fig. 2a.

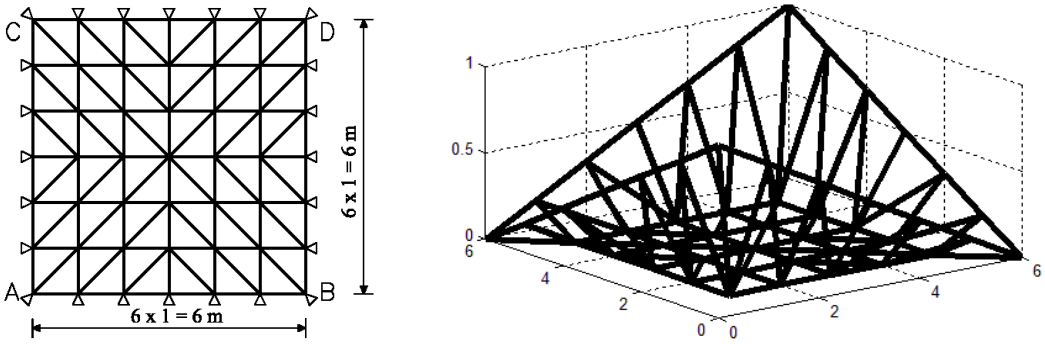

Fig. 1a Plan view of example 1. Fig. 1b Perspective view of starting position of example 1a.

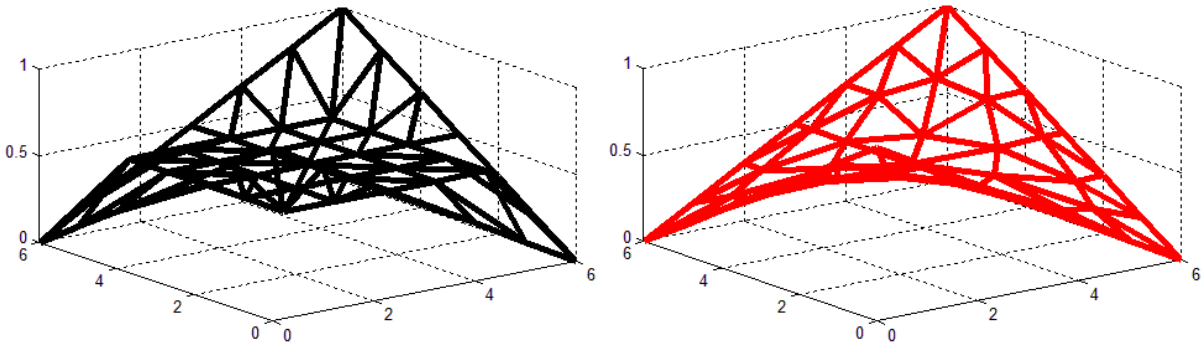

Fig. 2a Perspective view of starting position of example 1b. Fig. 2a Final position of example 1.

Example 2

It is a fictitious membrane structure with 108 degrees of freedom. The coordinates of nodes (in meters) are: A = [0, 0, 0], B = [8, 0, 0], C = [0, 8, 0], D = [8, 8, 3]. The first initial setting of construction is shown in Fig. 3b. The second initial setting of construction is shown in Fig. 4a.

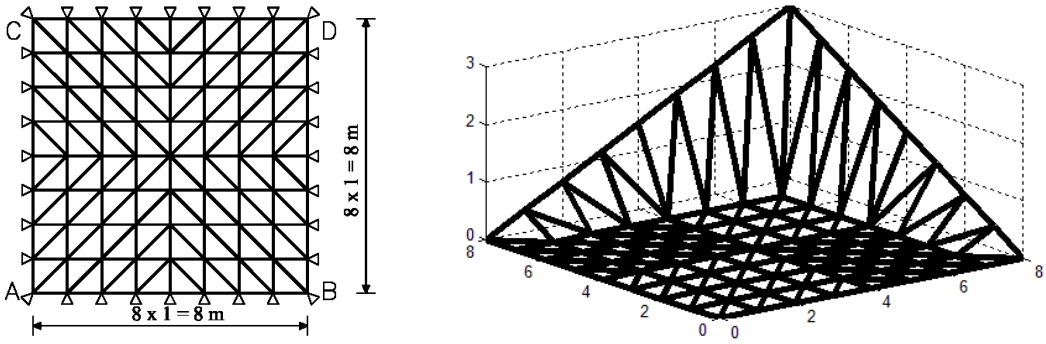

Fig. 3a Plan view of example 2. Fig. 3b Perspective view of starting position of example 2a.

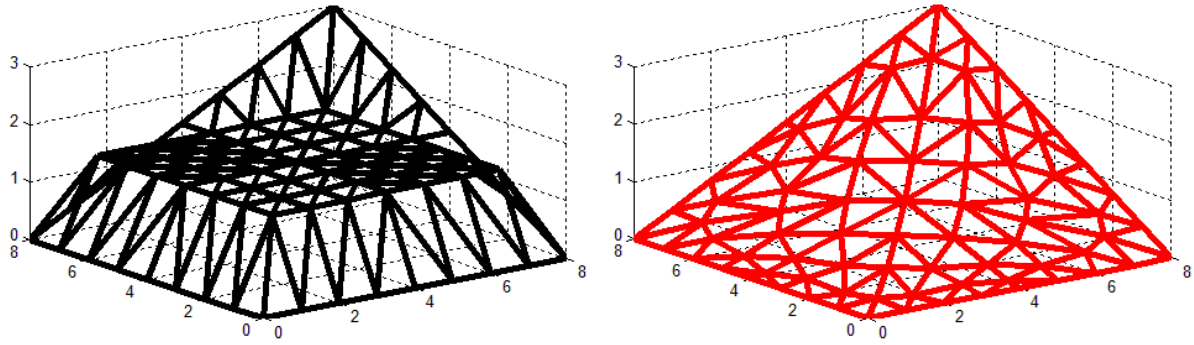

Fig. 4a Perspective view of starting position of example 2b. Fig. 4a Final position of example 2.

Example 3

It is a fictitious membrane structure with 189 degrees of freedom. The coordinates of nodes (in meters) are: A = [0, 0, 0], B = [10, 0, 0], C = [0, 10, 0], D = [10, 10, 0], E = [5, 5, 1]. The first initial setting of construction is shown in Fig. 5b. The second initial setting is shown in Fig. 6a.

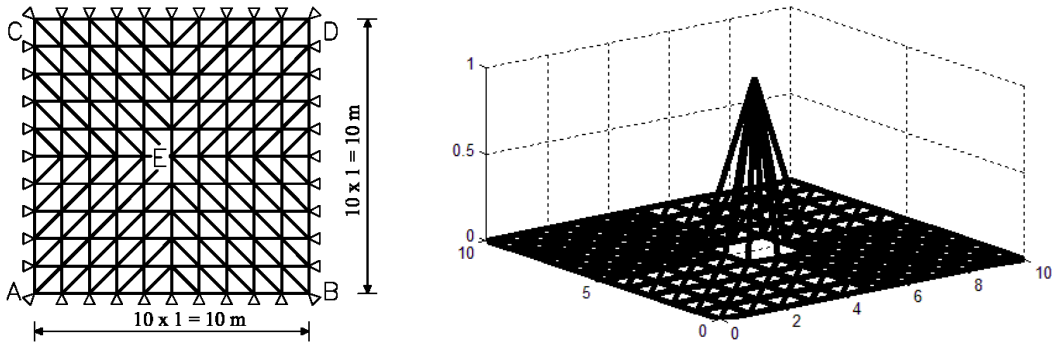

Fig. 5a Plan view of example 3. Fig. 5b Perspective view of starting position of example 3a.

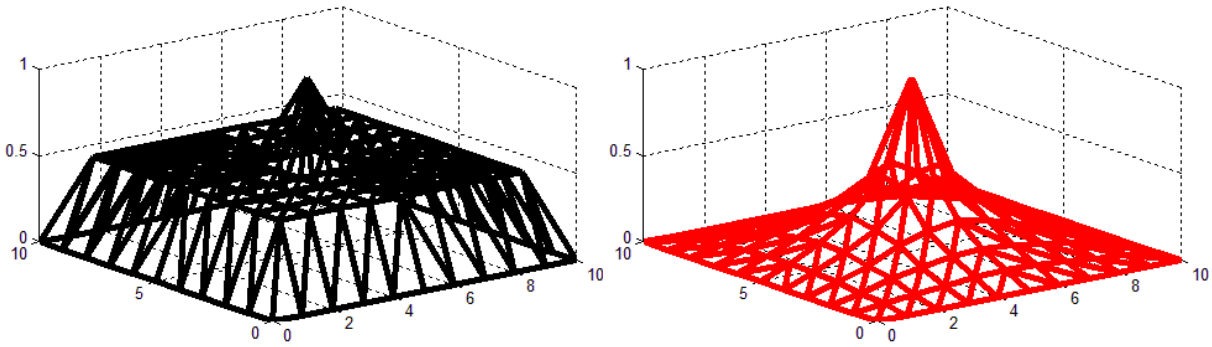

Fig. 6a Perspective view of starting position of example 3b. Fig. 6a Final position of example 3.

Example 4

It is a fictitious membrane structure with 90 degrees of freedom. The coordinates of nodes (in meters) are: A = [0, 0, 0], B = [10, 0, 0], C = [0, 6, 0], D = [10, 6, 0], E = [3, 3, 1], F = [7, 3, 1]. The first initial setting of construction is shown in Fig. 7b. The second initial setting is shown in Fig. 8a.

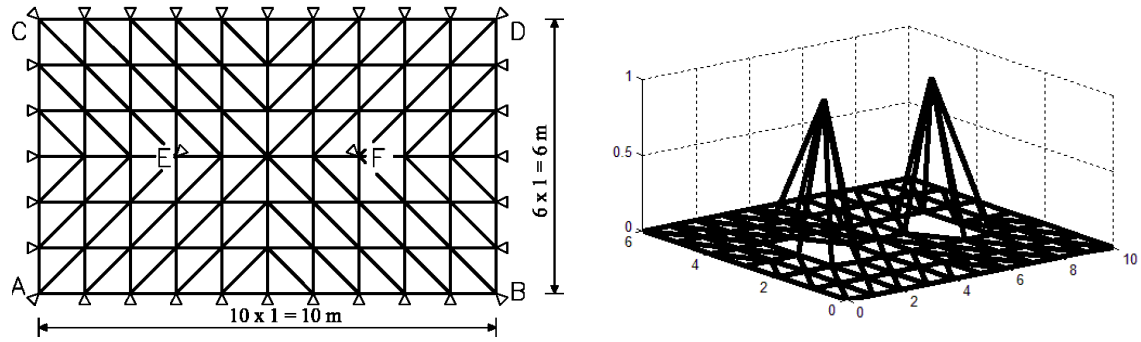

Fig. 7a Plan view of example 4. Fig. 7b Perspective view of starting position of example 4a.

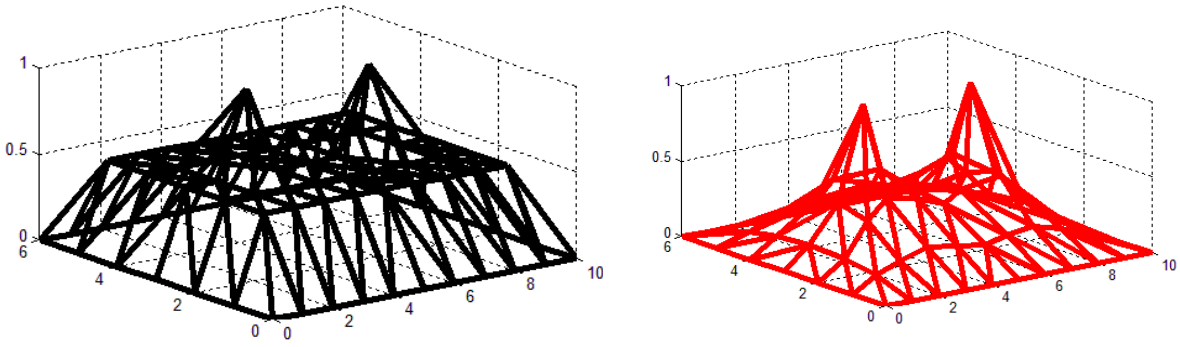

Fig. 8a Perspective view of starting position of example 4b. Fig. 8a Final position of example 4.

DISCUSSION

Summary of results is shown in Tab 2. The methods are sorted by the number of errors (sum of all examples) and by the total number of iterations. The results imply that it is impossible to determine clearly the best scheme. It appears that the schemas that use the same mass for the whole structure (odd schemas) are faster than schemas that use different masses for each joint (even schemas).

Tab. 2 Outline of the results

		Number of iteration							
Schemas		1	2	3	4	5	6	7	8
Example 1	a	234	250	267	261	185	176	187	204
	b	167	179	172	162	140	185	125	162
Example 2	a	429	-	404	-	444	-	558	-
	b	526	551	476	546	454	345	473	356
Example 3	a	101	98	98	107	105	94	118	83
	b	143	-	175	-	263	447	146	310
Example 4	a	332	1121	565	298	577	629	308	549
	b	415	467	289	171	301	339	276	400
Sum		2347	2666	2446	1545	2469	2215	2191	2064
Errors		0	2	0	2	0	1	0	1
Rank		2	8	3	7	4	6	1	5

CONCLUSION

It may be concluded that the scheme 7 based on kinetic damping with a linear approximation of the peak and with the mass divided the same for all nodes and with recalculating of masses after each restart of the kinetic energy has proved the most comprehensive results.

ACKNOWLEDGEMENT

The results presented in this paper are outputs of the research project “P105/11/1529 - Cable - membrane structures analyses” supported by Czech Science Foundation and project “SGS14/029/OHK1/1T/11- Advanced algorithms for numerical modeling in mechanics of structures and materials” supported by the Faculty of Civil Engineering, Czech Technical University in Prague.

REFERENCES

[1] LEWIS, W. J. *Tension structures: form and behaviour*. London: Thomas Telford, 2003. 201 p. ISBN 0-7277-3236-6.

[2] DAY, A. S. An introduction to dynamic relaxation. *The Engineer*. January 1965, 218-221, ISSN 0013-8029.

[3] TOPPING, B.H.V. and IVÁNYI, P. *Computer Aided Design of Cable Membrane Structures*. Kippen, Saxe-Coburg Publications, 2008. 233 p. ISBN 978-1-874672-11-1.

[4] BARNES, M. R. Form and stress engineering of tension structures. *Structural Engineering Review*, 1994, **6** (3-4), 175-202. ISSN 0952-5807.

[5] CUNDALL, P. A. Explicit finite-difference methods in geomechanics. In: *Proceedings E.F. conf. numerical methods in geomechanics.* Blacksburg, June 1976, pp 132-150.

[6] HÜTTNER, M., MÁCA J., Membrane structures – dynamic relaxation. In: *Proceedings of the 4rd conference: NMM 2013 Nano & Macro mechanics*. Praha: ČVUT, 2013, pp 75-82. ISBN 978-80-01-05332-4.

EFFECT OF TITAN DIOXIDE AND DIAMOND NANOPARTICLES ON POLY (VINYL-ALCOHOL) NANOFIBER TEXTILES STIFFNESS

Kateřina INDROVÁ[1], Zdeněk PROŠEK[2], Jaroslav TOPIČ[3], Václav NEŽERKA[4], Tomáš PLACHÝ[5], Pavla RYPAROVÁ[6] Pavel TESAREK[7]

***Abstract**: The paper deals with the influence of the incorporated particles to the mechanical properties of the nanofiber textiles made using electrospinning (a needle-less variant), nanofiber textiles are made on the basis of aqueous PVA solution. During preparation of this solution it is possible to add nanoparticles – in our case nanodiamonds and particles of titan dioxide. Two different concentrations were used for both types of particles, 0.5 and 1.0 % wt. of a PVA amount. The influence of nanoparticles on the stiffness and tensile strength were monitored. It can be seen from the obtained results that the influence of the applied nanoparticles on the stiffness is negligible and values of the tensile strength a little bit decreased.*

***Keywords**: nanoparticle, diamond, titan dioxide, nanofiber textiles, stiffness*

INTRODUCTION

Nanofiber textiles are widely used in many areas, e.g. healthcare. One of their advantages is that their properties can be modified by incorporated nanoparticles [1, 2]. The properties can be not only

[1] Bc. Kateřina Indrová, Czech Technical University in Prague, Faculty of Biomechanical Engineering, Sítná 3105, 272 01 Kladno, Czech Republic, Katerina.indrova@fbmi.cvut.cz

[2] Bc. Zdeněk Prošek, Czech Technical University in Prague, Faculty of Civil Engineering; Thákurova 7, 166 29 Prague 6 – Dejvice, Czech Republic, zdenek.prosek@fsv.cvut.cz

[3] Bc. Jaroslav Topič, Czech Technical University in Prague, Faculty of Civil Engineering; Thákurova 7, 166 29 Prague 6 – Dejvice, Czech Republic, zdenek.prosek@fsv.cvut.cz

[4] Ing. Václav Nežerka, Czech Technical University in Prague, Faculty of Civil Engineering; Thákurova 7, 166 29 Prague 6 – Dejvice, Czech Republic, vaclav.nezerka@fsv.cvut.cz

[5] Ing. Tomáš Plachý, Ph.D., Czech Technical University in Prague, Faculty of Civil Engineering; Thákurova 7, 166 29 Prague 6 – Dejvice, Czech Republic, plachy@fsv.cvut.cz

[6] Ing. Pavla Ryparová, Czech Technical University in Prague, Faculty of Civil Engineering; Thákurova 7, 166 29 Prague 6 – Dejvice, Czech Republic, pavla.ryparova@fsv.cvut.cz

[7] Ing. Pavel Tesárek, Ph.D., Czech Technical University in Prague, Faculty of Civil Engineering; Thákurova 7, 166 29 Prague 6 – Dejvice, Czech Republic, tesarek@fsv.cvut.cz

modified and improved (e.g. mechanical ones) but also new ones can be added, e. g. resistance to bacteria. Nanodiamont particles (NDP) [3] and titan dioxide belong among particles [4, 5], which have as other materials (e. g. silver or cooper) antibacterial character [6].

EXPERIMENTAL METHODS AND SAMPLES

The nanofibers for our study were produced for aqueous PVA solution in the laboratories of the Czech Technical University in Prague, Faculty of Civil Engineering. Nanospider™ NS Lab 500 S (Elmarco, Czech Republic) device was using and a needleless electrospinning method was applied. In particular a cylindrical electrode rotating at frequency of 5 Hz, a distance between electrodes was used of 140 mm, nanofiber production was carried out in laboratory conditions. Such approach was inspired by a previous study [7]. The PVA/weater polymer solution consisted of 375 g PVA Sloviol 16%, 117 g distilled water, 4.4 g glyoxal and 3 g phosphoric acid (75%). The final stabilization of the produced PVA fibers was accomplished by exposure to an elevated temperature of 140 °C for 10 minutes. NDP (NanoAmando, Nex Metals and Chemicals Corp, Ltd., Kyobaschi) of the diameter equal to 5 nm and titan dioxide (MKN TiO_2 – C7 photocatalyst/anatase) of the ones equal to 7 nm were added to the PVA solution by homogenization. Two concentrations of nanoparticles were tested – namely 0.5 and 1.0 wt. %. The overview of the produced nanofiber textiles composition can be found in Table 1.

Tab. 1 Specification of tested samples

Set	Incorporated particle	Conc. (wt. %)	Electric Current (mA)	Specific weight ($g.m^{-2}$)
PVA	-	-	0.21	3.3 ± 0.3
PVA (NDP 0.5)	Nanodiamond	0.5%	0.13	2.4 ± 0.4
PVA (NDP 1.0)	Nanodiamond	1.0%	0.13	3.2 ± 0.3
PVA (Ti 0.5)	Titan Dioxide	0.5%	0.21	3.2 ± 0.4
PVA (Ti 1.0)	Titan Dioxide	1.0%	0.21	3.2 ± 0.1

LabTest 4.100SP1 device was used for testing with a displacement controlled by the loading rate of 0.2 m/s. The 2 × 12 cm samples were cut off from each textile and the ends of each specimen were reinforced by an adhesive tape to withstand the attachment of the textiles into the clamps of the testing machine.

EXPERIMENTAL RESULTS

The Fig. 1 shows the obtained results of the stiffness of the tested specimens in comparison with the results of the reference set without nanoparticles. The values of specimens with nanoparticles are similar to the reference ones, only for concentration 0.5 % wt. titan dioxide small decrease has occurred (about 8 %). The bigger differences were measured for the tensile strength (Fig. 2) but also bigger standard deviations were calculated for these results.

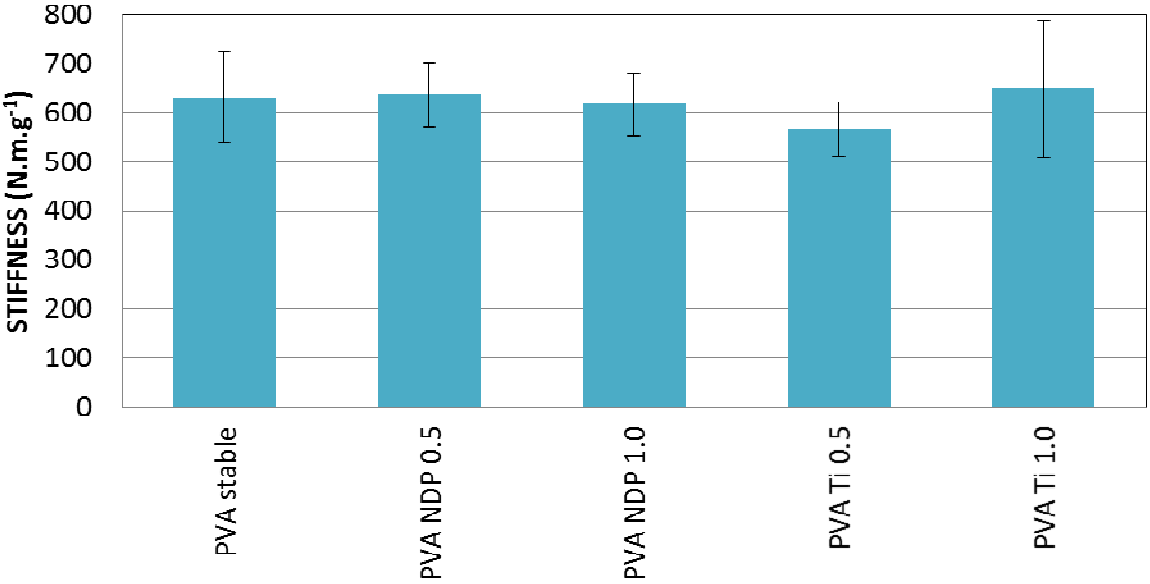

Fig. 1 Stiffness of the tested samples.

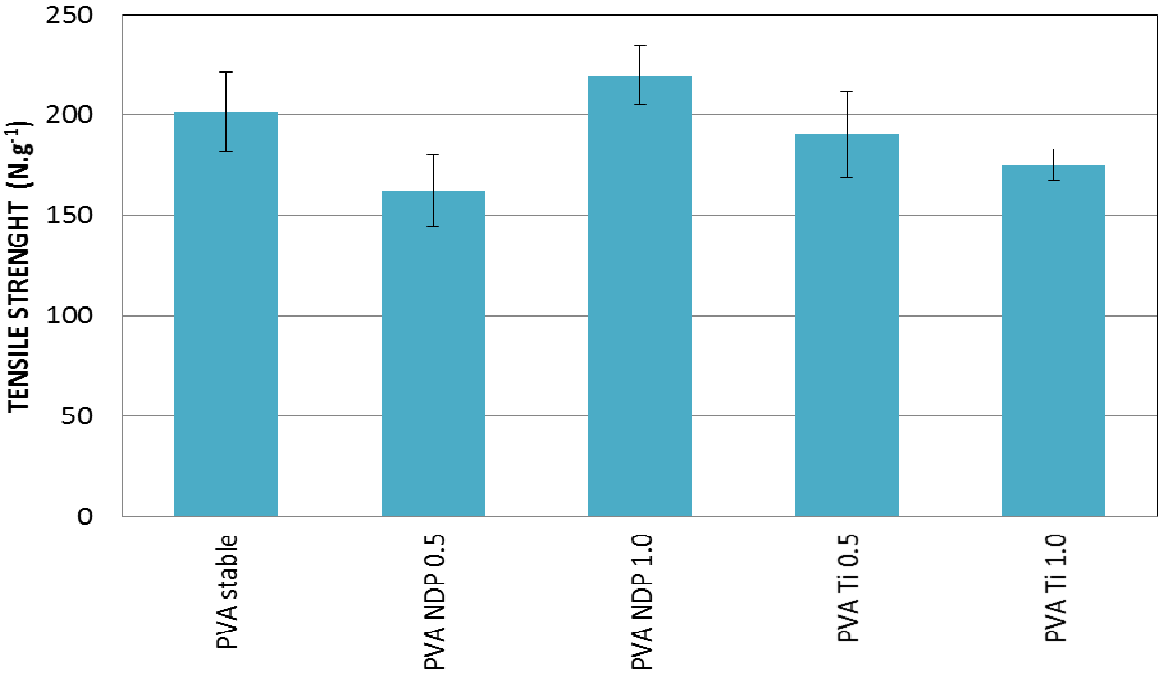

Fig. 2 Tensile strength of the tested samples.

CONCLUSION

From the obtained results it is evident that applied nanoparticles did not change mechanical properties significantly. The values of stiffness were the same and the values of the tensile strength a little bit decreased. There is also no influence of concentration on the results. In our case the difference between results of fibers with incorporated particles of concentrations 0.5 and 1.0 wt. % was negligible.

ACKNOWLEDGEMENT

This work was supported by grant agency of Ministry of Cultury DF12P01OVV037. Special thanks belong to the Center for Nanotechnology in Civil Engineering at Faculty of Civil Engineering CTU in Prague and Joint Laboratory of Polymer Nanofiber Technologies of Institute of Physics Academy of Science of Czech Republic and Faculty of Civil Engineering CTU in Prague.

REFERENCES

[1] KIM, H., ITO, T., KIM, B., WATANABE, Y., KIM, I. Mechanical Properties, Morphologies, and Microstructures of Novel Electrospun Metallized Nanofibers, *Adv. Eng. Mater*. 2011, **13,** 376-382. ISSN: 1527-2648

[2] ANDRADY, L. A. *Science and technology of polymer nanofibers*, New Jersey, 2008, pp. 24-25. ISBN: 978-0-471-79059-4.

[3] BEHLER, K. D. et al. Nanodiamond-Polymer Composite Fibers and Coatings. *ACS NANO*, 2009, **3**, 363-369. DOI: 10.1021/nn800445z.

[4] LOU, Y. H., et al. Improvement of the Mechanical Properties of Nano-TiO2/Poly(Vinyl Alcohol) Composites by EnhancedInteraction Between Nanofiller and Matrix. *Polymer Composites*, 2010, **31**(7), 1184-1193. ISSN: 1548-0569.

[5] LI, X., et al. Fabrication and properties of PVA-TIO_2 hydrogel composites. *Chinese Materials Conference, Procedia Engineering*, 2011, **27**, 1488-1491, 2012. DOI: 10.1016/j.proeng.2011.12.612.

[6] RÁCOVÁ, Z., RYPAROVÁ, P., HLAVÁČ, R., TESÁREK, P., NEŽERKA, V. Influence of copper ions on mechanical properties of PVA-based nanofiber textiles, *Applied Mechanics and Materials.* 2014, **486**, 201-204. ISSN: 1662-7482.

[7] TESÁREK, P., RYPAROVÁ, P., RÁCOVÁ, Z., KRÁLÍK, V., NĚMEČEK, J., KROMKA, A., NEŽERKA, V. Mechanical properties of single and double-layered PVA nanofibers, *Key Engineering Materials.* 2014, **586**, 261-264. ISSN: 1662-9795.

PROBABILISTIC PARAMETER IDENTIFICATION OF HETEROGENEOUS VISCOPLASTIC MATERIAL

Eliška JANOUCHOVÁ[1], Anna KUČEROVÁ[2], Jan SÝKORA[3]

Abstract: *The Bayesian inference provides a probabilistic description of the identified parameters, but the obtained distribution describes uncertainty in our knowledge of the deterministic values. In this contribution, we present a reformulation of the Bayesian inference to identify the parameters along with their variations in heterogeneous materials.*

Keywords: *Parameter identification, Bayesian inference, Markov chain Monte Carlo, Principal component analysis, Heterogeneous materials*

INTRODUCTION

Parameters influencing structural behaviour such as material properties involve uncertainties which need to be taken into account in an appropriate reliability analysis. Heterogeneous character of building materials causes spatial variations of mechanical parameters (such as elastic modulus, yield stress or tensile strength) affecting the material behaviour under the loading. This phenomenon can be observed during the laboratory testing on a set of specimens made of the same material. Due to the differences in morphology, the observations have often a significant variance, c.f. the illustration in Fig. 1a.

Parameter identification method based on Bayes' rule provides a probabilistic description of the uncertain parameters involving an expert knowledge as well as experimental data. According to this rule, the mean values of the updated distribution are equal to the best guess of the parameters' values with the uncertainty represented by the corresponding variance. However in the case of heterogenous materials the goal is not to reduce the uncertainties but only quantify them because the uncertainties in the parameters arise from the heterogeneity of the material. The direct application of the Bayesian

[1] Ing. Eliška Janouchová, Department of Mechanics, Faculty of Civil Engineering, Czech Technical University in Prague, eliska.janouchova@fsv.cvut.cz

[2] Ing. Anna Kučeroá, Ph.D., Department of Mechanics, Faculty of Civil Engineering, Czech Technical University in Prague, anicka@cml.fsv.cvut.cz

[3] Ing. Jan Sýkora, Ph.D., Department of Mechanics, Faculty of Civil Engineering, Czech Technical University in Prague, jan.sykora.1@fsv.cvut.cz

approach leads to a wrong estimation of the model parameters' distributions because, in this case, the probabilistic description of the parameters does not reflect the uncertainty in their values caused by experimental errors but the actual probability distribution of the parameters in these materials.

PARAMETER IDENTIFICATION

The most common method of parameter estimation is based on fitting the response of material model to experimental data. This approach leads to optimising parameters so as to minimise the difference between the data and the model response. The optimisation problem is, however, often ill-posed and thus requires the employment of robust optimisation algorithms. This method is suitable for identification from experimental data obtained for a single specimen because the result of such an optimisation process is only the single-point estimate of parameter values, as you can see in Fig. 1b. If the data for multiple experiments are available, this strategy is usually implemented for determination of parameters' mean values and any information beyond the mean is omitted. Other possibility is to fit the data from each particular specimen separately and to compute the distribution from the obtained parameter sets, but this strategy becomes computationally demanding with an increasing number of tested specimens.

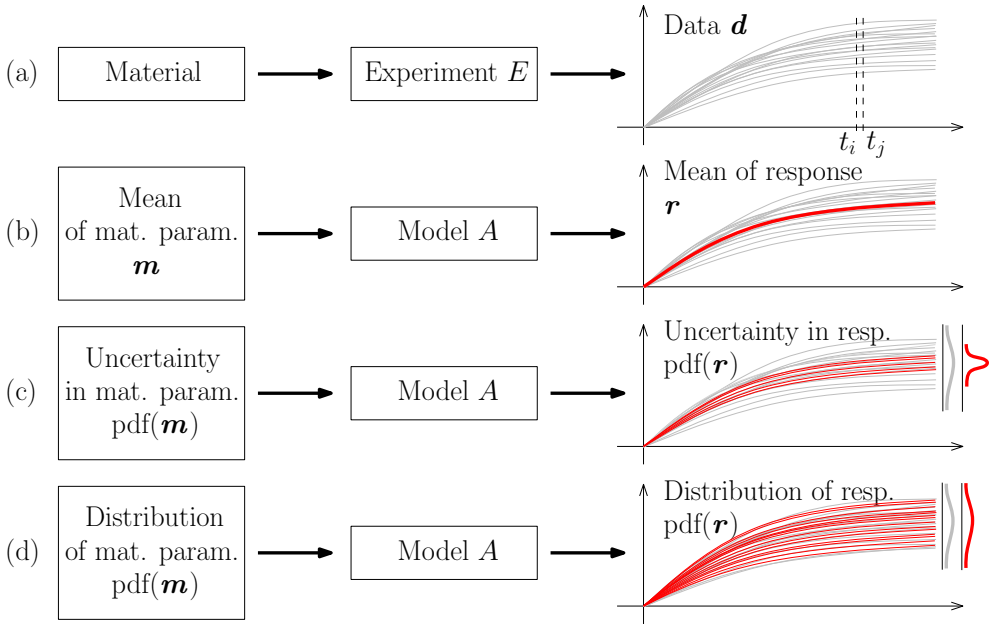

Fig. 1 Scheme of an experiment and different approaches to parameter identification.

Advances in surrogate modelling and increasing computational capacity of modern computers permitted many researches to focus on parameter identification in probabilistic setting. The Bayesian approach to parameter identification (Fig. 1c) has several appealing advantages comparing to traditional data fitting, e.g. identification problem is well-posed, results provide probabilistic description of the actual knowledge about the parameters and not just a single value etc.

The principal idea of the Bayesian identification is based on a common way of thought when the resulting belief about a random event is given by a combination of all available information. This

approach introduces the concept of uncertainty in our subjective knowledge of the identified parameters [1]. The principle of the Bayesian inference is demonstrated in Fig. 2. Such an identification starts with a parameters' prior distribution quantifying our preliminary and typically very uncertain knowledge of parameters' value. The observations then enter through the likelihood function quantifying uncertainty in measurement errors. The posterior state of knowledge is obtained as the combination of the prior and likelihood resulting in posterior distribution, which contains higher amount of information and thus less uncertainty.

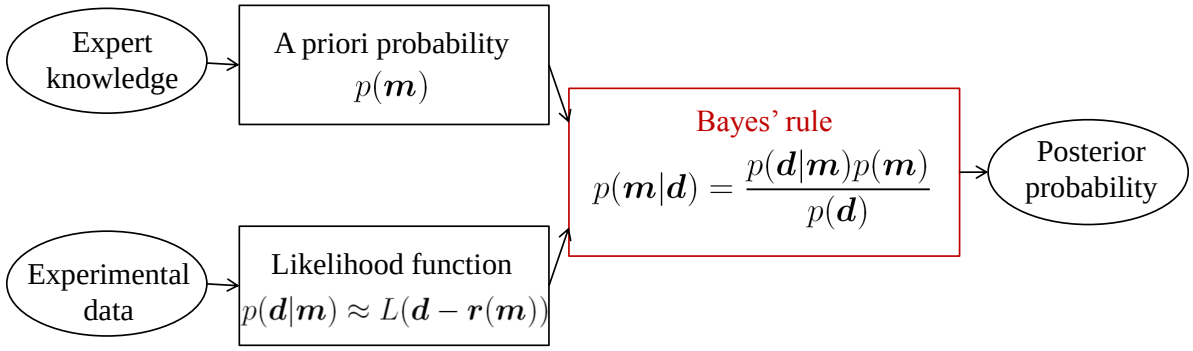

Fig. 2 Principle of Bayes' rule for parameters $\boldsymbol{m}$, observed data $\boldsymbol{d}$ and model response $\boldsymbol{r}(\boldsymbol{m})$.

The formulation of the posterior distribution includes the whole structural model. For this reason, the corresponding statistical moments cannot be generally computed analytically. The solution of inverse problem consists in exploration of the posterior distribution using Markov chain Monte Carlo (MCMC) sampling, see e.g. [2], and thus the inverse problem is treated as a well-posed problem in an expanded stochastic space. The principal drawback of this strategy consists in enormous computational demands arising from a huge number of model simulations required by MCMC method. In order to accelerate this sampling procedure in identification process, the evaluations of a numerical model can be replaced by evaluations of a computationally efficient model surrogate. In particular, the model response in the stochastic space can be approximated by polynomial chaos expansion [3].

PROBABILISTIC ESTIMATION OF HETEROGENEOUS MATERIAL PARAMETERS

This contribution focuses on developing a method for identification of parameters along with their variations in heterogeneous materials. In such situation, the calibration of a given material model can be formulated as a search for probabilistic distribution of its parameters providing the distribution of the model response corresponding to the distribution of the observed data, see Fig. 1d. The developed method is initially inspired by the Bayesian inference, where the posterior distribution of the model parameters is obtained via MCMC sampling of the product of the prior and likelihood. As it is focused on the distribution of the data described by the likelihood, the influence of the prior information is suppressed to a mere starting point for sampling the likelihood alone. Nevertheless, the main modification needs to be done to the formulation of the likelihood itself.

Formulation of likelihood

In the Bayesian inference, the variance of the likelihood represents our uncertainty in the parameters' values due to the lack of information or experimental error. In modelling of heterogeneous materials the probabilistic description of the parameters does not reflect the uncertainty in their values, as it is in the classical Bayesian approach, but the actual probability distribution of the parameters in materials. Numerically, the obstacle consists in dependency of observed response components, e.g. displacements measured at two consecutive loading levels.

This problem can be solved by the principal component analysis (PCA) transforming the correlated observations into the set of new quantities called principal components (PC). The principal components are uncorrelated and sorted in decreasing order of their variances corresponding to the eigenvalues of the covariance matrix. The first few PC account for most of the statistical variability in all of the original data. PCA allows us to reduce the dimensionality of observed data consisting of a large number of correlated variables, while retaining as much as possible of the variation present in the data [4]. Fig. 3 shows a simple example of PCA in two dimensions.

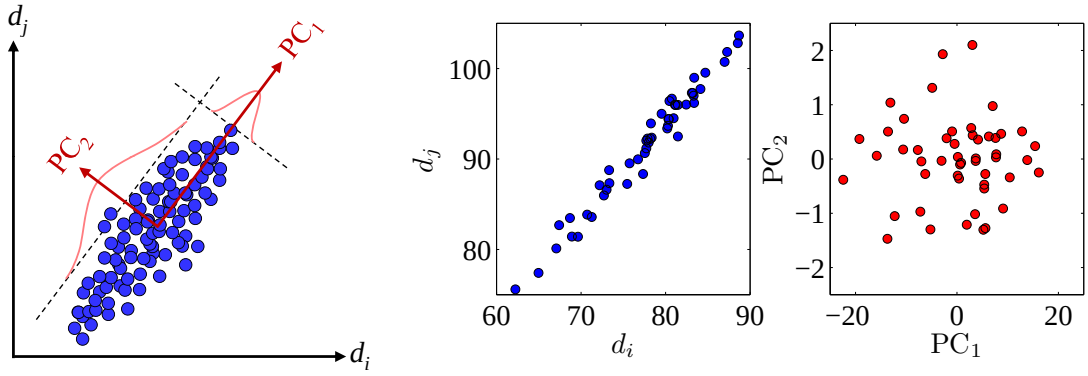

Fig. 3 An example of principal component analysis.

SENSITIVITY ANALYSIS

Global sensitivity analysis (SA) is an important tool for investigating the relationship between the model inputs and model outputs. In parameter identification it can be used to determine the most sensitive component of the model response to the identified parameter. In other words, it specifies the most suitable quantity to be measured in order to increase efficiency of the identification. This is a basic information for planning the laboratory experiments.

Several approaches to SA have been developed, see e.g. [5]. Widely used sampling-based approach aims at an evaluation of Spearman's rank correlation coefficient (SRCC) based on simulations performed for the design of experiments [6]. Another approach is to use effectively the mentioned polynomial approximation which allows to evaluate the sensitivity in the form of Sobol' indices analytically from its coefficients [7].

NUMERICAL EXAMPLE

The presented numerical example is a part of the ESA project Reliability Analysis and Life Prediction with Probabilistic Methods. For this reason, the detailed information and results are confidential therefore all the numerical data are scaled. We obtained a pseudo-experimental set of 50 curves from the cyclic loading test of a heterogeneous viscoplastic material. The response of corresponding numerical model is influenced by six uncertain parameters with log-normal prior. Task is to identify the relevant parameters within the given loading test and their probability density functions (PDF) corresponding to the measured experimental curves.

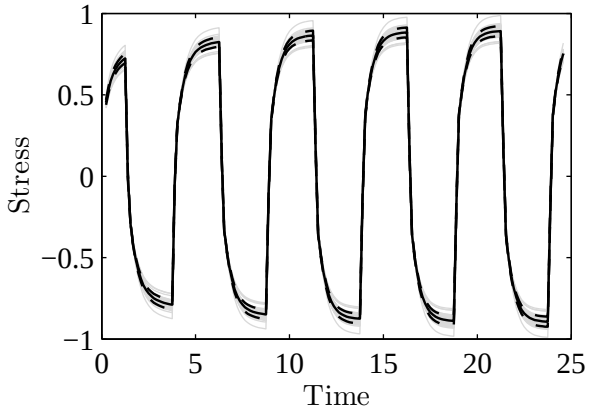

Fig. 4 Pseudo-experimental data set of curves from cyclic loading test with the marked mean values and standard deviations.

The first step of identification procedure is PCA of the experimental data set with the results shown in Tab. 1. There are variances of the particular PC and also cumulative percentage of the explained variation present in the data. In this example, only five PC are sufficient to explain all the variability which can indicate that only 5 parameters are important.

Tab. 1 Variances and variances explained corresponding to PC of experimental curves.

PC	VAR [-]	VAR explained [%]
1	9588.425	96.310
2	342.552	99.751
3	22.569	99.978
4	1.641	99.994
5	0.543	100.000
6	0.016	100.000
7	0.003	100.000
8	0.000	100.000

To separate the relevant parameters from the irrelevant ones SA can be successfully employed. Fig. 5 shows sensitivity of the stress expressed by SRCC and sensitivity of the particular PC in the form of Sobol indices. In this example, the 6th parameter does not play any role within the given loading test.

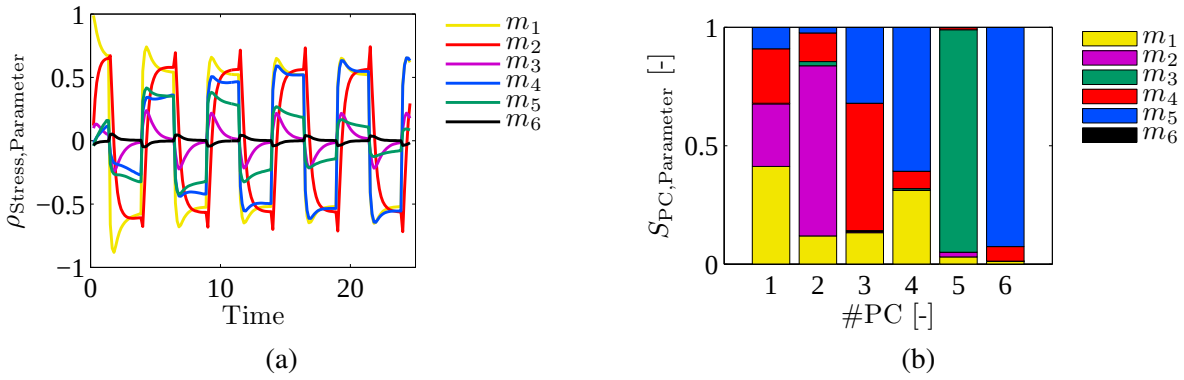

Fig. 5 Sensitivity expressed by SRCC (a) and Sobol indices (b).

The irrelevance of m_6 can be revealed as well by the probabilistic identification procedure, see Fig. 6, where the posterior of m_6 corresponds to the prior. There is also shown the difference between sampling the posterior and likelihood alone. More precise results, especially variances of the identified parameters, are obtained by sampling the likelihood, which is obvious from the numerical results listed in Tab. 2.

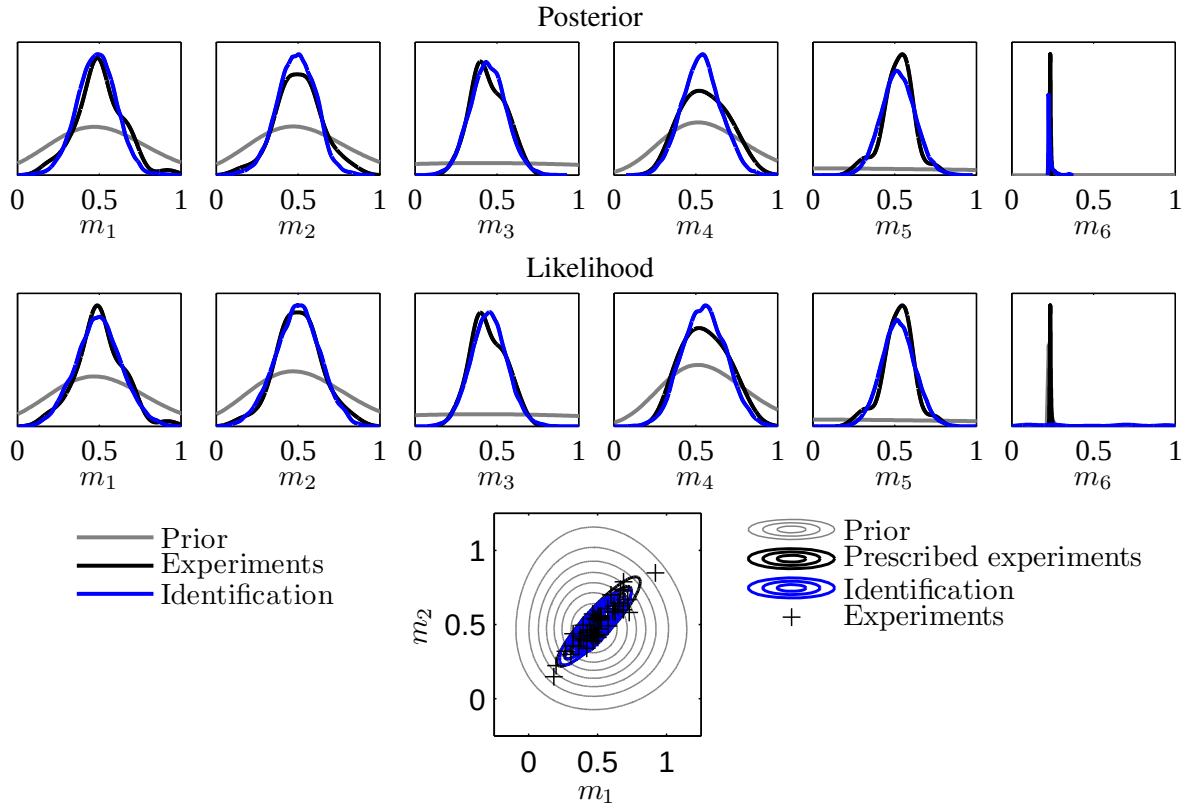

Fig. 6 PDFs of the identified parameters.

The identification procedure provides the joint distribution of the identified parameters. In this example, two of the experimental inputs are sampled as strongly correlated and this relation is detected from the identification, see Fig. 6. The problem will arise if the experimental parameters are fully correlated, in this case, the optimisation of particular experimental curves can be used to reveal the correlation.

Tab. 2 Mean values and variances of parameters from the prior knowledge, experiments, sampling of the posterior and sampling of the likelihood.

	m_1	m_2	m_3	m_4	m_5	m_6
Prior						
MEAN	0.511	0.522	0.473	0.580	0.508	0.236
VAR	0.093	0.092	1.041	0.076	3.086	$5 \cdot 10^{-4}$
Experiments						
MEAN	0.503	0.506	0.448	0.557	0.520	0.237
VAR	0.020	0.019	0.010	0.017	0.009	$1 \cdot 10^{-5}$
Posterior						
MEAN	0.485	0.490	0.448	0.536	0.522	0.239
VAR	0.014	0.014	0.012	0.014	0.011	0.001
Likelihood						
MEAN	0.496	0.498	0.452	0.552	0.522	0.475
VAR	0.020	0.019	0.012	0.018	0.011	0.095

In Fig. 7 the model output corresponding to the identified parameters' distributions is compared to the experimental data. For a sake of clarity, there are also the distributions of the model response corresponding to two particular time steps. The expert's estimation represented by the green prior leads to a greater variance while the identified red distribution corresponds to the real behaviour of the material.

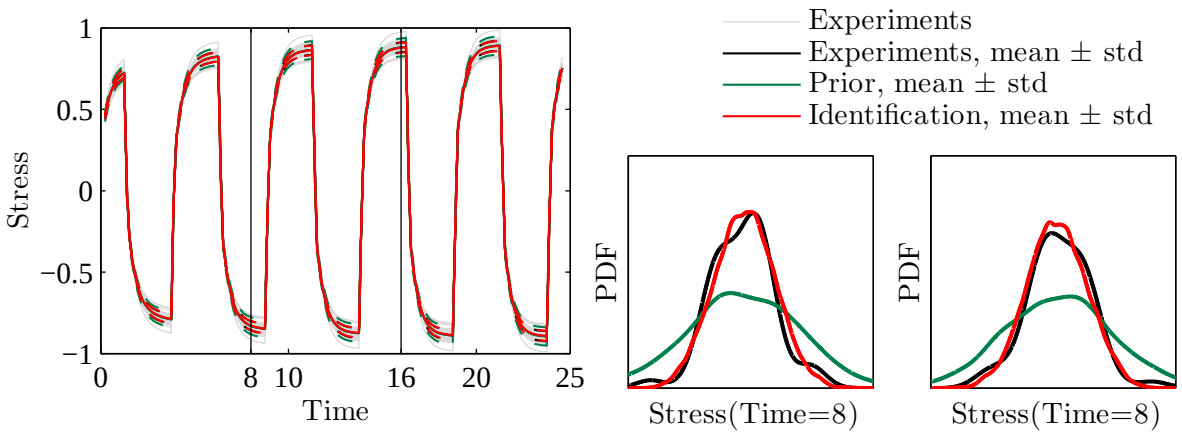

Fig. 7 Comparison of experimental data and model response corresponding to the identified parameters.

Finally, an experimental error is added to each point of the experimental curves. It is a normally distributed variable with standard deviation equal to 2 % of corresponding output standard deviation. This error size is critical because a bigger error becomes more important than some of the parameters

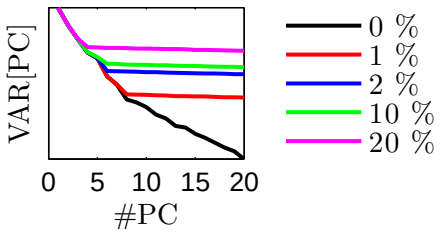

Fig. 8 Variation of principal components' variances due to the increasing experimental error.

which makes their identification impossible. Fig. 8 illustrates influence of the increasing error on PC. In the case of the critical error, the identification provides sufficiently accurate results depicted in Fig. 9.

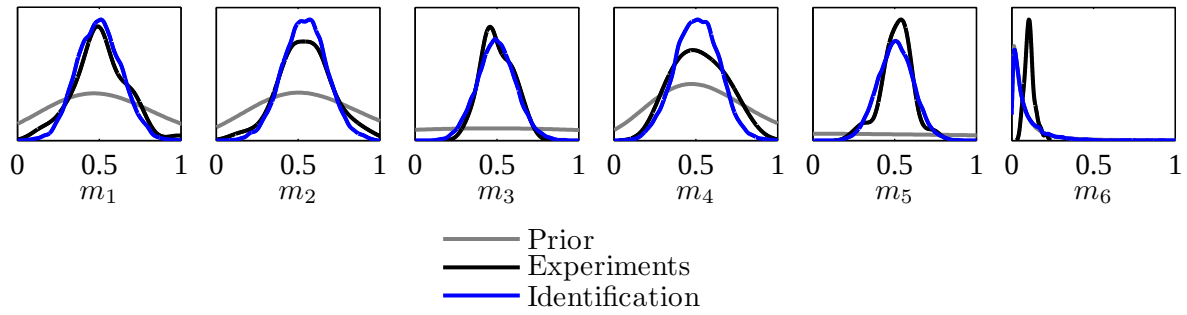

Fig. 9 PDFs of the identified parameters.

CONCLUSION

The presented contribution focuses on probabilistic identification of heterogeneous material parameters. The identification procedure is based on MCMC sampling of the likelihood function. We use PCA to formulate the likelihood. The variances of PC define the number of relevant parameters influencing the model output and the maximal size of experimental error not disturbing the identification process.

ACKNOWLEDGEMENT

The financial support of this research by the Czech Technical University in Prague (SGS project No. 14/028/OHK1/1T/11) and the Czech Science Foundation (GA CR project No. 105/12/1146) are gratefully acknowledged.

REFERENCES

[1] GELMAN, A. et al. *Bayesian data analysis.* 2nd ed. Boca Raton, Fla.: Chapman & Hall/CRC, 2004. 668 p. ISBN 1-58488-388-X.

[2] GEYER, C. J. Handbook of Markov Chain Monte Carlo In: *Introduction to Markov Chain Monte Carlo.* Boca Raton, Fla.: Chapman & Hall/CRC, 2011, pp. 3-48. ISBN 978-1-4200-7942-5.

[3] MATTHIES, H. G. Uncertainty quantification with stochastic finite elements. In Erwin Stein, René de Borst, and Thomas J. R. Hughes, editors, *Encyclopaedia of Computational Mechanics*. John Wiley & Sons, Chichester, 2007. Available from: doi:10.1002/0470091355.ecm071

[4] JOLLIFFE, I. *Principal component analysis.* 2nd ed. New York: Springer, 2002. 487 p. ISBN 03-879-5442-2.

[5] SALTELLI, A., CHAN, K. and SCOTT, E. M. *Sensitivity analysis.* New York: Wiley, 2000.

[6] HELTON, J.C. et al. Survey of sampling-based methods for uncertainty and sensitivity analysis. *Reliability Engineering & System Safety* 2006, **91**(10-11), pp. 1175-1209. ISSN 0951-8320.

[7] BLATMAN, G. and SUDRET, B. Efficient computation of global sensitivity indices using sparse polynomial chaos expansions. *Reliability Engineering* 2010, **95**(11), pp. 1216-1229.

ANALYSIS OF THE PROPERTIES OF THE SURFACE LAYERS OF DENTAL IMPLANTS

Alice KAPKOVÁ[1], Aleš JÍRA[2], František DENK[3], Lubomír KOPECKÝ[4]

***Abstract**: The present paper is focused on the micromechanical analysis of material properties and the microscopic analysis performed to evaluate the surface morphology of enosseal part of dental compensation with cylindrical shafts as well as plasma-surface modified hydroxyapatite. Using the nanoindentation the differences in elastic modulus and hardness of the examined implants in the shaft supporting portion and the surface are compared. The mechanical tests clearly show that the differences are mainly in the peripheral layer, in the range of about 17-157 GPa. Moreover, the hydroxyapatite surface is studied by means of terms of elemental analysis and microscopy.*

***Keywords**: dental implant, hydroxyapatit, nanoindentation, Young's modulus*

INTRODUCTION

Physical and chemical properties of implant surfaces are discussed with regard to the biological and clinical behavior. Chemically modified surface of dental implants shortens healing, exhibits excellent oseoconduction properties and high primary stability of the implant [1]. Individual studies prove [2, 3] that the surface roughness affects the rate of implant osseointegration and biomechanical fixation. The surface of present implants based on titanium core is frequently modified by sandblasting, chemical etching in mineral acids or plasma modification of hydroxyapatite. Generally, the development of chemically modified surfaces led to the new generation of implants. These surfaces are designed to exhibit a specific type of reactivity designated as the bioactivity [4]. Bioactive surfaces are characterized by the formation of calcium phosphate on the surface of implant promptly after implantation, when the synthesis of bone mineral osteogenic cells is still not possible. The characteristic properties of these surfaces are the high wettability (hydrophilic character), high surface area and high hydration [4, 5]. In

[1] MDDr. Ing. Alice Kapková, Faculty of Civil Engineering, Czech Technical University in Prague, alice.kapkova@fsv.cvut.cz

[2] Ing. Aleš Jíra, Ph.D., Faculty of Civil Engineering, Czech Technical University in Prague, jira@fsv.cvut.cz

[3] Ing. Arch. Ing. František Denk, Faculty of Civil Engineering, Czechn Technical University in Prague, denk.f@seznam.cz

[4] RNDr. Lubomír Kopecký, Faculty of Civil Engineering, Czech Technical Universtiy in Prague, kopecky@fsv.cvut.cz

the present work, measurements were performed on implants which coatings were made by means of plasma sprayed hydroxyapatite. This material is chemically defined as $Ca_{10}(PO_4)_6(OH)_2$. The hydroxyapatite is very fragile and cannot carry the prosthetic load. Therefore, it cannot be used for the production of separate load-bearing implants, but only for coating. [6] Hydroxyapatite has osteoinductive properties which promote the new bone formation.

METHODICS

Within the experiments we have primarily focused on determining the micromechanical surface properties of the implant stem using nanoindentation. Moreover, themicroscopic analysis of the surface was carried out by means of the electron microscope XL30 ESEM-TPM - Philips [7, 8]. Individual samples were analyzed sequentially to obtain the surface morphology as well as stem composition (elemental analysis). All measurements were performed for several magnifications (20× - 1000×).

To study the evolution of elastic modulus through the individual layers of implants, the nanoindentation tester NHT CSM Instruments equipped with Berkovitch tip was utilized. This approach allows for determination of basic material characteristics at the micro level [9]. These basic characteristics include Young's modulus, hardness of the material, plastic and viscous parameters. Using the nanoidentor the load vs. indentation depth diagram is obtained (Fig 1).

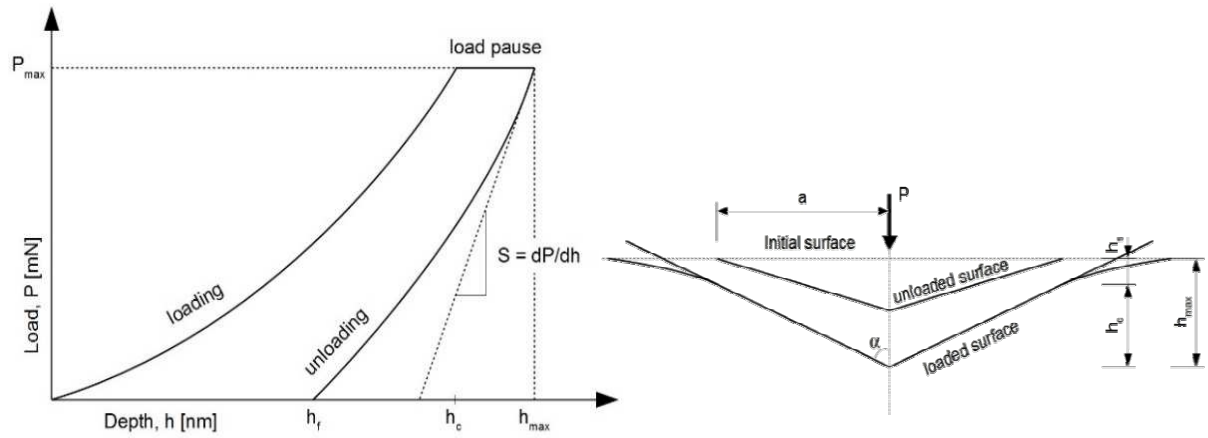

Fig. 1 Typical indentation curve – load vs. depth (left) and scheme of the simulation under the indenter (right)

Material characteristics are derived according to Oliver-Pharr (O & P) [6]:

$$h_c = h_{max} - \varepsilon \frac{P_{max}}{\frac{dP}{dh}} \qquad (1)$$

where ε is a constant that depends on the indenter geometry (for Berkovich and spherical indenter the value of ε is 0.75). The reduced modulus E_r is evaluated as

$$E_r = \frac{dP}{dh}\frac{1}{2\beta}\frac{\sqrt{\pi}}{\sqrt{A}} \quad (2)$$

where β stands for the geometrical factor correcting the non-symmetrical indenter shape (for Berkovich indenter the value of β is 1.034 and for spherical indenter β is 1.0) and A denotes the projected contact area of the indenter at the peak. The hardness H is calculated as

$$H = \frac{P_{max}}{A(h_c)} \quad (3)$$

where A is the contact area at load Pmax and hc stands for indentation depth.

The flexible contact idealization is utilized to obtain the Young's modulus (E) as

$$\frac{1}{E_r} = \frac{(1-\nu^2)}{E} - \frac{(1-\nu_i^2)}{E_i} \quad (4)$$

where ν is Poisson's ratio of the tested material, E_i and ν_i are elastic modulus and Poisson's ratio of the indenter, respectively.

Five different dental implants were examined (Var. I-V). All tested implants had a cylindrical shaft and a peripheral coating produced by plasma spraying of hydroxyapatite. The titanium alloy used for implant's stems was $Ti_{64}AI_4V$. Var. I was provided by the manufacturer No.1, while the rest (Var. II-V) by the manufacturer No.2. Note that each of the implants is from different batch. (Manufacturer names are deliberately hidden.)

The implants were embedded in an epoxy resin and then cut and polished to an acceptable quality of surface. The transverse and frontal section measurements were performed for the Var. II, III and IV. Because of limited number of specimens, the measurements on transversal section were carried out (Var. I, V). The parameters needed for the nanoidenter setup were chosen with regard to the expected depth of the indent in the range of 700-1000 nm for metal parts (stem) and 300-500 nm for the surface layers of implants. The loading was controlled by the maximum value of applied force.

RESULTS

The elemental analysis by electron microscopy shows large differences in the composition of each variant (Tab. 1) - only elements exceeding 1% at least for one of the specimens are presented. Unfortunately, it is not possible to compare the original composition of the surface with measured data because these data were not provided by the manufacturers All the studied implants are coated with hydroxyapatite [Ca_{10} (PO_4) $_6$ (OH) $_2$], but their elemental composition varies considerably. In particular, the implant I has higher carbon content and lower content of calcium and phosphorus.

Tab. 1 Percent (atomic) representation of chemical compounds on the implant surface at high magnification (1000X) and small area on which the measurement was performed

Element	implant				
[%]	I	II	III	IV	V
C	15.09				/
O	52.19		57.30	62.04	/
Al	0.4	2.90	0.51	0.24	/
Si	0.15	1.18	0.40	0.15	/
P	12.01	34.42	15.02	14.47	/
Ca	18.09	61.40	25.94	22.55	/
Ti	1.47			0.21	/

Large differences in chemical composition are seen for specimens II, III and IV (all from the same manufacturer). In this case, the implants were selected from different batches. Note that the manufacturer changed the chemical composition of the coating from batch to batch. The morphology of the implant surfaces is very similar for all the examined variants. Surface coatings are free of sharp edges and the pore size is almost identical (Fig 2).

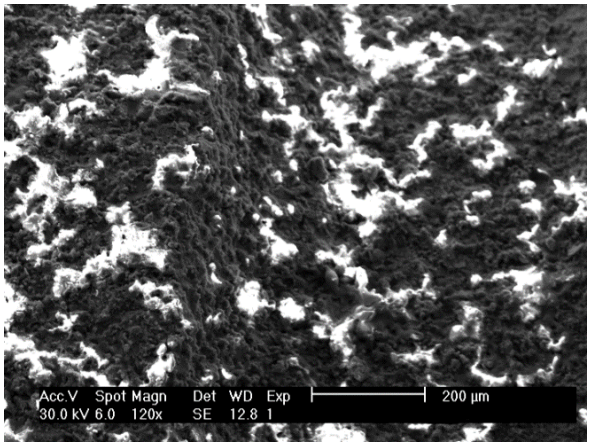

VAR I

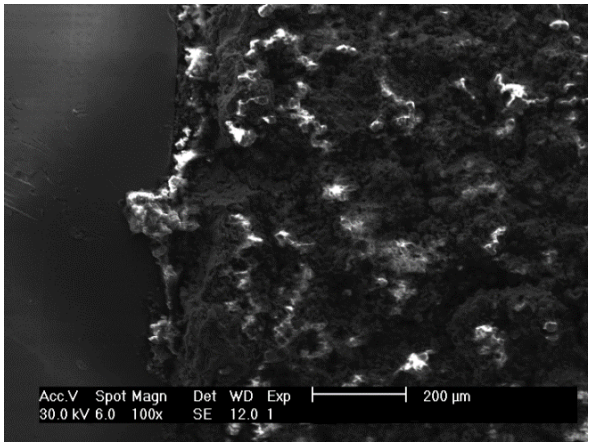

VAR II

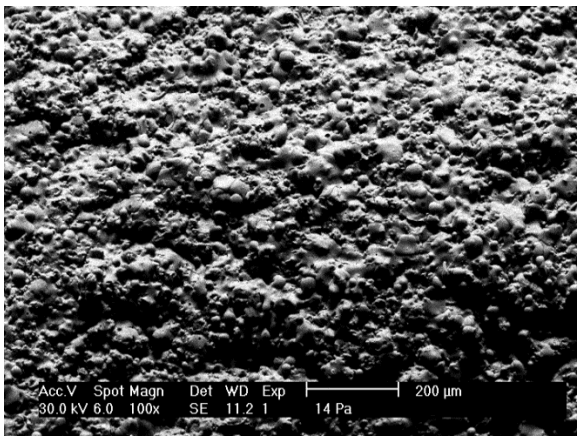

VAR III

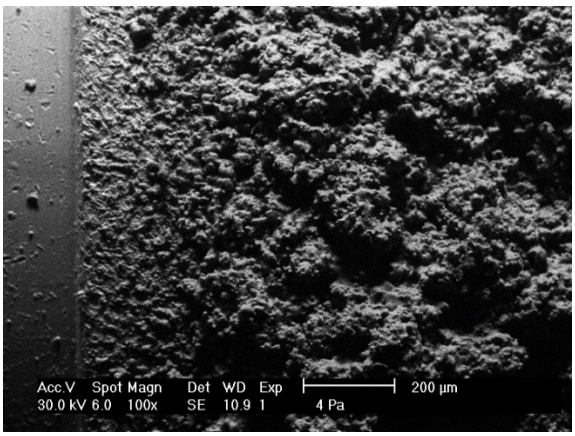

VAR IV

Fig. 2 *Coating implants at 100-120x magnification of the electron microscope*

Var. V was not supplied in a sterile form, therefore the elemental analysis was omitted for this specimen.

Within micromechanical analysis, we focused on the analysis of the elastic modulus E and the actual stem of the implant surface layer, the hardness of the stem and the implant surface and the thickness of the coating layer. Measurements using cyclic loading (loading in four steps, which leads to cycles of "loading - unloading" (Var. II-IV)) did not affect the measured porosity at the required depth of indent. Therefore, the other samples were loaded only with one cycle of "loading - unloading". The obtained results are summarized in Tab. 2.

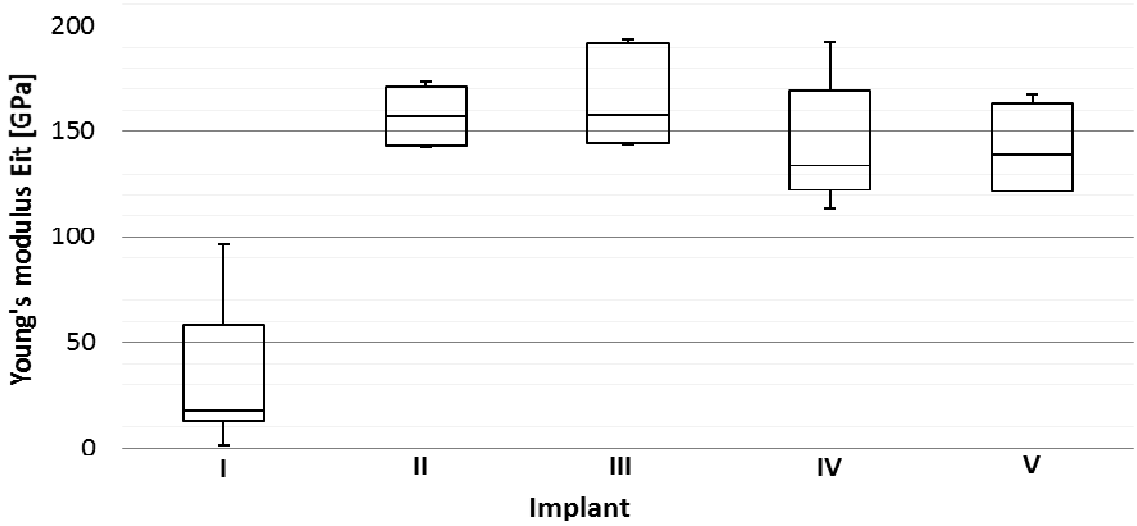

Fig. 3 The evolution of Young's modulus in the peripheral layer of implant (minimum, lower quartile, median, upper quartile, maximum)

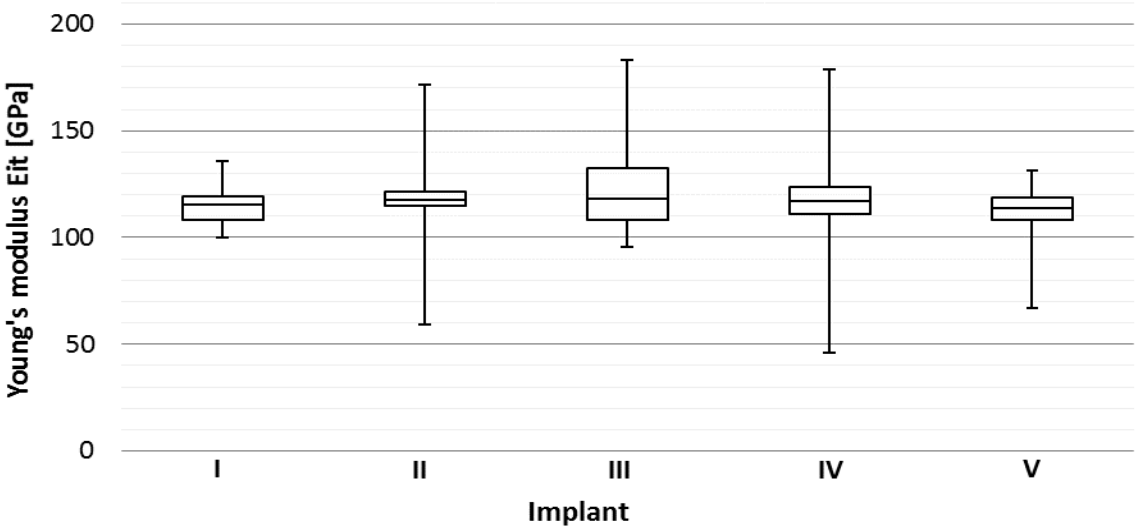

Fig. 4 The evolution of Young's modulus in the stem of implant (minimum, lower quartile, median, upper quartile, maximum)

The Young's moduli of the implant stems are similar for all variants and confirm the data supplied by the manufacturers.

Tab. 2 Summary of experimentally determined elastic modulus (Eit), hardness (Hit) and thickness of the modified surface layer of selected implants and their fins. The resulting value is calculated as the median of measured values

	implant							
	I	**II**		**III**		**IV**		**V**
		long.	trans.	long.	trans.	long.	trans.	
Eit stem [GPa]	115.5	126.9	117.4	129.1	118.1	129.9	116.9	113.8
Eit surface [GPa]	17.4	145.6	157.0	147.1	157.5	133.5	133.9	139.1
Hit stem [kPa]	3 894	4 258	4 148	4 579	4 289	4 804	4 062	3687
Hit surface [kPa]	569	6 723	7 698	7 733	8 141	5 106	5301	8119
coating thickness[µm]	49	67	63	144	135	187	180	99

Despite the fact that the plasma-coated hydoxyapatit was common for all specimens, a large scatter in the values of elastic modulus and hardness of surfaces was observed. Samples II-V show values of E relatively close to each other, but compared to the sample I are about 8× larger.

The microscopic analysis revealed a relatively large variance in the thickness of the surface layer (Fig. 5).

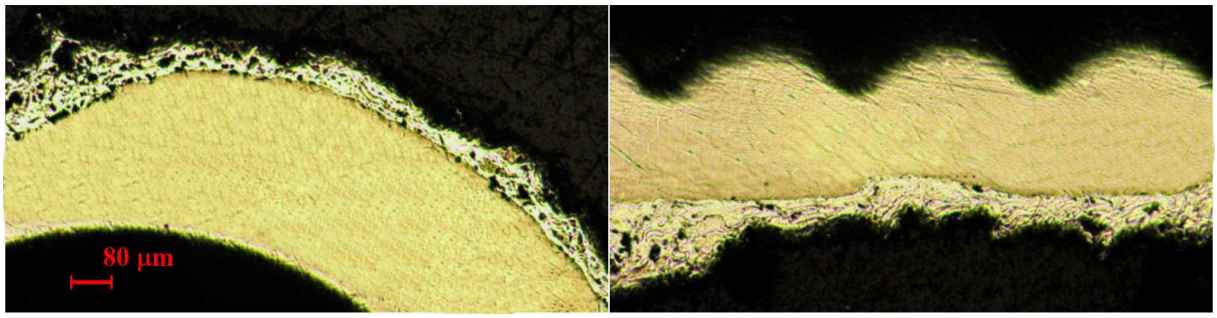

Fig. 5 *Microscopic images - transverse (left) and longitudinal (right) cut of the implant II showing non-uniform thickness of the surface layer*

CONCLUSION

The present study was focused on the analysis of intraosseous dental implants. All implants had the titanium alloy stem ($Ti_{64}AI_4V$) of cylindrical shape whose outer surface layer was formed by plasma spraying of hydroxyapatite ($Ca_{10}(PO_4)_6(OH)_2$). The modulus of elasticity of the stem implant is almost identical for all studied variants and confirms the data supplied by the manufacturer. Significant differences in the mechanical and chemical properties were observed for the implant surfaces, even though it the same material was utilized. The effect of these differences on long-term implant stability must be verified by means of clinical applications. An equally important finding is the uneven thickness of the surface layer. During the biological processes following implantation the hydroxyapatite surrounding tissues is consumed and so the uneven thickness could negatively affect the healing process.

ACKNOWLEDGEMENT

The financial support by the Technology Agency of the Czech Republic (TAČR project no. TA03010886) and Faculty of Civil Engineering, Czech Technical University in Prague (SGS project No. SGS14/122/OHK1/2T/11) is gratefully acknowledged.

REFERENCES

[1] JÍRA, A., NĚMEČEK, J. Nanoindentation of human tooth dentin. *Key Engineering Materials*. 2014, **606**, 133-136. ISSN: 10139826.

[2] GRUÉHENNEC, L., SOUEIDAN, A., LAYROLLE, P. and AMOURING, Y. Surface treatments of titanium dental implants for rapid osseointegration. *Dental materials*. 2007, **23**(7), 844-854. ISSN 01095641.

[3] ALBREKTSSON, T., BRANEMARK, P.I., HANSSON, H.A. and LIDNSTROM, J. Osseointegrated titanium implants. Requirements for ensuring a long-lasting, direct bone-to-implant anchorage in man. *Acta Orthop Scand*. 1981, **52**(2), 155-181). ISSN 0300-8827.

[4] ELLINGSEN, J.E. Increasing Biocompatibility by chemical modification of titanium implant surfaces. In: *The Bio-Implant Interface: Improving Biomaterials and tissue reactions*. CRC Press. Boca Raton. 2003, pp. 323-340. ISBN 978-0-203-49143-0.

[5] ŠIMŮNEK, A. et al. Alkali treatment –new concept of titanium implant surface modification. *Clinical Oral Implants Research*. 2004, **15**, 289-303. ISSN 1600-0501.

[6] ARIAS, J.L., MAZOR, M.B., POU, J., LEON, B. and PERÉZ-AMOR, M. Stochiometric transfer in pulsed laser position of hydroxyapatite. *Applied Surface Science*. 2000, 434-438. ISSN 0169-4332.

[7] OLIVER, W. and PHARR, G. An improved technique for determining hardness and elastic modulus using load and displacement sensing indentation experiments. *Journal of Material Research*. 1992, **7**(6), 1564-1583. ISSN 2044-5326.

[8] ŠEJNOHA, M., ŠMILAUER, V., NĚMEČEK, J. and KOPECKÝ, L. Application of micromechanics in engineering practice. In: *8th Internation Conference on Engineering Computational Technology.* Croatia: 2012, pp. 1-17. ISBN: 978-190508855-3.

[9] FISHER-CRIPPS, A.C. Nanoindentation. *Springer Verlag*. 2002. ISBN 0-387-95394-9.

REINFORCEMENT OF GLUED LAMINATED TIMBER BEAMS - POSSIBILITIES

Pavel KLAPÁLEK[1], **Lenka MELZEROVÁ**[2]

Abstract*: This article aims to summarize and describe the most commonly used methods for reinforcement of beams made of glued laminated timber (GLULAM). The introduction will describe why and when it is good to reinforce beams and which methods exist. Each method will be collectively described, including pros, cons and possible usage. In the conclusion, the methods will be compared and evaluated objectively. This article was created as a research for follow-up work that will be more in depth focused on chosen method for reinforcement of glue laminated timber beams.*

Keywords*: Reinforcement, glued laminated timber, GLULAM, FRP, steel, carbon fiber.*

INTRODUCTION

Currently, the timber elements made of glued laminated timber, are very popular in civil engineering, mainly due to the excellent ratio of weight to capacity. GLULAM elements, such as simple beams with rectangular shape, saddle beams of various types, arches and frames, are mostly used for roof structures. Timber structures but generally exhibit a greater deflections under load than similar elements made of steel or concrete. GLULAM is doing in this respect a little better, but still mostly about the use of the GLULAM in the structure (by the standards) decides size of deflection. GLULAM has a relatively low tensile strength perpendicular to the fibers (delamination), for example an arc structure is often necessary to reinforce to increase load capacity [4]. Glued laminated timber has been manufactured since the end of 19th century, but massively has been used since the 50th years of the 20th century. Already in the sixties the technologists and manufacturers became interested in the possibility of reinforcing the GLULAM [3].

Just to improve worse properties of a material, it is appropriate to use other materials for reinforcing methods to increase their strength. Reinforcement also allows the use of dimensionally smaller elements that have the same strength as the elements without reinforcement. Consequently also reduce the weight of the structure and reducing the enclosed space. Reinforcement is then a system

[1] Ing. Pavel Klapálek, Department of Mechanics, Faculty of Civil Engineering, CTU in Prague; Thákurova 7, 160 00, Prague, Czech Republic; pklapalek@gmail.com

[2] Ing. Lenka Melzerová, Ph.D., Department of Mechanics, Faculty of Civil Engineering, CTU in Prague; Thákurova 7, 160 00, Prague, Czech Republic; melzerov@fsv.cvut.cz

composed of two or more substances which is responsible for the resulting element to supply the new or improve the old features. Task of one substance in the material is then usually to improve one property, usually the strength, while the other serves as a binder. The result of such connection is then product, which is generally called a composite material [1]. The best known representative of the composite material is the reinforced concrete. This article discusses the elements, made of timber, reinforced with other materials, such as timber of other species, wood-based materials, glass or carbon fiber or steel, glued to timber (Fig. 1).

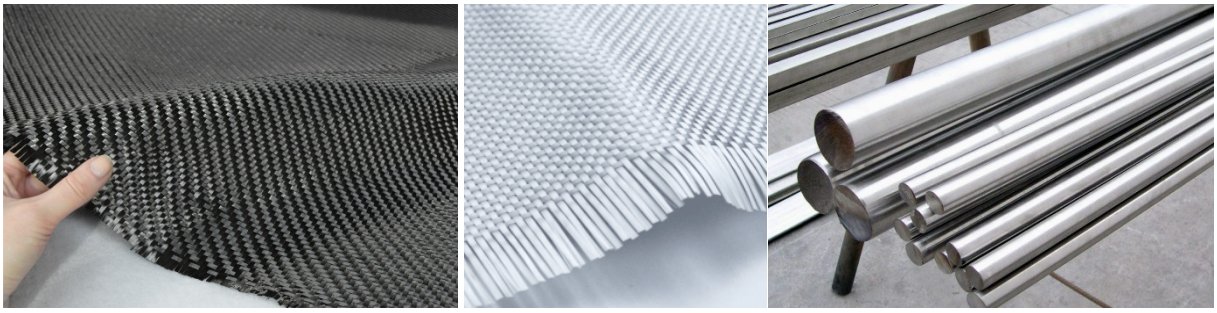

Fig. 1 From left: carbon fiber sheet, glass fiber sheet and steel rods (http://www.easycomposites.co.uk/)

Basic division and methods

When reinforcing a timber structures you must fundamentally distinguish whether an element, that needs to be reinforced, has been already embedded in the structure (in-situ) or in production. The article focuses rather on the second group, thus reinforcing during the production.

The first group is used, for example, during the reconstruction of historical buildings, if you need to increase the bearing capacity of the structure (changes regarding the use of the object) or repair of damaged elements. There are several possible ways to increase the bearing capacity of the construction in-situ. The first way is to use *long screws* (Fig. 2) that are screwed perpendicular to the already existing shear cracks and thus help to carry the load of the beam to different locations, which are not damaged, or solidify GLULAM beams to withstand more tension perpendicular to the fibers [6].

Fig. 2 Self-tapping continuously-treaded screws and threaded rods of different size

The second method is called *attaching*. Attachments are made of timber (plate, beam, LVL products, plywood), steel (U-profile, salary) or other materials. Attachments are applied mostly from one or two sides of the element, sometimes even from three or four sides. Elements subjected to bending is recommended to attach vertically - i.e. from the top or bottom side of the element (Fig. 3). However, this is not always possible, e.g. in ceilings there must be maintained the original floor height or the original soffit. Timber elements can be reinforced over their entire length or just locally, e.g. in the middle, at one end, etc. The disadvantages are then enlarged cross-section and change of the architectural point of view [7].

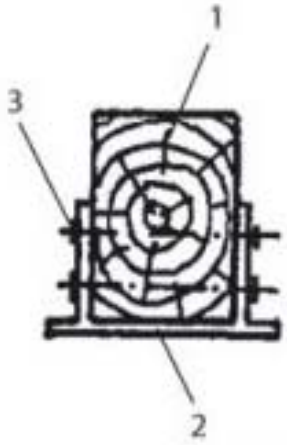

Fig. 3 Reinforcement of the beam by steel U-profile: 1 – timber beam, 2 – reinforcing steel U-profile, 3 – connection between two materials (http://www.asb-portal.cz/)

The second group is then the one which for our purposes we will devote more in detail. Reinforcing beams already in production has justified its advantages, the main one is controlled production and optimization of reinforcement. Reinforcing beams in the production can be divided into three basic methods, which mainly differ in the type of material used to reinforce the beams and its effects.

Reinforcement by high-strength lamellas made of timber

Reinforcement of the beam using high strength lamellas is one of the commonly used methods by producers of GLULAM beams. The beams are then provided, at the bottom, or even at the top edge, with the lamella of higher strength and quality than the rest of the beam (Fig. 4). Under a typical load of the beam, the most strained parts are lower (tension) and upper (pressure) edges. The used reinforcing lamellas are then up to several strength classes higher than the center of the beam. Because the technological process of production of GLULAM beams is basically unchanged, this solution is commonly used. The use of lower quality wood for the middle section helps to reduce the production costs in the tens of percent. The disadvantage might be the need to control the quality of the

reinforcing lamellas and to control the method of storing the beam in the structure, so that the proper orientation (mainly when reinforcing the beam at only one side) [5].

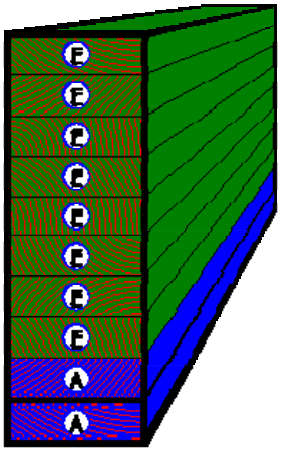

Fig. 4 Example of the GLULAM beam (E) reinforced with timber lamellas of higher strength (A) (http://www.americanlaminators.com/firp.html)

Reinforcement by gluing steel rods and wires

Reinforcing with steel bars and wires is a common method that has two uses. The first one is gluing of steel rods (even pre-stressed) or wires to the bottom or upper lamellas. The second one is gluing steel bars perpendicularly to the fibers to increase the bearing capacity of the material strength perpendicular to the fibers, it is most often used for high beams (up to 2.5 m) used on the large spans [2]. This type of reinforcement, however, entails a lot of problems, mainly arising from the incompatibility between wood and steel. You must use the appropriate connecting material (usually resins or polymers) (Fig. 5), but there is still often found corrosion of steel elements. Steel can also considerably increase the weight and decrease the load capacity when exposed to fire. Steel elongation at yield point is lower than at the timber in advance whereby there the use of plasticity of wood [9].

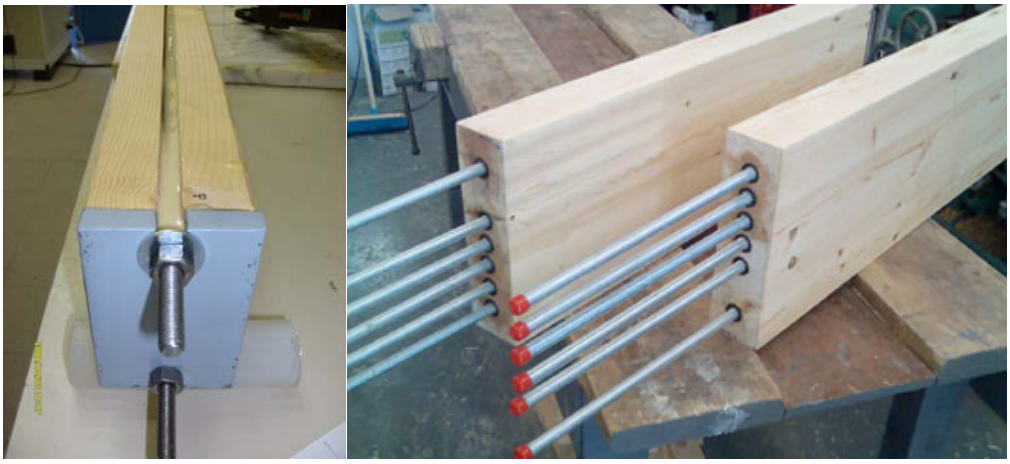

Fig. 5 Pre-stressed steel rods bonded to GLULAM beam by glue [2]

Reinforcement by composite fibers

For reinforcement by using high-strength materials, known as FRP (Fiber Reinforced Polymers), are used composite fibers made of aramid, carbon, glass, asbestos, PVA and others, the first three are the most commonly used in the civil engineering [1]. Composite fibers are an anisotropic material that has considerably improved characteristics in one direction only. They are preferred mainly due to the high tensile strength in the fiber direction, high stiffness and low weight. Possible use for reinforcement of the beam from LLD depends on the form in which the fibers are produced (plates, strips, rods, or fabrics) and how they are attached to the beam. To ensure the interaction between composites and timber, it is necessary to achieve the perfect conjunction, which is done with glue (Fig. 6). A simple gluing to the beams, however, has a major drawback that the fibers are used only at 40% of their capacity [5]. For a better use of fibers there is the possibility of pre-stressing them, firms are currently trying to pre-stress the system of timber beams in combination with carbon fibers [10]. Use of composite fibers for reinforcement of GLULAM in the Czech Republic is still relatively low, but this is not by malfunction of the solution, but rather by professionals that are lacking information. The material costs are high, but because the technology is still being developed and optimized, the price reduces every day. Already today, it is possible, when using the composite fibers for reinforcement, save up to 35% of total cost. This stems mainly from the possibility of using lower quality timber and reduction in size of elements (saving the cost of transport).

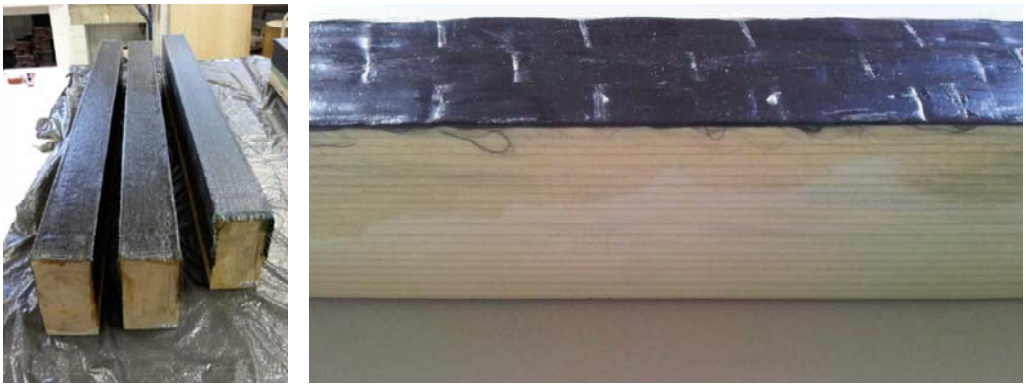

Fig. 6 Glulam beam reinforced by a carbon fiber sheet [2]

CONCLUSION

While exploring possibilities of reinforcing beams of glue laminated timber it is clear that there are many methods which are already widely used in building practice. Some methods, which include mainly the use of composite fibers, however, are still rarely used. However, these methods provide significant improvement of material properties and so it is necessary inform the public about these options. Nowadays, you can already save part of the costs with this method, but it is necessary to simplify use and prepare a unified design system.

ACKNOWLEDGEMENT

The financial support of this paper is by the Faculty of Civil Engineering, Czech Technical University in Prague (SGS project No. 14/122/OHK1/2T/11) is gratefully acknowledged. This outcome has been achieved with the financial support of the Ministry of Education, Youth and Sports of the Czech Republic, project No. LD12023 advanced methods for design, strengthening and evaluation of glued laminated timber.

REFERENCES

[1] AGARWAL, B., BROUTMAN, L. *Vláknové kompozity. Státní nakladatelství technické literatury*. Praha, 1987, 294 p.

[2] KOTLER, P. and ARMSTRONG, G. *Principles of Marketing*. 9th ed. New Jersey: Prentice-Hall, 2001. 785 p. ISBN 0-13-029368-7.

[3] DE LUCA, V. and MARANO, C., *Prestressed glulam timbers reinforced with steel bars*. Potenza, Italy, 2011, at Construction and Building Materials 30 (2012), p. 206-217.

[4] HORSKÁ, P. *Příprava polymerních kompozitů: skleněné vlákno/polyesterová pryskyřice* [online]. 2009. [cit. 2014-7-05]. Available from www: <https://dspace.vutbr.cz/xmlui/bitstream/handle/1012 /10336/BP%20all.pdf?sequence=1&isAllowed=y>.

[5] KOŘÍNEK, Z. *2. vlákna* [Online]. Undated. Pages 3-68. [cit. 2014-07-05]. Available from www: <http://mujweb.cz/zkorinek/vlakna.pdf >.

[6] KUKLÍK, P. and MELZEROVÁ, L., *Vyskopevnostní výztužné lamely v nosnících z lepeného lamelového dřeva* [online]. 2012. [cit. 2014-07-05]. Available from www: < http://stavba.tzb-info.cz/drevene-a-ocelove-konstrukce/8776-vyskopevnostni-vyztuzne-lamely-v-nosnicich-z-lepeneho-lameloveho-dreva>.

[7] REINPRECHT, L., Štefko, J.: *Dřevěné stropy a krovy – typy, poruchy, průzkumy a rekonstrukce*. ABF – ARCH Praha, 2000, 242 p.

[8] REINPRECHT, L., *Rekonstrukce dřevěných prvků protézováním, příložkováním a ukotvením do ocelových konzol* [online]. 2008. [cit. 2014-07-05]. Available from www: <http://www.asb-portal.cz/stavebnictvi/drevostavby/rekonstrukce-drevenych-prvku-protezovanim-prilozkovanim-a-ukotvenim-do-ocelovych-konzol>.

[9] REINPRECHT, L., ŠTEFKO, J., Dřevěné stropy a krovy, typy, poruchy, průzkumy a rekonstrukce. ABF, a.s., Nakladatelství ARCH, Praha, 2000, 252 p, ISBN 80- 86165-29-9.

[10] TINGLEY, D., A., CEGELKA, S. New Compression Based Design Principals for Reinforced Glulams. Materials for the New Millennium, 4th Materials Engineering Conference. 1996, p. 1479-1491.

[11] SIKA s.r.o. [Online]. 2010 [cit. 2014-07-05]. Available from www: http://cze.sika.com/content/dam/Czech_Republic/Main/01_General/cz_news/2010/20100525_cz_con_velkypartner.pdf

THE INTRODUCTION TO THE FORMATION OF LAMELLAR STRUCTURES OF OSTEONS

Miroslav PETRTÝL[1], **Romana LOVICHOVÁ**[2],
Pavel PADEVĚT[3], **Lubomír KOPECKÝ**[4], **Petr BITTNAR**[5]

***Abstract**: The cortical bone is a composite material with hierarchical structure. At microstructural levels one can distinguish two lamellar structures at the mature cortical bone: osteons, made from concentric layers of lamellae surrounding long hollow Haversian canals, and interstitial lamellae made of remnants of old osteons. The spatial arrangement of osteons has been already described by many authors however theirs 3D structural descriptions are more or less different. The aim of this paper is to clarify the current knowledge of lamellar structures of osteons.*

***Keywords**: Osteon, cortical (compact) bone, spongy (cancellous) bone, interstitial lamellae.*

INTRODUCTION

Bone is a dynamic tissue, constantly undergoing through the process of remodelling. Live bone tissue, like other biological systems, has an ability to optimize the structures on all its structural levels. Compact bone and cancellous bone are multifunctional biological tissues having from a biomechanical point of view a bearing function dominantly and in many cases also a protective function. Mature human cortical bone is composed primarily of densely arranged Haversian systems with a central canal inside - Haversian canal where run blood vessels and nerves. Excellent mechanical properties of healthy mature bone tissue are result from the existence of genetically pre-determined functions in all

[1] Prof. Ing. Miroslav Petrtýl, DrSc., Department of Mechanics, Faculty of Civil Engineering, Czech Technical University in Prague, Czech Republic, petrtyl@fsv.cvut.cz

[2] Ing. Romana Lovichová, Department of Mechanics, Faculty of Civil Engineering, Czech Technical University in Prague, Czech Republic, romana.lovichova@fsv.cvut.cz

[3] Ing. Pavel Padevět. Ph.D., Department of Mechanics, Faculty of Civil Engineering, Czech Technical University in Prague, Czech Republic, pp@cml.fsv.cvut.cz

[4] Ing. Lubomír Kopecký, Department of Mechanics, Faculty of Civil Engineering, Czech Technical University in Prague, Czech Republic, kopecky@fsv.cvut.cz

[5] Ing. Petr Bittnar, Department of Mechanics, Faculty of Civil Engineering, Czech Technical University in Prague, Czech Republic, petr.bittnar@fsv.cvut.cz

components of connective tissue and in the same time as result of mechanical/biomechanical effects in these tissues.

STRUCTURAL LEVELS OF CORTICAL BONE

At a nanostructural level (in the frame of nanometers to several hundred nanometers) the nanostructure of osteons can be characterized by multiphase nanocomposite material containing in volume unit organic components (approximately 32 – 45 %), inorganic components (approximately 33 – 43 %) and remaining amount of volume unit is water [1]. A key component of bone tissue is collagen of the Ist type. From the total amount of proteins in bone there is this kind or type of collagen represented by 90 %. The left proteins are included within the group of non-collagenous proteins [2]. The inorganic phase is composed of nano-crystals of HA mineral (calcium hydroxyapatite - $Ca_{10}(PO_4)_6(OH)_2$). Mineral components contribute to high stiffness and undesirable brittleness. Protein components contribute to the flexibility and deformability of tissue. A very important component of bone tissue is water, which from the biomechanical point of view contributes to hardening. Water molecules contribute to the strength of the bone to its optimum viscoelasticity and also toughness. The nano-composite structure of bone tissues, which are composed by mineralized collagen fibres and water, creates nano-basic functional compartment of the bone.

The sub-microstructural level, i.e. at the level of the lamellas of osteons (thicknesses of the individual lamella of up to several microns) are integrated in the structural component osteons i.e. lamellar composites consisting of bundles of mineralized collagen fibres Ist type, water with non-collagen proteins and ions (for example, nitrogen, calcium, etc.).

In the micro-structural level (in the range of tens to hundreds of microns) there are composed discrete osteons or interstitial lamellae of cortical bone. Osteon is longitudinally oriented microstructure element bone [2] about an irregular cylindrical shape with an outer diameter of about 200-250 μm formed concentric lamellae thicknesses of about 5-7 microns. Lengths osteons reach up to several mm. The concentric plates have an approximately circular to elliptical or oval cross section. The longitudinal axes of the osteons are mostly oriented to the direction of the first dominant principal deformations (or the first dominant principal stresses) [3]. The longitudinal axes of osteons are oriented (for example in femur) in the directions of left-rotary helixes (in the medial wall) and in the directions of right-rotary helixes (in the lateral wall) [3].

OSTEON - BASIC MEZO-STRUCTURAL SUPPORTING ELEMENT OF BONES

The main pillars of mezzo/micro-structural levels of bone are osteons. To bring an exact definition of its elastic/viscoelastic properties and strength was and still is a very challenging task. Lamellas of osteons were very extensively tested in terms of "in vitro", for example [4]. Severity choice objective model live tissue largely depends on the definition of the orientation of fibres in the lamellas

mineralized osteons and their elastic/viscoelastic (elastoplastic) characteristics, which are lamellar fibres inhomogeneous and depend not only on the distribution of collagen nano-fibres (in multiphase composite compartment of nano-levels) but also on the intensity of the formation with free ions in the intercellular space. The ions contained in the intercellular fluids actively regulate bone metabolism in bone cells.

Sub-microstructures of collagen bundles and fibres in the bone lamellae of osteons are highly influenced by mechanical effects [5]. Orientation of the mineralized collagen fibres in the lamellas of osteons are due not only genetic transcription, but also the response of live tissue to the dominant strains [3, 6, 7]. Therefore, it is not yet paid great attention to the orientation of collagen fibres and bundles in lamellar structures in osteons. The descriptions of collagen fibres/bundles in lamellar structures in osteons are more or less different.

The first pioneered developers focused on collagen fibres in the lamellas of secondary osteons were Ebner (1874), Gebhardt (1906) [8] and Weidenreich (1923) (Fig. 1 - left), who consistently documented the alternation of lamellae with longitudinal helical filaments with lamellae transverse fibres (with the lower slope).

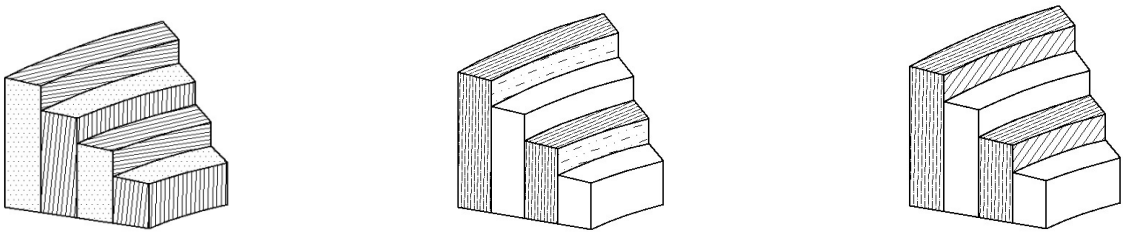

Fig. 1 The orientation of the mineralized fibres in the lamellae of osteons by Ebner– Gebhardt – Weidenreich (1874 - 1923) (left), by Ranvier (1875) (middle), by Ziegler (1908) (right)

In 1875 Ranvier published changing of "homogeneous" lamellas (without specification of fibre orientation) with lamellas containing short fibres (Fig. 1 -middle). A similar conclusion was reached by Ziegler (1908) that only the term "homogenized" lamella replaced with the term "intermediate substance" (Fig. 1 - right). Except of these lamellas he described the lamellas with longer helical filaments.

Ruth (1947) also introduced a harmonic pattern of the lamellas, so that between each "compact" lamellas there is found diffuse (thin) lamella with randomly oriented fibres. He characterized infrequent ("diffused") lamellas wider than the adjacent "compact" (fibrous) lamellas. It cannot be overlooked that Ruth was the first who pointed out the linking of collagen fibres in the wider "diffusion" slat with adjoining "compact" lamellas with one-direction oriented mineralized collagen fibres (Fig. 2 - left). In 1952, Rouiller published a model very similar to the model of Ruth. He described wider "cemented" lamellas to which random (from adjacent lamellae oriented mineralized fibres) enter non-oriented collagen fibres (Fig. 2 - right).

Fig. 2 The orientation of the mineralized fibres in the lamellae of osteons by Ruth (1947) (left), by Rouiller (1952) (right)

In 1970 and 1976 Ascenzi and Bonucci characterized lamellas so that at each subsequent - adjoining lamellae are situated mineralized collagen fibres oriented in the direction of the helix. They described the right-rotary oriented collagen fibres in the lamellae with their left-rotary orientation of collagen fibres in successive lamellae (Fig. 3 - left). Changes in the slope of collagen fibres (in each successive lamella) were brought by Gebhardt.

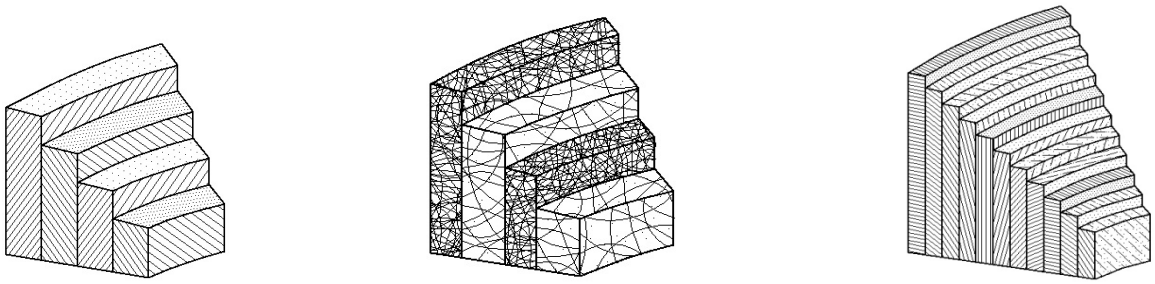

Fig. 3 The orientation of the mineralized fibres in the lamellae of osteons by Ascenzi and Bonucci (1970-1973) (left), by Marotti (1988–1993) (middle), by Giruad-Guille, Wagermeier (1993–2006) (right)

In 1988 Marotti set up harmonious alternation of two types of lamellas in osteons, i.e. lamellas "weak" ("thick", darker), rich in "tangled" fibres and lamellas "strong" (having clearly less dense interlocking mineralized collagen fibres of the 1st type) (Fig. 3 - middle). Marotti et al. simultaneously demonstrated that stronger light layers comprise about 10 to 15% larger amounts of calcium and phosphorus than the weaker (darker) layers. In 1993 Marotti performed deeper analysis by polarized light microscopy (PLM), scanning electron microscope (SEM) and transmission electron microscopy (TEM) and confirmed the findings in the proximity group conclusions concerning on the classical model Gebhardt.

In 1988 Giruad-Guille introduced model TPA (Twisted Plywood Architecture of collagen fibrils [5] that is based on the rotation of sub-layers ("sublamellae"), formed by parallel collagen fibres, rotating around the centreline of osteons (Fig. 3 - right). The work Giruad-Guilleho followed by T. Hofmann et al. (2006), [9] and Wagermeier W. et al, (2006), [10], who described the helical structure of the mineralized collagen fibres in the lamellas of osteons.

SHELL SUB-LAMELLAR SEGMENTS IN THE SLATS OF OSTEONS

With the respect to differences in the descriptions of lamellar structures of osteons by various researchers, the authors of this work focused on the micro-ultrascopic structure analyses of bone fragments (grafts) removed from the proximal part of the human femoral shaft. Fragments of compact bone (man´s bone at the age of 62 years) were studied using an optical microscope Bresser LCD Micro and scanning electron microscope (SEM) brand 0XL30-ESEM from FEI manufacturer. In planes perpendicular to the longitudinal axis of the microscope (Fig. 4), there were observed known microstructures of osteons with narrow dark lamellae and with bright wider lamellae and lacunae of osteocytes. The new findings were discovered during observation of bone grafts in perpendicular direction to the longitudinal lamellar structures (Fig. 5) using the scanning electron microscope. At 800-multiple enlargement there were easily observed narrow lamellas from which shell sublamellas appear that are formed from parallel bundles of mineralized collagen fibres irregular circular cross-section with a diameter of approximately 4-5 μm, generating only a single sublayer. Segment shell sublamellas do not create continuous concentric rings. The mid-surfaces of the monolayer (segment) plates are curved or even flat. The described findings indicated that at the substructural levels there exist sublamellas with less/small flat surfaces in which there are found collagenous bundles of the same directional orientation, whereas adjoining-sublamellas are all mineralized collagen bundles oriented in different direction.

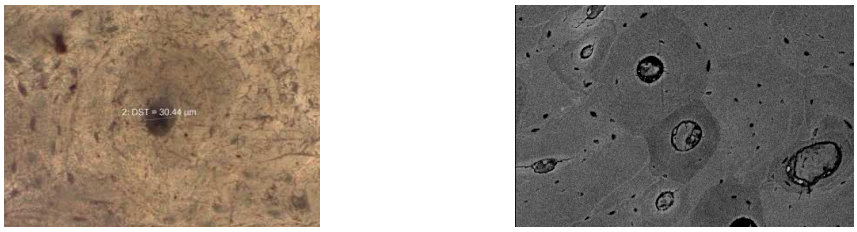

Fig. 4 The distribution of osteons and interstitial lamellaes in cross section observed by the optical microscope (left) and by scanning electron microscope (SEM) (right).

CONCLUSION

From the microscopic analyses there can be done the following key conclusions:

1) Osteon lamellas consist of sublamellas that form ("restricted areas") lamellar sublayers that include a set of parallel collagen bundles having the same orientation. The diameters of collagen bundles are about 4-5 microns.
2) Shell segments have plane or slightly warped middle-plane.
3) Parallel mineralized collagen bundles have straight or slightly curved centerline.
4) Directional orientations parallel mineralized collagen bundles in shell sublamellas have different orientation than the parallel bundles of neighboring sublamellas.
5) Segment shell lamellas create the sublamellar *vaults* in the more mineralized lamellas.
6) Layered segment sublamellas are more concentrated near the lacunaes of osteocytes.

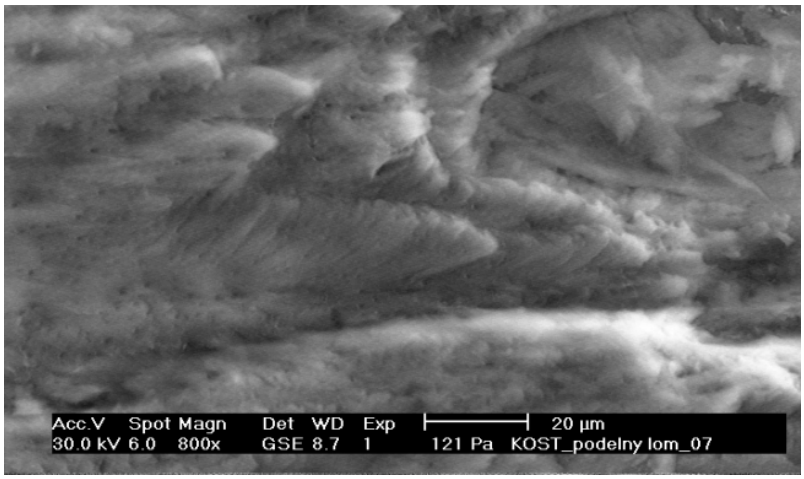

Fig. 5 Shell sublamellas consist of parallel bundles of mineralized collagen fibres irregular circular cross-section with a diameter of approximately 4-5 µm, generating only a single sublayer (sublamella). Shell segments in the image captured by SEM have the mid-surface planar or curved, or slightly warped.

ACKNOWLEDGEMENT

This study was funded by the SGS project No. 14/122/OHK1/2T/11 of the Faculty of Civil Engineering, Czech Technical University in Prague.

REFERENCES

[1] OLSZTA, M.J., et al., Bone structure and formation: a new perspective. *Mater. Sci. Eng. R Rep.* 2007, **58**, pp. 77–116.

[2] ČIHÁK, R., Anatomie 1. 3rd ed. Praha: Grada Publishing, a.s. 2011. 552 p. IBSN 978-80-247-3817-8.

[3] PETRTÝL, M., HEŘT J. and FIALA P., Spatial organization of the haversian bone in man. *Journal of Biomechanics*. 1996, **29** (2), 161–167, 169.

[4] TAKANO, Y., TURNER, CH., et al., Elastic anisotropy and collagen orientation of osteonal bone are dependent on the mechanical strain distribution, *J. Orthop. Res*. 1999, **17**(1) pp. 59-66.

[5] GIRAUD-GUILLE, M. M., Twisted plywood architecture of collagen fibrils in human compact bone osteons. *Calcified Tissue International*. 1988, **42**, pp. 167–180.

[6] ROBLING, A.G., et al, Biomechanical and molecular regulative of bone remodelling, *Ann. Rev.Biomed. Eng.* 2006, **8**, pp. 455-498.

[7] HSICH, Y.-F. and TURNER Ch., Effects of loading frequency on mechanically induced bone animation, J. Bone. *Miner.Res.* 2001, **16**, pp. 918-924.

[8] MAROTTI, G., A new theory of bone lamellation. *Calc. Tissue Iint.* 1993, **53**(1), pp. 41-56.

[9] HOFMANNA, T., et al., Assessment of anisotropic elastic properties of secondary osteon lamellae; *J.Biomech*. 2006, **39**(12), pp. 2282-2294.

[10] WAGERMEIER, W., et al, Spiral twisting of fibres orientation inside bone lamellaes. *Bioin. phases*. 2006, **1**(1), pp. 1-5.

ELASTIC SIMULATION IN OOFEM BASED ON THE IDEA OF QUASICONTINUUM

Karel MIKEŠ[1]

***Abstract**: The quasicontinuum (QC) method is a relatively new computational technique. This technique is a combination of continuum and atomistic approaches. The key idea of QC is to reduce the computational cost by reducing degrees of freedom (DOF) of the fully atomistic approach. Instead of dealing with all atoms, a small relevant subset of atoms is selected to represent the whole system. These atoms, the so-called repatoms, are used to approximate the DOF of other atoms [1]. This article provides a comparison of a method using a discrete particle model based on this idea with a pure particle approach, both implemented in OOFEM [2].*

***Keywords**: Quasicontinuum method, discrete particle model*

INTRODUCTION

The quasicontinuum (QC) method was proposed by Tadmor, Ortiz and Phillips [3] in 1996. The original application of this computational technique was a simulation of large atomistic systems described by long-range conservative interaction potentials. In this article, we focus on discrete particle systems with short-range interactions. Such systems are typically used in simulations of heterogeneous materials. Particles in these systems are distributed randomly and do not form regular lattices like in atomistic systems, but the idea of QC can still be used.

The idea of quasicontinuum method

The main idea of the QC method is to reduce the DOF and computational demand without losing the exact atomistic description in regions where it is required. Therefore, two types of regions in the solved domain are considered. In the regions of high interest, the pure particle approach is required and all particles contribute to DOF. By contrast, in the regions of low interest, continuum assumptions can be used and the number of DOF is significantly reduced.

Only a small subset of particles is selected to represent the entire system. These particles, the so-called repnodes, represent the nodes of a triangular mesh that are used to interpolate the DOF of other particles in the region of low interest. The position of the node of interpolation mesh is not arbitrary, but has to coincide with one of the repnodes, i.e., with a particle carrying DOF. In the regions of high interest, all particles are selected as repnodes to provide the exact particle representation.

[1] Bc. Karel Mikeš, Faculty of Civil Engineering, CTU in Prague, karel.mikes.1@fsv.cvut.cz

The regions of high interest can be set explicitly as constant during the entire simulation process, or can be changed as needed in each time step. A suitable change of the regions of high interest is often associated with a substantial increase of accuracy and, in several specific cases, it is necessary to represent the correct physical behavior, e.g., in the crack propagation process.

In this article, a method based on the idea of quasicontinuum is compared with the pure particle approach in 2D. Accuracy is expressed in terms of errors in displacement and strain. The number and position of repnodes are adaptively changed to achieve the optimal result.

METHODOLOGY

The simulation algorithm is composed of the following steps:

- generation of particles and trusses
- selection of repnodes and interpolation elements
- computation in OOFEM

Generating of particles and trusses

In the first step, the required number of particles is generated in the solved 2D domain. The position of each particle is generated randomly until the required number of particles is generated or the maximal number of iterations is reached. The minimal distance between each two particles R_P is prescribed and checked in all iterations. Finally, each two particles whose distance is less than prescribed value $R_t = kR_P$ are connected by a link because only a short-distance interaction model is considered. Factor k should be selected from the range $\langle 1.8,1.9 \rangle$ to obtain the optimal truss density, see Fig. 1.

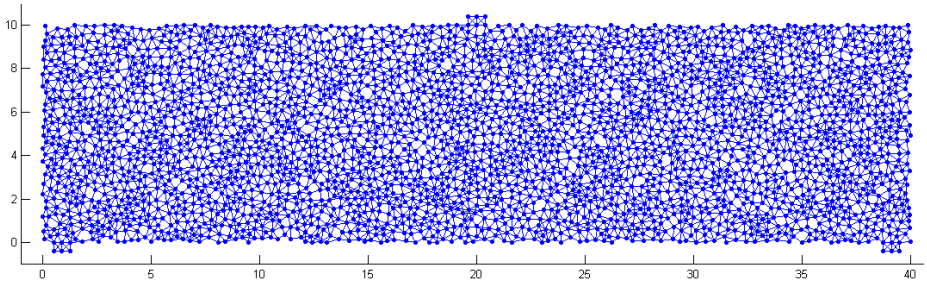

Fig. 1 Particles connected by links for $R_t = 1.9\ R_P$.

A quadtree structure is used to make the distance checking faster. The solved domain is bounded by a rectangular region, which region is recursively subdivided into four quadrants several times. Then only the necessary neighboring quadrants are scanned during distance checking. Numerical tests showed that this method becomes efficient for systems with at least a few thousands of particles.

Boundary conditions are realized through the use of 6 regular nodes to prevent local effects. Only one node in the middle is subjected to the appropriate boundary condition. All 6 nodes are labeled as

repnodes. Interpolation elements formed by these nodes are not taken into account because they are located outside the solved domain.

For the pure particle approach, an OOFEM input file is created in this step. Every single particle represents a node with two DOF (vertical and horizontal displacement) and the links are described by 1D truss elements.

Rep nodes selection and interpolation elements

In the QC approach, most of the DOF are approximated. For that purpose, a sufficient subset of particles is selected as repnodes. At first, all particles in regions of high interest are selected as repnodes. Then all existing repnodes are considered as nodes of the new 2D mesh and triangulation is finished in the whole domain. All newly created nodes of the mesh are shifted to the position of the nearest particle and this particle is labeled as a repnode, too. Sometimes, two or more nodes of one mesh element happen to be shifted to the same position, which leads to degeneration of a triangular element to a line or a point. Such degenerated elements are detected and removed. This process allows to create an interpolation mesh with variable density with the nodes in the position of particles. See Fig. 2 and Fig. 4.

Now everything needed for the creation of an OOFEM input file is ready. All nodes (particles) connected with truss elements contribute to the stiffness matrix but only repnodes have independent DOF. Repnodes with two DOF (vertical and horizontal displacement) represent nodes of a triangular mesh. Triangular elements are assigned zero thickness and thus do not contribute to the global stiffness matrix. These elements are used only to approximate displacements of nodes not selected as repnodes.

Computation in OOFEM

In OOFEM implementation, nodes carrying DOF are modeled as regular nodes. Nodes with interpolated DOF are realized with a special type of node called hanging node. This type of node allows interpolation of its DOF by the nearest interpolation element. It means that interpolation of a node outside of the interpolation element is also possible.

In this article, linear interpolation of hanging nodes is used. Trusses connecting particles are modeled as purely elastic.

RESULTS

Bending beam

The first example is a three-point bending test with geometry according to Fig. 1. The pure particle model consists of 2989 particles and the number of unknown DOF is 5974. In the first interpolation mesh, there is no region of high interest and the number of unknown DOF is reduced to 232; see Fig. 2

top. In the second interpolation mesh there are two regions of high interest and the number of unknown DOF is reduced to 1924; see Fig. 2 bottom. Absolute values of absolute errors of the strain in trusses in comparison with the pure particle model are plotted in Fig. 3.

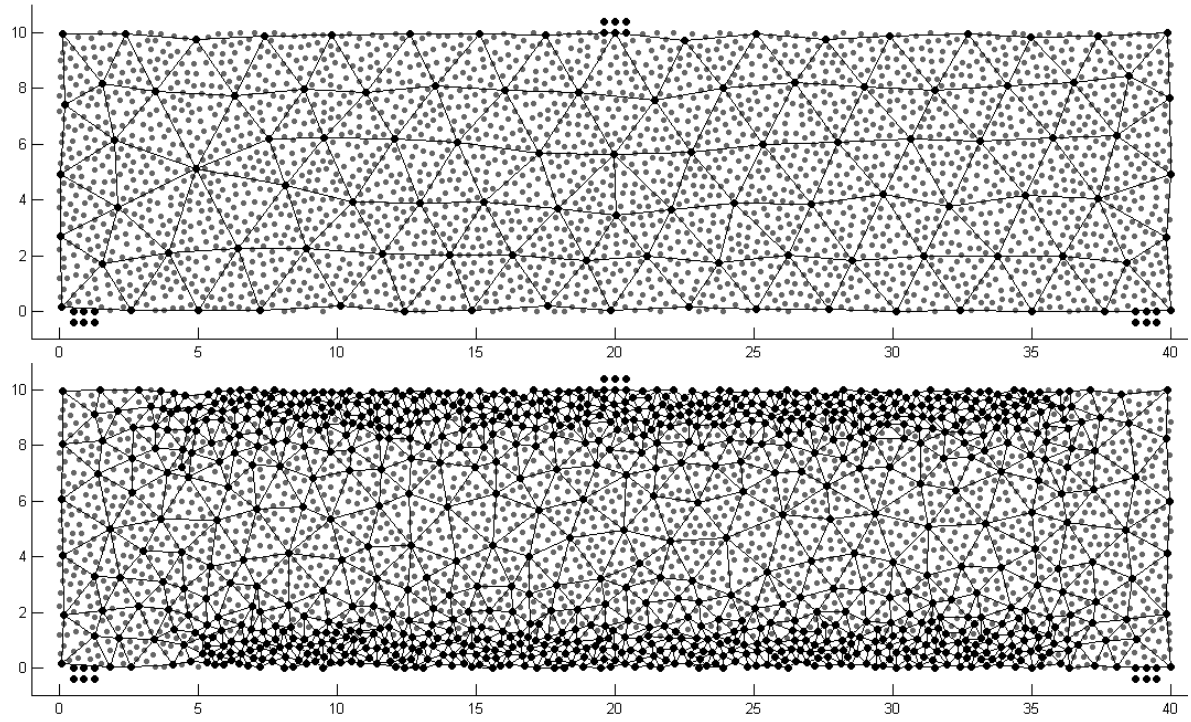

Fig. 2 Interpolation with no region of interest (top), two region of interest (bottom). Repnodes with interpolation elements (black) and particles with interpolated DOF (grey).

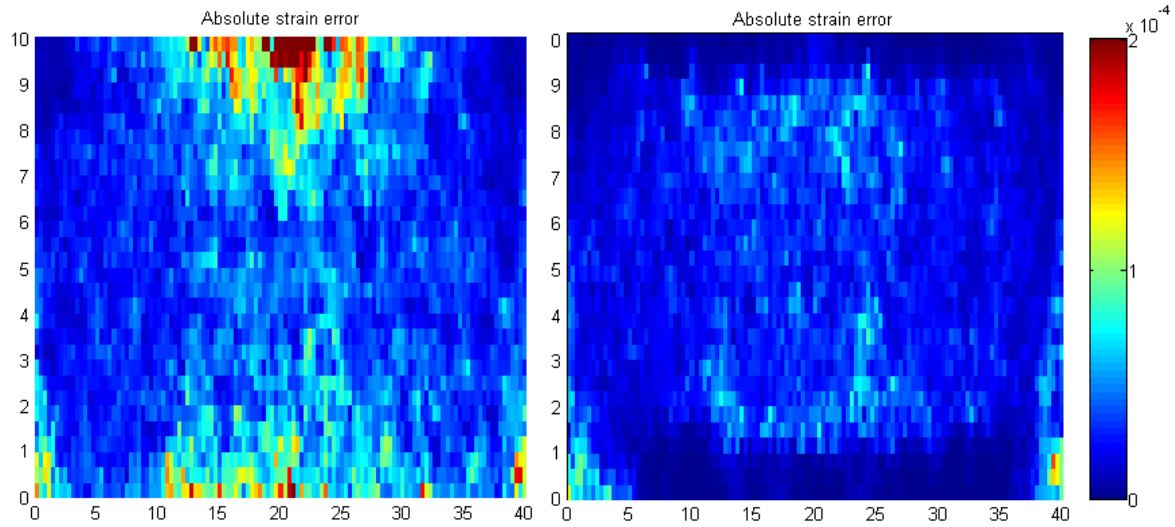

Fig. 3 Absolute strain error of the first interpolation mesh (left) and the second (right).

In the first case, the maximum error is reached near the top and the bottom of the beam. After addition of these parts to the regions of interest, the errors almost vanish.

Bending beam with the notch

The second example is a three-point bending test of a beam with the same geometry but containing a crack. The crack is modeled as a vertical segment connecting points [20, 0], [20, 5]. Trusses which intersect the crack are removed. Interpolation mesh with no region of interest respects the crack geometry; see Fig. 4 top. The number of unknown DOF is reduced from 5974 to 228. The second interpolation mesh has a significant region of interest in the middle; see Fig. 4 bottom. The number of unknown DOF is reduced to 1100. Absolute values of absolute errors of the strain in trusses in comparison with the pure particle model are plotted in Fig. 5. The maximum error is reached near the crack tip. After addition to the region of interest, this error vanishes and other error values are of the order of 10^{-5} instead of 10^{-4}.

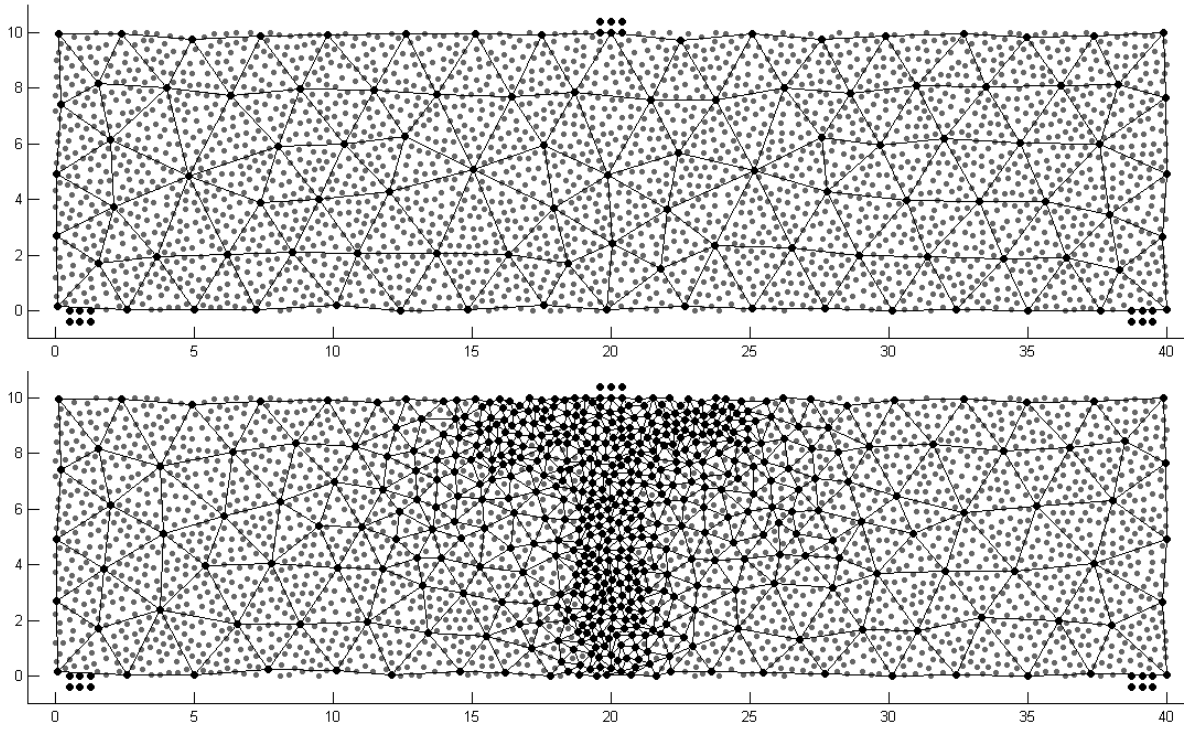

Fig. 4 Interpolation with no region of interest (top), significant region of interest (bottom). Repnodes with interpolation elements (black) and particles with interpolated DOF (grey).

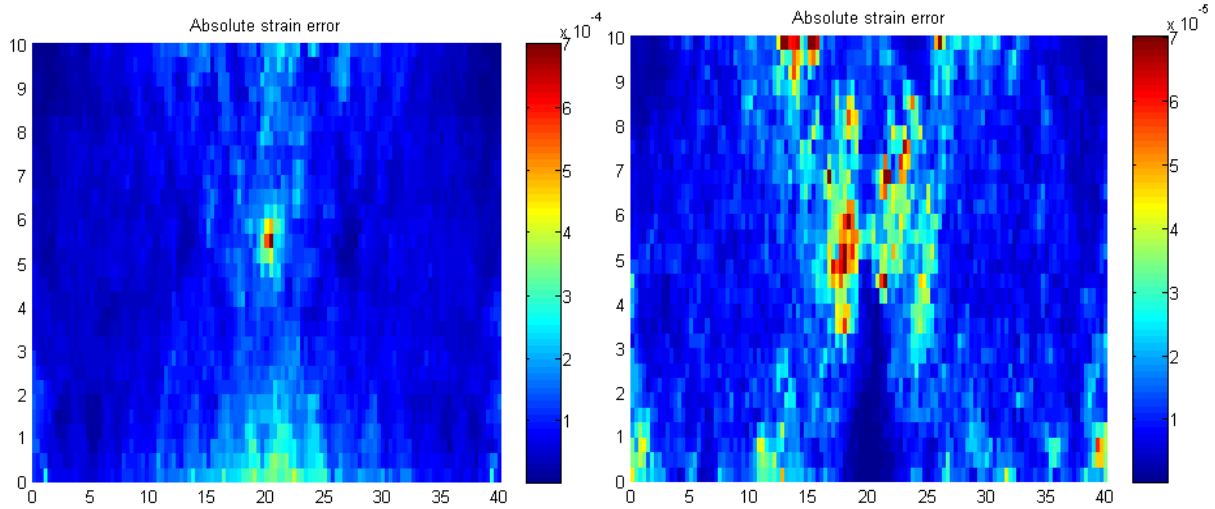

Fig. 5 Absolute strain error of the first interpolation mesh with the crack (left) and the second (right).

CONCLUSION

The presented examples have shown that the QC-based method leads to a substantial reduction of unknown DOF. The error caused by this reduction can be effectively reduced by suitably setting the region of high interest. Finally, a significant simplification of the problem can be reached at the price of an acceptable error.

FUTURE RESEARCH

Future work will be focused on an extension of this method to 3D. Also, addition of non-elastic truss interaction is necessary to simulate plastic behavior and damage of the material.

ACKNOWLEDGEMENT

The financial support of this research by the Faculty of Civil Engineering, Czech Technical University in Prague (SGS project No. 14/029/OHK1/1T/11) is gratefully acknowledged.

REFERENCES

[1] MILLER, R. E. and TADMOR, E. B. The quasicontinuum method: Overview, applications and current directions. *Journal of Computer-Aided Materials Design.* 2002, **9**, 203–239. ISSN 1573-4900.

[2] *OOFEM project home page* [online]. [cited 2014-7-14]. Available from: http://www.oofem.org

[3] TADMOR, E. B., ORTIZ, M. and PHILLIPS, R. Quasicontinuum analysis of defects in solids. *Philosophical Magazine A*, 1996, **73**, 1529–1563. ISSN 1478-6435.

INFLUENCE OF THE CEMENT PASTE WITH FLY ASH TREATMENT ON THE FRACTURE ENERGY

Barbora MUŽÍKOVÁ[1]

***Abstract**: The research solves the issue of the fracture energy calculation on cement paste beam specimens using the Hillerborg and Jenq-Shah methods. The research solves the differences between the two methods, the effect of the treatment way on calculation results and the consequence of adding the fly ash as a binder. The aim is to compare all of these effects on value of the fracture energy.*

***Keywords**: fracture energy, treatment, cement paste, nonlinear fracture mechanic*

INTRODUCTION

This research compares two different ways of measuring fracture energy on cement past beams which have different prescriptions and ways of treatment.

Replacing cement by fly ash

The fly ash used in this research came from the power plant in Tušimice, it is a mixture from three blocks. The fly ash is added as a binder not just as a filler to improve characteristics such as workability of the green cement paste, lower hydration heat and a higher level of fracture energy. Other reasons to use fly ash are environmental and economic reasons. [1]

There were four different prescriptions of the cement paste with fly ash marked as R1, R2, R3 and R4. Their compilations are shown in Tab. 1 Prescription.

Tab. 1 Prescriptions.

	Filler %	Binder %	Binder %		Water–cement ratio
			Cement %	Fly ash %	
R1	75	25	100	0	0.5
R2	75	25	75	25	0.5
R3	75	25	60	40	0.5
R4	75	25	50	50	0.5

[1] Bc. Barbora Mužíková, Department of Mechanics, Faculty of Civil Engineering, Czech Technical University in Prague, barbora.muzikova@fsv.cvut.cz

Ways of treatment

There were two ways of treatment, on the air and in water bath. The first method is suitable for the air agglutinants which are characteristic for the carbonation reaction in. They are not ever-lasing in water. The fly ash, lime and gypsum are examples. The second way was in water bath. This way supports the hydration reaction in hydration binders – cements, hydration lime. [2] [3] [4]

Development of linear elastic fracture mechanic

The begging of linear elastic fracture mechanics is around 1920–1930 when Griffith brought the energetic (global) criterion which describes the behaviour of elastic homogeneous materials such as glass. In the years 1940–1960 Irwin improved this idea to the local criterion – effective critical stress intensity factor describing elastic–plastic homogeneous material for example metals with finite dilatability.

The concrete was considered as a brittle material but its behaviour is more complicated. Cracks, pores, inclusions have an important effect on it. It is a quasi–brittle material that means that before reaching the peak load there is a slight hardening. After reaching the peak load the deformation rises together with decreasing compressive strength or strength in tension. This problem is solved by the nonlinear fracture mechanic (NLFM). [5] [6]

Methods of NLFM

There are three methods described in this research – the Hillerborg`s method of fictitious crack, the Jenq–Shah`s method of two parameters – these two were tested in practice – and Bazant`s method of size effect, which requires many specimens of various sizes.

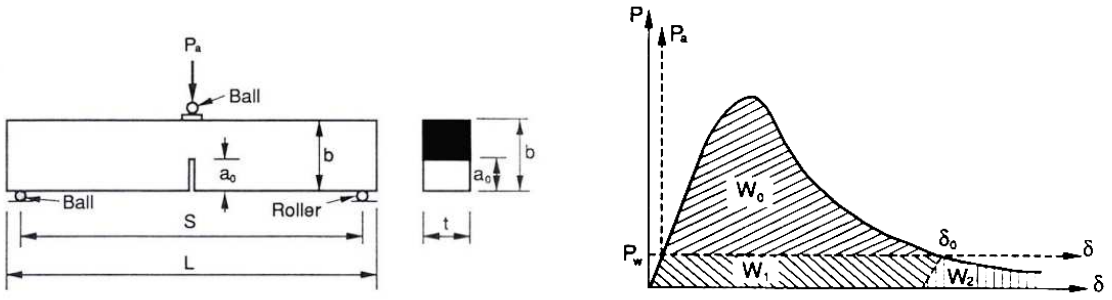

Fig. 1 Hillerborg`s method [7].

The Hillerborg`s method

The Hillerborg`s method of fictitious crack (marked as *M1*) was carried on three point bending test. The beam was loaded with constantly rising stress. The loading stress P and the displacement of loading point δ were measured. The notch depth a_0 was a half of the height of the specimen. The P–δ curve was the output of the test – shown in the Fig. 1 and Fig. 2. Integration of the area below the

curve was the fracture work *W*, it was divided by the area of the new crack and the result was the fracture energy G_F. [7]

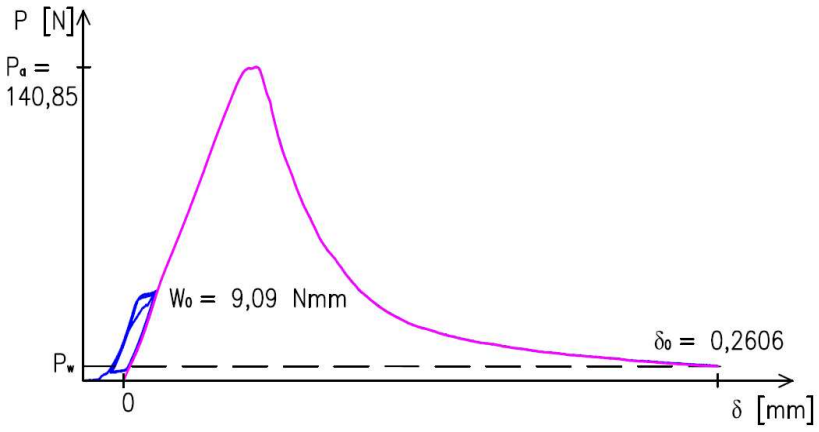

Fig. 2 The P–δ curve from Hillerborg`s method.

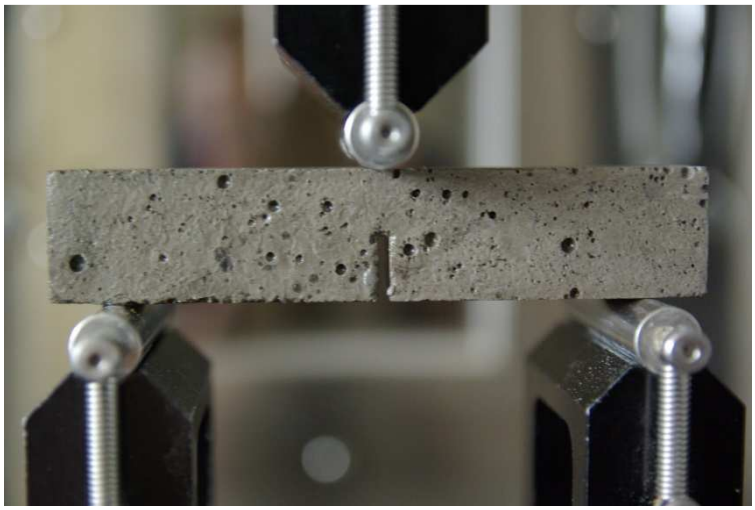

Fig. 3 Real test of Hillerborg`s method.

The Jenq–Shah`s method

The Jenq–Shah`s method of two parameters (marked as *M2*) is based on measuring crack mouth opening displacement *CMOD* and the loading stress σ. The notch depth a_0 was a third of height of the beam in this case. The *CMOD* was measured by a strain gauge.

The beam was loaded up to 95 % of its peak load and then it was unburdened and loaded again. Due to this cycle of loading and reloading it was possible to determine the coefficient of compliance in loading C_i and in unburdening C_u from the σ–*CMOD* curve. If the coefficients of compliance are known, the critical stress intensity factor K_{Ic} can be determined and then the fracture energy G_f. [7]

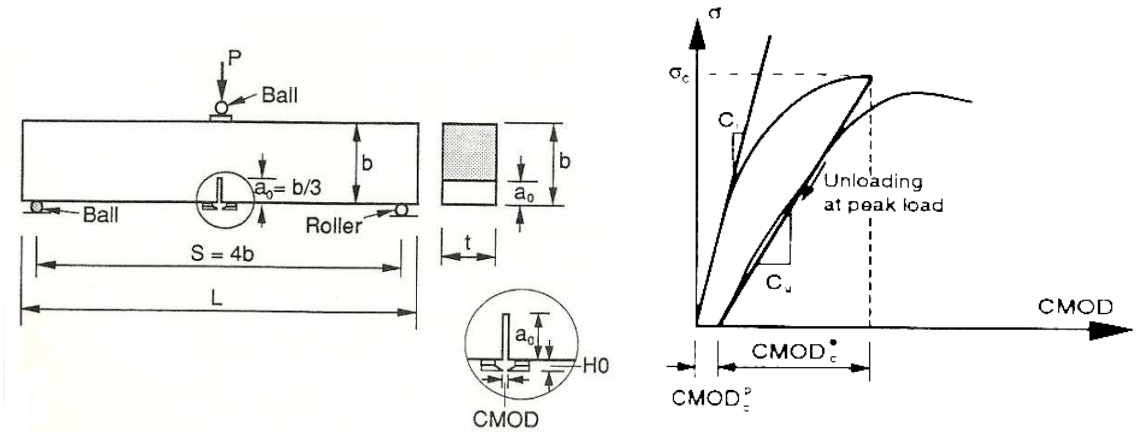

Fig. 4 Jenq–Shah`s method [7].

RESULTS OF TESTING

Estimated results

There were 94 pcs of beam specimens (size of each beam was 20x20x100 mm) of four prescriptions (one of 24 beams), each one has been divided in half in dependence of the way of treatment (one of 12 beams) and again divided in half in dependence of the way of testing.

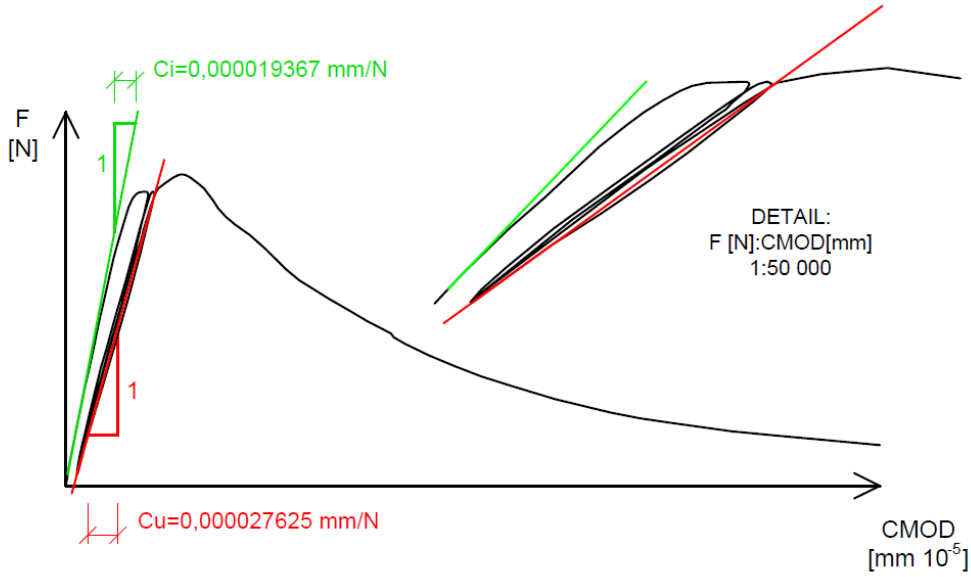

Fig. 5 The σ–CMOD curve from Jenq–Shah`s method.

That means there were 6 specimens of the same characteristics. It was supposed that the fly ash risen the fracture energy but just up to some percentage of content, specimens treated in water and tested by Jenq–Shah's method had higher level of fracture energy.

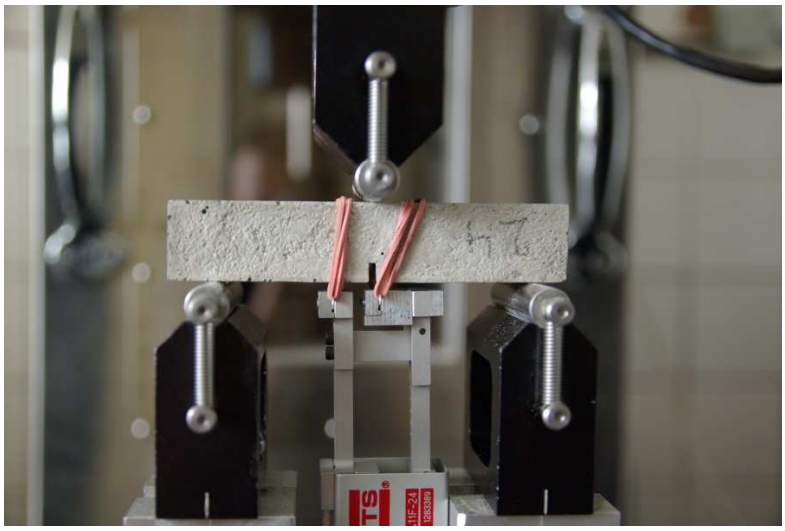

Fig. 6 The real test of Jenq–Shah`s method.

Results

In the Fig. 7 there are shown the results of the testing. Adding fly ash as binder has a good effect on the fracture energy, the ideal amount is around 25–40 %. More suitable treatment is in the water, although these specimens have lower level of fracture energy, but the fracture energy in this case is depended on the specific gravity and can arise cracks there. The method *M1* is easier to apply and calculate. It can be done automatically and the results are with high accuracy.

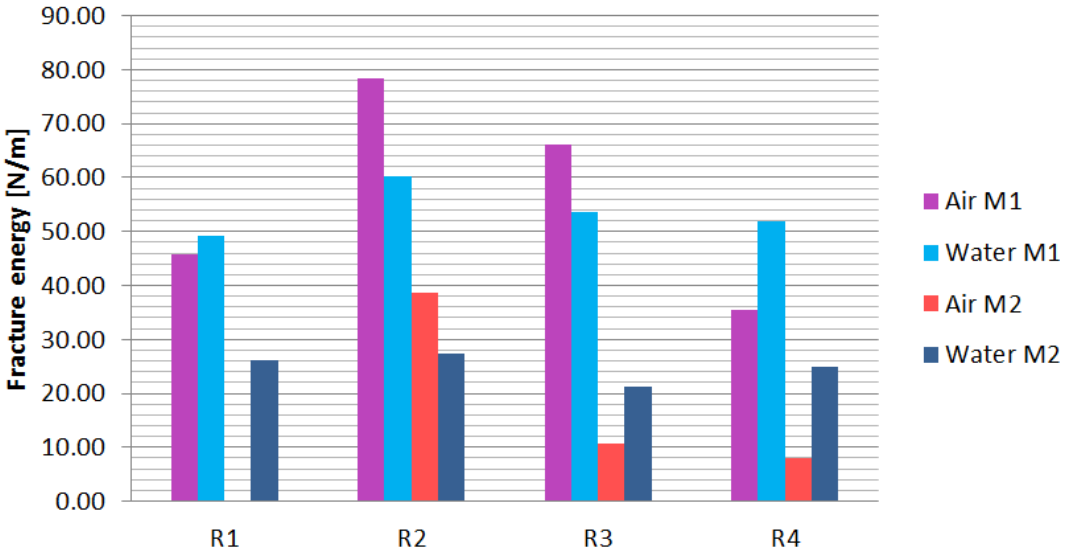

Fig. 7 Fracture energy.

The method *M2* is hard to apply to get results with good accuracy, at some specimens there were not measured the coefficients of compliance in unburdening because the peak load was reached – such as at *R1* Air *M2*, there were no useful data measured. The most important is the time when the unburdening is done it had the main force on the final fracture energy, which is shown in Fig. 8.

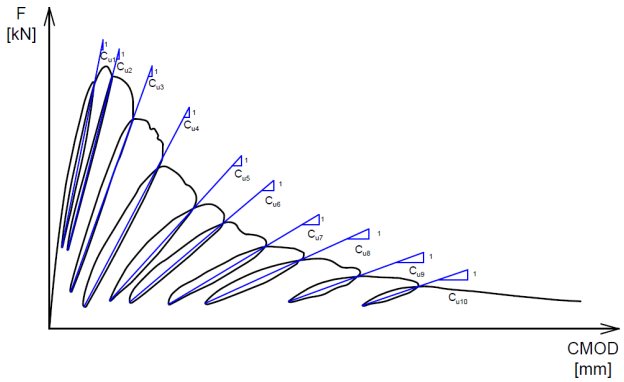

Fig. 8 Unburdening.

CONCLUSION

To sum up the better solution is to choose the Hillerborg`s method because the results are measured with better accuracy. It is also easier to carry on the testing. Better treatment is in the water bath. Ideal amount of fly ash is 25–40 %.

ACKNOWLEDGEMENT

The financial support of this experiment by the Faculty of Civil Engineering, Czech Technical University in Prague SGS project No. 14/122/OHK1/2T/11 is gratefully acknowledged.

REFERENCES

[1] FEČKO PETR A KOLEKTIV: *Popílky*. Ostrava: VŠB – Technická univerzita Ostrava, 2003. pp. 9-10, pp. 23-24. ISBN 80-248-0327-5.

[2] SVOBODA LUBOŠ A KOLEKTIV: *Stavební hmoty*. 2nd ed. Brno: Jaga group, 2007. pp. 157-162. ISBN: 978-80-8076-057-1.

[3] KŘÍSTEK RICHARD: *Matematické modely karbonatace betonu a vápenné malty* [online]. [cited 2014-03-01]. Available from: http://www.fce.vutbr.cz/veda/dk2003texty/pdf/4-1/rp/kristek.pdf.

[4] PAVLÍKOVÁ MILENA: *Chemie anorganických stavebních pojiv II* [online]. [cited 2014-03-01] Available from: http://tpm.fsv.cvut.cz/vyuka/ychs/cementbeton.pdf.

[5] KERŠNER ZBYNĚK: *Aspekty lomové mechaniky kvazikřehkých stavebních materiálů. Brno: Vysoké učení technické v Brně,* 2012. pp. 6-7. ISBN 978-80-214-4428-7.

[6] JIRÁSEK MILAN, ZEMAN JAN: *Přetváření a porušování materiálů. Dotvarování, plasticita, lom a poškození.* Praha: České vysoké učení technické v Praze, 2006. pp. 111-120. ISBN 80-01-03555-7.

[7] SHAH SURENDRA P., SWARTZ STUART E., OUYANG CHENGSHENG: *Fracture mechanics of concrete*. 1st ed. New York: John Wiley and Sons, 1995. pp. 110-188. ISBN 0-471-30311-9.

UNIFORM SPACE-FILLING DESIGN OF EXPERIMENTS IN HYPERSPHERE

Eva MYŠÁKOVÁ[1], **Matěj LEPŠ**[2]

Abstract: *Design of experiments (DoE) is an essential part in engineering analyses, especially in meta-modeling or probability computations. Although most commonly the design is created in a hypercubical design domain, there are cases when it is needed or even efficient to use the design domain in a shape of a hypersphere. Therefore several methods for generation of a random design of experiments in such domains are presented in this contribution. Presented methods employing clustering tools and an algorithm for removal of superfluous points from overcrowded design are compared in terms of quality of the resulting designs and time requirements.*

Keywords: *design of experiments, hypersphere, space-filling, uniformity, clustering*

INTRODUCTION

A design of experiments (DoE) is a set of (design) points covering the design domain. It creates an essential part in both physical [1] and computer experimentation, meta-modeling [2], sensitivity analyses [3] or probability computations [4]. The main goal is to gain maximal information about the system with a minimal number of evaluations (design points). Therefore it is necessary to focus on a quality of the design used. The basic requirements lie in space-filling and orthogonality. Many criteria for design evaluation from both points of view are available, see for example [5]. Most commonly the designs of experiments are created in a hypercube. But generation of the designs in domains of different shapes is also needed. Our contribution [6] proposes several methods for irregular domains and this contribution concentrates on the hyperspherical domains.

UNIFORM SAMPLING IN HYPERSPHERE

Probably the simplest and intuitive way to generate points in a circle (2D hypersphere) is to repeatedly generate points in a circumscribed square and exclude those points which lies outside the circle. This procedure is very simple, since it needs to compute the distances of the points to the centre of the circle

[1] Ing. Eva Myšáková, Faculty of Civil Engineering, Czech Technical University in Prague, eva.mysakova@fsv.cvut.cz

[2] doc. Ing. Matěj Lepš, Ph.D., Faculty of Civil Engineering, Czech Technical University in Prague, leps@cml.fsv.cvut.cz

and compare it with the circle radius. Although this method is quick in low dimensions, it becomes very ineffective when dimension grows as indicated by formulae in Equation 1 for the ratio between the volume of a hypersphere [7] and a hypercube:

$$V_{hypersphere} = R^n \frac{2\pi^{\frac{n}{2}}}{n\Gamma(\frac{n}{2})}; \quad V_{hypercube} = a^n = (2R)^n; \quad \frac{V_{hypersphere}}{V_{hypercube}} = \frac{\pi^{\frac{n}{2}}}{2^{n-1}n\Gamma(\frac{n}{2})}, \qquad (1)$$

where R is the radius of the hypersphere, n denotes the dimension, a is a length of a side of the hypercube and Γ is the gamma function. Figure 1 then shows how rapidly falls the ratio between the volumes with increasing dimension. This ratio corresponds to probability that the random point lies in the hypersphere. Simply, for example in 20D, it is necessary to create more than 40 million points in a hypercube to achieve the probability that at least one of them lies in a hypersphere.

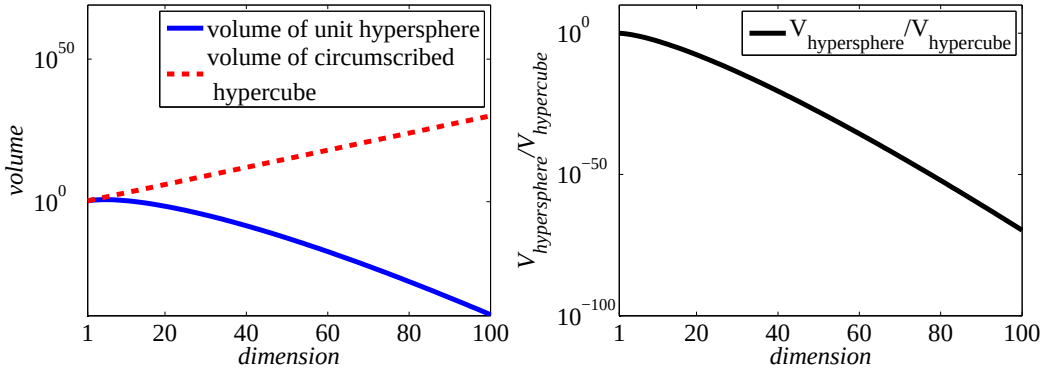

Fig. 1 Volume of unit hypersphere and circumscribed hypercube (left) and ratio of these volumes (right).

So it is clear that other methods for point generation in a hypersphere are required. Common and often used method [8] is described by Equation 2:

$$X = U^{\frac{1}{n}} \frac{Y}{\|Y\|_2} \qquad (2)$$

In n-dimensional space, when Y is a vector of n normal distributed random numbers, $\|Y\|_2$ is its Euclidean norm and U is a random number from uniform distribution, then X is uniformly distributed within the hypersphere. In other words, the normally distributed random points are projected on the surface of the hypersphere and then the random radius is simulated by multiplication by n^{th} root of the uniformly distributed number.

SPACE-FILLING DESIGN OF EXPERIMENTS

The described method provides randomly distributed points in a hypersphere, but it requires a large number of samples to guarantee that the set is uniform, see Figure 2. Therefore it seems appropriate to use this quick method for generation of a large set of points and then apply some advanced technique to

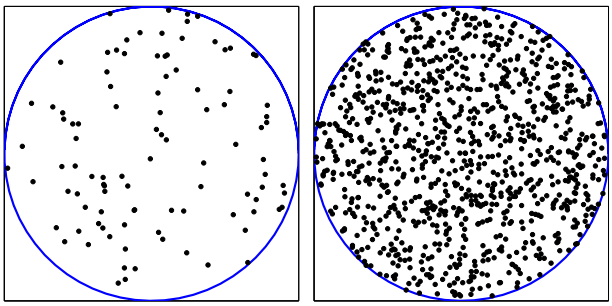

Fig. 2 Set with 100 (left) and 1000 (right) points in 2D.

create the final design of experiments with a reasonable number of points based on this initial set.

Clustering tools

The first method is proposed in [8] and it uses the K-means clustering [9] applied on the large initial point set. The idea is to find K clusters whose centres represent the final DoE with K design points. As shown in Figure 3 (left), such design should be uniformly distributed and space-filling.

Removal of superfluous points

The second method was proposed in [10] for regular design domains. It is based on repetitive removal of points from the intentionally overcrowded initial point set. The points are not removed randomly, but heuristically. In each iteration the actual closest pair of points is found and one of these points is removed. This procedure ensures increasing value of Euclidean Maximin distance criterion (EMM) of the point set in each step. There are two slightly different variants of this method. They differ in a selection of the point to be removed from the found closest pair. In a variant denoted as *removal* the choice is random, in *removal_NEW* the point whose second shortest distance to other points is smaller is removed. Resulting design of both variants are shown in 2D in Figure 3 (middle and right).

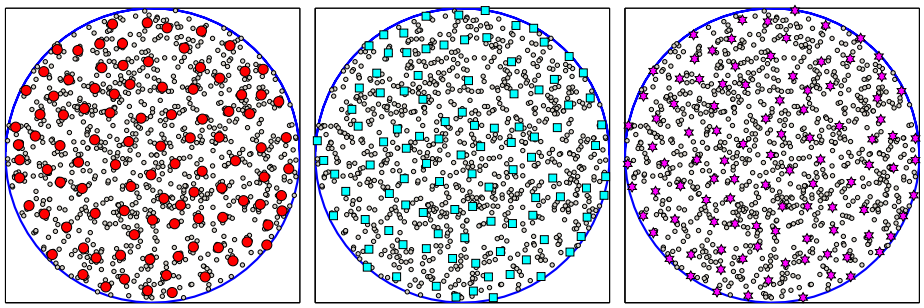

Fig. 3 Usage of K-means clustering (left), removal (middle) and removal_NEW (right) in 2D.

RESULTS

Because of the method nature, the DoEs created by clustering cannot achieve such results in some metrics as designs created by removal algorithms. It is because the cluster centres are not placed on the domain boundary. Therefore all resulting designs were spread over the whole domain as illustrated in

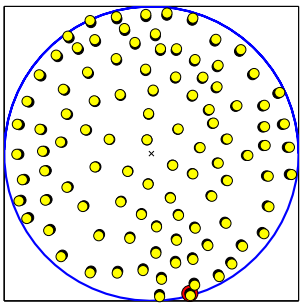

Fig. 4 Spreading of design over whole domain. Legend: black points = original DoE; red point = most distant point (from centre) shifted on boundary of circle; yellow points = spread DoE.

Figure 4 to provide comparable results. The operation is described in Equation 3:

$$X_{spread} = \frac{X}{\max \|X_i\|_2}; \qquad i = 1, ..., n, \tag{3}$$

where n is a number of dimensions, X is the original design, $\max \|X_i\|_2$ is an Euclidean norm of the most distant design point and X_{spread} is the design spread over the domain.

Following criteria were used for comparison of the quality of resulting designs, see e.g. [5]:

- criterion Audze-Eglais (AE)
- Euclidean Maximin distance (EMM)
- the largest element of correlation matrix (cc)
- Pearson correlation coefficient (PMCC)
- Spearman correlation coefficient (SRCC)
- Kendall correlation coefficient (KRCC)
- condition number (CN)
- ML_2 dicrepancy (ML)

All the criteria are minimized with exception of the Euclidean Maximin distance. For clarity of the results this criterion is considered with an opposite sign, so it should be minimized as well.

Presented methods for creation of DoE were compared on examples of 2, 3, 10 and 20-dimensional hyperspheres. The initial sets have 1000, respectively 5000 points and they were reduced to one tenth. The results represent statistics from 10 runs. Figure 5 shows standardized values of criteria for presented methods. We can see that in low dimensions the algorithms employing removal outrun the clustering. Though in higher dimensions the designs created by clustering win in criteria that evaluate correlation.

Another side in which the clustering overplays the removal is time. The time demands of this method are significantly lower as indicated in Figure 6. But there is no need to use the same number of initial points for all methods. As we can see in Figure 7, in some cases it is sufficient to use several times lower number of initial points for removal algorithm. The impact is almost negligible in comparison with savings on time demands. Thus, proper choice of the initial set size enables comparable time demands with no cardinal changes in quality distribution of the resulting designs.

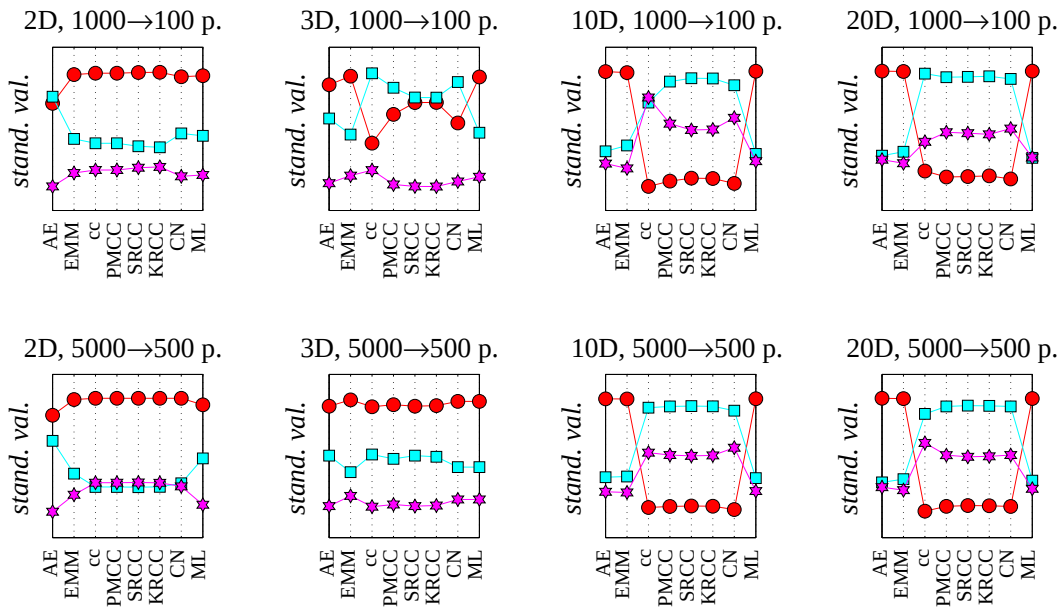

Fig. 5 Evaluation of designs created by presented methods. Legend: red circles = clustering; cyan squares = removal; magenta hexagrams = removal_NEW.

CONCLUSIONS

The contribution presents several methods for generation of the design of experiments inside a hypersphere which plays an important role in many engineering fields. Although the most common design domain has the shape of hypercube, sometimes it is necessary to create the design in hyperspherical domains. Methods operating in such domains were compared in terms of quality of the resulting DoEs and in terms of their time demands.

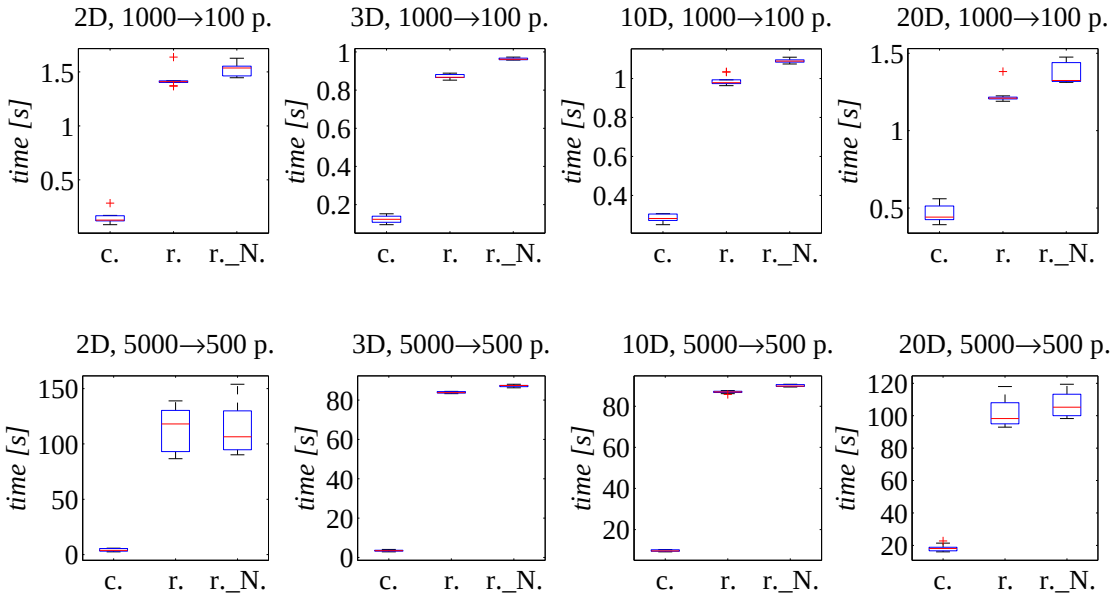

Fig. 6 Time demands of presented methods.

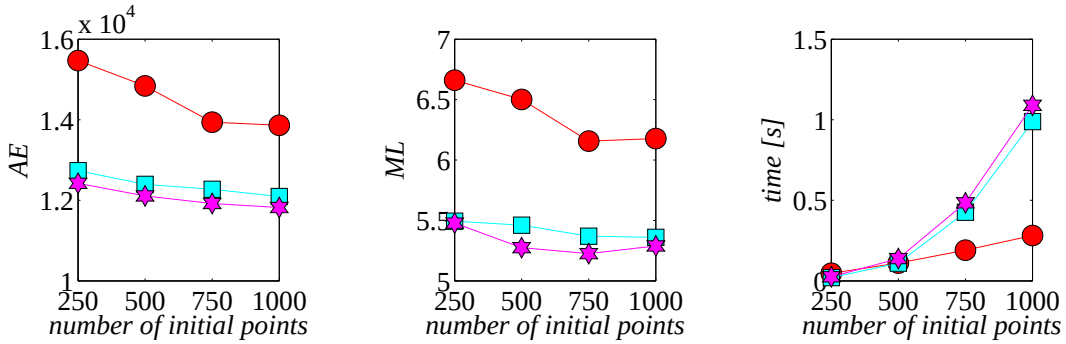

Fig. 7 Influence of overcrowding level. 10D example, final design with 100 points. Legend: red circles = clustering; cyan squares = removal; magenta hexagrams = removal_NEW.

ACKNOWLEDGEMENT

The financial support of this contribution by the Faculty of Civil Engineering, Czech Technical University in Prague (SGS project No. 14/028/OHK1/1T/11) is gratefully acknowledged.

REFERENCES

[1] MONTGOMERY, D. C. *Design and Analysis of Experiments.* Wiley, 8 edition, June 2012. ISBN: 978-1118146927

[2] FORRESTER, A. and SÓBESTER, A. and KEANE, A. *Engineering Design via Surrogate Modelling: A Practical Guide.* John Wiley & Sons Ltd, 2008. ISBN 978-0-470-06068-1.

[3] SALTELLI, A. and CHAN, K. and SCOTT, E. M. *Sensitivity analysis.* NY: Wiley, New York, 2009. ISBN: 978-0470743829.

[4] BUCHER, C. *Computational Analysis of Randomness in Structural Mechanics.* Taylor & Francis, 2009. ISBN: 978-0415403542.

[5] JANOUCHOVÁ, E. and KUČEROVÁ., A. Competitive comparison of optimal designs of experiments for sampling-based sensitivity analysis. *Computers & Structures.* 2013, **124**, 47-60.

[6] MYŠÁKOVÁ, E. *Optimalizace uniformity počítačových návrhů pro omezené návrhové prostory.* Praha, 2013. Diploma Thesis. České vysoké učení technické v Praze. Fakulta stavební.

[7] WEISSTEIN, E. W. Hypersphere. In: *MathWorld* [online]. 2011-04-21 [cited 2014-06-18]. Available from: http://mathworld.wolfram.com/Hypersphere.html.

[8] DUBOURG, V. *Adaptive surrogate models for reliability analysis and reliability-based design optimization.* 2011. Ph.D. thesis. Université Blaise Pascal, Clermont-Ferrand, France.

[9] MACQUEEN, J. B. Some methods for classification and analysis of multivariate observations. In: *Proceedings of 5th Berkeley Symposium on Mathematical Statistics and Probability.* University of California Press, 1967, pp. 281-297. ISSN: 0097-0433.

[10] MYŠÁKOVÁ, E. and LEPŠ, M. Comparison of space-filling design strategies. In: *Proceedings of the 17th International Conference Engineering Mechanics.* Ústav termomechaniky AV ČR, 2011, pp. 399-402. ISBN 978-80-87012-33-8.

52-BAR TRUSS OPTIMIZATION BENCHMARK: COMPUTATIONAL ENHANCEMENTS

Matěj LEPŠ[1], **Josef NOSEK**[2], **Eva POHLÍDALOVÁ**[3]

***Abstract**: Structural-sizing optimization needs an enormous computational power. Our contribution shows a progress on a specific benchmark problem. We propose a combination of a reduction trick from an engineering point of view accompanied with a large scale distributed computing system.*

***Keywords**: Size optimization, benchmark, 52-bar truss, parallel processing, BOINC,*

INTRODUCTION

Different types of optimization problems occur in engineering tasks. This contribution is focused on size optimization of truss bar structures. It this discipline the geometry of a structure is fixed whereas cross-selections of bars can be changed. In detail, cross-selection areas are selected from a prescribed discrete list. Simple at the first look, it is a complicated combinatorial problem. For instance, in case of a 10-bar truss with a list of 10 cross-sectional areas there are $10^{\wedge 10}$ possible combinations. Assuming that each evaluation takes only 100 ms, the evaluations of all possible combinations will take more than 30 years.

Node	F_{hor}	F_{vert}
17	100 kN	200 kN
18	100 kN	200 kN
19	100 kN	200 kN
20	100 kN	200 kN

Tab. 1

[1] Doc. Ing. Matěj Lepš, Ph.D., Faculty of Civil Engineering, CTU in Prague, Thákurova 7, 166 29 Prague, Czech Republic, leps@klobouk.fsv.cvut.cz

[2] Ing. Josef Nosek, Faculty of Civil Engineering, CTU in Prague, Thákurova 7, 166 29 Prague, Czech Republic, pepa.nosek@seznam.cz

[3] Bc. Eva Pohlídalová, Faculty of Civil Engineering, CTU in Prague, Thákurova 7, 166 29 Prague, Czech Republic, eva.pohlidalova@fsv.cvut.cz

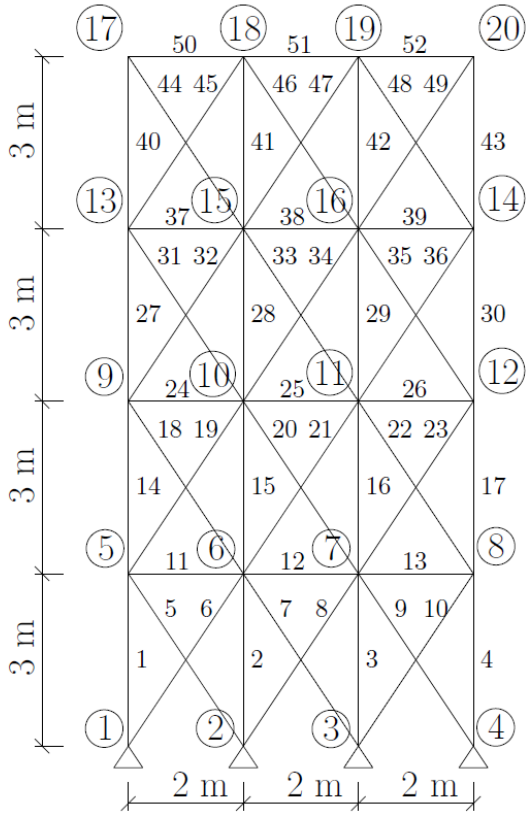

Fig. 1

Group	Bars
A_1	1, 2, 3, 4
A_2	5, 6, 7, 8, 9, 10
A_3	11, 12, 13
A_4	14, 15, 16, 17
A_5	18, 19, 20, 21, 22, 23
A_6	24, 25, 26
A_7	27, 28, 29, 30
A_8	31, 32, 33, 34, 35, 36
A_9	37, 38, 39
A_{10}	40, 41, 42, 43
A_{11}	44, 45, 46, 47, 48, 49
A_{12}	50, 51, 52

Tab. 2

This paper focuses on 52-bar truss benchmark problem (Fig. 1) that has been considered previously by many researchers, see e.g. [1]. Bars are grouped to 12 groups, see Table 2. The cross-sectional areas, as design variables are selected from the following available set of catalog values: 71,613; 90,968; 126,451; 161,29; 198,064; 252,258; 285,161; 363,225; 388,386; 494,193; 506,451; 641,289; 645,16; 792,256; 816,773; 940; 1008,385; 1045,159; 1161,288; 1283,868; 1374,191; 1535,481; 1690,319; 1696,771; 1858,061; 1890,319; 1993,544; 2019,351; 2180,641; 2238,705; 2290,318; 2341,191; 2477,414; 2496,769; 2503,221; 2696,769; 2722,575; 2896,768; 2961,284; 3096,768; 3206,445; 3303,219; 3703,218; 4658,055; 5141,925; 5503,215; 5999,998; 6999,986; 7419,34; 8709,66; 8967,724; 9161,272; 9999,98; 10322,56; 10903,204; 12129,008; 12838,684; 14193,52; 14774,164; 15806,42; 17096,74; 18064,48; 19354,8; 21612,86 mm^2. The structure has only one loading case as is defined in Table 1. Constraints are defined as maximum and minimum allowed stresses in each bar limited to 180 MPa. Note that there are no displacement constrains.

The final goal our research is to get the guaranteed global optimum of the presented 52 bar truss optimization benchmark by an enhanced enumeration method [2]. Knowledge of guaranteed global optimum is very useful for comparison and evaluation of optimization methods. Actually, such optimum of the 52-bar truss is still unknown. The following part of this paper present few enhancements on a path to the goal.

COMPUTATIONAL ENHANCEMENT

Because the proposed task has extremely large computational requirements, we need to find as much simplifications as possible. First simplification was to write a faster algorithm to solve the structural problem. We have rewritten the algorithm as a force-based method. The resulting program is at least two times faster than the previous version.

Secondly, we added new constraints based on maximum allowed stresses in several cut of the structure. The whole procedure will be presented only on one of these conditions. Suppose that the overall horizontal force must be transmitted by non-vertical bars. Then, we can calculate a minimum cross-selection area of non-vertical bars that must bear the the given force.

Particularly, the total horizontal force is F_{tot}=100x4 = 400 kN. A part of a horizontal force from aligned bars can be calculated in a following way:

$$F_{tot} \dots total\ horizontal\ force$$
$$l_{bar} \dots lenght\ of\ cross\ bar$$
$$n \quad \dots number\ of\ cross\ bar$$
$$l_{bar} \dots lenght\ of\ cross\ bar$$
$$A \quad \dots cross\ section\ of\ each\ bar$$
$$\sigma_{max} \dots maximal\ stress, tension$$
$$F_{tot} = \frac{2}{l_{bar}} * n * A * \sigma_{max}$$
$$\frac{F_{tot} * l_{bar}}{2 * n * \sigma_{max}} = A$$
$$\frac{F_{tot} * l_{bar}}{2 * n * \sigma_{max}} \leq A_{min}$$
$$\frac{400 * 3.60555}{2 * 6 * 180000} \leq A_{min}$$
$$A_{min} \geq 667.6944\ mm^2$$

This means a leaning bar cannot have a cross-selection area lover than 667 mm^2. These additional constraints bring 2.5 times speed up to the presented optimization problem. Such a speed-up is significant, however the remaining computational demand is still huge:

$m = 64^{12} \cong 47 * 10^{12}$ .. number of combination without added constrain

$n = 64^8 * 51^4 \cong 19 * 10^{12}$ .. number of combination with added constrain

Actually biggest available computation source for our task is a volunteer computing project called CONVECTOR which started at our faculty a year ago.

CONVECTOR

Convector is based on a middleware BOINC [4] which is an open source middleware based on a client–server technology. The BOINC project is based at the U.C. Berkley Space Sciences

Laboratory and has been funded by the National Science Foundation since its start in 2002. There are other projects like "Bayanihan" [5] witch use ubiquitous and easy to use technology such as web browsers and Java. Although the BOINC has more difficulties from usage point of view, it offers more possibilities[6]. Actually project CONVECOTOR has more than 5000 connected hosts, and is still growing up, see Fig. 2.

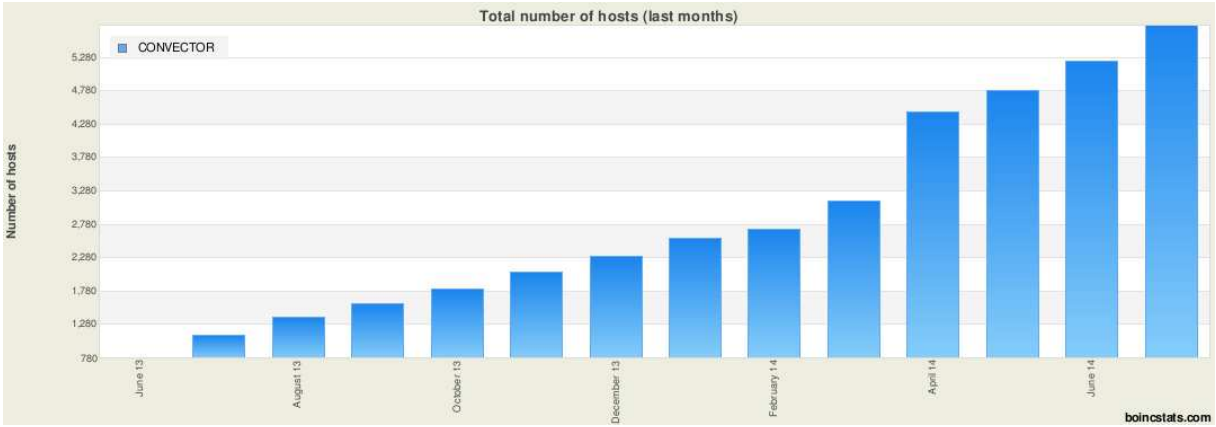

Fig. 2

CONCLUSION

This project calculated global optimum of 10 bar truss. Lot of work has been done on this task, but computational effort is still huge. Estimated computational time is in a matter of years. Actual supposed time to calculate complete task is approximately 240 years. So we still looking for new computational enhancements .

ACKNOWLEDGEMENT

This work was supported by the Grant Agency of the Czech Technical University in Prague, a grant No. SGS14/028/OHK1/1T/11.

REFERENCES

[1] J. S. WU A P. T. CHOW, „*Steady-state genetic algorithms for discrete optimization*" Computers & Structures, sv. 56(6):, pp. 979-991, 1995

[2] POSPÍŠILOVÁ, A. – LEPŠ, M.: Global Optima for Size Optimization Benchmarks by Branch and Bound Principles. In: Acta Polytechnica. 2012, vol. 52, no. 6, p. 74-81. ISSN 1210-2709. 2012.

[3] POHLÍDALOVÁ, E: *Silová metoda pro tradiční příklady rozměrové optimalizace*, Soutěž o Cenu akademika Bažanta, Soutěžní práce, 2014

[4] DAVID P. ANDERSON, *BOINC: A System for Public-Resource Computing and Storage*, 5th IEEE/ACM International Workshop on Grid Computing. November 8, 2004, Pittsburgh, USA

[5] L. F. SARMENTA A H. SATOSHI, „*Bayanihan: building and studying web-based volunteer computing systems using Java,*" Future Generation Computer Systems, pp. 675-686, 1999.

[6] J. NOSEK, "*Use BOINC for Volunteer computing*" Engineering Mechanic, 2013

THE MOISTURE PROPERTIES OF THE BINDER GEL WITH FLY ASH

Tereza OTCOVSKÁ[1], **Pavel PADEVĚT**[2]

***Abstract**: Use of fly ash additives has an impact of moisture properties of binder gels (cement paste).The particular object of interest is capillary action of water in the binder gels with different concentration of fly ash in the mixture. Fly ash is a waste product produced during combustion of coal. According to the type of combustion, it produces pulverised coal combustion (PCC) fly ash or fluidized bedcombustion (FBC) fly ash. There are substantial differences among moisture properties of binder gels with FBC fly ash additives compared with the binder gels with PCC fly ash additives.*

***Keywords**: binder gel, fluidized bed combustion fly ash, pulverized coal combustion fly ash, capillary action, moisture*

INTRODUCTION

There are two main arguments why it is reasonable to use fly ash as a binder gel. First, fly ash is a waste material produced by the combustion of solid fuels, mainly coal. Combustion of coal is one of the most environmentally unfriendly methods of energy production. Therefore, it makes sense to use waste materials from the process to the greatest extent possible to at least reduce negative impacts on environment. Second, the high financial and energy intensity of cement production creates a demand for the substitution of cement in the binder gel with alternative binders. To some extent, fly ash could play this role [1, 2].

The examination of material qualities of binder gel with the addition of fly ash and long-term testing of those qualities could bring a new perspective on this waste material and allow its more intense use in civil engineering. We focused on the moisture properties of binder gels with addition of fly ash from fluidized bed combustion (FBC) in this article. We also compared moisture properties of binder gels with FBC fly ash with the pulverised coal combustion (PCC) fly ash.

[1]Ing.Tereza Otcovská, Department of Mechanics, Faculty of Civil Engineering, Czech Technical University in Prague, tereza.otcovska@fsv.cvut.cz

[2]Ing. Pavel Padevět, Ph.D., Department of Mechanics, Faculty of Civil Engineering, Czech Technical University in Prague, pavel.padevet@fsv.cvut.cz

BASIC TYPES AND PROPERTIES OF FLY ASHES

There are two basic types of fly ash divided by the different methods of coal combustion in which they were produced: pulverised coal combustion (PCC) fly ash and fluidized bed combustion (FBC) fly ash.

Pulverised coal combustion (PCC) fly ash is created at temperatures above 1100 °C. The final properties of binder gel are affected primarily by the shape of a grain and by granulometry composition. The particles of the PCC fly ash are ball-shaped and they have a smooth surface in most cases. PCC fly ashes therefore do not decrease the quality of final product – on the contrary, they sometimes even improve it. [3]

Fluidized bed combustion (FBC) fly ash is created at temperatures between 795 °C to 1025°C in the fluid bed (in which there is coal surrounded by inert particles stabilizing the process of combustion). This method of combustion is less environmental damaging (because of lower emissions). On the other hand, the typical FBC fly ash has a multi-layer structure and has a large relative surface, which has negative effects on the quality of the final product. [3]

BINDER GELS WITH FLY ASH ADDITIVE AND THEIR PRODUCTION

There is a difference in the production of cement paste with FBC fly ash additive compared with the production of cement paste with the PCC fly ash additive or cement paste with the cement binder only. The highly porous nature of the FBC ash fly's grain requires higher consumption of the mixing water, i.e. using of higher water coefficient.

Tab. 1 Composition of the binder gels

Set	**Water coefficient [-]**	**Cement and fly ash ratio**
A	0.4	Cement only
B	0.6	65.7/34.3
C	0.7	50/50
D	0.9	30/70
E	0.95	10/90
F	0.4	50/50
G	0.4	60/40

During the experiment (conducted by our team) 5 sets of binder gel were created with different concentration of FBC fly ash in the mixture (sets A to E) and 2 sets of binder gel with different concentrations of PCC fly ash (sets F and G). The ratio between cement and fly ash in the mixture were 100/0, 65.7/34.3, 50/50, 30/70, 10/90 in case of FBC fly ash and 50/50 and 60/40 in case of PCC

fly ash. The figure in front of the back slash represents weight content of the cement and the figure behind back slash represents weight content of the fly ash. The water coefficient was referenced to the 100 % content of cement in the binder, i.e. it represents ratio of the weight of the water to the weight of the binder in the mixture. It was necessary to use a higher volume of the mixing water because of high porousness of the FBC fly ash. This means that with the increasing content of fly ash the water coefficient raised consequently. The final composition of the binder gels is recorded in the table (Tab. 1).

The test objects of cuboid shape with a cross-section profile 40 to 40 mm and height of 160 mm were created for every set. Test objects were removed from the forms approximately after 48 hours of solidification and they were assigned with a letter of respective set and with a number. One half of the test objects with fly ash additive were impregnated by chemical injection. Objects of sets E and D (i.e. bodies with highest content of the FBC fly ash) disintegrated during the process of impregnation. All objects with the PCC fly ash additive were impregnated, too.

Afterwards, the sides of all objects were painted with epoxide coating, but their bases were left uncovered (See Fig. 1). The epoxide coating had to secure one-directional spreading of the moisture in the object only and simultaneously to prevent contact of the objects with water other than on their bases.

The objects with epoxide coating were loaded into laboratory dryer Memmert and dried at temperature of 105 °C until their moisture contents were equal to zero. It was possible to start with experimental measuring immediately afterwards.

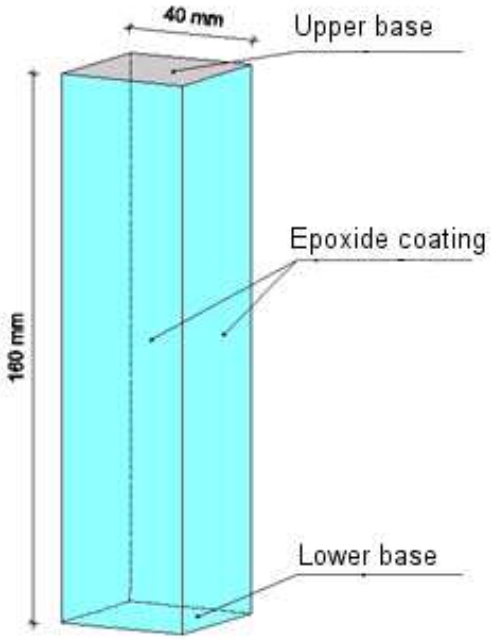

Fig. 1 Sketch of the test object

MEASURING OF THE CAPILLARY ACTION OF WATER IN THE BINDER GELS AND EVALUATION OF MEASURED DATA

The objects, after having been dried, were weighed and placed in a specially designed water container in which their bases were dipped for 1,5 cm of their height. It means that surface of the water in the container was maintained at a constant level. A water container with the test objects was placed in the air-conditioned testing chamber WKL for 59 days.

We chose a moisture content defined by Formula 1 as a physical quantity to compare capillary action of different sets of test objects. Measurement of the weighting of test objects were performed while they were in an air-conditioned chamber and in this way an increase in the weight of the objects was observed. Final figures of moisture content of non-impregnated test objects are displayed in the chart (Fig. 2) and summarized in the table (Table 2).

$$u = \frac{m_v - m_s}{m_s}.100\ \% = \frac{m_k}{m_s}.100\ \%\ [\%] \qquad (1)$$

The obvious outcome of this experiment is that ability of water to capillary action tested material increases in correlation with an increase in the content of FBC fly ash in the mixture. The water content in set B (with 34.3 % content of FBC fly ash in binder) was 1.7 times higher than in set A (with 0 % of FBC fly ash in binder). In set E (with 90 % of FBC fly ash in the binder) it was even 5.5 times more than in set A. It is evident that the impact of the presence of FBC fly ash to capillary action is substantial.

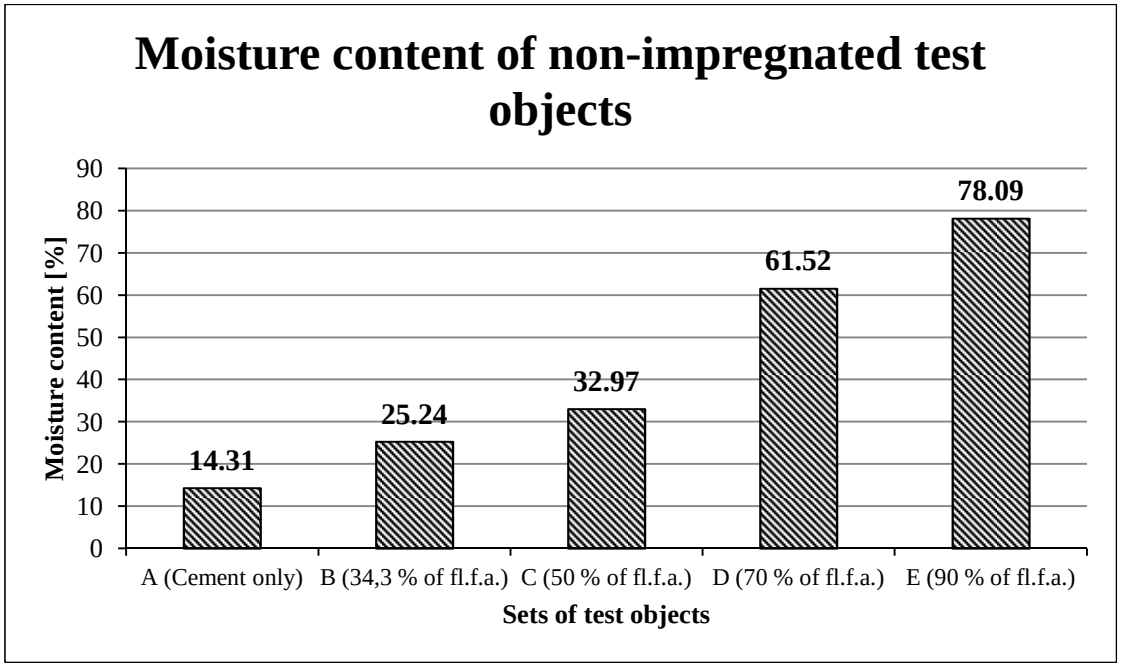

Fig. 2 Final values of moisture content of non-impregnated test objects

Tab. 2 Final values of moisture content of non-impregnated test objects

Set	Water coefficient [-]	Cement / fly ash ratio	Type of fly ash	Final figures of moisture content[%]
A	0.4	Cement only	-	14.31
B	0.6	65.7/34.3	FBC	25.24
C	0.7	50/50	FBC	32.97
D	0.9	30/70	FBC	61.52
E	0.95	10/90	FBC	78.09

The final values of moisture content of impregnated test objects are displayed in chart (Fig. 3) and summarized in table (Table 3). It is evident that the moisture properties of binder gels with PCC fly ash additive are far more beneficial than that of gels with FBC fly ash. According to literature, the PCC fly ash in the mixture could improve features of the binder gel; however, the use of FBC fly ash has quite the opposite effect [*3*, *4*]. It is probably the main reason why we discovered bigger differences of moisture content among test objects with higher content of fly ash in the mixture (sets B and G), than among those with lower content of fly ash in the mixture (sets C and F).

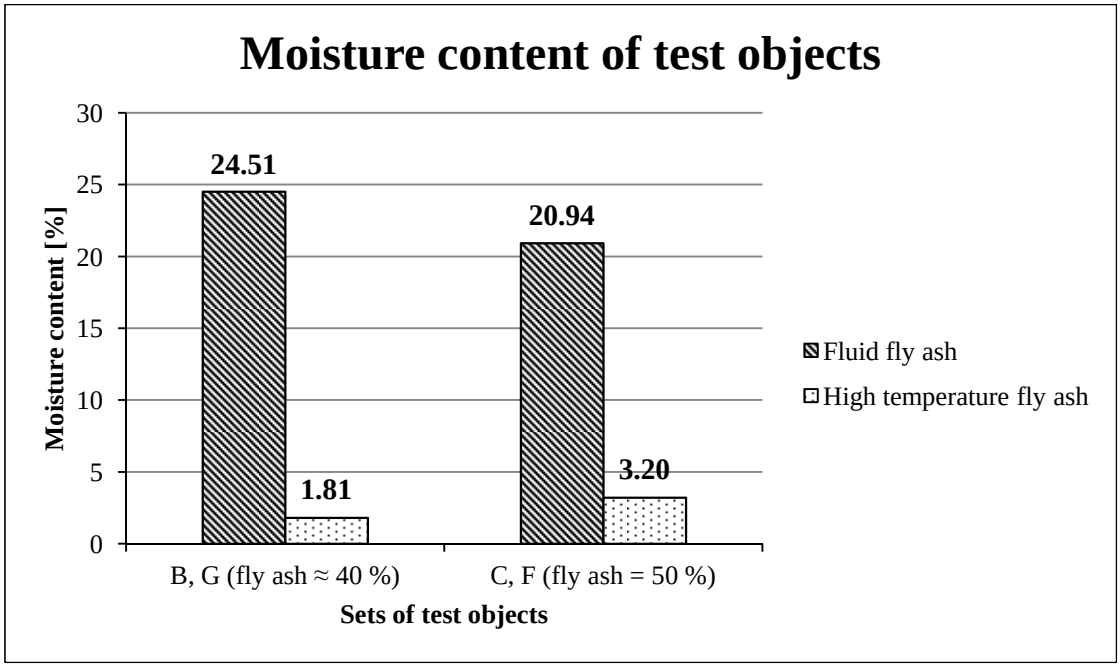

Fig. 3 Final values of moisture content of impregnated test objects

Tab. 3 Final values of moisture content of impregnated test objects

Set	Water coefficient [-]	Cement / fly ash ratio	Type of fly ash	Final figures of moisture content [%]
B	0.6	65.7/34.3	FBC	24.51
G	0.4	60/40	PCC	1.81
C	0.7	50/50	FBC	20.94
F	0.4	50/50	PCC	3.2

CONCLUSION

The presence and concentration of FBC fly ash increase capillary action of water in the binder gel. Therefore, we conclude that FBC fly ash deteriorates moisture properties of binder gels. This conclusion however could not exclude limited use of the FBC fly ash, not least because of economic and environmental advantages of such use.

Our experimental research of moisture properties of binder gels with fly ash additive concluded that while the presence of FBC fly ash has negative impacts on moisture properties, the presence of PCC fly ash has the opposite effect (i.e. it improves moisture properties of the gel).

ACKNOWLEDGEMENT

The financial support of this experiment by the Faculty of Civil Engineering, Czech Technical University in Prague (SGS project No. SGS14/122/OHK1/2T/11) is gratefully acknowledged.

REFERENCES

[1] PETRŮ, J. *Studium možnosti uplatnění stavebního a demoličního odpadu jako plniva v geopolymerních systémech*. Ostrava, 2010. Doctoral Thesis. VŠB-Technical University of Ostrava.

[2] MELICHAR, J., MÁCA, V., ŠČASNÝ, M. *Měrné externí náklady výroby elektrické energie v uhelných parních elektrárnách v České republice*. Prague, 2012.

[3] FEČKO, P. at al. *Popílky*. Ostrava, 2003. CUEC Working Paper 1/2012. ISBN 80-248-0327-5.

[4] BENSCHEID, N. et al. *Příručka - Popílek v betonu, Základy výroby a použití*. Düsseldorf, 2013. ČEZ Energetické produkty, s.r.o. ISBN 978-80-260-4226-6.

ON INVERSE FORMULATION OF RELIABILITY-BASED DESIGN OPTIMIZATION

Adéla POSPÍŠILOVÁ[1]

Abstract: *A multi-objective Reliability-based design optimization (RBDO) deals with a search for a set of trade-off solutions with a minimum costs and the maximum reliability of the structure. A performance measure, as a difference between the value of the limit state function and the zero level, is constant in the classical RBDO formulation. From a different point of view, some tasks require a fixed reliability but searching for the compromising solutions for the minimization of costs and maximization of the performance measure to find the most advantageous solutions. This task is called an inverse Reliability-based design optimization (iRBDO) and is formulated in a multi-objective sense in this contribution. To evaluate the performance measure, an inverse Monte Carlo is employed.*

Keywords: *Reliability-based design optimization, inverse reliability-based design optimization, Monte Carlo simulations, multi-objective optimization, structural safety*

INTRODUCTION

Optimization and search methodologies have become very popular for making products more desirable. The shape of a structure, the amount of reinforcement, the cross-sections, sheet thicknesses, design of the concrete mixture, and many other properties can be optimized [1, 2, 3, 4]. Nowadays, it has become apparent that the optimization with deterministic variables is not sufficient enough due to the uncertainties in a material, a construction, loading etc. The deterministic optimization techniques can often lead to the unacceptable results [5]. Yao et al. [6] define the uncertainty as the incompleteness in knowledge and the inherent variability of the system and its environment. The parameter uncertainties are then associated with input data; the structural uncertainties express that the model need not clearly describe the physics of the problem [7]. Uncertainties can be represented by means of interval bounds that is the vaguest definition; by membership functions which are used in fuzzy logic approaches; or by probability density functions that provide the best description of uncertainty [7].

The optimal design provides a small probability of failure assuming that structural economy and the system variability to unexpected variations is reduced. These requirements divide the optimization under uncertainty into two big branches [5]. The economical design with large safety is provided by

[1] Ing. Adéla Pospíšilová, Faculty of Civil Engineering, Czech Technical University in Prague, adela.pospisilova@fsv.cvut.cz

the *Reliability-based design optimization* (sometimes referred just as the *Reliability-based optimization*) concentrating on worse-case scenarios that occur only in extreme events. The everyday fluctuations are covered in the *Robust design optimization* that minimizes the price as well as sensitivity to small changes in loading, structural parameters, geometry, etc. Schuëller and Jensen [8] include the third branch of optimization under uncertainty - *model updating and system identification*. The goal is to reduce the discrepancies which arise when the model prediction is compared with the test data [8].

A classical formulation of the single-objective *Reliability-based design optimization* (RBDO) minimizes the objective cost function (e.g. a structure weight, benefits, construction costs or expected lifetime costs etc.) with respect to deterministic constraints as well as probabilistic constraints evaluating a probability of failure. This formulation requires a definition of the maximum allowable probability of failure. Within the single-objective optimization, the bound for the minimum reliability has to be set up to the required value because the single-objective optimization usually terminates at the boundary of the constraint function dividing the space into the feasible and unfeasible domain. Sometimes, it is not clear, how restrictive the bound value should be. Therefore, it is beneficial to reformulate the single-objective formulation into the multi-objective optimization with the cost function as the first objective and the reliability (or a probability of failure) as the second objective [9] to obtain the final set of the compromising solutions called *Pareto-front*. Subsequently, the expert chooses the most beneficial solution from the final set.

The multi-objective Reliability-based design optimization task is defined as

$$\begin{aligned}
&\min_{\mathbf{d}\in\mathbb{D}} && C(\mathbf{d}) && (1)\\
&\min_{\mathbf{d}\in\mathbb{D}} && p_F(\mathbf{X},\mathbf{d}) && (2)\\
&\text{subject to} && H_i(\mathbf{d}) \le 0,\ i=1,\dots,n_e && (3)\\
& && p_F^{min} \le p_F(\mathbf{X},\mathbf{d}) \le p_F^{max} && (4)\\
& && \bar{z} = const. && (5)
\end{aligned}$$

The first line represents minimization of costs $C(\mathbf{d})$, where $\mathbf{d}$ is a vector containing design variables (usually means of some random variables) and $\mathbb{D}$ is a domain for the choice of the vector $\mathbf{d}$. The second line corresponds to the minimization of the probability of failure $p_F(\mathbf{X},\mathbf{d})$, where matrix $\mathbf{X}$ contains a set of random variables. The objective space can be constrained by the deterministic functions $H_i(\mathbf{d})$, where the number of constraint i is from 1 to n_e. The probability of failure $p_F(\mathbf{X},\mathbf{d})$ can be constrained as well to obtain more realistic solutions, in which the lower bounding by p_F^{min} eliminates solutions with unattainable probabilities of failure and the upper bounding by p_F^{max} provides solutions safe enough. The probability of failure for a given threshold value $\bar{z}$ (called a *performance measure*) in n-dimensional

space of random variables $X_1 \dots X_n$ is

$$p_f(\mathbf{X}, \mathbf{d}) = \mathbf{Prob}[g(\mathbf{X}) \leq \bar{z}] = \int_{g(\mathbf{X}) \leq \bar{z}} \cdots \int f_{\mathbf{X}}(\mathbf{x}) \mathrm{d}\mathbf{x} = F_{\mathbf{x}}(\bar{z}), \tag{6}$$

where $f_{\mathbf{X}}(\mathbf{x})$ is a joint probability distribution function and $g(\mathbf{X}) \leq \bar{z}$ denotes the failure domain. $F_{\mathbf{X}}(\bar{z})$ signifies the cumulative distribution function evaluated at the prescribed threshold value $\bar{z}$.

The inverse task to RBDO can be formulated to obtain solutions with a prescribed probability of failure but maximizing the performance measure and still minimizing costs. This contribution formulates this *inverse Reliability-based design optimization* (iRBDO) task and shows the methodology on a classical benchmark for evaluating the reliability assessment as well as for the RBDO problems. The overall structure of this paper takes the form of four sections, including this introductory section. Section Two begins by laying out the inverse Reliability-based design optimization concepts. The third chapter is concerned with the application of the methodology on the 23-bar truss structure. The final section draws upon the entire paper and concludes this contribution.

INVERSE RELIABILITY-BASED DESIGN OPTIMIZATION

As being said, the goal of a Reliability-based design optimization is to find Pareto-front of trade-off solutions taking into account the reliability of the structure (or probability of failure) and costs (or volume, weight of the structure etc.). Pareto-front of the RBDO problem can be understood as a plane two-dimensional cut of the three-dimensional general reliability optimization task with reliability, costs and performance measures as three criteria depicted in Figure 1. The performance measure is set to a given constant value during the whole optimization task. The ideal solution would be the one with the

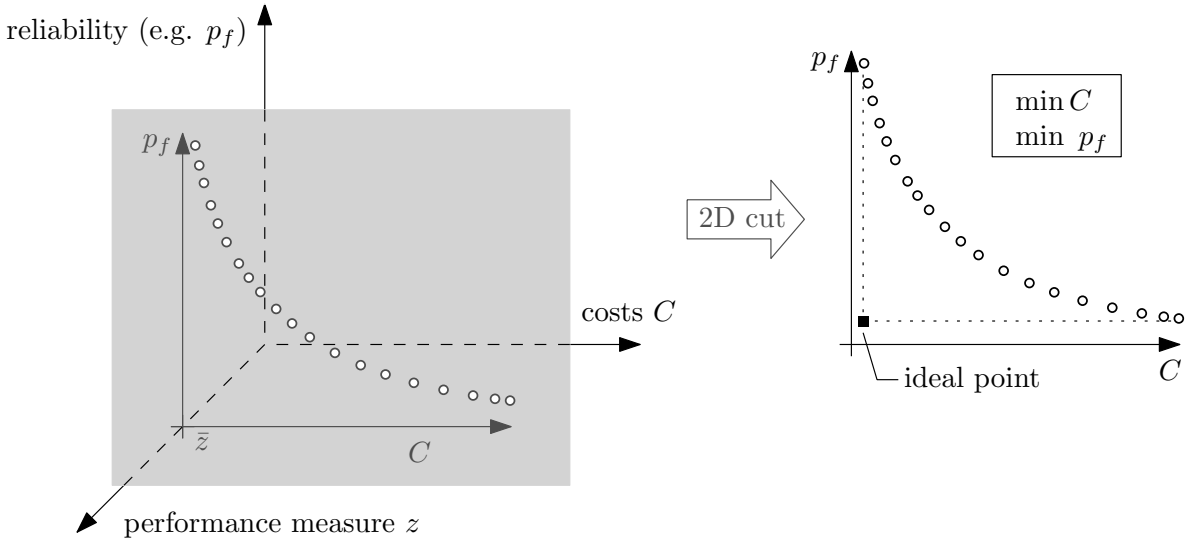

Fig. 1 Reliability-based design optimization: Pareto-front as a two-dimensional cut in general reliability optimization problem. The performance measure is set to a given value $\bar{z}$.

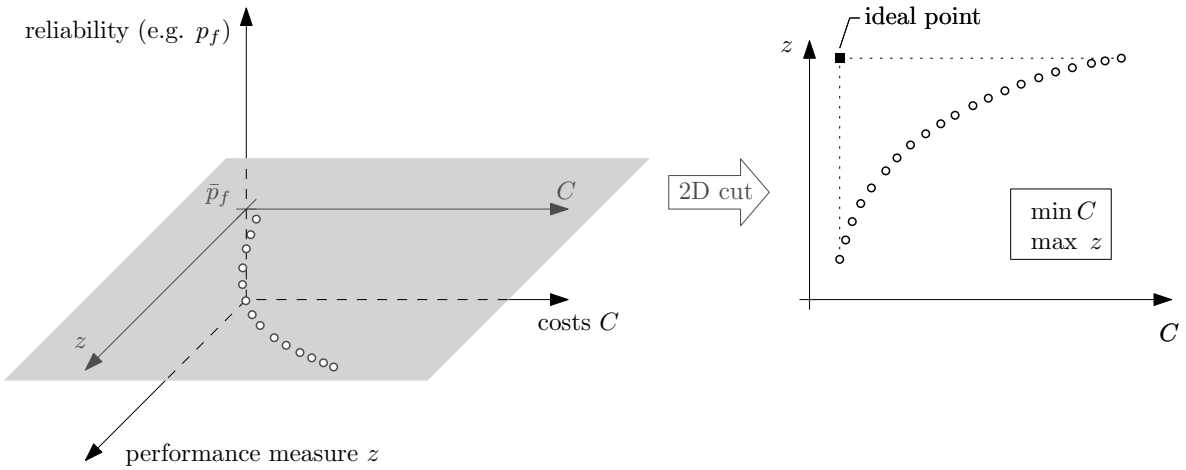

Fig. 2 Inverse Reliability-based design optimization: Pareto-front as a two-dimensional cut in general reliability optimization problem. The probability of failure is set to a given value $\bar{p}_f$.

minimum costs and the minimum probability of failure as depicted in Figure 1, however, this solution does not exist because two optimized criteria are antagonistic. Instead of it, the set with compromising solutions (Pareto-front) is located with a condition to be as closest as possible to the ideal point.

The inverse task is to fix a probability of failure to a given fixed value $\bar{p}_f$ and to find Pareto-front of costs and performance measures, see Figure 2. We call this problem an inverse Reliability-based design optimization. The costs should be as cheapest as possible, the minimization is used for this criterion. A performance measure is understood as a reserve between the value of the limit state function and the limit state when the failure occurs. If two solutions with a constant probability of failure, a constant cost and different values of performance measures are compared, the performance measure (a reserve) is preferred to be the greatest. Thus, the performance measure criterion is maximized. Figure 2 shows a non-existent ideal point and Pareto-front that is the better the closer is to the virtual ideal point. Inverse Reliability-based design optimization is mathematically formulated as

$$\min_{\mathbf{d}\in\mathbb{D}} \quad C(\mathbf{d}) \tag{7}$$

$$\max_{\mathbf{d}\in\mathbb{D}} \quad z(\mathbf{X},\mathbf{d}) \tag{8}$$

$$\text{subject to} \quad H_i(\mathbf{d}) \leq 0,\ i = 1,\ldots,n_e \tag{9}$$

$$z^{min} \leq z(\mathbf{X},\mathbf{d}) \leq z^{max} \tag{10}$$

$$\bar{p}_f = const. \tag{11}$$

The first line is again minimization of costs $C(\mathbf{d})$, the second line corresponds to the maximization of the performance function $z(\mathbf{X},\mathbf{d})$. The objective space can be constrained by deterministic constraints $H_i(\mathbf{d})$ and by limitation the performance measure $z(\mathbf{X},\mathbf{d})$ from below z^{min} and from above z^{max}.

Evaluation of the performance measure is an inverse task to evaluation of the probability of failure.

A crude Monte Carlo simulation is the most robust simulation method for a probability of failure assessment, which generates samples as pseudorandom numbers from a given distribution and assesses how many samples felt into the failure domain. It computes the integral over the failure domain defined in Equation 6 as

$$p_f = \frac{1}{m}\sum_{k=1}^{m} I_G(\mathbf{x}^{(k)}) = \frac{n_f}{m}. \tag{12}$$

The indicator function $I_G(\cdot)$ is equal to 1 if the k^{th} realization $\mathbf{x}$ of m total samples is in the failure region and zero otherwise. An unbiased estimate of the probability of failure p_f is approximately equal to the ratio between a number of the samples in the failure domain n_f and a number of all samples m. The inverse problem to Equation 6 is gaining the performance measure z for the prescribed probability of failure $\bar{p}_f$. The number of samples in the failure domain is therefore from Equation 12

$$n_f = \bar{p}_f \cdot m. \tag{13}$$

The m number of samples are evaluated by the performance function $g(\mathbf{X})$ and are sorted in ascending order according to the $g(\mathbf{X})$. The performance measure z is then approximately equal to the value of the performance function of solution with the rank n_f in sorted Monte Carlo population. The whole routine is depicted in Figure 3.

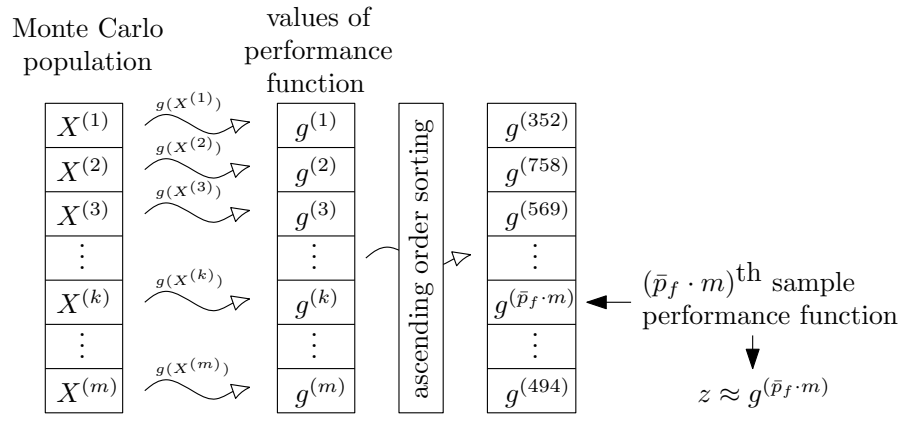

Fig. 3 The scheme of inverse Crude Monte Carlo simulation method for obtaining a performance measure z.

RESULTS ON 23-BAR TRUSS STRUCTURE

The 23-bar planar truss bridge benchmark with a probabilistic description of the problem was firstly published in [10]. Subsequently, a single-objective optimization problem was defined in [11]. A topology is depicted in Figure 4 on the left. Truss bars are divided into two groups; the upper chord and the lower chord are contained in the first group; the diagonals creates the second group. Young's moduli and cross-sections are normally distributed variables; loadings are random variables with Gumbel dis-

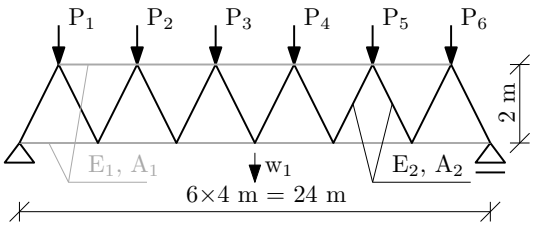

Variable		Distribution	Mean	St. dev.
E_1, E_2	Pa	Lognormal	$2.1 \cdot 10^{11}$	$2.1 \cdot 10^{10}$
A_1	m^2	Lognormal	μ_{A1}	$2 \cdot 10^{-4}$
A_2	m^2	Lognormal	μ_{A2}	$1 \cdot 10^{-4}$
$P_1, \ldots, P_6$	N	Gumbel	$5 \cdot 10^4$	$7.5 \cdot 10^3$

Fig. 4 A 23-bar plane truss bridge.

tribution, see Figure 4 on the right. The design rule in this task is that the mid-span displacement should not exceed $w_{\max} = 10$ cm, mathematically expressed

$$G(\mathbf{x}) = w_{\max} - |w_1(\mathbf{x})|; \tag{14}$$

$G(\mathbf{x})$ greater than or equal to a performance measure z denotes safety of the system, $G(\mathbf{x})$ lesser than the performance measure z indicates failure. Note, that the performance measure is equal to zero in the original formulation.

The probability of failure in inverse RBDO task was set to the $p_F = 1.15376 \cdot 10^{-3}$ which is approximately comparable to the reliability index equal to 3 from the original benchmark formulation.

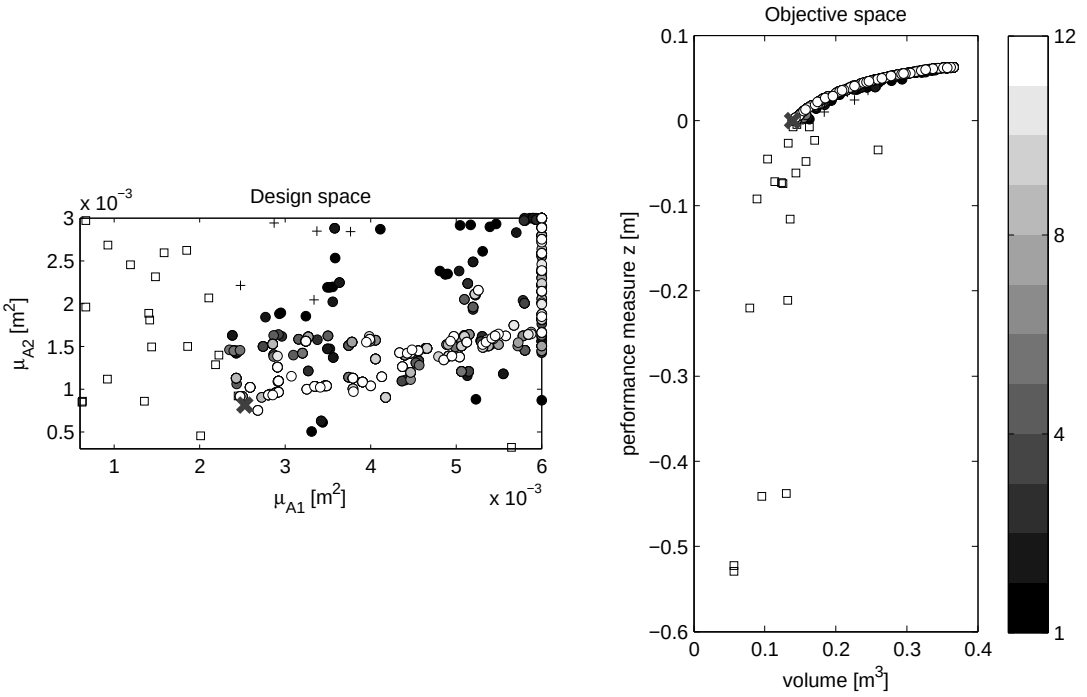

Fig. 5 All generations of the NSGA-II depicted in the design space (left) and in the objective space (right). The initial population is depicted by the pluses for feasible solutions and by squares for the unfeasible solutions. Circles represent admissible solutions with performance measures greater than zero. The grey cross represents the optimal solution presented in [11].

All generations obtained by the Non-dominated Sorting Genetic Algorithm II (NSGA-II)[2] are depicted in Figure 5. To get more meaningful solutions, Pareto-front was constrained in the performance measure criterion from below to zero because the negative reserve is nonsense in this example (the displacement should not exceed 10 cm). The single-objective optimum for RBDO published in [11] was used to validate the results for inverse RBDO. This optimum should be lying on the final front. The optimal single-objective design vector $\mathbf{d} = [2.53 \cdot 10^{-3}, 8.13 \cdot 10^{-4}]$ m^2 was used to calculate a probability of failure $p_F = 1.15376 \cdot 10^{-3}$ by the crude Monte Carlo simulation utilizing 10^8 Halton sequences samples for a high accuracy. The performance measure was fixed to zero as in the original benchmark formulation. This optimum was recomputed by the inverse Monte Carlo simulation to get back the performance measure. The measure is equal to $-5.31 \cdot 10^{-6}$ which is approximately zero as expected since the probabilistic constraint is the active constraint.

CONCLUSIONS

The purpose of the current contribution was to formulate the inverse task to Reliability-based design optimization. We proceeded from the multi-objective formulation [9] that was extended into the three-criteria reliability optimization task to minimize costs, minimize probabilities of failure and maximize performance measures. The RBDO is thereafter a planar cut with a fixed performance measure. The inverse Reliability-based design optimization fixates the probability of failure and it is thereafter a planar cut with minimizing costs and maximizing performance measures. Since those two criteria are antagonistic, the final Pareto-front of trade-off solutions is necessary to obtain by a multi-objective optimizer. The Non-Dominated Sorting Genetic Algorithm II is fast and efficient for a low number of criteria and therefore is beneficial for this task.

The formulated optimization was implemented and tested on well-known 23-bar truss benchmark that is used for the reliability assessment as well as for the RBDO problems frequently. The multi-objective RBDO task [9] was reformulated to the inverse RBDO problem and the final Pareto-front was obtained. The single-objective optimum [11] was utilized for the validation of multi-objective results because the final Pareto-fronts of the RBDO task and the iRBDO task are intersecting exactly in this single-objective optimum.

[2] The NSGA-II was set to 50 individuals in each generation and totally 12 generations. A probability of mutation is set to 0.1, a probability of cross-over is equal to 0.9 and a probability of selection to 0.9 as well.

ACKNOWLEDGEMENT

The financial support of this research by the Czech Science Foundation, project No. P105/12/1146 is gratefully acknowledged.

REFERENCES

[1] POSPÍŠILOVÁ, A., LEPŠ, M., RYPL, D. and PATZÁK, B. Shape optimization using isogeometric analysis and particle swarm optimization. In: *Proceedings of the Eleventh International Conference on Computational Structures Technology*. Stirlingshire: Civil-Comp Press, 2012, Paper 220. ISBN 978-1-905088-54-6.

[2] LEPŠ, M. *Single and Multi-Objective Optimization in Civil Engineering with Applications*. Praha, 2005. PhD thesis. Czech Technical University in Prague, Faculty of Civil Engineering.

[3] POSPÍŠILOVÁ, A. and LEPŠ, M. Global optima for size optimization benchmarks by branch and bound principles. *Acta Polytechnica*, 2012, **52**(6), 74-81. ISSN 1210-2709.

[4] LEPŠ, M. Soft computing methods in concrete mix performance approximation and optimization, 2009.

[5] HUYSE, L. Solving problems of optimization under uncertainty as statistical decision problems. In: *19th AIAA Applied Aerodynamics Conference.* American Institute of Aeronautics and Astronautics, 2001, pp.1-10. ISBN 1563474816.

[6] YAO, W. et al. Review of uncertainty-based multidisciplinary design optimization methods for aerospace vehicles. *Progress in Aerospace Sciences*, 2011, **47**(6), 450-479. ISSN 0376-0421.

[7] ZANG, T. A. et al. *Needs and opportunities for uncertainty-based multidisciplinary design methods for aerospace vehicles*. National Aeronautics and Space Administration, Langley Research Center, 2002.

[8] SCHUËLLER, G. and JENSEN, H. Computational methods in optimization considering uncertainties – An overview. *Computer Methods in Applied Mechanics and Engineering*, 2008, **198**(1), 2-13. ISSN 0045-7825.

[9] POSPÍŠILOVÁ, A. and LEPŠ, M. Multi-objective optimization with Asymptotic sampling for RBDO. In: *Proceedings of the Third International Conference on Soft Computing Technology in Civil, Structural and Environmental Engineering*. Stirlingshire: Civil-Comp Press, 2013, Paper 2. ISBN 978-1-905088-58-4.

[10] LEE, S. H. and KWAK, B. M. Reliability based design optimization using response surface augmented moment method. In: *6th World Congresses of Structural and Multidisciplinary Optimization.* International Society for Structural and Multidisciplinary Optimization (ISSMO), 2005, pp. 1-11.

[11] DUBOURG, V. *Adaptive surrogate models for reliability analysis and reliability-based design optimization*. Clermont-Ferrand, 2011. PhD thesis. Blaise Pascal University - Clermont II.

COMPARISON OF ADVANCED SIMULATION TECHNIQUES FOR RELIABILITY ASSESSMENT

Adéla POSPÍŠILOVÁ[1], **Matěj LEPŠ**[2]

Abstract: *A crude Monte Carlo simulation is a robust method for all types of reliability problems, however, it is time consuming especially for low failure probabilities that are frequent in civil engineering designs. Nowadays, advanced simulation techniques such as Importance sampling or Asymptotic sampling are quite popular for reducing the computational efforts. In this contribution, the comparison of several methods is shown on illustrative examples.*

Keywords: *Reliability, Monte Carlo simulation, Asymptotic sampling, Importance sampling, First order reliability method*

INTRODUCTION

A probability of failure in an n-dimensional space of random variables $X_1 \dots X_n$ is computed as

$$p_F = \mathbf{Prob}[g(\mathbf{X}) \leq 0] = \int_{g(\mathbf{X})\leq 0} \cdots \int f_{\mathbf{X}}(\mathbf{x}) \mathrm{d}\mathbf{x}, \tag{1}$$

where $f_{\mathbf{X}}(\mathbf{x})$ is a joint probability distribution function, $g(\cdot)$ stands for a *limit state function* and $g(\mathbf{X}) \leq 0$ denotes the failure domain. The exact solution can be computed analytically only for a special type of problems (by Gauss quadrature approaches, Laplace approximation approaches, etc.). For better scaling purposes, the approximate general reliability index β is computed from the p_F as an inverse cumulative distribution function of the standard normal distribution $\beta = \Phi^{-1}(1 - p_F)$.

Analytical approximation techniques such as a First-order reliability method (FORM) or a Second-order reliability method (SORM) and *simulation techniques* such as crude Monte Carlo (MC) and variance reduction techniques are commonly used. FORM [1, 2, 3] is very often preferred for its speed and only few necessary evaluations of the g-function ($K \cdot (n + 1)$ g-function calls for forward and

[1] Ing. Adéla Pospíšilová, Faculty of Civil Engineering, Czech Technical University in Prague, adela.pospisilova@fsv.cvut.cz

[2] doc. Ing. Matěj Lepš, Ph.D., Faculty of Civil Engineering, Czech Technical University in Prague, leps@cml.fsv.cvut.cz

backward difference formula where K is a number of iterations to find a design point and n is a number of variables, $K \cdot (2n+1)$ calls for central difference formula) which is usually computationally the most expensive part. The drawback is that the obtained probability of failure is inaccurate in case of high non-linearity in the vicinity of the design point. SORM [1] utilizing second order derivatives is more precise because it substitutes the limit state function with the second-order approximation surface but also computationally more expensive for second derivatives utilization; nevertheless, Breitung [4] and others [1] developed a second-order correction formula that decreases computational expenses.

Simulation techniques are utilized either in case that analytical approximation techniques are insufficient for large number of variables or for highly non-linear systems. The most robust method is a Monte Carlo simulation, however, it is computationally expensive. The *variance reduction techniques* such as importance sampling [5], directional sampling [6], subset simulation [7], line sampling [8] or asymptotic sampling [9] have been recently introduced for structural reliability problems. Importance sampling samples from an importance sampling distribution instead of the original distribution and the ratio of those two distributions is used to scale the probability of failure. Directional sampling uses generation of uniformly distributed direction vectors and performs a one-dimensional integration along each direction. Subset simulation formulates the small p_F as a product of larger conditional probabilities obtained by Markov Chain Monte Carlo method. Line sampling converts multi-dimensional problems in a standard normal space into the several conditional one-dimensional problems that are easier to solve. Asymptotic sampling takes advantage of the asymptotic behaviour of the probability of failure and scales random variables over the standard deviation to get more samples from the failure domain.

This paper investigates the usefulness of advanced simulation methods with comparison to the crude Monte Carlo simulation and FORM. The overall structure of the study takes the form of four chapters, including this introductory chapter. The second chapter is concerned with the brief description of Monte Carlo simulation, FORM, Importance sampling and Asymptotic sampling. Chapter Three presents results and comparison of the named methods on testing examples. Finally, the conclusion in the last chapter gives a brief summary and critique of the findings.

METHODOLOGIES

Crude Monte Carlo

A probability of failure in Equation 1 is possible to be rewritten as an expected value

$$\bar{p}_F = \int_{-\infty}^{\infty} \dots \int_{-\infty}^{\infty} I_g(\mathbf{x}) f_{\mathbf{X}}(\mathbf{x}) \mathrm{d}\mathbf{x}, \qquad (2)$$

where $I_g(\mathbf{x})$ is an indicator function that is equal to one for a failure domain $g(\mathbf{x}) \leq 0$ and zero otherwise. Simulation methods generate samples as pseudo-random or quasi-random numbers from a given

distribution and assess how many samples felt into the failure domain. The ratio between failures n_f and a number of all samples m denotes the unbiased estimator for probability of failure which is

$$p_F \approx \frac{1}{m}\sum_{i=1}^{m} I_G(x^{(i)}) = \frac{n_f}{m}. \tag{3}$$

There are several possibilities for the sampling schemes, from general pseudo-random generators, over Latin Hypercube Sampling, to quasi-random numbers as Halton sequences and Sobol sequences. We found that the best ratio between the quality of the Design of Experiment and overall time is provided by Halton sequences, see e.g. [11].

The coefficient of variation $C.o.V.$ of the approximated probability of failure can be used to estimate the quality of the result

$$C.o.V._{MC} = \frac{\sigma_{MC}}{\bar{p}_F} \approx \sqrt{\frac{1-p_F}{m \cdot p_F}} \approx \sqrt{\frac{1}{m \cdot p_F}}\Bigg|_{p_F \to 0} \tag{4}$$

where σ_{MC} is a standard deviation of the Monte Carlo results. The variance of the Monte Carlo results σ^2_{MC} depends on the number of samples (the lower variance, the better). For a common pseudo-random generator, the number of samples is very high to obtain a precise approximation of p_F. A common rule of thumb recommends a number of samples from $10/p_F$ ($C.o.V.$ approx. 32%) over $100/p_F$ ($C.o.V.$ approx. 10%) up to $500/p_F$ samples ($C.o.V.$ approx. 5%). Note, that the number of samples is not dependent on a number of variables but only on the probability of failure.

Importance Sampling

The number of samples necessary for a failure probability estimation by Monte Carlo grows quadratically for linearly decreasing probability of failure. Therefore, the advanced simulation techniques are introduced. *Importance sampling* (abbrev. IS, also referred as *weighted sampling*) is one of them. IS samples from a different distribution called importance sampling distribution (ISD). The goal is to sample in the important region to get more knowledge about interesting areas. In the best case of ISD choice, samples are located close to the failure region. For obtaining the approximated probability of failure, the weighting factor, which is the ratio of the original PDF $f_{\mathbf{X}}(\mathbf{v})$ and the importance sampling PDF $h_{\mathbf{V}}(\mathbf{v})$, is used to scale the indicator function $I_g(\mathbf{v})$

$$p_F = \int_{-\infty}^{\infty} \dots \int_{-\infty}^{\infty} I_g(\mathbf{v}) \frac{f_{\mathbf{X}}(\mathbf{v})}{h_{\mathbf{V}}(\mathbf{v})} f_{\mathbf{X}}(\mathbf{v}) \mathrm{d}\mathbf{x} \approx \frac{1}{m}\sum_{i=1}^{m} \frac{f_{\mathbf{X}}(\mathbf{v})}{h_{\mathbf{V}}(\mathbf{v})} I_g(\mathbf{v}). \tag{5}$$

The importance sampling probability density function $h_{\mathbf{V}}(\mathbf{v})$ has to be picked very carefully. With very poor choice of $h_{\mathbf{V}}(\mathbf{v})$, the importance sampling can be more costly than classical Monte Carlo.

It is obvious from

$$\sigma^2 p_F \approx \frac{1}{m-1}\left[\frac{1}{m}\sum_{i=1}^{m}\frac{f_{\mathbf{X}}(\mathbf{v})^2}{h_{\mathbf{V}}(\mathbf{v})^2}I_g(\mathbf{v}) - p_F^2\right] \tag{6}$$

that optimal sampling density is

$$h_{OPT}(\mathbf{v}) = \frac{f_{\mathbf{X}}(\mathbf{v})}{p_F}I_g(\mathbf{v}). \tag{7}$$

Unfortunately, this distribution requires the knowledge of the probability of failure. Several strategies to obtain importance sampling density are presented in the literature, namely approaches based on kernel density estimators or design points found by e.g. FORM [12] which is used in this contribution.

First Order Reliability Method (FORM)

A First Order Reliability Method (FORM) [13] is an analytical approximation method working on transforming the original space (OS) to the standard normal space (SNS) and substituting the limit state function for a hyperplane in the design point $\mathbf{u}^*$. The approximation of the reliability index β_{FORM} is the shortest distance from the origin of SNS to the design point lying on the limit state surface. The design point can be found by the optimization task $\mathbf{u}^* = \min\left(\sqrt{\mathbf{u}^T\mathbf{u}}\right)$ subject to $g(T_{SNS\to OS}(\mathbf{u})) = 0$. e.g. by Hasofer-Lind-Rackwitz-Fiessler (HLRF) algorithm [14] that converges in few steps in most cases, however, this optimization algorithm does not guarantee the global optimum solution.

Asymptotic sampling

An Asymptotic sampling is a relatively novel methodology that predicts a reliability index from an asymptotic behaviour of the probability of failure in an n-dimensional i.i.d normal space [9, 10]. A principal idea is to sequentially scale random variables over the standard deviation σ to get more samples from a failure domain. The reliability index of the problem with original distributions is obtained by an approximation of the asymptotic behaviour given by

$$\beta_{AS} = A\varphi + \frac{B}{\varphi}, \tag{8}$$

where φ denotes a scale factor that is expressed as $\varphi = \frac{1}{\sigma}$. Equation (8) can be written in a terms of a scaled reliability index for better fitting purposes. Coefficients A and B are obtained by a regression analysis through several so called *support points*.

Each support point represents a MC estimate of the reliability index for a specific scale factor φ. The number of samples for one MC simulation m with the same σ's is determined in advance as well as the number of necessary samples belonging to the failure domain N_0 and the decrease coefficient φ_d for the factor φ. If the number of failures is higher than N_0, the reliability index β_i and the corresponding factor φ_i are stored as one support point. In other case the factor φ is decreased. After gathering a sufficient number of support points K, the procedure is stopped and coefficients A and B are obtained

Tab. 1 2D examples.

Example No.	type	limit state function	note
1	linear	$g(\mathbf{x}) = 50x_1 - 100x_2 + 250$	
2	convex	$g(\mathbf{x}) = 0.1(x_1^2 + x_2^2 - 2x_1x_2) - \frac{x_1+x_2}{\sqrt{2}} + 2.5$	
3	concave	$g(\mathbf{x}) = -0.5(x_1^2 + x_2^2 - 2x_1x_2) - \frac{x_1+x_2}{\sqrt{2}} + 3$	
4	linear system	$g_1(\mathbf{x}) = -x_1 - x_2 + 3\sqrt{2}$	series system
5		$g_2(\mathbf{x}) = -x_2 + 3$	parallel system
6	non-linear system	$g_1(\mathbf{x}) = 3 + \frac{(x_1-x_2)^2}{10} - \frac{x_1+x_2}{\sqrt{2}}$ $g_2(\mathbf{x}) = 3 + \frac{(x_1-x_2)^2}{10} + \frac{x_1+x_2}{\sqrt{2}}$ $g_3(\mathbf{x}) = x_1 - x_2 + \frac{7}{\sqrt{2}}$ $g_4(\mathbf{x}) = x_2 - x_1 + \frac{7}{\sqrt{2}}$	series system

through curve fitting. Summation of A and B then represents an estimated reliability index β_{AS} for unscaled random variables as an extrapolation of φ equal to 1.

BENCHMARKS

Several examples utilizing mathematical functions as well as physical models were chosen to demonstrate the behaviour of briefly summarized methodologies above. We use crude Monte Carlo simulation utilizing Halton quasi-random sequences with $C.o.V.$ equal to 10% and 1%, then we find a design point by FORM and evaluate the probability of failure for it. The design point is thereafter used to shift the original sampling density for the Importance sampling and the last results belong to the Asymptotic sampling.

Example 1-6: 2D mathematical examples

We start with simple examples that are listed in Table 1. Random variables X_1 and X_2 have standard normal distribution. Graphical illustrations of all methods for all 2D examples are depicted in Figure 2. The results and some statistics are in Table 2.

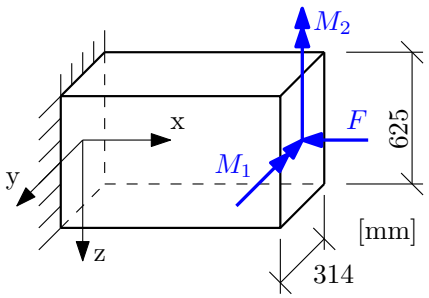

Variable		Distribution	Mean	St. dev.
M_1	N.mm	Lognormal	$2.5 \cdot 10^8$	$7.5 \cdot 10^7$
M_2	N.mm	Lognormal	$1.25 \cdot 10^8$	$3.75 \cdot 10^7$
F	N	Lognormal	$2.5 \cdot 10^6$	$5 \cdot 10^5$
σ_0	Pa	Lognormal	$5 \cdot 10^4$	$4 \cdot 10^3$

Fig. 1 A short column under oblique bending.

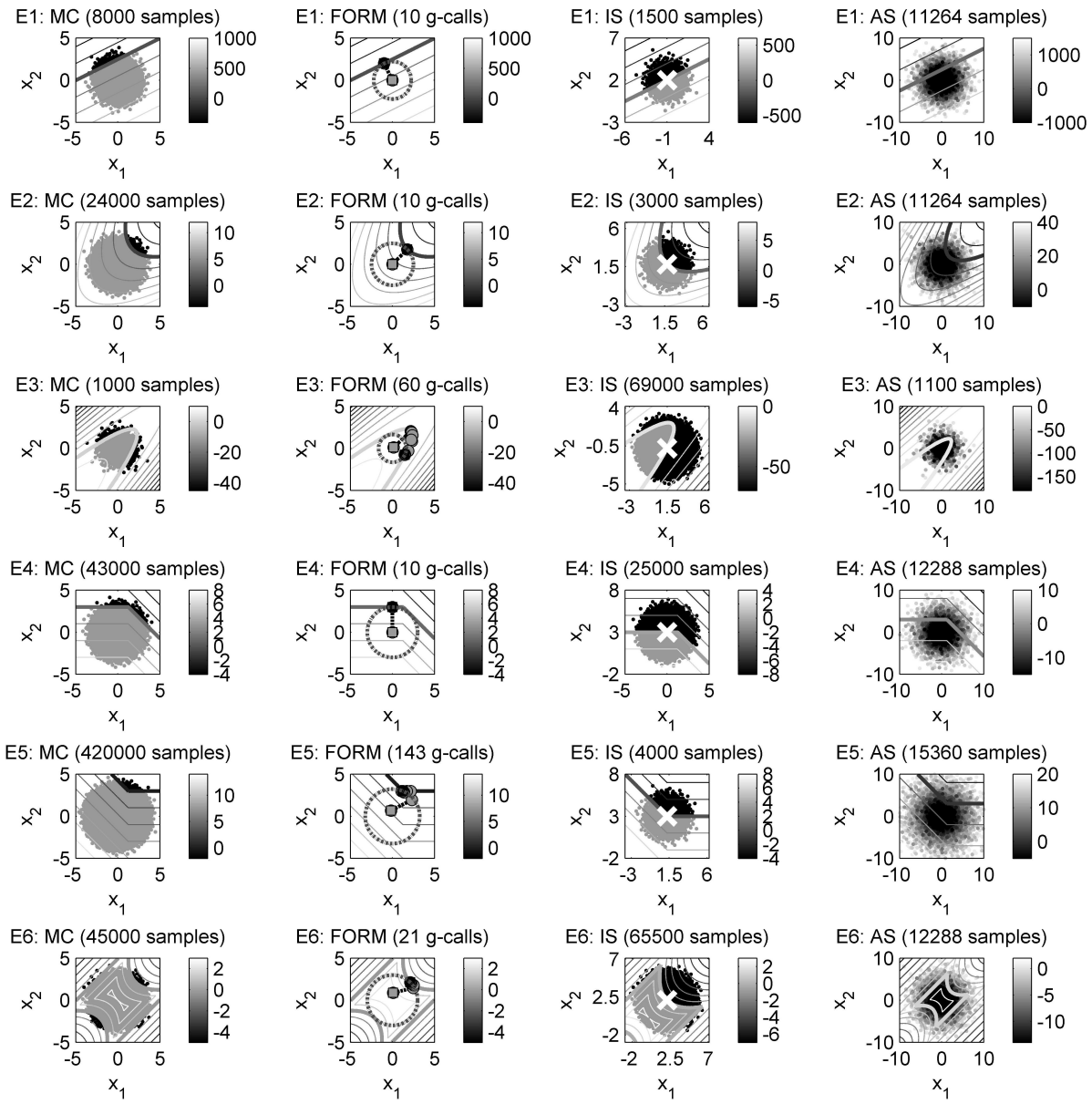

Fig. 2 2D examples (Example 1 - 6). Each column is dedicated to a specific method, each row to a different example. The highlighted contour is a limit state contour ($g(\mathbf{x}) = 0$). In MC and IS as well, grey dots are used for samples in a safe domain, black for samples in a failure domain. In FORM, the dashed line is the search path of HLRF or active-set algorithm, which is used only in case that HLRF was not able to find any optimum. The dash-and-dot line is for the β distance from the SNS origin. In AS, all incremental generations are depicted by lighter dots in which the darkest population is the initial one.

Example 7: A short column under oblique bending

A short column under axial loading F and bi-axial bending M_1 and M_2 as depicted in Figure 1 on the left is considered. The column has a rectangular cross-section with width b equal to 625 mm and height h equal to 314 mm; those dimensions are overtaken from optimization in [16]. Geometrically and physically linear behaviour is assumed.

The collapse of the structure occurs with the ultimate plastic state. Thus, the reliability of the column

Tab. 2 Results for 2D examples 1 - 6. DP is an abbreviation for a design point, in case of two design points, one is randomly chosen for IS. The number of g-function calls (no. g-calls) is the same as a number of sampling points in simulation techniques, however it differs from the number of iterations in FORM due to necessity of evaluations the derivatives. δp_F is used for relative error where MC with C.o.V. equal to 1% is considered as the true value of a quantity. The positive δp_F represents overestimation and negative δp_F underestimation the probability of failure p_F.

		Example 1	Example 2	Example 3	Example 4	Example 5	Example 6
MC	$p_{f,MC}$	$1.23 \cdot 10^{-2}$	$4.17 \cdot 10^{-3}$	$1.05 \cdot 10^{-1}$	$2.33 \cdot 10^{-3}$	$2.38 \cdot 10^{-4}$	$2.31 \cdot 10^{-3}$
	$C.o.V.$	10.0%	10.0%	9.2%	9.8%	10.0%	9.8%
	δp_F	-3.29%	-0.95%	0.64%	-3.91%	-0.04%	3.95%
	no. g-calls	$8 \cdot 10^3$	$2.4 \cdot 10^4$	$1 \cdot 10^3$	$4.3 \cdot 10^4$	$4.2 \cdot 10^5$	$4.5 \cdot 10^4$
MC	$p_{f,MC}$	$1.27 \cdot 10^{-2}$	$4.21 \cdot 10^{-3}$	$1.04 \cdot 10^{-1}$	$2.43 \cdot 10^{-3}$	$2.38 \cdot 10^{-4}$	$2.22 \cdot 10^{-3}$
	$C.o.V.$	1.00%	1.00%	1.00%	0.98%	1.00%	0.99%
	no. g-calls	$7.8 \cdot 10^5$	$2.4 \cdot 10^6$	$8.6 \cdot 10^4$	$4.2 \cdot 10^6$	$4.2 \cdot 10^7$	$4.5 \cdot 10^6$
FORM	$p_{f,FORM}$	$1.27 \cdot 10^{-2}$	$6.21 \cdot 10^{-3}$	$4.86 \cdot 10^{-2}$	$1.35 \cdot 10^{-3}$	$5.83 \cdot 10^{-4}$	$1.35 \cdot 10^{-3}$
	DP$_1$: u_1	-1	1.7678	-0.7645	0	1.2427	-2.1213
	DP$_1$: u_2	2	1.7678	1.4716	3	3	-2.1213
	DP$_2$: u_1	-	-	1.4716	2.1213	-	2.1213
	DP$_2$: u_2	-	-	-0.7645	2.1213	-	2.1213
	δp_F	0.06%	47.61%	-53.39%	-44.38%	144.65%	-39.28%
	alg.	HLRF	HLRF	HLRF	HLRF	active-set	active-set
	no. g-calls	10	10	30	10	202	21
IS	$Ep_{f,IS}$	$1.25 \cdot 10^{-2}$	$4.22 \cdot 10^{-3}$	$9.88 \cdot 10^{-2}$	$2.48 \cdot 10^{-3}$	$2.39 \cdot 10^{-4}$	$1.19 \cdot 10^{-3}$
	$C.o.V.$	1.08%	0.98%	0.99%	0.94%	0.99%	0.90%
	δp_F	-1.25%	0.25%	-5.27%	2.31%	0.15%	-46.42%
	no. g-calls	$1.5 \cdot 10^3$	$3 \cdot 10^3$	$6.9 \cdot 10^4$	$2.5 \cdot 10^4$	$4 \cdot 10^3$	$6.6 \cdot 10^4$
AS	$Ep_{f,AS}$	$1.46 \cdot 10^{-2}$	$4.52 \cdot 10^{-3}$	$1.46 \cdot 10^{-1}$	$3.06 \cdot 10^{-3}$	$1.24 \cdot 10^{-4}$	$2.38 \cdot 10^{-3}$
	$C.o.V.$	3.84%	7.46%	6.68%	6.97%	12.92%	8.62%
	δp_F	14.95%	7.39%	39.46%	25.90%	-48.04%	6.90%
	no. g-calls	$1.13 \cdot 10^4$	$1.13 \cdot 10^4$	$1.1 \cdot 10^3$	$1.23 \cdot 10^4$	$1.43 \cdot 10^4$	$1.13 \cdot 10^4$

can be defined by the limit state function

$$g(\mathbf{x}) = 1 - \frac{4M_1}{bh^2\sigma_0} - \frac{4M_2}{b^2h\sigma_0} - \left(\frac{F}{bh\sigma_0}\right)^2, \tag{9}$$

in which σ_0 is the yield stress. The axial force F, bending moments M_1 and M_2 and yield stress σ_0 are statistically independent lognormal random variables with given means and coefficients of variation listed in Figure 1 on the right. Results and statistics are presented in Table 3.

Example 8: A 23-bar truss

The 23-bar planar truss bridge benchmark with a probabilistic description of the problem was firstly published in [17]. A topology is depicted in Figure 3 on the left. Truss bars are divided into two

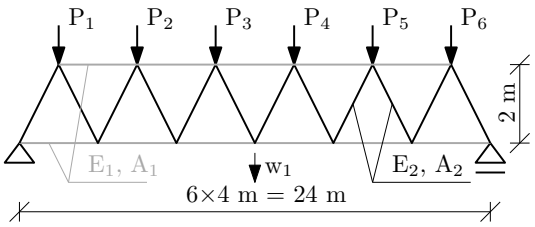

Variable		Distribution	Mean	St. dev.
E_1, E_2	Pa	Lognormal	$2.1 \cdot 10^{11}$	$2.1 \cdot 10^{10}$
A_1	m^2	Lognormal	$2 \cdot 10^{-3}$	$2 \cdot 10^{-4}$
A_2	m^2	Lognormal	$1 \cdot 10^{-3}$	$1 \cdot 10^{-4}$
$P_1, \ldots, P_6$	N	Gumbel	$5 \cdot 10^4$	$7.5 \cdot 10^3$

Fig. 3 A 23-bar plane truss bridge.

groups; the upper chord and the lower chord are contained in the first group; the diagonals creates the second group. Young's moduli and cross-sections are normally distributed variables; loadings are random variables with Gumbel distribution, see Figure 3 on the right. The design rule in this task is that the mid-span displacement should not exceed $w_{\max} = 10$ cm, mathematically expressed

$$g(\mathbf{x}) = w_{\max} - |w_1(\mathbf{x})|; \tag{10}$$

$g(\mathbf{x})$ greater than or equal to zero denotes safety of the system, $G(\mathbf{x})$ lesser than zero indicates failure.

All methods were used again to obtain the probability of failure and the results as well as statistics are summarized in Table 4.

CONCLUSION

The present study was designed to compare several reliability approximation methods and their results on examples with 2 variables that was possible to visualise as well as on slightly more complicated benchmarks. This study has shown that in cases with low number of design variables, the Importance sampling utilizing a design point needs more samples for highly non-linear systems and also becomes less precise with increasing non-linearity that is crucial. Asymptotic sampling surprisingly estimated the probability of failure for the linear system as bad as possible from all methodologies (note that the

Tab. 3 Results for a short column under oblique bending. Probabilities of failure for particular methods are shaded. The darker gray is used to highlight the most precise value. Asymptotic sampling as well as importance sampling was run 1000 times for obtaining $C.o.V.$ The design point obtained by FORM through HLRF algorithm $\mathbf{u}^* = (1.6069, 1.5925, 1.4382, -1.8115)^T$ in SNS was transformed to the original space and used for IS. δp_F is used for relative error where MC with $C.o.V.$ equal to 1% is considered as the true value of a quantity. The positive δp_F represents overestimation and negative δp_F underestimation the probability of failure p_F.

	MC	MC	FORM	IS	AS
p_F	$1.23 \cdot 10^{-3}$	$1.21 \cdot 10^{-3}$	$6.07 \cdot 10^{-4}$	$1.12 \cdot 10^{-3}$	$1.33 \cdot 10^{-3}$
$C.o.V.$	9.94%	1.00%	-	1.04%	7.30%
δp_F	1.89%	0%	-49.77%	-7.08%	9.05%
no. g-calls	$8.2 \cdot 10^4$	$8.2 \cdot 10^6$	207	$4.2 \cdot 10^4$	$2.25 \cdot 10^4$

Tab. 4 Results for a 23-bar truss. Probabilities of failure for particular methods are shaded. The darker gray is used to highlight the most precise value. Asymptotic sampling as well as importance sampling was run 1000 times for obtaining $C.o.V.$ The design point obtained by FORM through HLRF algorithm $\mathbf{u}^* = (-1.1635, -0.1767, -1.1635, -0.1766, 0.1162, 0.3552, 0.5460, 0.5460, 0.3552, 0.1162)^T$ in SNS was transformed to the original space and used for IS. δp_F is used for relative error where MC with $C.o.V.$ equal to 1% is considered as the true value of a quantity. The positive δp_F represents overestimation and negative δp_F underestimation the probability of failure p_F.

	MC	MC	FORM	IS	AS
p_F	$4.39 \cdot 10^{-2}$	$4.36 \cdot 10^{-2}$	$2.81 \cdot 10^{-2}$	$4.38 \cdot 10^{-2}$	$4.88 \cdot 10^{-2}$
$C.o.V.$	9.73%	0.98%		1.07%	3.88%
δp_F	0.62%	0%	-35.58%	0.38%	11.77%
no. g-calls	$2.3 \cdot 10^3$	$2.3 \cdot 10^5$	273	$1 \cdot 10^4$	$1.13 \cdot 10^4$

FORM result is exact for this example), however AS beats IS in the last 2D example that is the most complicated one with lesser number of g-function evaluations. Figure 2 shows that for highly non-linear systems with narrow safe region, placing the IS density to the design point is not always the best way. The question is whether this benchmark has equal physical model interpretation.

The short column under oblique bending contains four design variables from lognormal distributions. The FORM gives unsurprisingly the worst result, the IS and AS provides almost the same relative error, the difference is in the number of samples (AS is lesser with higher $C.o.V.$). The preferable method would be AS for its overestimation of the probability of failure in contrast to the IS that underestimates and that can lead to unsuitable design. The last test was made on 23-bar truss bridge that utilizes 10 random variables from different distributions, the worst result is obtained again by FORM, the best result is got by IS except for the MC with $C.o.V.$ equal to 1%.

ACKNOWLEDGEMENT

The financial support of this research by the Czech Science Foundation, project No. P105/12/1146, and by the Grant Agency of the Czech Technical University in Prague, grant No. SGS14/028/OHK1/1T/11 is gratefully acknowledged.

REFERENCES

[1] NIKOLAIDIS, E., GHIOCEL, D. M. and SINGHAL, S. *Engineering design reliability handbook*. 1st ed. CRC Press, 2005. 474 p. ISBN 0-8493-1180-2.

[2] BUCHER, C. *Computational Analysis of Randomness in Structural Mechanics*, 1st ed. London: CRC Press, 2009. 230 p. ISBN 978-0-415-40354-2.

[3] RACKWITZ, R. Reliability analysis—A review and some perspectives. *Structural safety.* 2001, **23**(4), pp. 365-395. ISSN 0167-4730.

[4] BUCHER, C. and WOLFF, S. slangTNG - scriptable software for stochastic structural analysis. In: *Proceedings of the sixteenth working conference of the IFIP Working Group 7.5 on Reliability*

and Optimization of Structural Systems. Yerevan: American University of Armenia Press, 2012, pp. 49-56.

[5] IBRAHIM, Y. Observations on applications of importance sampling in structural reliability analysis. *Structural Safety.* 1991, **9**(4), pp. 269-281. ISSN 0167-4730.

[6] NIE, J. and ELLINGWOOD, B. R. Directional methods for structural reliability analysis. *Structural Safety*. 2000, **22**(3), pp. 233-249. ISSN 0167-4730.

[7] AU, S.-K. and BECK, J. L. Estimation of small failure probabilities in high dimensions by subset simulation. *Probabilistic Engineering Mechanics.* 2001, **16**(4), pp. 263-277. ISSN 0266-8920.

[8] PRADLWARTER, H. et al. Application of line sampling simulation method to reliability benchmark problems. *Structural Safety.* 2007, **29**(3), pp. 208-221. ISSN 0167-4730.

[9] BUCHER, C. Asymptotic sampling for high-dimensional reliability analysis. *Probabilistic Engineering Mechanics.* 2009, **24**(4), pp. 504-510, ISSN 0266-8920.

[10] SICHANI, M. T., NIELSEN, S.; BUCHER, C. Applications of asymptotic sampling on high dimensional structural dynamic problems. *Structural Safety*. 2011, **33**(4), pp. 305-316. ISSN 0167-4730.

[11] POSPÍŠILOVÁ, A. and LEPŠ, M. Multi-objective optimization with Asymptotic sampling for RBDO. In: *Proceedings of the Third International Conference on Soft Computing Technology in Civil, Structural and Environmental Engineering*. Stirlingshire: Civil-Comp Press, 2013, Paper 2. ISBN 978-1-905088-58-4.

[12] SCHUËLLER, G., PRADLWARTER, H. and KOUTSOURELAKIS, P. A critical appraisal of reliability estimation procedures for high dimensions. *Probabilistic Engineering Mechanics.* 2004, **19**(4), pp. 463-474. ISSN 0266-8920.

[13] HASOFER, A. M. and LIND, N. C. Exact and invariant second-moment code format. *Journal of the Engineering Mechanics Division.* 1974, **100**(1), pp.111-121. ISSN 0044-7951.

[14] RACKWITZ, R. and FLESSLER, B. Structural reliability under combined random load sequences. *Computers & Structures.* 1978, **9**(5), pp. 489-494. ISSN 0045-7949.

[15] DUBOURG, V. *Adaptive surrogate models for reliability analysis and reliability-based design optimization*. Clermont-Ferrand, 2011. PhD thesis. Blaise Pascal University - Clermont II.

[16] ROYSET, J., DER KIUREGHIAN, A. and POLAK, E. Reliability-based optimal structural design by the decoupling approach. *Reliability Engineering & System Safety.* 2001, **73**(3), pp. 213-221. ISSN 0951-8320.

[17] LEE, S. H. and KWAK, B. M. Reliability based design optimization using response surface augmented moment method. In: *Proceedings of the 6th World Congress on Structural and Multidisciplinary Optimization*. Rio de Janeiro: International Society for Structural and Multidisciplinary Optimization (ISSMO), 2005.

INFLUENCE OF MORPHOLOGY ON MICROMECHANICAL PROPERTIES OF WOOD CELL

Zdeněk PROŠEK[1], Jaroslav TOPIČ[2], Václav NEŽERKA[3], Pavel TESÁREK[4], Kateřina INDROVA[5], Vlastimil KRÁLÍK[6]

***Abstract**: The presented article deals with the relationship between micromechanical properties of wood tissues and the angle of microfibrils in cells of spruce wood. Cell wall is composed of more layers of various spiral angles of cellulose microfibrils and their study is complicated because of the limited size and difficult identification. For this reason, we used a combination of optical microscopy and nanoindentation. In particular, optical microscopy was used to determine the topography of the sample and nanoindentation for mapping the micromechanical properties. Microfibril angle was consequently derived based on the recorded modulus of elasticity.*

***Keywords**: Micromechanical properties, spruce wood, geometry, nanoindentation, modulus mapping*

INTRODUCTION

Before the electron microscopy was available, Bailey and Kerr [1] used iodine staining and polarization microscopy to for investigation of wood tissues. They found that the secondary wall is composed of three layers, commonly referred to as outer (S_1), middle (S_2) and inner (S_3). While investigating the cell cross-section they found that the outer and inner layers are brighter than the middle one due to different orientation of fibrils within the individual layers.

[1] Ing. Zdeněk Prošek, Czech Technical University in Prague, Faculty of Civil Engineering; Thákurova 7, 166 29 Prague 6 – Dejvice, Czech Republic, zdenek.prosek@fsv.cvut.cz

[2] Ing. Jaroslav Topič, Czech Technical University in Prague, Faculty of Civil Engineering; Thákurova 7, 166 29 Prague 6 – Dejvice, Czech Republic, zdenek.prosek@fsv.cvut.cz

[3] Ing. Václav Nežerka, Czech Technical University in Prague, Faculty of Civil Engineering; Thákurova 7, 166 29 Prague 6 – Dejvice, Czech Republic, vaclav.nezerka@fsv.cvut.cz

[4] Ing. Pavel Tesárek, Ph.D., Czech Technical University in Prague, Faculty of Civil Engineering; Thákurova 7, 166 29 Prague 6 – Dejvice, Czech Republic, tesarek@fsv.cvut.cz

[5] Bc. Kateřina Indrová, Czech Technical University in Prague, Faculty of Biomedical Engineering; Nám. Sítná 3105, 272 01 Kladno, katerina.indrova@fbmi.cz

[6] Ing. Vlastimil Králík, Faculty of Civil Engineering, Czech Technical University in Prague, Thákurova 7, 166 29 Prague 6 – Dejvice, Czech Republic, vlastimil.kralik@fsv.cvut.cz

The middle layer of the secondary wall forms the major part of wood cells and therefore it is the most important component from the mechanical point of view. It is composed of 30 to 150 lamellas. The middle layer has a superior influence on the properties of wooden cells. Properties of the middle layer have the major impact on the wood anisotropy, shrinkage, strength and ductility [1].

Wimmer et al. [2] utilized nanoindentation in 1997 to investigate the mechanical properties of wood cells and published the records about the stiffness of spruce earlywood, latewood and transition wood for the first time. His results are summarized in Table 1 and compared to the results provided by other authors. Wagner et al. [9] found a relationship between the indentation depth and obtained results, and established the depth of 200 to 250 nm as optimal to obtain the most accurate results. The indentation depth is not the only factor influencing the results; a lignin content and angle of fibrils in the tested cell wall have an impact on the micromechanical properties as well. A. Jäger et al. [10] found a dependence of the angles of fibrils on the nanoindentation results, and they came to the conclusion that the elastic modulus and hardness are proportional to the amount of fibrils in the cell walls. There were attempts to measure the micromechanical properties of the outer secondary wall S_1, but these failed because the results were influenced by the surrounding layers. From this reason all successful nanoindentation measurements were conducted only on the middle secondary wall S_2.

Tab. 1 Indentation modulus and microfibril angle of the secondary cell wall layer S_2

Type of wood	Author	References	Elastic modulus (GPa)	MFA (°)
Latewood	Wimmer and Lucas, 1997	[3]	15.81	3
	Gindl, 2002	[4]	17	0
	Gindl, 2002	[5]	18	0
	Gindl, 2004	[6]	15.34	5
	Gindl, 2004	[7]	17.08	5
	Konnerth, 2009	[8]	20	0
Earlywood	Gindl, 2002	[4]	11.5	35
	Gindl, 2004	[7]	8	50
	Konnerth, 2009	[8]	12.5	17.5

The difference between the elastic stiffness of earlywood and latewood cell walls is attributed to the different chemical composition and angle of fibrils. The earlywood cells contain more lignin and less cellulose, resulting in a reduced elastic stiffness. The work of Gindl et al. [7] focused on the micromechanical properties of individual phases in the wood tissues suggest that lignin, which bonds to hemicellulose, does have significant impact on the value of elastic stiffness.

METHODOLOGY AND RESULTS

Both kinds of wood cells, i.e. earlywood and latewood, were indented at various cell regions by using methods of standard indentation and modulus mapping. The standard indentation loading function, consisting of a constant loading (5 seconds), holding period (8 seconds) and unloading stage (5 seconds), was pursued. The maximum loading capacity of the indenter was 400 μN. Figure 6 shows a 4 × 5 indentation matrix captured during in-situ monitoring, using the Hysitron Tribolab® scanning device. In order to avoid any interaction between individual indents, their minimum spacing was set to 3 μm.

In the case of modulus mapping method, the dynamic force was harmonically superimposed (with the amplitude 5 μN and frequency of 150 Hz) to the nominal quasi-static contact force 12 μN. Such measurement was conducted on the area of 16 × 16 μm. With respect to the negligible viscosity, indicated by the relatively small magnitude of the measured loss moduli, the values of storage moduli can be considered as the reduced elastic stiffness modulus, obtained by means of quasi-brittle nanoindentation test. Results from standard nanoindentation and modulus mapping are presented in Figure 1.

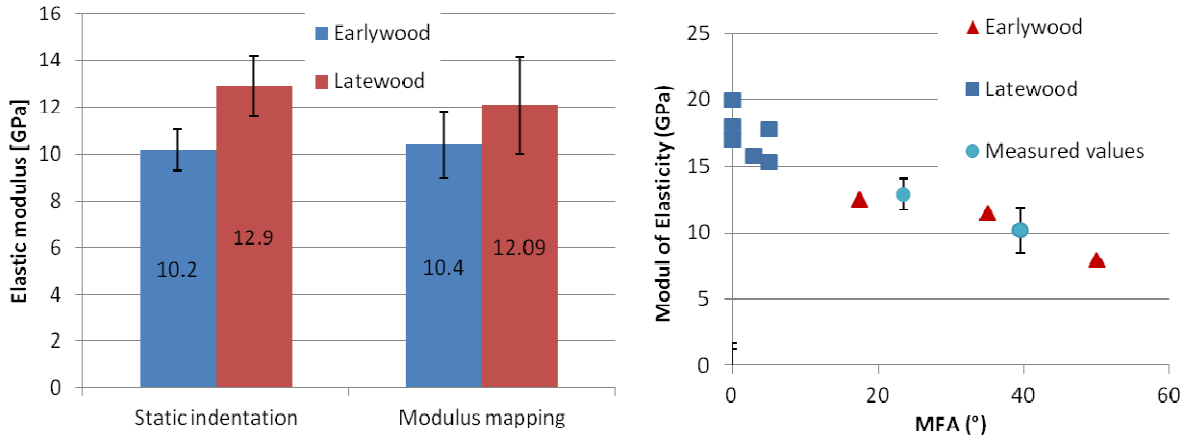

Fig. 1 Elastic stiffness of tracheid walls (left), the modulus of elasticity of tracheids walls depending on the angle of microfibrils (right)

The influence of the orientation angle of fibrils on the elastic stiffness was investigated by Jäger et al. [10], who found a clear correlation between these quantities. Based on their equation describing the relationship between the orientation of fibrils and elastic modulus (Figure 1), the fibrils of earlywood cell walls in our samples were oriented in the angle 39.5° and 23.5° in the case of latewood. These values are relatively large, which might have been a result of a defect in the vicinity of the extracted samples or sample preparation. According to Gindl et al. [7] the compressed wood defect increases the angle of fibrils up to 50° and Wagner et al. [9] found that polishing of the samples can increase the angle as well.

CONCLUSION

The results of our study provide detailed information about the micromechanical properties of two basic types of cells. Microfibril angles were derived from the values of elastic stiffness obtained by means of nanoindentation technique called modulus mapping. Microfibril angles were established as 39.5 ° for earlywood and 23.5 ° for latewood wood cells. The future research will be focused on the investigation of fibrils using optical microscopy and X-ray diffraction to be compared with the nanoindentation results and Jäger equation.

ACKNOWLEDGEMENT

The financial support of this experiment by the Faculty of Civil Engineering, Czech Technical University in Prague (SGS project No. SGS14/122/OHK1/2T/11 and SGS14/029/OHK1/1T/11) is gratefully acknowledged. Special thanks belong to the Center for Nanotechnology in Civil Engineering at Faculty of Civil Engineering CTU in Prague

REFERENCES

[1] TSOUMIS, G. *Science and technology of wood: Structure, Properties, Utilization*. New Yourk: Chapmann and Hall, 1991. 494 p. ISBN 0-412-07851-1.

[2] WIMMER, R. et al. Longitudinal hardness and Young's modulus of spruce tracheid secondary walls using nanoindentation technique. *Wood Sci Technol*. 1997, **31**(2), 131-141. ISSN 0043-7719.

[3] WIMMER, R. and LUCAS, B. N. Comparing mechanical properties of secondary wall and cell corner middle lamella in spruce wood. *IAWA*. 1997, **18**(1), 77–88.

[4] GINDL, W., GUPTA, H. S. and GUNWALD, C. Lignification of spruce tracheid secondary cell walls related to longitudinal hardness and modulus of elasticity using nano-indentation. *Canadian Journal of Botany*. 2002, **80**(10), 1029-1033. ISSN 0008-4026.

[5] GINDL, W. and GUPTA, H. S. Cell-wall hardness and Young's modulus of melamine-modified spruce wood by nano-indentation. *Comp Part*. 2002, **33**(8), 1141–1145. ISSN 1359-835X.

[6] GINDL, W. et al. Mechanical properties of spruce wood cell walls by nanoindentation. *Appl Phys*. 2004, **79**(8), 2069–2073. ISSN 0947-8396.

[7] GINDL, W. et al. The significance of the elastic modulus of wood cell walls obtained from nanoindentation measurements. *Comp Part*. 2004, **35**(11), 1345–1349. ISSN 1359-835X

[8] KONNERTH, J. el al. Actual versus apparent within cell wall variability of nanoindentation results from wood cell walls related to cellulose microfibril angle. *J Mater Sci*. 2009, **44**(16), 4399–4406. ISSN 0022-2461.

[9] WAGNER, L. et al. Nanoindentation of wood cell walls: effects of sample preparation and indentation protocol. *J Mater Sci*. 2009, **49**(1), 94–102. ISSN 0022-2461.

[10] JÄGER, A. et al.: The relation between indentation modulus, microfibril angle, and elastic properties of wood cell walls. *Composites*. 2011, **42**(6), 677–685. ISSN 1359-835X

FRACTURE PROPERTIES OF FIBER REINFORCED LIME-BASED MORTAR

Michal PŘINOSIL[1], **Petr KABELE**[2]

***Abstract**: In this paper, the amount of dissipated energy, i.e. energy necessary to break sets of notched specimens during three-point bending test, is experimentally investigated. The sets are prepared from lime-based mortar reinforced with short synthetic fibers. We considered two types of the matrix (pure lime, lime-metakaolin), two types of polyvinyl alcohol fibers in four volume fractions (0.5÷2.0%). As the reference, we tested also two sets from plain mortar without fiber reinforcement.*

***Keywords**: fiber reinforced mortar, lime-based mortar, fracture energy, energy absorption, three-point bending test*

INTRODUCTION

Conventional mortars based on lime binder could be characterized by a low strength, low tensile strain capacity and low energy absorption capacity. This results in a small durability of applications of these materials, such as repair and reconstruction of historical objects. Elimination of these drawbacks would avoid mentioned problems. The effect of metakaolin on mechanical properties of hardened mortar is well known [1]. Another approach improves cohesive behavior of cracks using fiber reinforcement. Its presence was proved in historical mortars [2].

In our research, we develop high-performance fiber reinforced lime-based mortar suitable for the restoration and maintenance of historic objects. The goal is to design the composite using micromechanics and fracture mechanics so that under excessive tensile deformations mortar exhibits strain-hardening response and multiple cracking (a large amount of fine cracks) instead of damage localize in one crack as in conventional mortar. Therefore, mortar retains its integrity and ability to carry further loading.

The main objective of this work is to describe the influence of the fiber reinforcement on fracture properties of lime-based mortar. To this end, three-point bending test on notched specimens was

[1] Ing. Michal Přinosil, Department of Mechanics, Faculty of Civil Engineering, Czech Technical University in Prague, Thákurova 7, 166 29, Prague 6, Czech Republic, michal.prinosil@fsv.cvut.cz

[2] prof. Ing. Petr Kabele, PhD., Department of Mechanics, Faculty of Civil Engineering, Czech Technical University in Prague, Thákurova 7, 166 29, Prague 6, Czech Republic, petr.kabele@fsv.cvut.cz

performed. The investigated parameters are energy absorption capacity (the amount of dissipated energy) and the energy related to the cross-sectional area of the beam above notch (in ligament).

MATERIALS

The composite consists of a filler, binder, water, fiber reinforcement and eventual additive (plasticizer) to improve workability. The filler is represented by fine quartz sand with maximum particle size 0.3 mm. As the binder, hydrated air lime powder CL90 from the company Vápenka Čertovy schody a.s. and metakaolin Mephisto L05 from ČLUZ s.r.o. Nové Strašecí were chosen. The reason for adding it into the mixture is to improve the tensile strength, to reduce shrinkage and to improve rheological properties.

In our previous research, we dealt with the experimental investigation of individual components of the composite (micro scale). Firstly, we examined the influence of the composition of pure matrix (without reinforcement) on tensile and fracture properties (Young's modulus, tensile strength, bilinear approximation of tensile traction-separation relation and fracture energy) [3]. Based on the results, ratio of the filler and binder, ratio of individual types of the filler (with different maximum particle size) and the water ratio (calculated as the ratio of weight of the water and weight of filler and binder) were chosen.

Afterwards, we examined several types of fiber reinforcement from different material (organic,

Tab. 1: The composition of the composite (weight proportions)

Component	Producer	Product	L	LM
Binder			1.000	
Lime	Čertovy schody, a.s.	Čerťák CL90	1.000	0.750
Metakaolin	ČLUZ s.r.o.	Mefisto L05	0.000	0.250
Filler			3.000	
Sand, d_{max} 0.1 mm	Sklopísek Střeleč, a.s.	ST2	1.846	
Sand, d_{max} 0.3 mm	Sklopísek Střeleč, a.s.	STJ25	1.154	
Water			1.200	
Plasticizer	Stachema Kolín s.r.o.	Melment L10/40	0.024	
Fibers	Kuraray Co., Ltd.	RSC 15×8, PVA	0.5% - 0.029 1.0% - 0.059	
		REC 15×12, PVA	1.5% - 0.088 2.0% - 0.118	

polyvinyl alcohol – PVA, polypropylene – PP and glass), with different geometry (length and diameter) and eventually with surface treatment [4], [5]. Tensile parameters (Young's modulus, tensile strength and tensile yielding strength in case of bilinear shape of stress-strain diagram) and their interaction with lime-based mortar (described by friction, chemical bond and hardening parameter [6]) were experimentally evaluated.

Based on the results above mentioned experiments, the final composition of the composite for experimental research was proposed. Two types of matrix (lime – labeled L, lime-metakaolin – labeled LM), two types of PVA fibers (RSC 15×8 – labeled S, REC 15×12 – labeled E) produced by Kuraray corp. in four volume fractions V_f (0.5%, 1.0%, 1.5%, 2.0%) were selected. Moreover, two sets (L, LM) of plain mortar without reinforcement were included as the reference. The weight parts of individual components are shown in Tab 1.

METHODOLOGY

Preparing specimens

Mix process was performed in the mixer with vertical axis of rotation with frequency 25 Hz. Firstly, all dry ingredients of filler and binder were blended. Then, one-half of water during 30 s was added and the mixing continued for 180 s. After that, the second half of water was added with the same procedure. Subsequently, the plasticizer was poured into the mixture during 30 s. It was followed by addition of one-half of the amount of fibers and the product was mixed until the homogeneous state (about 60 s). Finally, rest of fibers was added with the same procedure. Between each two steps, the

Fig. 1 Testing set-up

mixture was hand-mixed and homogeneous state was controlled.

From each fresh mixture a set of 6 standard beams with dimensions 40×40×160 mm were prepared according [7]. They were demolded the next day and placed for 7 days in environment of high humidity (over 85%). After that, they were stored approximately for one year in laboratory conditions (temperature 22°C, relative humidity over 50% and concentration of carbon dioxide over 500 ppm). During this period, a thin notch reaching approximately 35÷40% of beam's high was created. Then, all important dimensions were measured and the front surface (in means of the experiment) of specimens was covered by a spray with contrasting color for image analysis of displacements (Figure 1).

Testing set-up

Three-point bending test was performed by means of the MTS Alliance RT/30 machine with load cell 30 kN. Controlled crosshead displacement had typical step 0.2 mm/min for fiber-reinforced sets and 0.05 mm/min for reference sets without reinforcement. The support span was 120 mm. During the test, the applied force P, crosshead displacement u and crack mouth opening displacement (CMOD) using attached extensometer were continuously recorded (Fig. 1). Furthermore, the high resolution images of specimens above the notch were taken by digital camera with time period 10 s for controlled analysis of displacements.

From measured data, the initial idle branch was removed and replaced by maximal slope of initial branch using software FitData [8] and the tail of load-displacement curve was linearly extrapolated up to P = 0 N with corresponding displacement u_0. Final load-displacement diagrams are shown in the Annex. The total dissipated energy W_f was calculated as the area under load-displacement diagram:

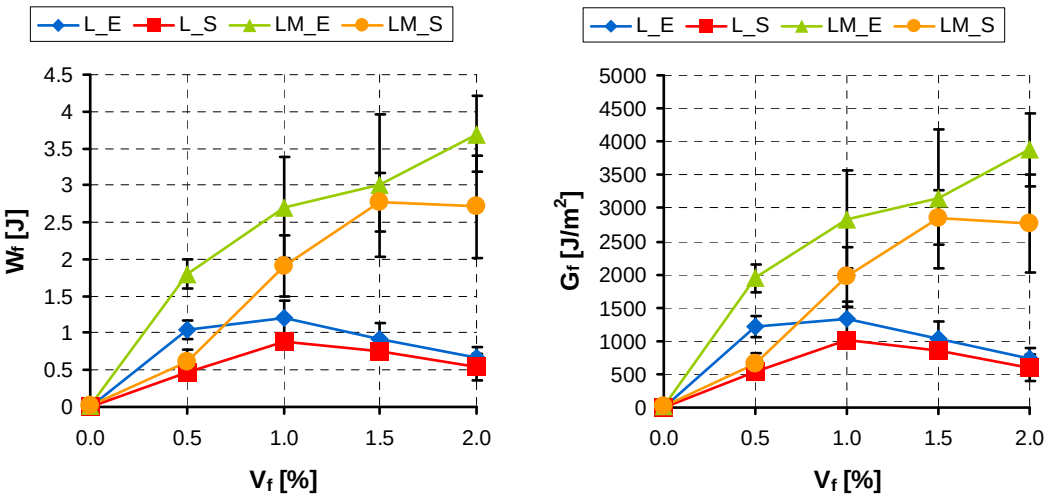

Fig. 2 Total dissipated energy (left) and the energy divided by area of ligament (right)

$$W_f = \int_0^{u_0} P du \tag{1}$$

and the dissipated energy divided by area of ligament A_{lig}, which in cases of plain mortar corresponds to fracture energy (but for fiber-reinforced mortars cracking in several cracks it doesn't):

$$G_f = \frac{W_f}{A_{lig}} \tag{2}$$

RESULTS

Figure 2 and Table 2 show the dependences of dissipated energy and the energy related to cross-sectional area of the ligament on volume fractions of fibers, fiber and matrix type. From the results, it is clear that the fiber reinforcement significantly improves both characteristics. For fibers REC 15×12, the values are higher than for fibers RSC 15×8. It could be explained by greater length of REC fibers or their better interaction with the matrix. The load-displacement diagrams listed in Annex show that in case of RSC fibers load decreases faster than in case of REC fibers. It is associated with their length. It also points out that fibers are pulled out from the matrix (instead of rupture).

Similar results are for those types of the matrix, where lime-metakaolin reaches higher values than pure lime, but the character is different. In the case of the lime matrix, energy increases up to volume fractions 1.0% and then decreases. In the case of lime-metakaolin mortar, the values arise with increasing volume fraction (except for LM_S in V_f = 2.0%). These differences in behavior may be caused by the lower tensile strength of pure lime mortar and therefore the mortar for high volume fractions is not able to carry the load from fibers (mortar is over-reinforced and it is the weakest link).

Tab. 2: The results of the experiment

Fibers	V_f [%]	Matrix L		Matrix LM	
		W_f [J]	**G_f [J/m^2]**	**W_f [J]**	**G_f [J/m^2]**
	0.0	0.007	7.10	0.013	13.44
E	0.5	1.046	1215.57	1.801	1942.79
	1.0	1.202	1340.60	2.700	2822.07
	1.5	0.920	1039.33	3.004	3140.75
	2.0	0.665	739.71	3.693	3876.95
S	0.5	0.475	537.22	0.619	665.30
	1.0	0.882	1012.47	1.905	1966.82
	1.5	0.753	848.51	2.771	2855.56
	2.0	0.539	589.90	2.715	2774.76

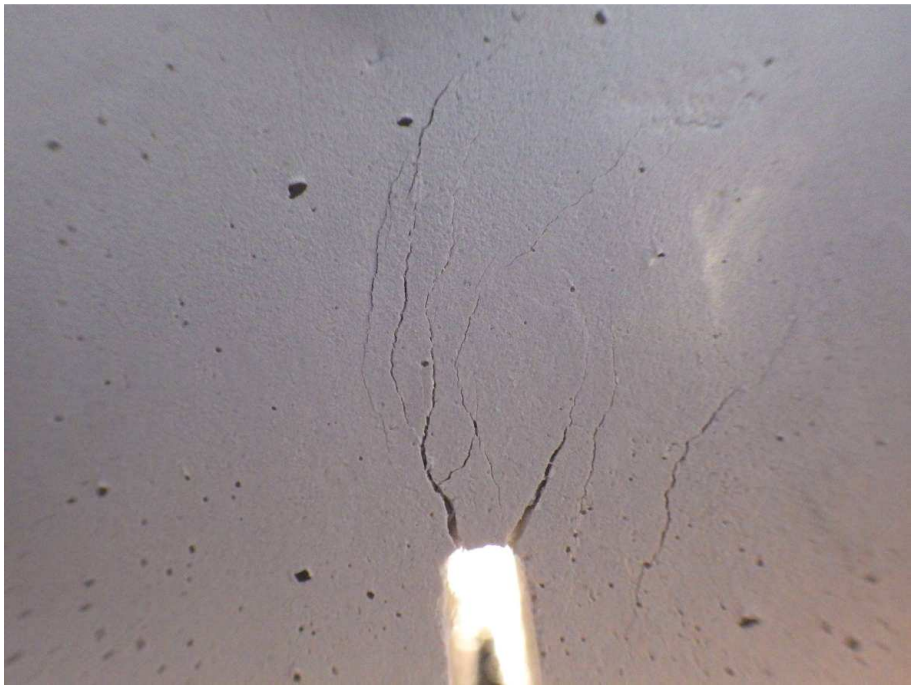

Fig. 3 Cracking in lime-metakaolin mortar

The results also show that the values of lime mortar have lower scatter than lime-metakaolin. It is associated with the number of formed cracks, because the total amount of dissipated energy depends on it. The lime mortar cracked in a small number of cracks, while lime-metakaolin mortar cracked in most cases in several cracks (Fig. 3).

CONCLUSION

Energy absorption capacity of lime-based mortar reinforced with two types of short synthetic fibers in four volume fractions has been experimentally investigated. For this purpose, 16 sets made of fiber reinforced mortar and 2 reference sets without reinforcement of experimental beams with notch were prepared and tested in the three-point bending test.

The results reveal that even a small volume fraction of fibers in the composite greatly improves the total amount of dissipated energy and show that the energy absorption capacity of fiber composites depends on the matrix, on the fiber reinforcement and on the interaction between these two phases. The results also show that in case of lime-metakaolin mortar the total amount of dissipated energy is higher than of pure lime mortar and the trend increases up to volume fraction 2%. Moreover, the results show that the mortar with metakaolin cracks in the form of distributed cracks (multiple cracking), which is highly desirable phenomenon with regard to the tensile deformation capacity and durability of application of the material. On the other hand, in the case of pure lime mortar the total amount of dissipated energy increases up to volume fraction 1%, where the ability to carry forces from fibers of the matrix is exhausted, and then amount of absorbed energy decreases.

These results are important for final mixture proposal of the composite in order to achieve maximum energy absorption capacity as well as good workability of a fresh mix, which with increasing amount of fibers in the mixture decreases.

ACKNOWLEDGEMENT

The financial support of this research by the Czech Technical University in Prague under project SGS14/029/OHK1/1T/11 is gratefully acknowledged.

REFERENCES

[1] ROVNANÍKOVÁ, P. Vápenné malty modifikované metakaolinem (Lime mortar modified by metakaolin). In: *Sanace a rekonstrukce staveb 2008*. Brno: WTA CZ, 2008. pp. 56-61. ISBN: 978-80-02-01998- 5.

[2] HOŠEK, J., LOSOS, L. *Historické omítky: průzkumy, sanace, typologie*. 1. vyd. Praha: Grada, 2007, 167 p. Stavitel. ISBN 978-80-247-1395-3.

[3] PŘINOSIL, M., KABELE, P. Influence of composition on tensile and fracture properties of lime-based mortar. In: PLACHÝ, T. a kol, eds. *Proceedings of the Conference Nano & Macro Mechanics 2012*. Praha: ČVUT v Praze, Fakulta stavební, 2012, pp. 187-194. ISBN 978-80-01-05097-2.

[4] PŘINOSIL, M., KABELE, P. Prediction of the behavior of lime mortar reinforced with fibers based on their micromechanical parameters. In: JASIEŃKO, J. eds. *Proceedings of the International Conference on Structural Analysis of Historical Constructions, SAHC 2012*. Wroclaw: Wroclaw University of Technology, Faculty of Civil Engineering, Institute of Building Engineering, 2012, pp. 883-889. ISBN 978-83-7125-216-7.

[5] KABELE, P., SLÍŽKOVÁ, Z. *Vysokohodnotné a kompatibilní vápenné malty pro extrémní aplikaci při restaurování, opravách a preventivní údržbě architektonického dědictví (High-performance and compatible lime mortars for extreme application in restoration, repair and preventive maintenance of architectural heritage).* Praha: ČVUT v Praze, Fakulta stavební, Katedra mechaniky & Akademie věd ČR, Ústav teoretické a aplikované mechaniky, 2013. Periodic report for the year 2013 to the project of Ministry of Culture of the Czech Republic No.DF11P01OVV008.

[6] LI, V.C., LEUNG, C.K.Y. Steady-state and multiple cracking of short random fiber composites. *Journal of Engineering Mechanics (ASCE)*. 1992, **118**(1), pp. 2246-2264. ISSN 0733-9399.

[7] ČSN EN 1015-11. *Zkušební metody malt pro zdivo - Část 11: Stanovení pevnosti zatvrdlých malt v tahu za ohybu a v tlaku*. Praha: Český normalizacnčí institut, 2000. 16 p.

[8] PŘINOSIL, M. *FitData: User's manual*. 2012 [online]. [cited 2014-06-30]. Available from: http://mech.fsv.cvut.cz/~prinosil/ index.php?id=FitData.

ANNEX

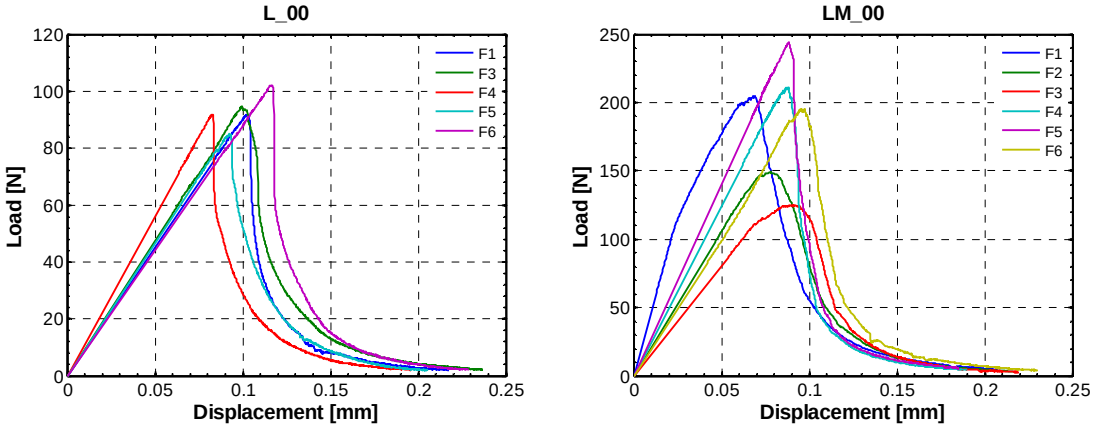

Fig. 4 Load-displacement diagrams of pure mortar (lime – left, lime-metakaolin – right)

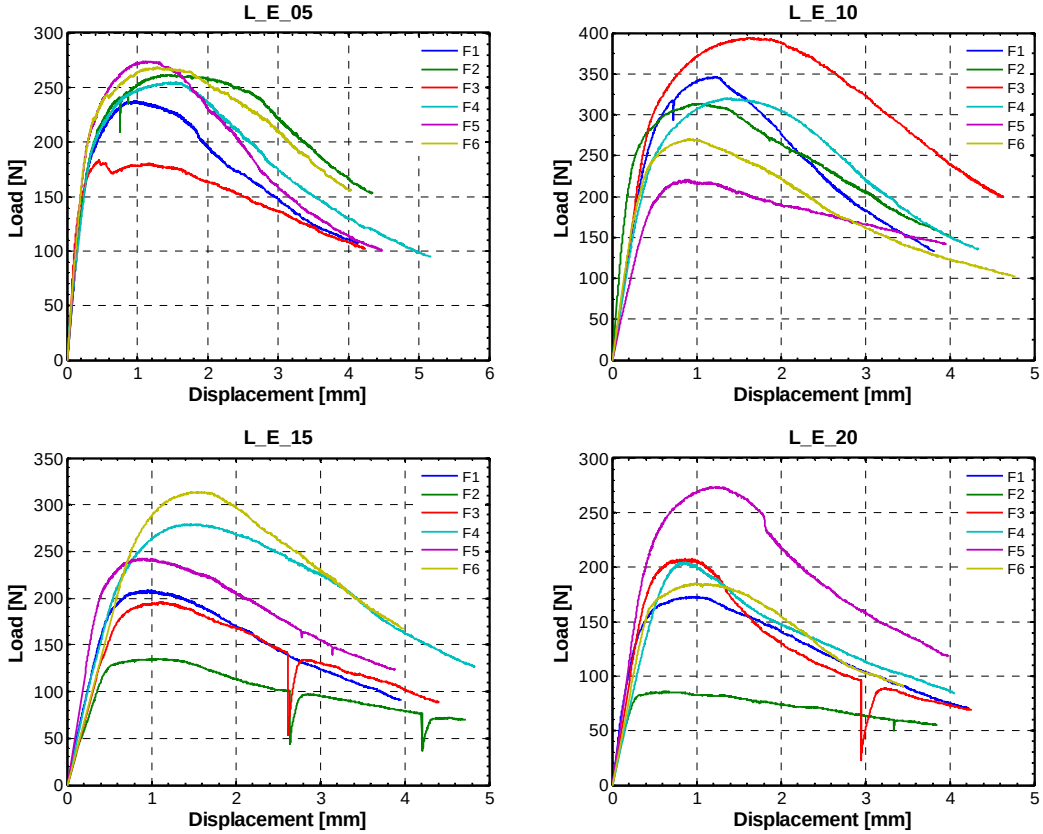

Fig. 5 Load-displacement diagrams of lime mortar reinforced with REC 15×12

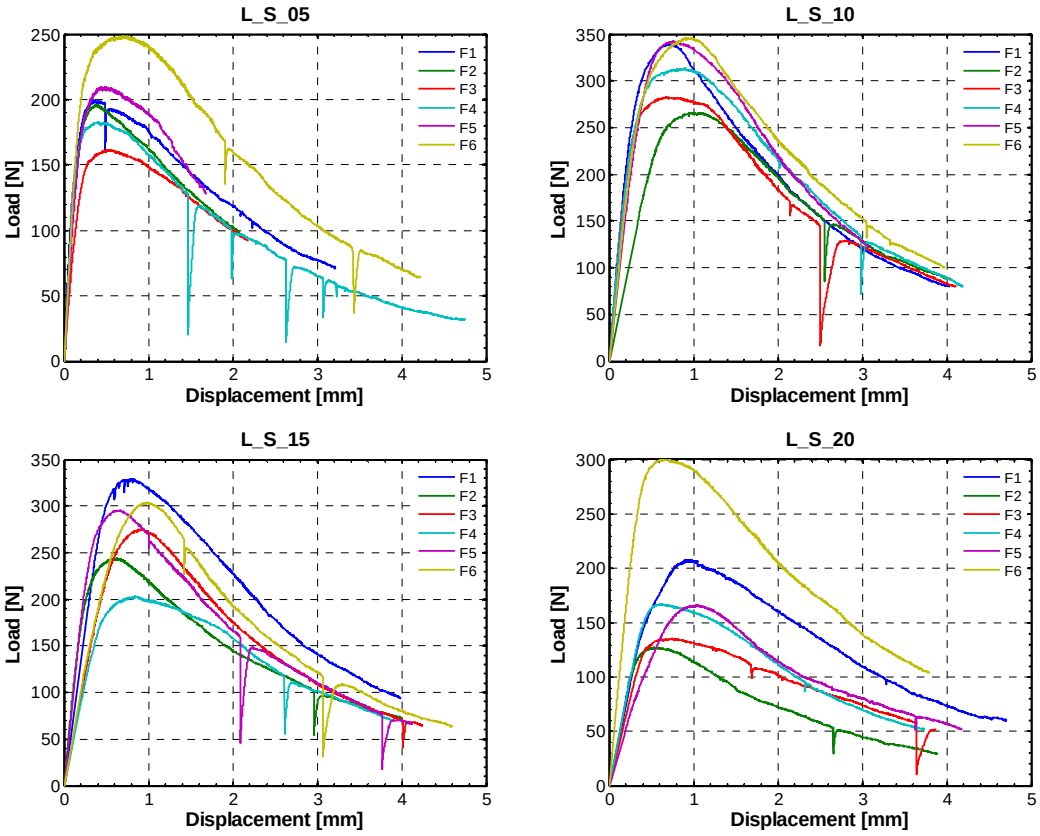

Fig. 6 Load-displacement diagrams of lime mortar reinforced with RSC 15×8

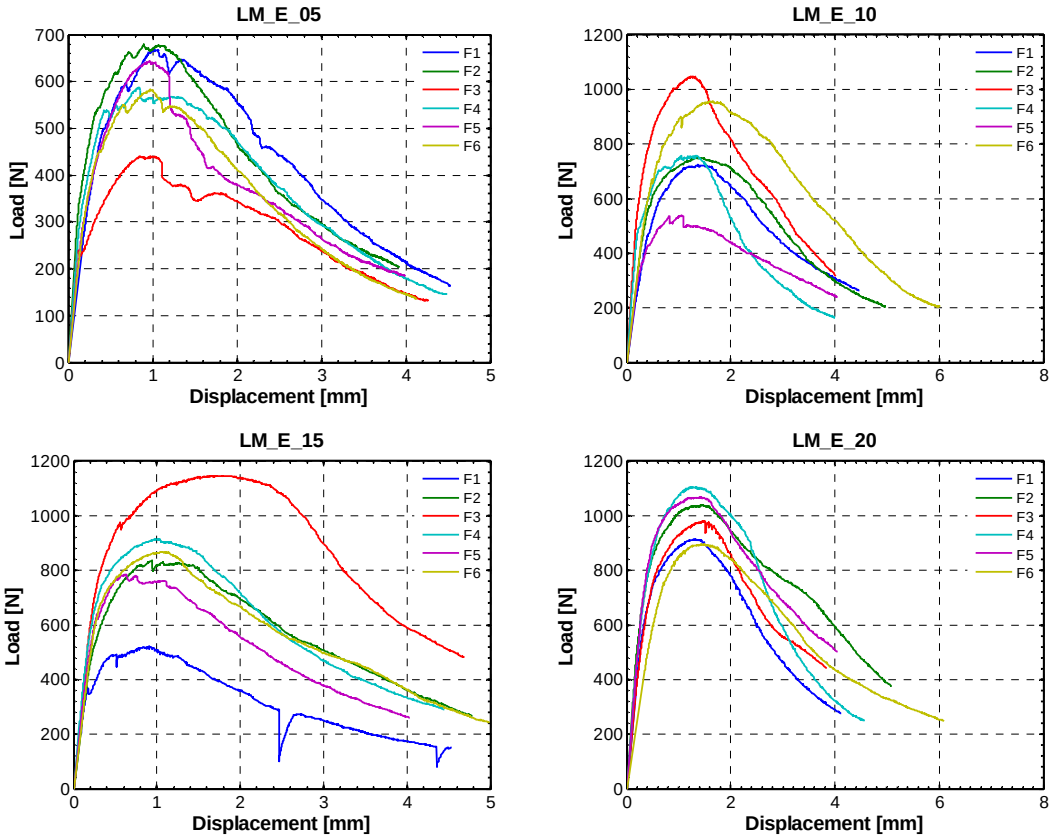

Fig. 7 Load-displacement diagrams of lime-metakaolin mortar reinforced with REC 15×12

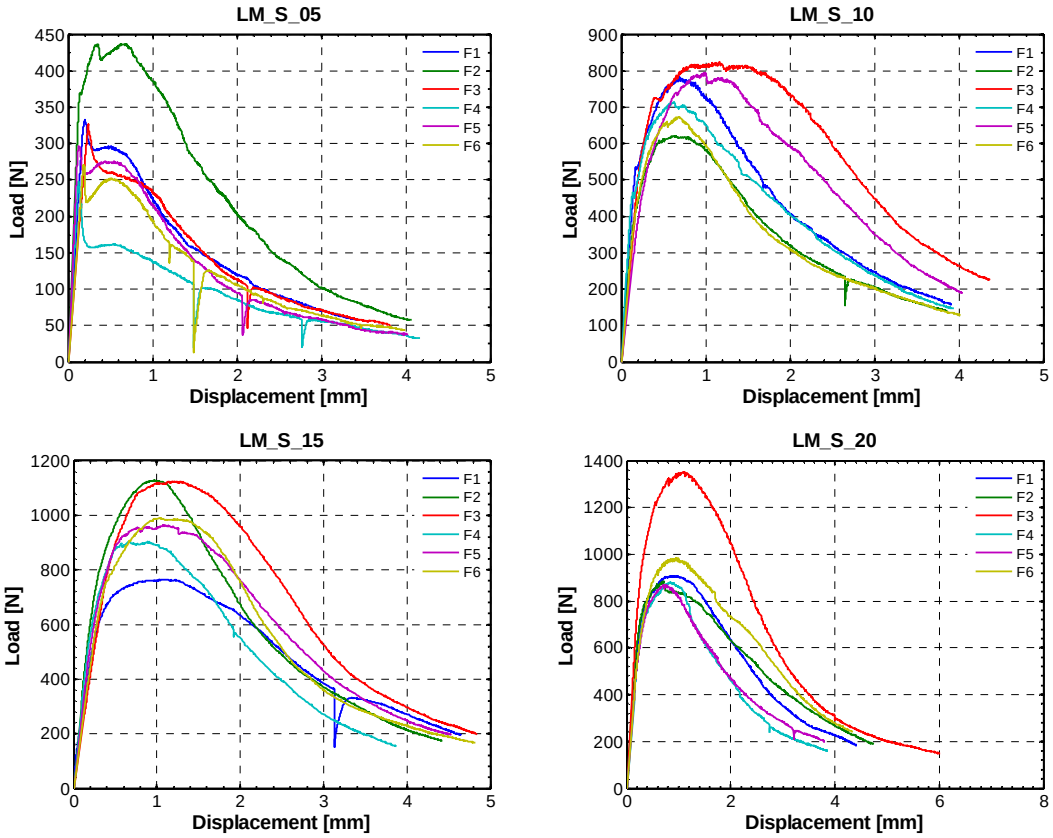

Fig. 8 Load-displacement diagrams of lime-metakaolin mortar reinforced with RSC 15×8

NONLINEAR ANALYSIS OF FUNCTIONALLY GRADED FIBER REINFORCED CEMENTITIOUS COMPOSITES

Tereza SAJDLOVÁ[1], **Petr KABELE**[2]

***Abstract**: Functionally graded members combining high-strength UHPFRC with steel fibres and high-ductility SHCC with PVA fibres are the subject of presented numerical analysis. The UHPFRC material is used to provide sufficient load carrying capacity while SHCC material is applied as a durable and corrosion-resistant surface layer. Simulated experiments include three point bending test of a beam. Nonlinear material model is applied to simulate its mechanical behaviour. The material properties are determined and implemented into the model. The results show advantages of layered UHPFRC-SHCC elements and serve as an impulse for further testing and development of the technology of layered elements.*

***Keywords**: fibre reinforced composites, functionally graded members, finite element method, nonlinear material model, traction-separation law*

INTRODUCTION

Functionally Graded Materials (FGM) consist of two or more layers of material with variable composition and microstructure. FGM utilizing fibre reinforced cementitious composites (FGFRCC) are the object of this study. Development of FGFRCC can be divided into two main directions. In the first one the cementitious matrix and the fibre material are the same in each layer. The composition of layers differs only in fibre volume fraction. The purpose of the first layered system is to use fibres as efficiently as possible and thereby reduce the amount of fibres in the structural element and its cost while maintain the load bearing capacity. Ultra High Performance Fibre Reinforced Concretes (UHPFRC) [1] are used for this application. They are typical by high compressive and tensile strengths (exceeding 150 and 7 MPa, respectively), high Young's modulus of elasticity (50 GPa) and very dense matrix with high binder content. Short steel fibres are added to the composite mainly to reduce its brittleness after cracking and also to increase tensile strength.

The second group of FGFRCC combines materials with the different fibres, specifically steel fibres in UHPFRC which was described previously and polyvinylalcohol (PVA) fibres in the material called

[1]Ing. Tereza Sajdlová, Department of Mechanics, Faculty of Civil Engineering, Czech Technical University in Prague, tereza.sajdlova@fsv.cvut.cz

[2]Prof. Ing. Petr Kabele, Ph.D., Department of Mechanics, Faculty of Civil Engineering, Czech Technical University in Prague, tereza.sajdlova@fsv.cvut.cz

Strain Hardening Fibre Reinforced Cementitious Composite (SHCC) [2]. In contrast to UHPFRC, composition of SHCC materials is not optimized to achieve high strength, but the aim is to obtain a material which is able to sustain high tensile macroscopic deformations (typically in units of percent). This is achieved by addition of short polymeric fibres to a relatively weak matrix, following a systematic micromechanics-based material design [3]. The tensile deformation capacity is then attributed to formation of a large number of very fine cracks, with widths not exceeding order of 10^{-1} mm. This multiple cracking process is associated with overall strain hardening behaviour. SHCC are characterized by a low Young's modulus of elasticity (15-20 GPa) and medium tensile and compressive material strength (4-5 MPa, respectively 40 MPa).

The idea of the second layered system is to utilize the respective materials' superior properties while reducing the effects of their drawbacks. The UHPFRC material with steel fibres is used to provide sufficient load carrying capacity without the need of conventional reinforcement, while SHCC material with polymeric fibres is applied as a durable and corrosion-resistant surface layer. SHCC surface layer prevents unwanted staining of architectural elements and protruding of steel fibres from surfaces, which may get in contact with human skin. The envisioned products involve lightweight facade panels, architectural elements, street furniture, lost formwork etc.

Numerical modelling using finite element method can simplify the design of material (strength of concrete matrix, fibres volume, etc.) and structural members (layers composition). It is therefore necessary to develop new material models (or modify existing models) that describe the behaviour of FRCC (strain hardening, multiple cracking) and the properties of the interface between the layers.

In this paper we present results of preliminary FGFRCC finite element analyses. We focus on the determination of material model for fibre reinforced concrete. Then the determined model is utilized for numerical analyses of layered UHPFRC-SHCC structural element. The goal is to explore the efficiency of SHCC to keep tight width of surface cracks and possibility of delamination of the SHCC layer from the UHPFRC substrate.

NUMERICAL MODEL

As our goal includes analysis of crack width evolution, the fibre reinforced materials are modelled using the individual-crack-based approach [4], where, even in the multiple-cracking state, each crack is represented on the finite element level and its response is characterized by the traction-separation relationship. To this end, the crack band model is employed and the band width is related to the element size. This implies that the minimum crack to crack spacing that the model can capture corresponds to the element size. In simulations of layered elements, regular meshes of 4-node quadrilateral elements with size of 5 mm are used. In layered systems we assume a perfect bond at the materials interface, but the interfacial stresses are monitored. As data, which would allow us to credibly calibrate the interface failure condition, are not available, when discussing the possibility

of delamination, we compare the interfacial stresses with the cracking strength of the weaker material (SHCC).The calculations are carried out with the finite element program Atena v. 5.0.3 [5].

MATERIALS AND MATERIAL CHARACTERISTICS

The UHPFRC considered in the present study was developed at the Klokner Institute of CTU in Prague [6] and it corresponds to the class C110/130. A fine-grained concrete matrix is reinforced with steel fibres BASF Masterfiber® 482 in the volume fraction 1.5 %. The fibres are 13 mm long and their diameter is 0.2 mm. Experimental verification of cylinder compressive strength after 28 days is 125 MPa, Young's modulus is 45 GPa.

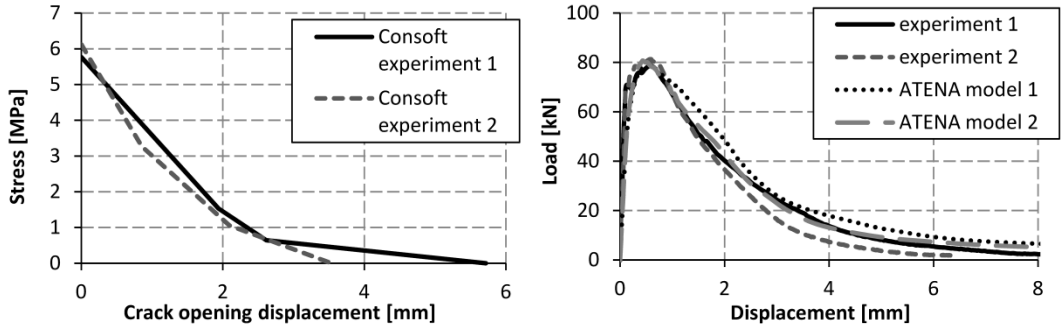

Fig. 1: CONSOFT results: traction-separation relation of UHPFRC (a), comparison of experimental results and numerical simulations of four-point bending tests (b)

The UHPFRC traction-separation relation is determined by inverse analysis of results of four-point bending tests with evolutionary algorithms-based program CONSOFT [7] developed by prof. Dr.-Ing. Volker Slowik. Before the start of CONSOFT analysis it is necessary to specify the initial function parameters and their limits. The experiment is then numerically simulated and initial parameters are modified during an iterative process to achieve the best possible accordance between experimental results and numerical model. Trilinear shape of softening curve is selected.

The best results of inverse analysis are shown in Fig. 1(a). Softening curves are implemented into material model 3DNLC2 Cementitious User in the ATENA software and the model is validated by the numerical simulations of four-point bending tests. The results of numerical simulations in Fig. 1(b) are in a perfect accordance with the experimental results.

The second material considered in the simulations is high-ductility SHCC reinforced by 2% by volume of high-strength polyvinylalcohol (PVA) fibres, 8 mm long and 0.04 mm in diameter. Experimental results were not available for this material thus its material characteristics have been adopted from the literature [8] and they are listed in Tab. 1 together with UHPFRC parameters. The traction-separation relation, estimated on the basis of experimental results reported by Larusson et al. [8], is shown in Fig. 2 (a).

Tab.1: Material parameters of UHPFRC and SHCC used in calculations

Material	Young modulus [GPa]	Compressive strength [MPa]	First crack strength [MPa]
UHPFRC	45	125	5.77
SHCC	18	60	3.5

NUMERICAL EXPERIMENTS: THREE-POINT BENDING TESTS ON BEAMS

Three-point bending tests on small beam specimens are simulated. The analyzed series includes a plain UHPFRC beam (100×100×400 mm, span 300 mm) and two cases, when a layer of SHCC (10 and 20 mm) is added to the bottom of the beam. The minimum thickness of the SHCC layer, 10 mm, is selected considering limitations of the production technology, which consists in sequential casting of the materials.

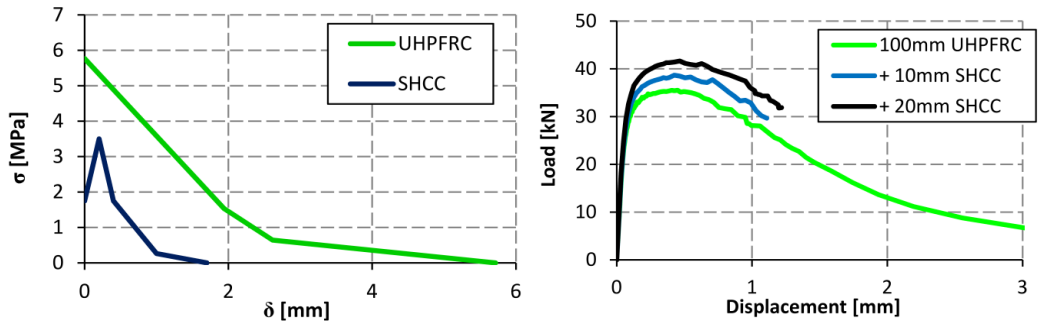

Fig. 2: Traction-separation relations of UHPFRC and SHCC materials used in calculations (a), calculated load-displacement curves of the plain and layered UHPFRC-SHCC beams (b)

Fig. 2 (b) shows that the load capacity of the beam increases by the addition of SHCC layer, but the load-point displacement at the peak remains almost the same. Fig. 3displays the distributions of crack width along the bottom surface of the beams at the peak loads. It is obvious that in the plain UHPFRC beam the crack opening displacement is more localized toward the centre of the beam. With both 10 and 20 mm layer of SHCC, the maximum crack width is reduced to about 50%. With the thinner layer, however, the average crack width is lower than with the thicker one, which is a consequence of the smaller height of the cross section in the former case. In all cases, however, the crack width does not exceed 150 μm, suggesting that a good resistance against potential penetration of water would be maintained until the ultimate failure state. In Fig. 4we show the distribution of stresses at the two materials interface. It is obvious that, even though some tensile stress and increased shear stress occur at the sides of the cracked region near the beam centre, the stresses do not exceed 50% of the cracking strength of the weaker material (SHCC), which means that delamination will not occur. It is noteworthy that actually much higher shear stress arises above the side supports. However, as the normal stress at the same location is a relatively high compression, it is unlikely that delamination would take place.

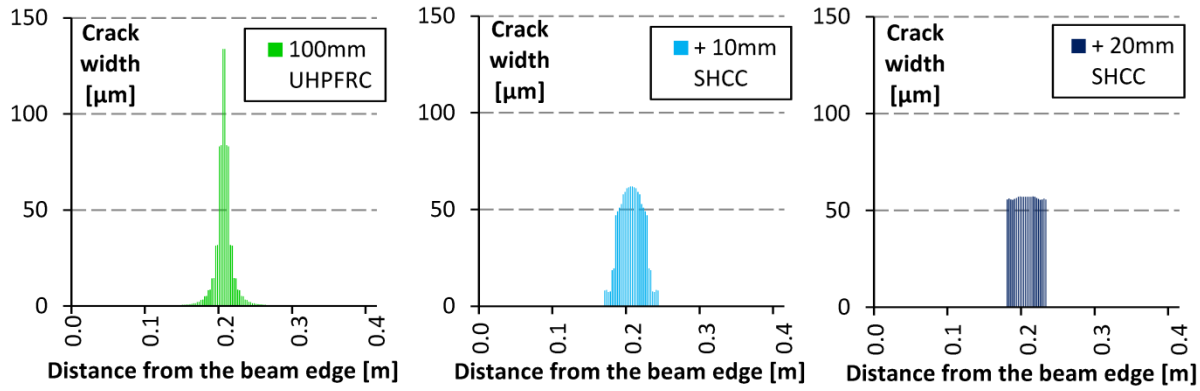

Fig. 3: Calculated distributions of crack width at the bottom surfaces of the beams at therespective peak loads

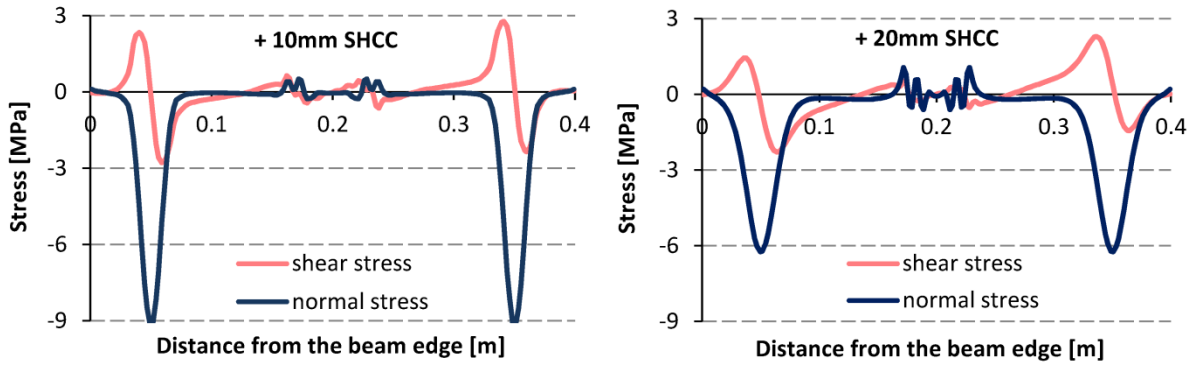

Fig. 4: Calculated distribution of normal and shear stresses at the interface between SHCC and UHPFRC layer of the beam

CONCLUSIONS

Finite element analyses of layered UHPFRC-SHCC structural elements have been performed in order to check their performance under bending moment. The appropriate material parameters of UHPFRC were determined by inverse analysis of experiments. SHCC material characteristics have been adopted from the literature. It has been proved that using of SHCC as a durable and corrosion-resistant surface layer is a prospective option. The numerical models did not show any potential mechanical and fracture problems.

The three-point bending test on small beam specimen was simulated and load-displacement curves, crack widths and interface stresses between UHPFRC and SHCC layer were monitored. Added layer of SHCC increased load capacity and reduced maximum crack width to about 50%. Interface stresses did not exceed cracking strength of material and delamination would not occur. Based on the presented results layered UHPFRC-SHCC structural elements can improve the characteristics of currently used materials.

The next task of the research project will be manufacturing of layered elements that will show potential technological problems and subsequent experimental testing to confirm the numerical models.

ACKNOWLEDGEMENT

The financial support of this experiment by the Faculty of Civil Engineering, Czech Technical University in Prague (SGS project No.SGS14/029/OHK1/1T/11) is gratefully acknowledged.

REFERENCES

[1] RESPLENDINO, J. and TOULEMONDE, F. *Designing and Building with UHPFRC*. John Wiley & Sons, 2013. ISBN 978-1-118-58755-3.

[2] KANDA, T., ROKUGO, K., KANAKUBO, T., KABELE, P., FUKUYAMA, H., UCHIDA, Y., SUWADA, H. and SLOWIK, V. *Strain Hardening Cement Composites: Structural Design and Performance. State-of-the-Art Report of the RILEM Technical Committee 208-HFC*. SC3, vol. 6. Springer Netherlands, 2013. ISBN 978-94-007-4836-1.

[3] LI, V. C. From micromechanics to structural engineering - the design of cementitious composites for civil engineering applications. In: *Structural Engineering/Earthquake Engineering (Proc. of Jsce)*. 1993, 10(2), pp. 37–48.

[4] KABELE, P. Finite element fracture analysis of reinforced SHCC members. In: *Advances in Cement-Based Materials*. Stellenbosch, South Africa, 2009, pp. 237–244. ISBN 978-0-415-87637-7

[5] ČERVENKA, V., JENDELE, L. AND ČERVENKA, J. ATENA Program Documentation Part 1: Theory. Cervenka Consulting, 2013.

[6] KOLÍSKO, J., TICHÝ, J., KALNÝ, M., HUŇKA, P., HÁJEK, P. AND TREFIL, V. Development of ultra high performance concrete (UHPC) on the basis of raw materials available in the Czech Republic. In: *Betonové konstrukce 21. století – Betony s přidanou hodnotou*, vol. 2012. ISSN 1213-3116.

[7] SLOWIK, V., VILLMANN, B., BRETSCHNEIDER, N. and VILLMANN, T. Computational aspects of inverse analyses for determining softening curves of concrete. In: *Computer Methods in Applied Mechanics and Engineering*. 2006, 195(52), pp. 7223–7236. ISSN 0045-7825.

[8] LÁRUSSON, L., FISCHER, G. and JÖNSSON, J. Mechanical interaction between concrete and structural reinforcement in the tension stiffening process. In: *High Performance Fiber Reinforced Cement Composites 6*, Springer, 2011. ISBN 978-94-007-2436-5.

STOCHASTIC WANG TILES GENERATION USING DEM AND YADE SOFTWARE

Jan STRÁNSKÝ[1]

Abstract: *An algorithm for generation of 2D stochastic Wang tiles is presented in this contribution. The algorithm is based on the discrete element method (DEM) and is therefore applicable for matrix-based structures with separate inclusions. Moreover, the approach is designed for dense packings. Periodic contact detection plays an essential role in the algorithm. An open source free DEM code YADE was used for all the computations. One exemplary realization of the generation process together with an illustration of actual tiling is presented at the end of the paper.*

Keywords: *Wang tiling, Discrete element method, Dense packing, Periodic contact detection.*

INTRODUCTION

For microstructure reconstruction, periodic unit cell (PUC) concept is nowadays a standard approach. It assumes that the periodic cell is grater than representative volume element (RVE) of the material, reflecting more or less the heterogeneity of underlying material level. The existing periodic cell can be copied in space (tiled) to create sufficiently large domain for analysis (numerical simulations for instance). The resulting domain is of course periodic, which is sometimes not desirable.

Wang tiling [1] can be understood as an extension of aforementioned PUC approach. Instead of having only one periodic cell, a set of Wang tiles is used instead. The number of tiles in the set is relatively small. For the stochastic case the minimum number is 8 for 2D and 16 for 3D space. The tiles are not independent, but have compatible boundaries. Each tile edge has its edge code. In the case of stochastic tiling, during the tiling process it is possible for at least two different tiles to be placed, of course respecting already placed tiles. Which one is placed, it is chosen randomly. See figure 1.

For boundaries compatibility, two possible approaches are possible, either the neighboring tiles have no common inclusions (figure 2 left) or have common boundary (figure 2 right). The latter approach is used in this contribution.

Using Wang tiling, the final reconstruction is not periodic.

[1] Ing. Jan Stránský, Department of Mechanics, Faculty of Civil Engineering, Czech Technical University in Prague, jan.stransky@fsv.cvut.cz

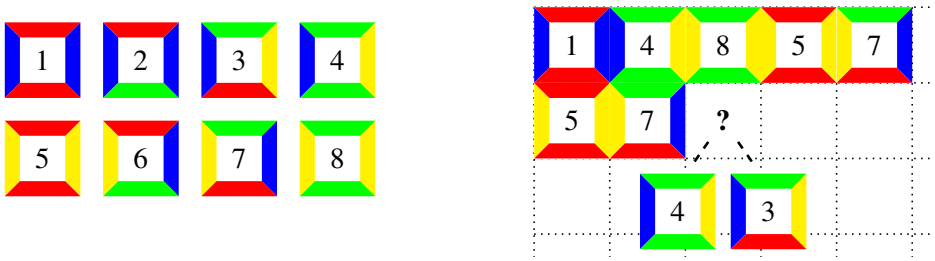

Fig. 1 Illustration of a Wang tile set and stochastic tiling

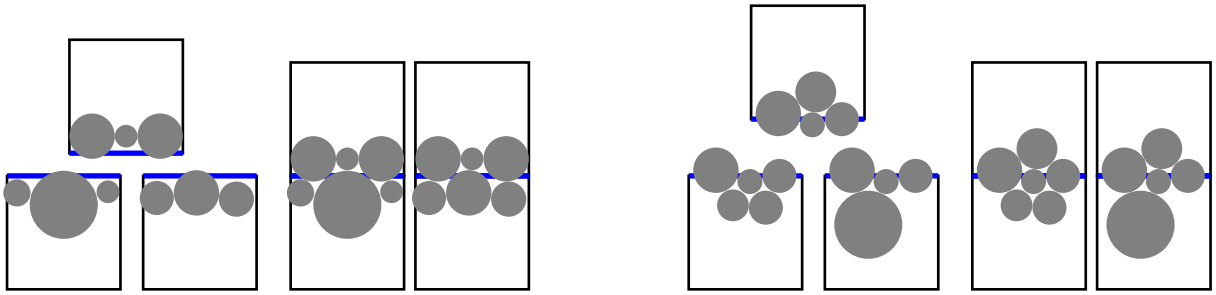

Fig. 2 Two possible approaches for compatible boundaries

The basic theory of DEM is introduced in section 2. The algorithm for Wang tiles generation using DEM is described in section 3 and illustrated on an example in section 4.

For the sake of clarity, most of the figures uses colors. If you have the grayscale version, please consider to read the color version.

DISCRETE ELEMENT METHOD AND PERIODIC CONTACT DETECTION

The discrete element method (DEM) is widely used numerical tool of solid mechanics. It represents material as a set of perfectly rigid particles interacting with each other. DEM solves numerically equations of motion of individual particles. Forces, occurring in the equations of motion, can be of prescribed nature (e.g. gravity or imposed boundary conditions) or are the result of interparticle interactions.

In its basic version it is naturally applicable for modeling of granular materials (as in its very first application [2]). Using different particle shapes and different contact laws, DEM can take large amount of various forms, see [3] for more information.

In this contribution, one of the most simplest variants will be used. Particles have spherical (or circular in 2D) shape. If two particles does not overlap, there is no interaction force between them. If they do overlap, the repulsive normal force is proportional to the overlap depth and the shear force is incrementally computed according to particles' mutual rotation and sliding and its value is bounded by a plastic limit. Simplifiedly, two overlapping sphere can be represented as a two spring model, see fig. 3 or [3].

$$F_N = k_N u_N, \qquad \Delta F_T = k_T \Delta u_T \tag{1}$$

YADE [3] is an open source software for DEM analysis. Its core is written in C++ (providing efficient

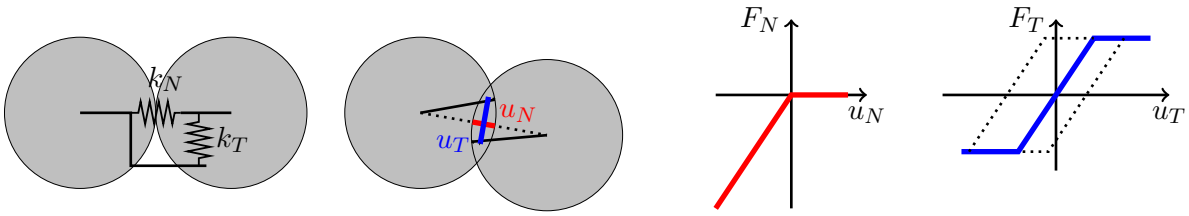

Fig. 3 Illustration of used contact law

execution of time consuming routines), user interface written in Python (modern dynamic object oriented scripting language, providing easy to use scripting while preserving the C++ efficiency) and extensible object oriented architecture allowing independent implementation of new features - new material model or new particle shapes for instance.

In the basic form, particles interact only with particles in their actual surrounding. Using periodic contact detection, particles interact also with *periodic images* of particles. Figure 4 shows a periodic cell, where red particles interact with red particles (standard solution), but also with gray particles, i.e. periodic images of other red particles.

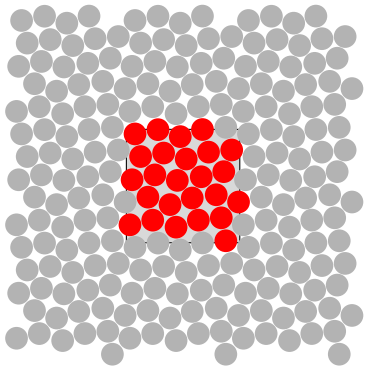

Fig. 4 Example of a periodic cell

ALGORITHM

The method presented in this contribution is summarized in algorithm 1.

Alg. 1 Overall algorithm

1: prepare independent periodic tiles ▷ figure 8
2: set proper boundary conditions ▷ figure 9
3: let the model relax ▷ figure 10
4: **while** the set does not fulfill our requirements **do**
5: improve individual tiles
6: let the model relax
7: **end while** ▷ figure 11

Each of its substeps is described in detail in following subsections.

Relaxation

Relaxation is a phase of simulation occurring in different places. If there is at least one overlap of particles, standard DEM simulation is run, moving overlapping particles from each other. Numerical damping is used to remove kinetic energy from the system. Every defined number of iterations, the overlap check is performed. If no overlap is present or the simulation is sufficiently close to static equilibrium, the simulation is calmed and stopped.

Independent periodic tiles

As a first step, an independent periodic cell is created for each tile in the set. To the periodic cell, one particle is placed randomly and the model is relaxed. Particles are placed one by one until there is no more space in the cell for them (after relaxation, in quasistatic equilibrium, some particles overlap).

Alg. 2 Generation of a periodic cell

```
1: while no overlap of particles exists do
2:     save state                                   ▷ state with no overlap
3:     insert randomly one particle
4:     let the model relax
5: end while          ▷ at the end of while loop, an overlap of particles exists
6: load last saved state                            ▷ where no overlap exists
```

Such periodic cell is created for each tile in the set. All periodic cells have the same fixed dimensions. See figure 8 for exemplary illustration.

"Wangization"

In the next step, particles will be put into virtual groups. One particle can be in several groups at once. Two particles would interact iff they are together in at least one group. Otherwise (there is no common group for the two particles), the would not interact even if they would overlap.

YADE implementation is such that each particle posses a bitmask variable called group mask. Each bit of the mask represents one group. Value 1 means that the particle belongs to the group, 0 means it does not. The common group test is done by logical and of masks of both particles (If there is at least one common bit, the particles can interact).

In the first step of "Wangization", particles of each periodic cell are put into corner groups. The bitmask representation is shown in figure 5. Each tile has its own four groups. This allows us to use for all tiles only one periodic cell. Particles would interact with particles only from their tile ignoring all others. Furthermore, the corner groups as shown in figure 5 breaks the periodic contact detection. Particles from lower left corner (bitmask 0001) interacts with all their physical neighbors, but not any more with the periodic image of lower right corner (bitmask 0010). So each tile is periodic geometrically (positions of particles does not change, only their group masks), but not from interactions' point of view.

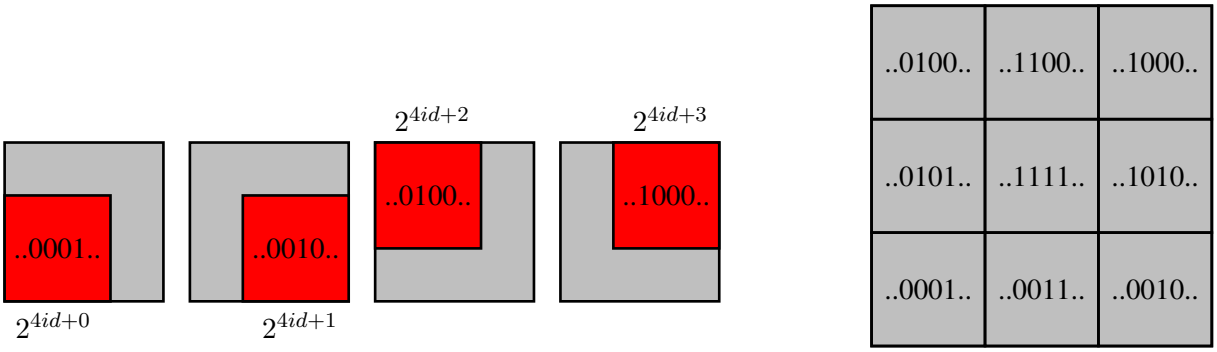

Fig. 5 Assignment of particles into corner groups

To summarize this stage, all particles are placed inside one periodic cell. Particles are allowed to interact only with particles from the same tile and, despite the fact with periodic cell, not periodically.

In the next step, particles close to negative boundaries (left and bottom) are called boundary particles. In each tile, boundary particles are chosen according to the same rule, e.g. position of the center of particle. Recall that each tile edge has an edge code. For each edge code, boundary particles from one tile are called masters, while boundary particles from all other tiles belonging to this edge code are deleted. The group mask of deleted particles is assigned to master particles, so master particles virtually take over the place of deleted particles and appears in several tiles at once. See figure 6 for illustration.

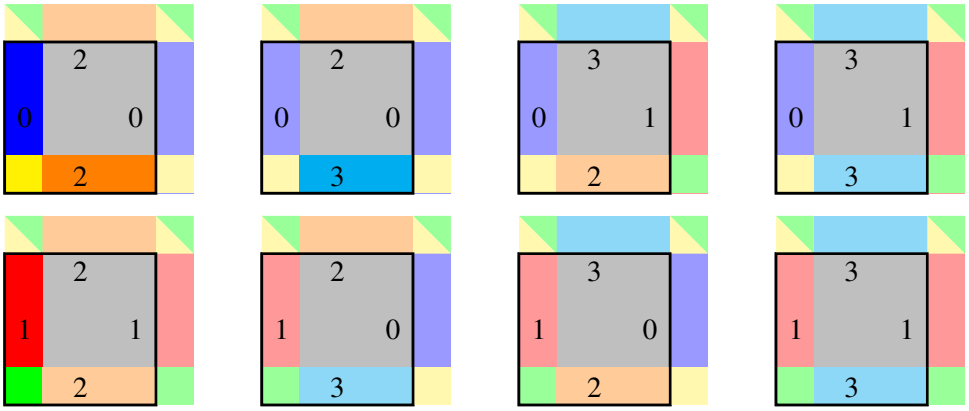

Fig. 6 Illustration of masters in "Wangization" process

In masters determination, x direction takes precedence. Bottom corners are naturally treated by the method, but the final tiling might be such that in the upper corners more than one combination is possible. For this purpose, extra particle groups are created for respective particles (master lower left corner particles and ordinary particles placed in the top right corner).

After this step, the model is relaxed. If the simulation reaches (quasi)static equilibrium while still having overlaps, one of the overlapping particles, preferably a non-boundary one, is deleted and the model is relaxed again.

The "Wangization" approach is summarized in algorithm 3 and is illustrated in figures 9 (before

relaxation) and 10 (after relaxation).

Alg. 3 "Wangization"

put particles into corner groups ▷ breaking periodicity
choose boundary particles
set boundary particles as masters or delete them
put boundary particles to respective other groups
create extra groups for corner particles
let the model relax
while no overlap of particles exists **do**
    delete an overlapping particle
    let the model relax
end while

A posteriori improvements

As the boundary layers interacts with several ordinary particles, artifitial gaps may ocure. In such case, it is possible to input one (or more) particles to the specific tile and again let the model relax.

Currently, improvements based on mere visual check was performed. An automatic check based on statistical descriptors should be used in future.

See figure 11 for exemplary illustration.

EXAMPLE

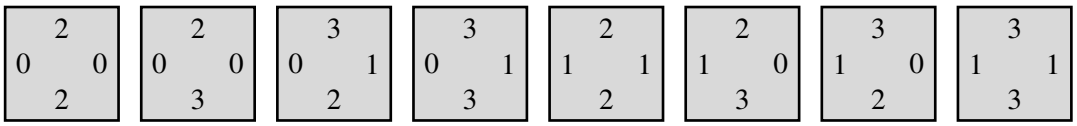

Fig. 7 Testing tile set

Decribed algorithm is illustrated on a testing tile set, see figure 7. The tiles are square and contain monodisperse circular inclusions with radius $10\times$ smaller than the tile size. Final stage of each of the algorithm substeps are visualised. Figure 8 shows 8 independent periodic tiles, figure 9 their "Wangization" and relaxed state is shown in figure 10. One particle is manually included into the 7th tile as an Illustration of a posteriori improvements, see figure 11. An example of actual tiling is illustrated in figure 12.

Thw whole generation process took 15 s on Asus K55A notebook with 2.30 GHz Intel Pentium CPU.

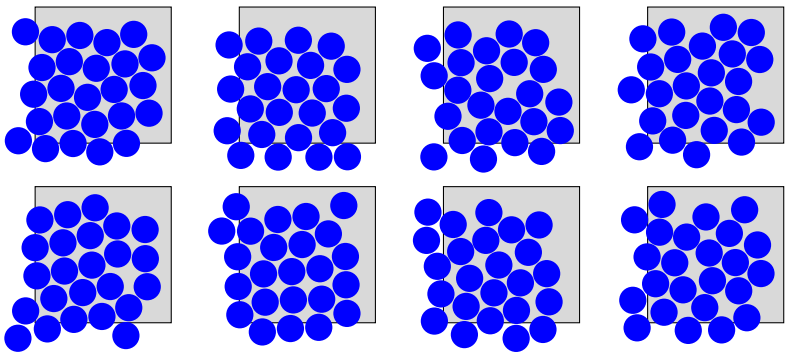

Fig. 8 8 independent periodic tiles

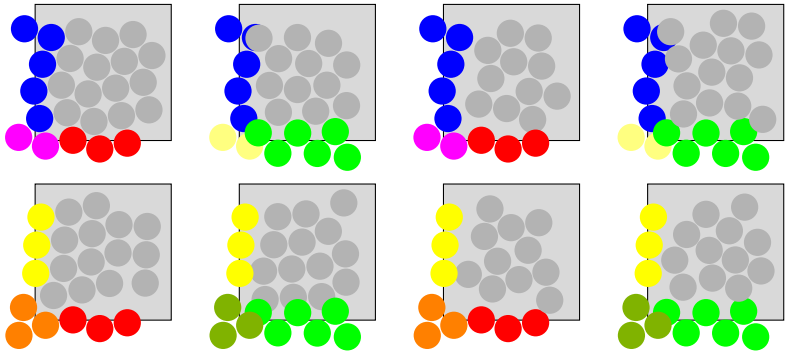

Fig. 9 Tiles after "Wangization"

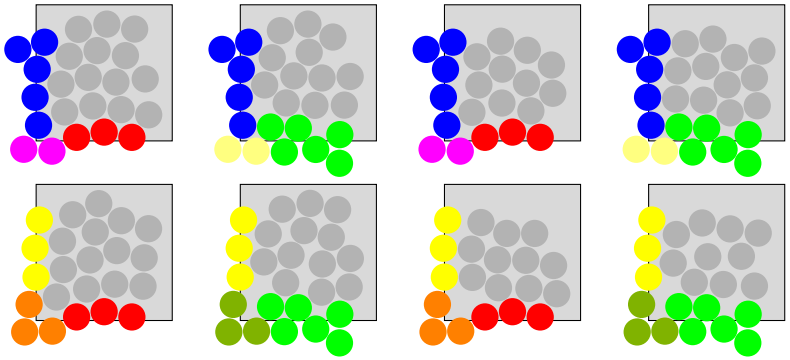

Fig. 10 Tiles after relaxation

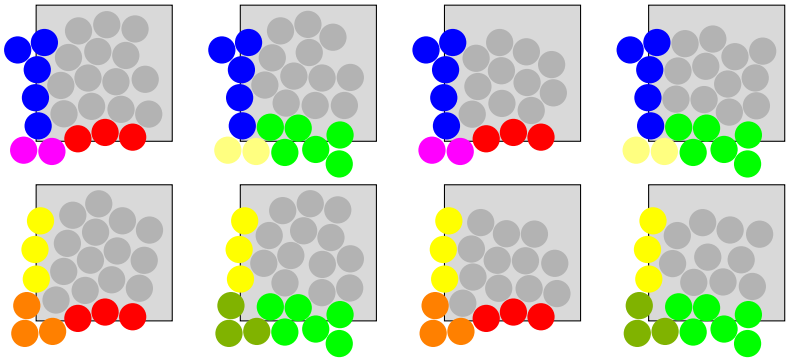

Fig. 11 Tiles after a posteriori improvements

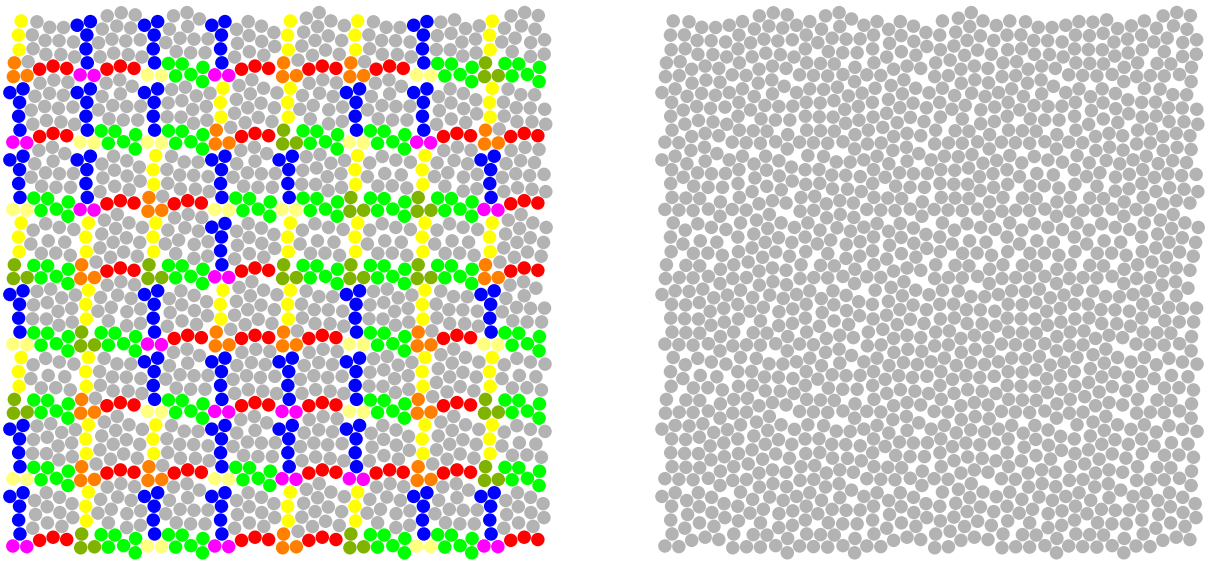

Fig. 12 Example of actual tiling – color and monochrome version

CONCLUSION

The presented algorithm was successfully applied for generation of stochastic Wang tiles with 2D monodisperse circular inclusions. Visually the resulting tiling does not have any significant defects, although a rigorous analysis is neccessary. The computational costs are in the author's opinion acceptable, but (again) a serious comparisons with other approaches should be done.

The algorithm is directly extensible to 3D as well as for polydisperse inclusion. Future work will therefore address those extensions together with statistical analysis of resulting tiling, possibly also with optimization of the generation process. Especially the a posteriori improvements should be automated.

ACKNOWLEDGEMENT

The financial support of this research by the Czech Technical University in Prague (SGS project No. 14/029/OHK1/1T/11) is gratefully acknowledged.

REFERENCES

[1] DOŠKÁŘ, M. *Wang tilings for real world material systems.* Prague, 2013. Diploma Thesis. Czech Technical University in Prague. Faculty of Civil Engineering.

[2] CUNDALL, P. A. and STRACK, O. D. L. A discrete numerical model for granular assemblies. *Géotechnique.* 1979, **29**(1), 47–65. ISSN 0016–8505.

[3] ŠMILAUER, V., CATALANO, E., CHAREYRE, B., DOROFEENKO, S., DURIEZ, J., GLADKY, A., KOZICKI, J., MODENESE, C., SCHOLTÈS, L., SIBILLE, L., STRÁNSKÝ, J., and THOENI, K. *Yade Documentation (V. Šmilauer, ed.). 1st ed.* [online]. The Yade Project, 2010 [cited 2014-06-30]. Available from: http://yade-dem.org/doc/.

OSCILLATION OF STRUCTURE EXCITED BY SIMPLE KINEMATIC PEDESTRIAN MODEL

Vladimír Šána[1], **Michal Polák**[2]

***Abstract**: The submitted paper deals with a vibration of a simply supported beam, which is loaded by walking kinematic pedestrian. In this paper pedestrian was modeled by the Rimless wheel model and the obtained results were compared with the DLF (Dynamic Loading Factor) model according to the Bachmann, which provides the best accordance with experimentally obtained results.*

***Keywords**: footbridge vibration; Rimless wheel model; human-induced vibration*

INTRODUCTION

The Rimless wheel model, shown at Fig. 1, was firstly introduced by *Margaria* in 1976 see [1]. This model is based on the motion of the inverted pendulum. The Margaria's model was simplified for the purposes of the dynamic excitation of a structure, presented in this paper.

Human walking process could be divided into two main parts, stance and swing phase. Stance phase is the moment when human's leg is in contact with a surface – inverted pendulum behaviour. On the other hand the swing phase can be described by regular pendulum movement.

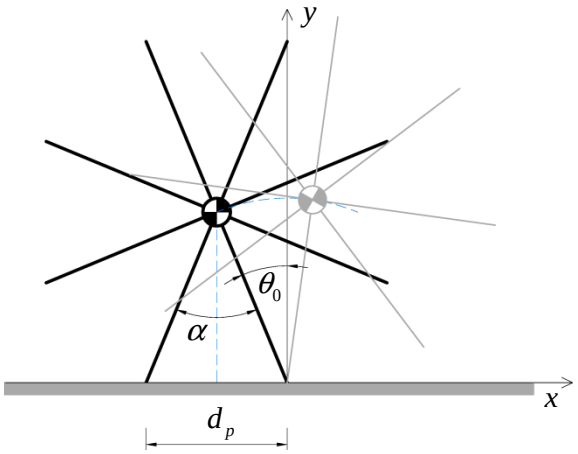

Fig. 1 The Rimless wheel model of kinematic pedestrian

[1] Ing. Vladimír Šána, Department of Mechanics, Czech Technical University in Prague, Faculty of Civil Engineering, vladimir.sana@fsv.cvut.cz

[2] prof. Ing. Michal Polák, CSc., Department of Mechanics, Czech Technical University in Prague, Faculty of Civil Engineering, polak@fsv.cvut.cz

MATHEMATICAL MODELING

Motion of the inverted pendulum is described by the second-order nonlinear differential equation (1) in polar coordinates, which could be linearized with using the Taylor – Mc Laurin's series. It means that $\sin\theta(t) \approx \theta(t)$ if the angle $\theta(t)$ is small enough. This assumption is fulfilled for the angles to $\theta(t) \approx \pi/4$ rad. Initial conditions, $\theta(t)\big|_{t=0}$ and $\dot{\theta}(t)\big|_{t=0}$ will be mentioned further in the paper.

$$\ddot{\theta}(t) - g/L_p \sin\theta(t) = 0 \tag{1}$$

$\theta(t)$ is the polar angle, measured from initial stance leg to terminal stance, g is the gravitational acceleration and L_p is distance between the surface and human's body COM (center of mass). Note that whole mass of pedestrian was concentrated into COM and mass of pedestrian's "leg" (pendulum hinge) was neglected.

The structure, which has been loaded by this model, is the footbridge across the Opatovska street, see [2], [3] and [4]. It is slab-on-girder structure, which acts as a simply supported beam. The values of variables, necessary for numerical solution, are summarized in the Numerical solution chapter.

Discretized structure is described by the system of second-order differential equations (2) in matrix notation. Vertical components from nodal deflection vector $\{\mathbf{r}\}$ have been considered only.

$$[\mathbf{M}]\{\ddot{\mathbf{w}}\} + [\mathbf{C}]\{\dot{\mathbf{w}}\} + [\mathbf{K}]\{\mathbf{w}\} = \{\mathbf{F}\} \tag{2}$$

$[\mathbf{M}]$ is the mass matrix, $[\mathbf{C}]$ is the damping matrix and $[\mathbf{K}]$ is the stiffness matrix, $\{\ddot{\mathbf{w}}\}\{\dot{\mathbf{w}}\}\{\mathbf{w}\}$ are vectors of nodal acceleration, velocity and deflection, $\{\mathbf{F}\}$ is loading vector.

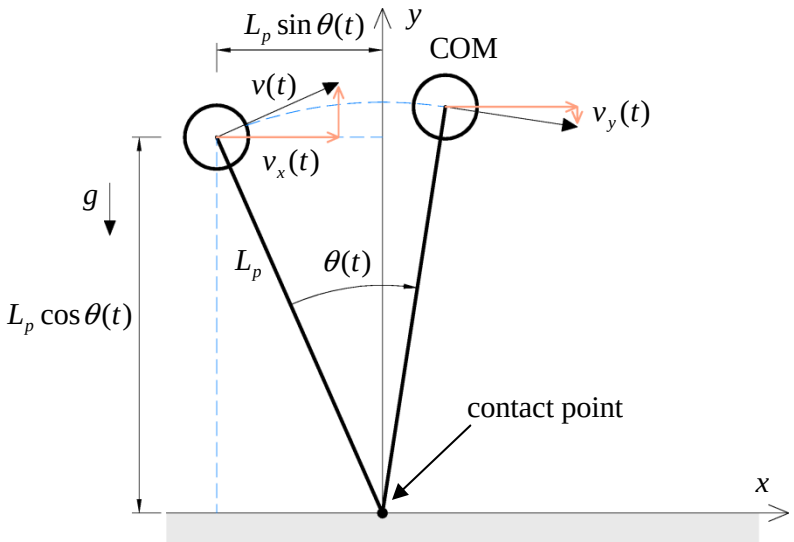

Fig. 2 The mathematical inverted pendulum

As a consequence of the discretization, mentioned before, the mass matrix $[\mathbf{M}]$ is diagonal. Damping of the structure was considered as viscous with respect the Rayleigh's model, and therefore the equation (2) can transferred into N independent differential equations by using modal decomposition method.

The direct interaction between the Rimless wheel and structure was not cogitated in this paper. The right-sided loading vector $\{\mathbf{F}\}$ was assembled with respect phases of walking process.

Firstly the initial contact occurred, where the force impulse acted for a very short time $\tau_{prim.}$, and therefore the contact force exceeds a force, which is equal to static weight. Contact between human's leg and the structure occurs when $\theta(t) = \alpha$, where α is the angle between two "legs" see Fig. 1. If the contact angle is defined, we are able to determine time of contact $T_{cont.}$, which depends on the velocity of motion. The angular velocity $\dot{\theta}(t)$ in time $T_{cont.}$ is also known from the numerical solution of equation (1). The angular velocity is transferred to the circumferential velocity by relation $v(t) = \dot{\theta}(t) L_p$, where L_p is the distance between human's COM and the contact point, see Fig. 2. In according to these assumptions the initial contact force is defined as

$$F_{cont.} = \frac{m_p v(T_{cont.})}{\tau_{prim.}} \tag{3}$$

where m_p is the pedestrian's body mass, $v(T_{cont.})$ is the circumferential velocity in time of contact $T_{cont.}$ and τ_{prim} is the acting force term.

Next phase describes the transmission of the body weight – inverted pendulum behaviour, where the vertical component of the contact force could be expressed by Newton's second law of motion $F_{pend.} = m_p \ddot{y}(t)$, m_p is pedestrian's body mass and $\ddot{y}(t)$ is the acceleration in vertical direction. This acceleration can be derived from the polar coordinates with using the transformation relation between Cartesian and Polar coordinates system as $y(t) = L_p \cos\theta(t)$. If the appropriate time derivatives are executed, the force is expressed by equation

$$F_{pend.} = -m_p L_p \left[\ddot{\theta}(t) \sin\theta(t) + \dot{\theta}^2(t) \cos\theta(t) \right] \tag{4}$$

The point of action of the forces $F_{cont.}$ and $F_{pend.}$ is located out of the nodes of the finite element mesh in specific time $t = T$, therefore these forces are transformed to the nodes by relations

$$F^i = \hat{F}\frac{b}{L_e}\left[1-\frac{a(a-b)}{L_e^2}\right] \tag{5}$$

$$F^j = \hat{F}\frac{a}{L_e}\left[1-\frac{b(b-a)}{L_e^2}\right] \tag{6}$$

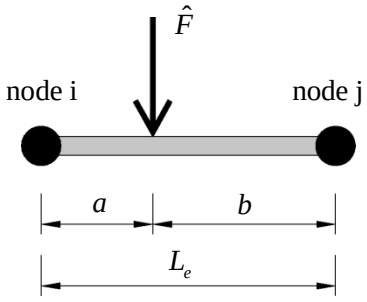

Fig. 3 Nodal forces expression

The effects of human-induced vibration were also described by the DLF model of pedestrian, which is stated by relation

$$F(t) = m_p g\left(1+\sum_{n=1}^{k}\alpha_n \sin\left(n2\pi f_p t\right)\right) \tag{7}$$

where m_p is pedestrian's body mass, g is gravitational acceleration, α_n is appropriate Dynamic Loading Factor and f_p is the pacing frequency. Bachmann's loading model, which provides best accordance with experimentally obtained data see [2], was used in the study presented in this paper.

NUMERICAL SOLUTION

Solution of linearized equations (1) and (2) was done by the Newmark's β integration method. The initial conditions for equation (1) were defined as

$$\theta_0 = \arcsin\frac{d_p}{2L_p} \wedge \dot{\theta}_0 = \frac{v_x}{L_p\cos\theta_0} \tag{8}$$

where d_p is the length of the pedestrian's step, L_p is distance between human body COM and contact point and v_x is horizontal component of the velocity vector in x direction. Note that the relation between velocity in horizontal direction and pacing frequency could be evaluated as $v_x \approx 0.9 f_p$. This conversion is based on the experimentally observed phenomenological aspects of human walking process. These initial conditions were generated at the beginning of each step, so that the loss of velocity due to impact did not occur.

The investigated structure was considered as inactive, with direct centre-line at the beginning of numerical analysis, therefore the initial vectors of nodal deflection and velocity were taken as

$$\{\mathbf{w}\}\big|_{t=0} = \{0 \quad \cdots \quad 0\}^T \wedge \{\dot{\mathbf{w}}\}\big|_{t=0} = \{0 \quad \cdots \quad 0\}^T \tag{9}$$

Following parameters were used for the numerical solution of equations (1) and (2):

Structure

bending stiffness $EI_y = 3.83\times10^9\ Nm^2$, continuously distributed mass $\mu = 5300\ kgm^{-1}$, logarithmic damping decrement $\vartheta = 0.09$ and length of the span $L = 25.1\ m$.

Pedestrian – Rimless wheel and DLF Bachmann's model

weight $m_p = 80\ kg$, distance between COM and structure's center-line $L_p = 1.1\ m$, horizontal component of velocity vector $v_x = 1.8\ ms^{-1}$. Geometry of the Rimless wheel model determines length of the pedestrian's step d_p and initial angle θ_0. Dynamic loading factors $\alpha_1 = 0.5$, $\alpha_2 = 0.1$ and $\alpha_3 = 0.1$

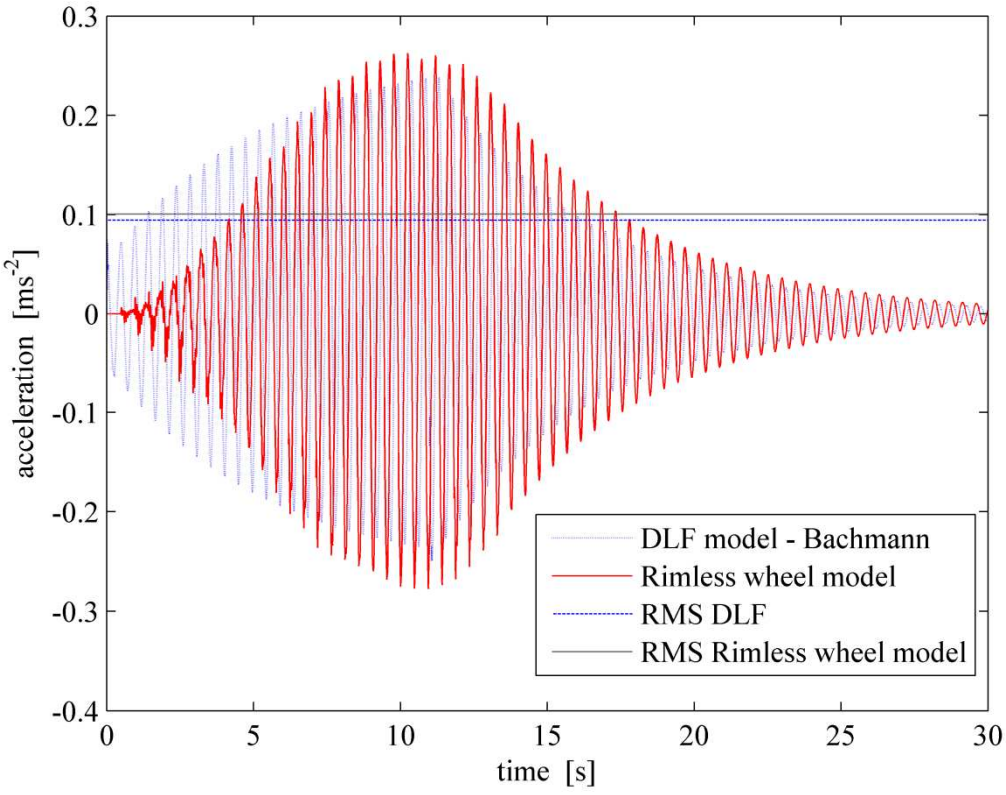

Fig. 4 Comparison of mid-span acceleration obtained from DLF and Rimless wheel loading model

CONCLUSION

The alternative model for description of loading, caused by walking pedestrian, was described in this paper. This kinematic model is based on the movement of the inverted mathematical pendulum and describes kinematic aspects of pedestrian's COM trajectory. The loading forces were expressed by equations (3) and (4), which described initial contact between foot and structure and the transmission of body weight during stance phase. DLF model was used for the comparative calculation of the acceleration response. It was applied in the most efficient spot of the structure – mid-point of the span.

It is obvious from Fig. 4 and from the evaluated RMS values: $a_{RMS,rimless} = 0.1$ $a_{RMS,DLF} = 0.09$ that Rimless wheel model provided sufficient results in comparison with DLF model of pedestrian.

ACKNOWLEDGEMENT

This paper has been created thanks to the project SGS project No. 14/122/OHK1/2T/11 supported by the Czech Technical University in Prague, which is gratefully acknowledged.

REFERENCES

[1] ALEXANDER, R. Simple models of walking and jumping. *Human Movement Science*. 1992, **11**, 3-9. ISSN 0167-9457

[2] ŠÁNA, V. and POLÁK, M. Comparison of current models for excitation of footbridges due to walking pedestrians and vandalism with experiment. In: *EURODYN 2014: the 9th international conference on structural dynamics.* Porto, 2014, pp. 983-990. ISBN: 978-972-752-165-4

[3] ŠÁNA, V. and POLÁK, M. Human-Induced Vertical Vibration of the Footbridge across Opatovicka Street. *Applied Mechanics and Materials*. 2014, in Print.

[4] ŠÁNA, V. and POLÁK, M. Dynamická analýza lávky pro pěší přes ulici Opatovická. I: *the 11th International Conference on New trends in Statics and Dynamics of Building Conference Proceedings.* Bratislava, 2013, pp. 205-208. ISBN 978-80-227-4040-1 (in Czech).

[5] BACHMANN, H. and AMMANN, W. *Vibrations in Structures Induced by Man and Machine*. Zürich, 1987. 165 p. ISBN 3-85748-052-X.

[6] BACHMANN, H., AMMANN, W. et al. *Vibration Problems in Structures: Practical Guideline.* Zürich, 1995. 231 p. ISBN 978-3-0348-9231-5.

[7] BRDIČKA, M., SAMEK L., SOPKO, B. *Mechanika kontinua*. Praha, 2005. 799 p. ISBN 80-200-1344-X (in Czech).

[8] MACUR, M. *Úvod do analytické mechaniky a mechaniky kontinua*. Brno, 2010. 601 p. ISBN 978-80-214-3944-3 (in Czech).

DYNAMIC PACKING ALGORITHM FOR 3D WANG CUBES GENERATION

David ŠEDLBAUER[1]

***Abstract**: This contribution deals with a concept of 3D Wang tiles (cubes) as a tool for the heterogeneous material modelling. A dynamic packing algorithm for the Wang cubes generation is introduced. This algorithm is based on a particle movement, particle growth and dynamical phenomenon such as elastic collisions. Hard particles are represented with spheres of equal radii. A set of 3D Wang cubes include 16 different cubes with specific boundary conditions which allow us to compose material domains using a stochastic tiling algorithm. In the presented work sets of Wang cubes with a higher volume fraction and required final hard particles positions are generated. This approach tests ability for further usage of a proposed algorithm for real microstructures.*

***Keywords**: Material modelling, Wang tiling, packing, dynamic algorithm, heterogeneous materials*

INTRODUCTION

For a heterogeneous material modelling several approaches how to represent a microstructure of such domains can be found. Most of these methods use a concept of the Representative Volume Element (RVE) [1], [2].The RVE can be defined as a small enough sample of a reconstructed medium that enable efficient usage of numerical methods for modelling but also include whole information about material domain. The main task in every definition of the RVE is determination of a size of such sample. In [3] it is shown that the sizes of the RVE need not to be equal for the same material. Therefore a concept of Statistical Volume Elements (SVEs) in [4] was proposed. For this approach effective properties are obtained over the whole set of these small elements.

For creation of the RVE or SVEs the most common approach is usage of the Periodic Unit Cell (PUC) [5]. However, during a reconstruction of heterogeneous media with the utilization of these unit cells unwanted artefacts of periodicity occur from the very nature of these concepts. In contrast to this approach is the concept of Wang tiling. In here an infinite aperiodic or a strictly aperiodic plane (material domain) can be stacked with a small set of tiles, Fig 1. These tiles/cubes can also be considered as the SVEs.

[1] Ing. David Šedlbauer, Department of Mechanics, Faculty of Civil Engineering, CTU in Prague, david.sedlbauer@fsv.cvut.cz

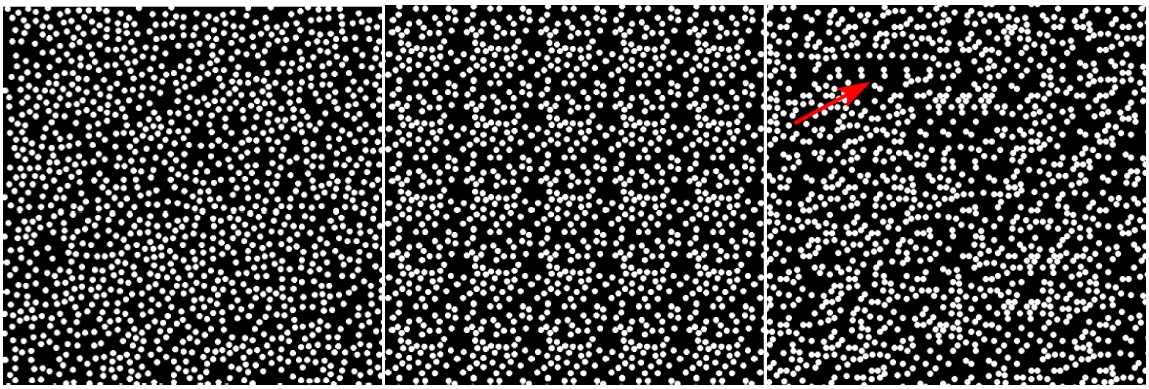

Fig. 1 Reconstructed medium, optimized microstructure using the PUC and Wang tiles [6]

The generation of a set of 3D Wang cubes can be seen as a highly constrained hard packing problem. The distribution of hard particles within a matrix largely determines a considerable amount of material properties, especially the mechanical ones. At the same time the integrity of particles (non-overlapping) need to be preserve. Therefore a dynamic packing algorithm for the 3D Wang cubes generation is proposed and tested for an artificial pseudo-material with a higher volume fraction and predefined placements of hard particles.

The main purpose of a testing is to find out whether is it possible with a proposed algorithm to reach the required particle positions with a fulfilment of stochastic tiling boundary conditions. In the future continuation of the work particles positions of a generated microstructure will be optimized based on the best so far particle positions with respect to a sameness between the reference and the generated medium. The concordance rate will be defined with a microstructure description using statistical descriptors.

WANG TILING IN 3D

Hao Wang in [7] asked whether a set of tetramino tiles (squares with coloured edges as codes) can stack an infinite plane. Originally he concluded that a periodic part of an infinite plate can be stacked with a set of finite number of tiles. Over time, researches find and reduced the tile set enables to pave an infinite plane. Finally, the set presented by Čulík in [8] contains only 13 tiles, Fig 2.

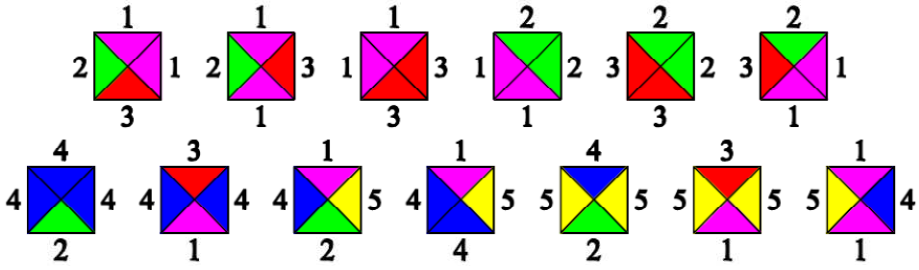

Fig. 2 The set of thirteen tetramino tiles for the tiling of an infinite plane

Nevertheless, in Material Engineering there is no need to have a strictly aperiodic plane. For such fields of interests a Stochastic Wang Tiling that ensures non-periodic but not a strictly aperiodic tiling is sufficient.

Generally the Wang tiling is characterized by a set of tiles where each single tile in 2D is represented as a square with codes (colours, letters etc.) on the edges. As for 3D tiling, the set form cubes with codes on walls. If we consider c_x, c_y, c_z as a number of different codes for walls in *x*, *y*, *z* directions, then the minimal number of cubes within a set is defined with the following formula:

$$N_{3D} = 2 \cdot c_x \cdot c_y \cdot c_z \qquad (1)$$

Equation *1* says that for every combination of codes for *x*, *y* and *z* direction there always must be a possibility to choose a next cube from two possible samples. This prescription is in accordance with the stochastic tiling algorithm introduced by Cohen et al. in [9]. If we consider two different codes for each direction (e.g. 1, 2 for *x;* 3, 4 for *y;* 5, 6 for *z)* minimal set of Wang cubes include sixteen cubes, Fig 3. The tiling algorithm expanded to three dimensions starts with the first cube randomly chosen and placed to the grid of a material domain. This grid represents a volume that will be filled with Wang cubes. The algorithm then adds cubes gradually row by row, column by column within a layer and then layer by layer. In Fig. 3 there is a set of Wang cubes where every cube is designated with a set of numbers that determine codes (left -x, right +x, front –y, back +y, lower –z, upper +z).

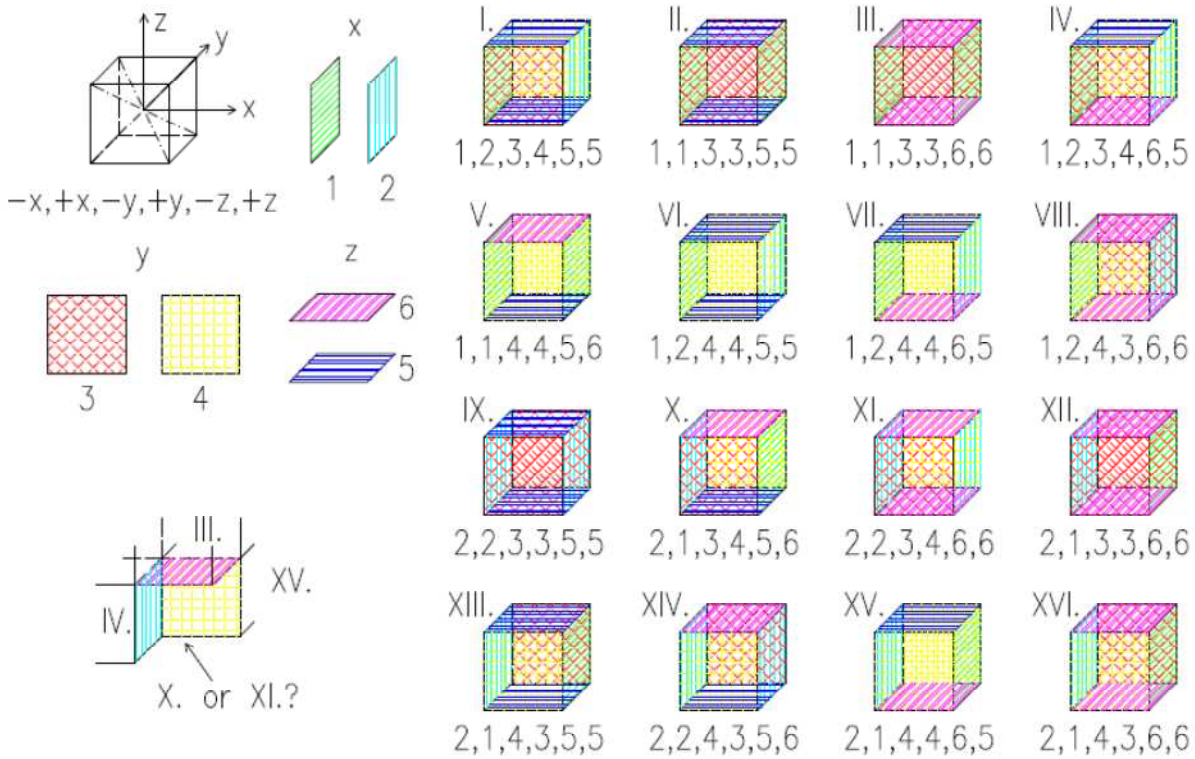

Fig. 3 The principle of the stochastic tiling in 3D, a minimal set of Wang cubes for the stochastic tiling

DYNAMIC PACKING ALGORITHM

The main idea of the proposed algorithm is to let particles grow from the initial zero volumes and allow them to move within their zones that ensure the compatibility of the Wang cubes according to rules of the stochastic tiling till a stopping criterion is achieved.

Considering the nature of practical problems of a heterogeneous material modelling we assumed that we were assigned a volume fraction V_f and geometric parameters (radii) of solid particles r. The cube size should be defined early in the process. Knowledge of the cube size, the required volume fraction and the given sphere radii enable us to determine the total number of spheres within the whole set and every single cube of the set respectively.

After setting of the above mentioned parameters, a number of time steps during which the whole process took place needs to be established. Then a given number of sphere centres are semi-randomly thrown into the matrix. To these centres, initial random velocities are assigned. Over time, the particles move semi-randomly and its radii increase consecutively until the final radii at the last time step are reached. During this motion the dynamic phenomena such as elastic collisions occur.

Boundary conditions

Before the start of the algorithm some boundary conditions that ensure ability of stochastic tiling with final set of Wang cubes need to be established. If a sphere during the motion leaves any of Wang cubes through the wall then this particle have to be copied into other cubes with the same coded wall as is the abandoned one. Unfortunately such copying is unacceptable in the terms of changes in the volume fraction of individual cubes as well as of the whole set. Therefore each single cube is divided into six marginal (border) volume parts corresponding to the walls of a cube and one central part. Width of the border parts is equal to the final maximal particle diameter, Fig 4.

The centres of particles that are at the beginning of the algorithm assigned to parts of the cube, move then only within this part. If we divided cubes into the border and the central parts a dead spaces occur on the edges of cubes where the particle centres can never get to, Fig 4. Note that just the centres of particles cannot go through the border and the central parts but the spheres are able to interfere to neighbouring parts and collide with particles of this part.

Collisions

During a particle motion two types of collision occur. The first one is a collision of particle with borders of the appropriate volume part. The second elastic collision is between particles. The main task is when these dynamic phenomena occur.

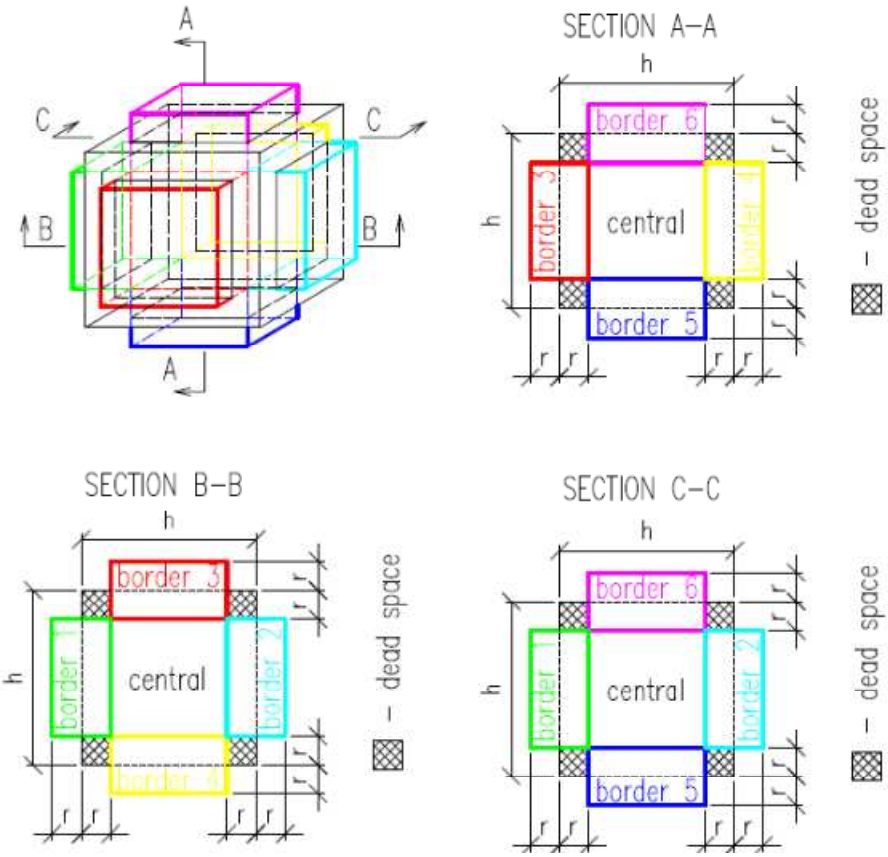

Fig. 4 Division of Wang cubes into border and central volume parts

The velocities after a rebound from a wall are according to the Law of Action-Reaction. The earliest time of a rebound from a wall Δt_e depends on the current sphere position and its velocity. Determination of Δt_e is according to the following equation:

$$\Delta t_e = min\{dx_{i,}/|vx_i|\,;\; dy_i/|vy_i|\,;\; dz_i/|vz_i|\}\,, \tag{2}$$

where $dx_{i,}$, dy_i, dz_i are the distances from the centre of the particle *i* to the wall of the appropriate volume part in a direction of the particle velocities vx_i, vy_i and vz_i respectively.

The earliest time of the second type of collision depends on the current sphere position and the position when the distance between the centres of this particle *i* and a particle *j* is equal to the sum of the radii of these particles. This time can be defined with the following formulas:

$$(x_j - x_i)^2 + (y_j - y_i)^2 + (z_j - z_i)^2 = (r_j + r_i)^2, \tag{3}$$

$$x_i = x_i^t + vx_i^t \cdot \Delta t_c,\;\; y_i = y_i^t + vy_i^t \cdot \Delta t_c,\;\; z_i = z_i^t + vz_i^t \cdot \Delta t_c,\;\; r_i = r_i^t + dr \cdot \Delta t_c, \tag{4, 5, 6, 7}$$

$$x_j = x_j^t + vx_j^t \cdot \Delta t_c,\;\; y_j = y_j^t + vy_j^t \cdot \Delta t_c,\;\; z_j = z_j^t + vz_j^t \cdot \Delta t_c,\;\; r_j = r_j^t + dr \cdot \Delta t_c, \tag{8, 9, 10, 11}$$

where $x_i, y_i, z_i, x_j, y_j, z_j$, are the collision coordinates of the sphere *i* and *j*, $x_i^t, y_i^t, z_i^t, x_j^t, y_j^t, z_j^t$, are the current coordinates of the sphere *i* and *j*. The current discs velocities are designated vx_i^t, vy_i^t, vz_i^t, vx_j^t, vy_j^t, vz_j^t, and r_i, r_j, r_i^t, r_j^t are the radii of the sphere *i* and *j* in the current time *t* and in the collision time. The growth rate of particles describes the variable dr and Δt_c is a time elapsed since the time *t* till the time of collision. The next collision time is a minimum of real positive roots of the equation 3.

The particle velocities after the second type of collision are calculated according to the Momentum conservation law and the Conservation of the energy law. Before this calculation the velocities of collide spheres must be transformed from the global coordinate system to a collision coordinate system. The vector of particles normal velocities is then in direction of connecting line between the centres of collide spheres *Si* and *Sj*. This direction determines the position and the orientation of the *x"* axis in the collision coordinate system. The transformation (rotation) matrix from the global coordinate system to the collision coordinate system follows the Euler Angle Sequence (1.2.3) [10], see equation 12 and Fig. 5. There the system is sequentially rotated by an angle γ along initial *z* axis and after that there is a rotation along new axis *y'* by an angle β. The third rotation is in our case unnecessary and rotation by angle α along axis *x''* is equal to zero.

$$T = \begin{bmatrix} \cos\beta \cdot \cos\gamma & \cos\beta \cdot \sin\gamma & -\sin\beta \\ -\sin\gamma & \cos\gamma & 0 \\ \sin\beta \cdot \cos\gamma & \sin\beta \cdot \sin\gamma & \cos\beta \end{bmatrix} \tag{12}$$

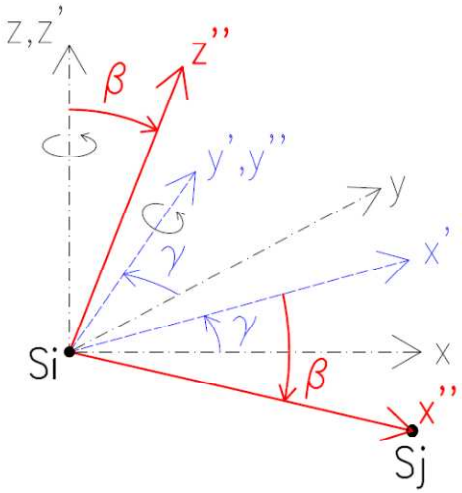

Fig. 5 Euler Angle Sequence (1.2.3)

PACKING EXAMPLES

Early tests of ability of the proposed dynamic packing algorithm were made on artificial media with the predefined volume fraction and the particle positions that should be achieved. This is because

of a further utilization of some optimization technique based on the best so far particle positions to which the particles are directed. The chosen examples are based on knowledge of a sphere packing in cubes with lower number of spheres but with the higher volume fraction.

There is also need to modify a particle velocities calculation. In the early investigation there were random velocities that changed only after elastic collisions with a respect to the Action-Reaction law with no allowance. For the task of achieving predefined particle positions the velocities are modified after each collision and a time step in accordance with equation 13.

$$v_i^{t+\Delta t} = w \cdot v_i^t + c \cdot (p_g - p_i) \tag{13}$$

where $v_i^{t+\Delta t}$ is the new velocity after a collision or a time step, v_i^t is the original velocity at the time *t*, *w* is a weight factor that is gradually reduced over time steps from the initial value 1 to the final value 0, *c* is a multiplier of difference between the required particle position p_g and the current particle position p_i. The parameter *c* has value 0,5. Of course it will be easy to set a high value for parameter *c* and zero for the weight factor to immediately reach the required positions and wait until the particles grow up to the final radii. But this approach can never test a functionality of the algorithm with a respect to a particle motion, elastic collisions and the boundary conditions of the Wang cubes.

Tab. 1 The packing examples for the 3D Wang tiling

number of particles in one cube	number of particles in bound parts	number of particles in central part	final radius of particles	achieved volume fraction	the highest possible volume fraction
2	0	2	0,634	0,26683	0,26683
8	1	5	0,500	0,52358	0,52360
8	2	2	0,500	0,52359	0,52360
27	6	9	0,333	0,52359	0,52360

CONCLUSION

In this paper a dynamic packing algorithm for the Wang cubes generation was introduced. In comparison with widely used concept of Periodic Unit Cell (PUC), the stochastic Wang tiling both in 2D and 3D is able to stack a final heterogeneous media with highly reduced unwanted artefacts of the periodicity. The minimal number of the Wang cubes within a set for the stochastic tiling is sixteen. In this work an artificial material composed of hard sphere particles within a matrix was taken into account.

The proposed algorithm is based on the particle movement and the growing of particle radii from the initial zero to the final required value. Due to dynamic phenomena of collision the final medium doesn´t suffer from unwanted particles overlapping. Some basic artificial materials with the predefined particle positions according to knowledge of packing of spheres within cubes are generated. This was

done to have some early tests of the algorithm for a future utilization of a particle optimization based on the best so far particles positions (given reference microstructure) to which particles approach.

ACKNOWLEDGEMENT

This outcome has been achieved with the financial support of the Grant Agency of the Czech Technical University in Prague, grant No. SGS14/028/OHK1/1T/11.

REFERENCES

[1] DRUGAN, W. J. and WILLIS, J. R. A. Micromechanics-based nonlocal constitutive equation and estimates of representative volume element size for elastic composites. *Journal of the Mechanics and Physics of Solids*, 1996, vol. 44, issue 4, pp. 497-524. DOI: 10.1016/0022-5096(96)00007-5.

[2] POVIRK, G. L. Incorporation of microstructural information into models of two-phase materials. *Acta Metallurgica et Materialia*, 1995, vol. 43, issue 8, pp. 3199-3206. DOI: 10.1016/0956-7151(94)00487-3.

[3] KANIT, T., FOREST, S., GALLIET, I., MOUNOURY, V., and JEULIN, D. Determination of the size of the representative volume element for random composites: statistical and numerical approach. *International Journal of Solids and Structures*, 2003, vol. 40, issue 13, pp. 3647-3679. DOI: 10.1016/S0020-7683(03)00143-4.

[4] NIEZGODA, S. R., TURNER, D. M., FULLWOOD, D. T. and KALIDINDI, S. R. Optimized structure based representative volume element sets reflecting the ensemble-averaged 2-point statistics. *Acta Materialia*, 2010, vol. 58, issue 13, pp 4432-4445. DOI: 10.1016/j.actamat.2010.04.041.

[5] KUMAR, N. C., MATOUŠ, K. and GEUBELLE, P. H. Reconstruction of periodic unit cells of multimodal random particulate composites using genetic algorithms. *Computational Materials Science*, 2008, vol. 42, issue 2, pp 352-367. DOI: 10.1016/j.commatsci.2007.07.043.

[6] NOVÁK, J., KUČEROVÁ, A. and ZEMAN, J. Compressing random microstructures via stochastic Wang tilings. *Physical Review E*, 2012, vol. 86, issue 4, 040104. DOI: 10.1103/PhysRevE.86.040104.

[7] WANG, H. Proving theorems by pattern recognition-II. *Bell System Technical Journal*, 1961, vol. 40, issue 1, pp 1-41. DOI: 10.1002/j.1538-7305.1961.tb03975.x.

[8] ČULÍK, K. An aperiodic set of 13 Wang tiles. *Discrete Mathematics*, 1996, vol. 160, issue 1, pp 245-251. DOI 10.1016/S0012-365X(96)00118-5.

[9] COHEN, M. F., SHADE, J., HILLER, S. and DEUSSEN, O. Wang tiles for image and texture generation. *ACM Transactions on Graphics*, 2003, vol. 22, issue 3, pp 287-294. DOI: 10.1145/882262.882265.

[10] DIEBEL, J. Representing attitude: Euler angles, unit quaternions, and rotation vectors. *Matrix*, 2006.

INFLUENCE OF RECYCLED AGGREGATE ON PHYSICAL, MECHANICAL AND DEFORMATION PROPERTIES OF CONCRETE

Magdaléna ŠEFFLOVÁ[1], **Tereza PAVLŮ**[2]

Abstract: *This article deals with physical, mechanical and deformation properties of concrete containing recycled concrete aggregate. Two types of recycled concrete aggregate were used for the production of the concrete, which originate from the same recycling plant. For the testing of concrete, a total of six concrete mixtures were made, one of which was a reference mixture and in others a coarse fraction of natural aggregate was in varying ratio replaced by recycled aggregate. The test results showed that using of recycled aggregate as a partial replacement for natural aggregate in concrete causes deterioration of its physical, mechanical and deformation properties.*

***Keywords**: recycled aggregate, recycled concrete, influence, properties of concrete*

INTRODUCTION

The use of construction waste as a source of aggregate for the production of new concrete is one way how to follow sustainable building. The increasing amount of construction and demolition waste on landfill, on the one hand, and the scarcity of natural resources for aggregate, on the other hand, encourages the use of construction and demolition waste as a source for construction aggregate. Use of recycled aggregate in concrete helps to reduce primary raw materials and the amount of construction and demolition waste in rubbish dumps.

In the Czech Republic, the recycled aggregate is used only for backfills. A reason why the recycled aggregate is not used in concrete is a low level of knowledge of the material. The poor and different quality of recycled aggregate in recycling plants in the Czech Republic is problem as well. It is necessary to test the properties of recycled aggregate and concrete with recycled aggregate.

[1] Ing. Magdaléna Šefflová, Czech Technical University Prague, Faculty of Civil Engineering, magdalena.sefflova@fsv.cvut.cz

[2] Ing. Tereza Pavlů, Czech Technical University Prague, Faculty of Civil Engineering, tereza.pavlu@fsv.cvut.cz

MATERIALS

Two samples of recycled aggregate were used in this study. The recycled aggregate was obtained from the same recycling plant. The recycled aggregate was divided into two fractions 4 – 8 mm and 8 – 16 mm. For differentiation, the first sample of recycled aggregate was marked A and the second sample of recycled aggregate was marked B.

Physical properties of recycled aggregate were tested by pycnometric method according to ČSN EN 1097 - 6 [1]. The average results are shown in Fig. 1 a Fig. 2. The density of recycled aggregate was about 18% less compared with natural aggregate. The water absorption capacity of recycled aggregate was about 7 times higher (fraction 8 – 16 mm) and about 10 times higher (fraction 4 – 8 mm) than the water absorption capacity of natural aggregate.

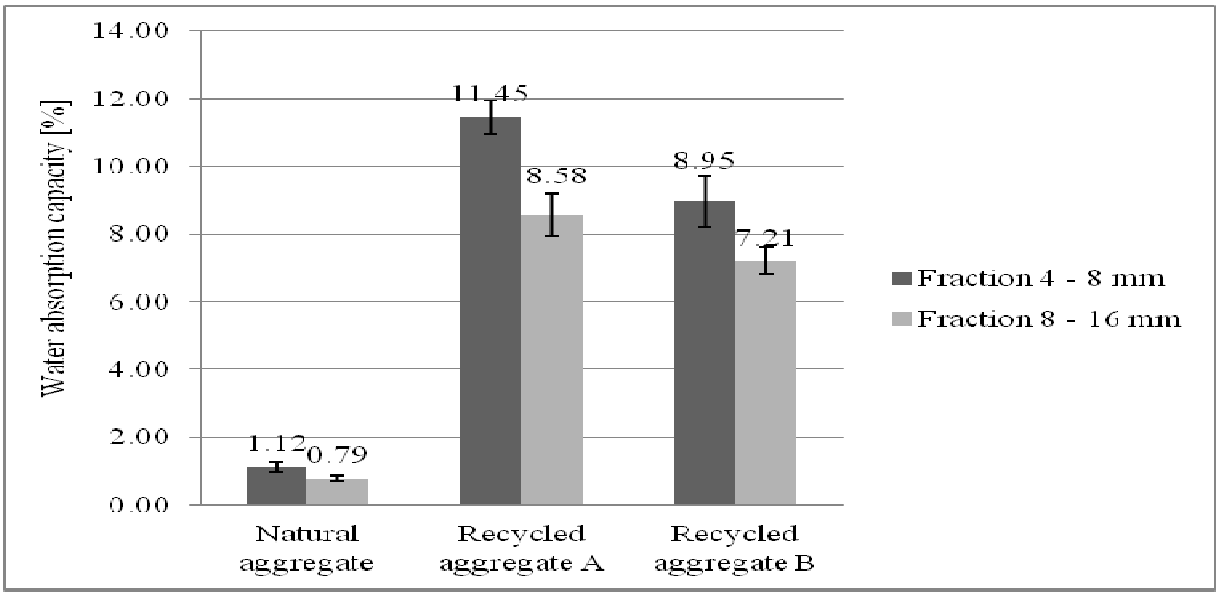

Fig 1 Water absorption capacity of natural and recycled aggregate

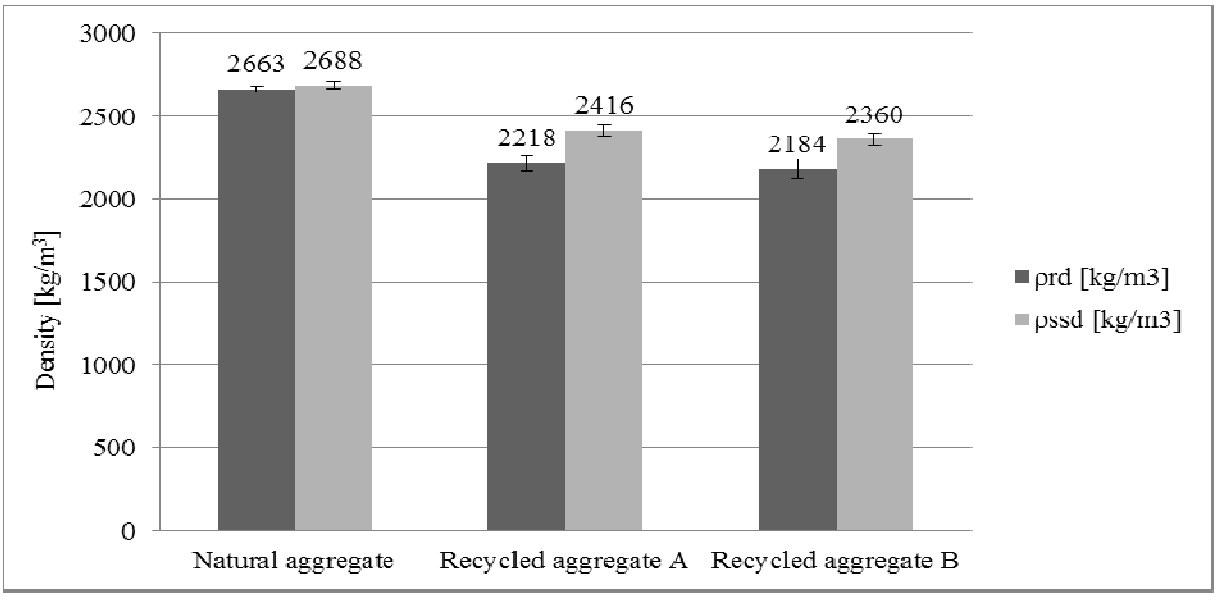

Fig. 2 Density of natural and recycled aggregate

PREPARATION OF CONCRETE MIXTURES

For the experiment, there were prepared six concrete mixtures. The first mixture was reference one with natural aggregate (REF). In other mixtures, natural aggregate was replaced by recycled aggregate of varying ratio. The fine fraction was natural sand in all mixtures. Two mixtures were prepared with concrete recycled aggregate A. In the second concrete mixture (50A), 50% of the natural aggregate was replaced by recycled concrete aggregate. In the third concrete mixture (63A), 63% of the natural aggregate was replaced by recycled concrete aggregate. Remaining three mixtures were prepared with recycled concrete aggregate B. In the fourth concrete mixture (31B), 31% of the natural aggregate were replaced by recycled concrete aggregate. In the fifth concrete mixture (50B), 50% of the natural aggregate were replaced by recycled concrete aggregate and in the sixth concrete mixture (62B), 62% of the natural aggregate were replaced by recycled concrete aggregate. Because of using only coarse fractions 4 - 16 mm of recycled aggregate, were maximal replacements 62% and 63%, which is 100% replacement for coarse aggregate.

For effortless comparison, all mixtures were designed with the same parameters:

- exposition class XF1
- effective water – cement ratio 0.5
- amount of cement 320 kg/m^3
- strength class C 30/37.

Amount of water was modified according to the water absorption capacity of recycled aggregate. For all concrete mixtures five cubes of dimensions 150x150x150 mm and three beams of dimensions 100×100×400 mm were made.

PROPERTIES OF HARDENED CONCRETE

There were tested physical, mechanical and deformation properties of hardened concrete. It is possible to say that there is a loss in the physical and mechanical properties of concrete with recycled aggregate [2, 3]. The properties of hardened recycled concrete depend on the quality and amount of recycled aggregate [2, 4, 5].

Density of hardened concrete

The density of hardened concrete were determined according to ČSN EN 12390 - 7 [6]. Fig. 3 shows the correlation between the density of hardened concrete and replacement ratios of recycled aggregate in concrete. With the increase of replacement ratios of recycled aggregate the density recycled aggregate concrete decrease. While the density of concrete containing 50% of concrete recycled aggregate B was 2233 kg/m^3, the density of concrete with 63% concrete recycled aggregate was 2146 kg/m^3. The decrease of density was similar to concrete with recycled aggregate A and

concrete with recycled aggregate B.

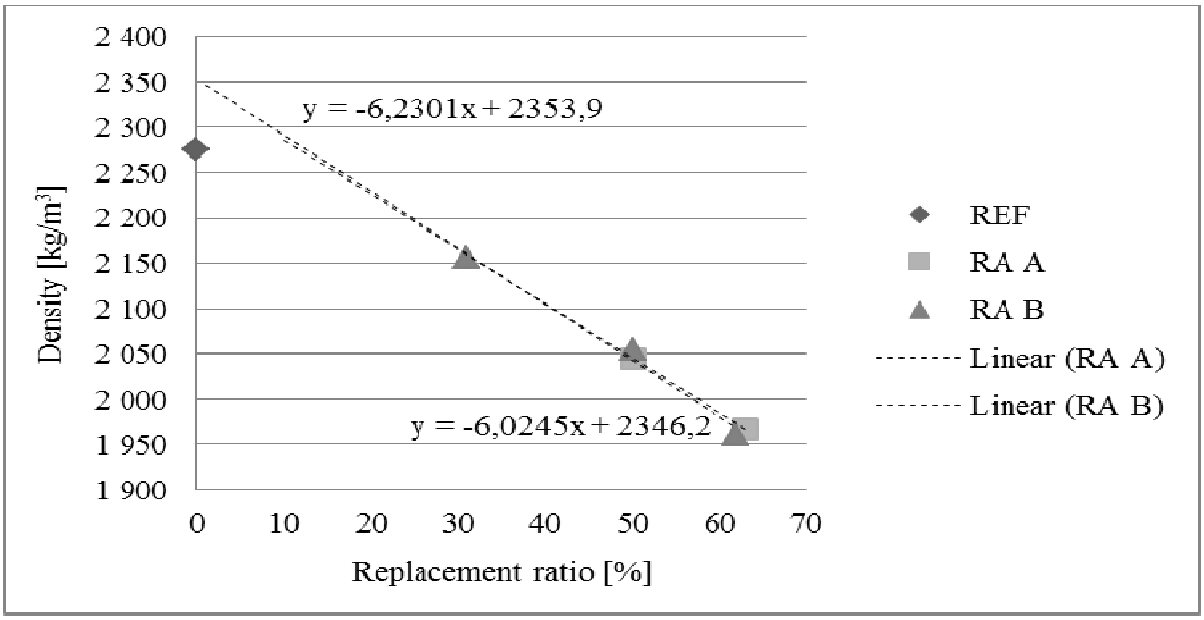

Fig. 3 Correlation between replacement ratio of recycled aggregate and density of concrete

Water absorption capacity

Water absorption capacity of hardened concrete was tested on 150 mm cubes. The average results are shown in Fig.4. Water absorption capacity of hardened concrete contained recycled aggregate increased about 2 times than reference concrete. It is determined that as the proportion of concrete recycled aggregate admixtures increased, water absorption capacity increased in hardened concrete with concrete recycled aggregate.

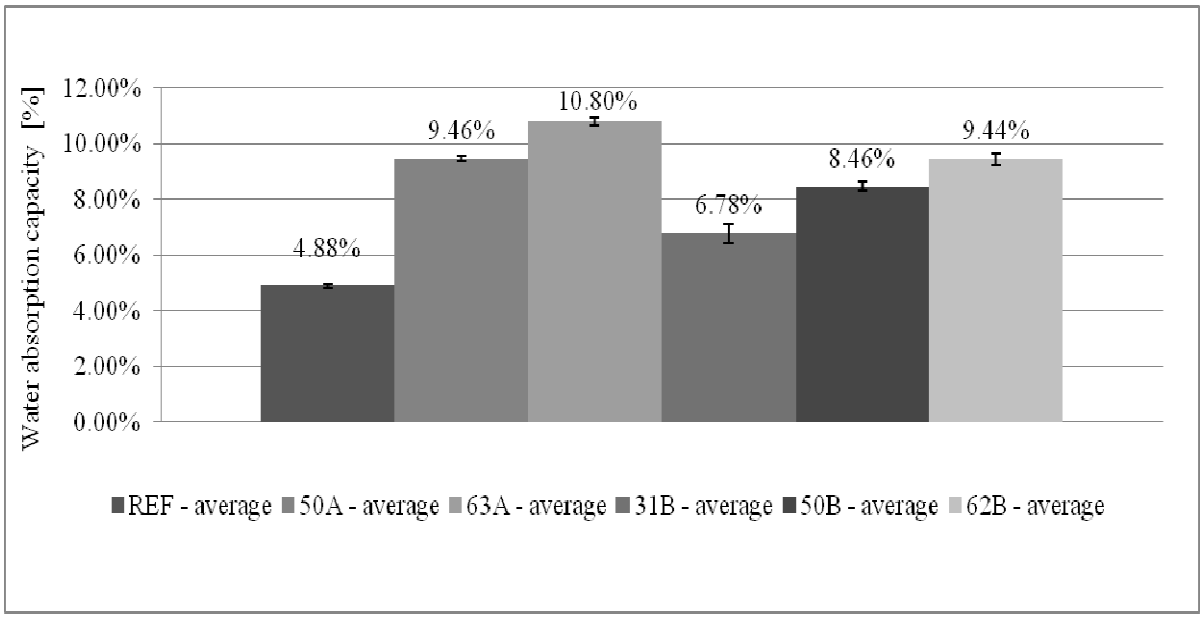

Fig.4 Water absorption capacity of reference and recycled concrete

Compressive strength

Tests of compressive strength were carried out on 150 mm cubes. The compressive strength were determined according to ČSN EN 12390 - 3 [7]. Five concrete cubes were casted for each concrete mix proportion for 35 days. The compressive strengths of the concrete mixes are shown in Fig. 5. The highest decrease of compressive strength was about 45 % for concrete samples with a 63 % replacement ratio of recycled aggregate. The decrease of compressive strength was depended on the amount of recycled aggregate. Fig. 6 shows the correlation between the compressive strength of hardened concrete and replacement ratio of recycled aggregate in concrete. This graph proved a linear dependence between the compressive strength of recycled aggregate concrete and amount of recycled aggregate in concrete mixtures. With the increase of replacement ratio of recycled aggregate the compressive strength recycled aggregate concrete decrease.

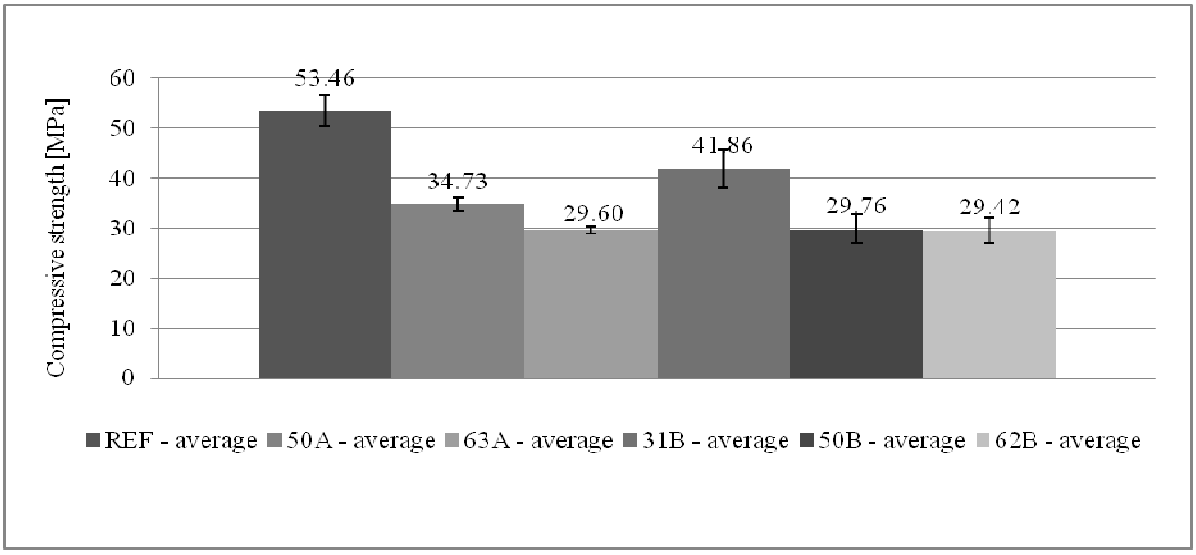

Fig. 5 Compressive strength of reference and recycled concrete

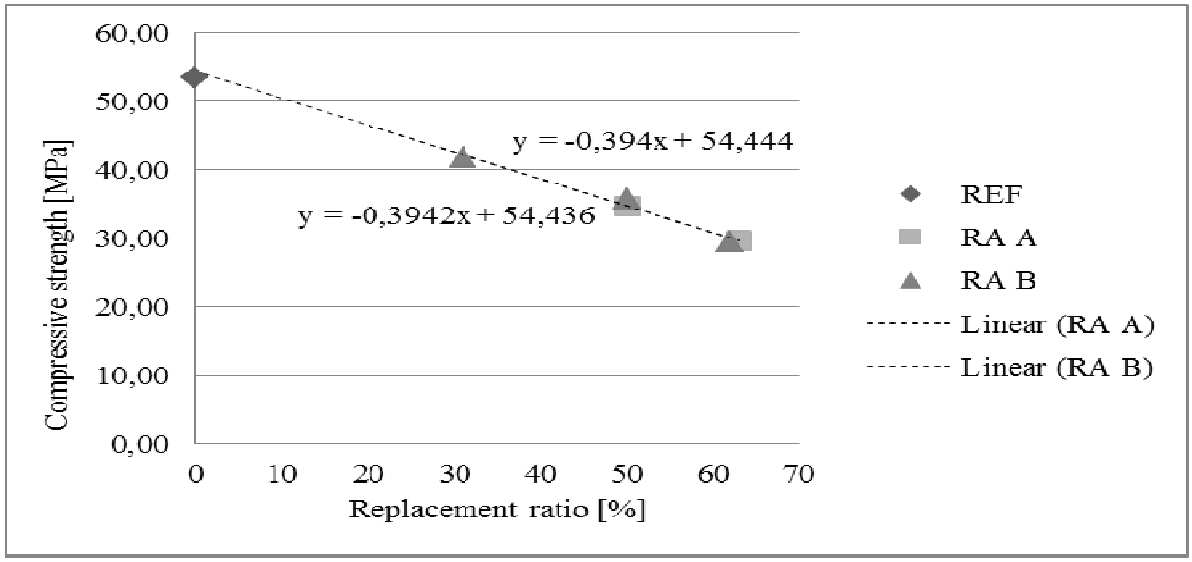

Fig. 6 Correlation between replacement ratio of recycled aggregate and compressive strength of concrete

Flexural strength

Tests of flexural strength were carried out on the beams of dimensions 100x100x400 mm. The flexural strength was determined according to ČSN EN 12390 - 5 [8]. Three concrete beams were casted for each concrete mix proportion for 28 days. The flexural strength was tested under a load in a four-point bending. The average results are shown in Fig. 7. The flexural strength of concrete containing 63% of concrete recycled aggregate A was about 5.11 MPa and the flexural strength of concrete containing 62% recycled aggregate B was about 3.66 MPa. The increase of flexural strength was caused by different circumstances during hardening concrete. The samples 63A were cured under water; other samples were cured on air.

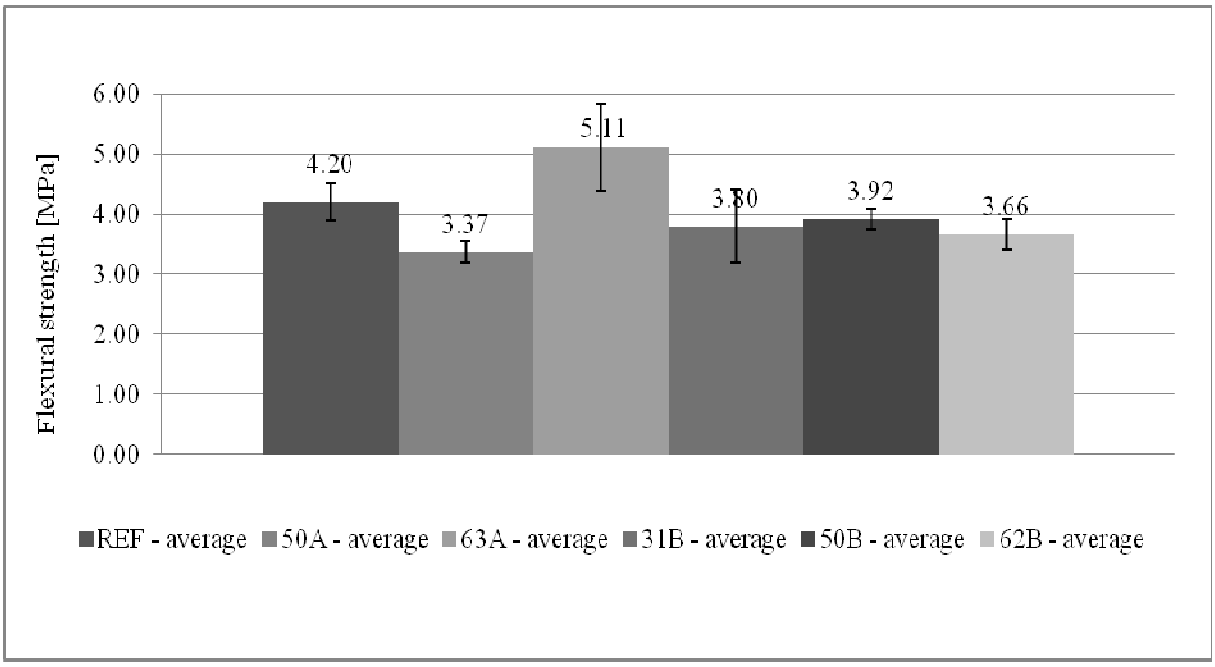

Fig. 7 Flexural strength of reference and recycled concrete

Modulus of elasticity

The modulus of elasticity was conducted on beams of dimensions 100×100×400 mm. The dynamic modulus of elasticity was tested by ultrasound method. Out of the ultrasound method results was calculated static modulus of elasticity:

$$E_s = 0.83\, E_d \text{ [9].}$$

The average results are shown in Fig. 8. The decrease of modulus of elasticity was different from concrete with recycled aggregate A and B. Modulus of elasticity of hardened concrete contained recycled aggregate A was decreased about 52% than reference concrete and of hardened concrete contained recycled aggregate B was decreased about 39%.

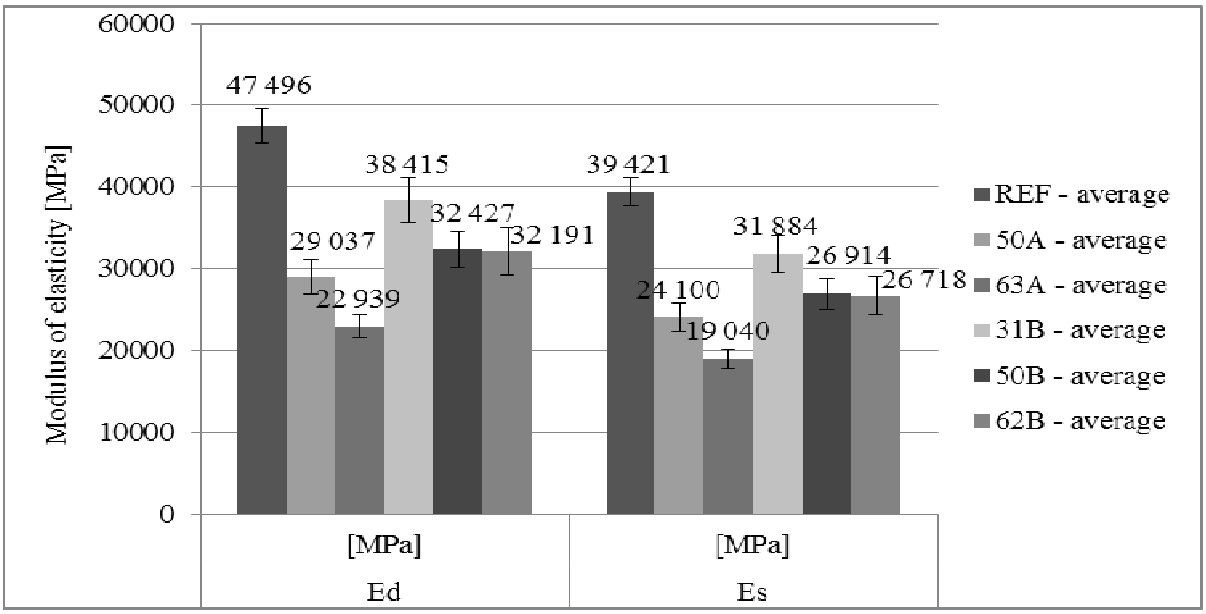

Fig. 8 Modulus of elasticity of reference and recycled concrete

CONCLUSIONS

In this paper, experimental results for the physical, mechanical and deformation properties of recycled concrete included a different replacement ratio of different types of recycled aggregate are presented and discussed. Regarding the physical, mechanical and deformation properties of concrete produced with recycled aggregate from constructions and demolitions, based on the results of this research it is possible to conclude that:

- The increased content of recycled aggregates causes a deterioration physical, mechanical and deformation properties of concrete with recycled aggregate.
- The use of recycled aggregate in concrete, it is concluded that the increasing replacement ratio of recycled aggregate in recycled concrete negatively influences resulting properties of concrete.
- The main degradation of properties was observed for compressive strength, where more than 45 % decrease for 100 % replacement of coarse fraction by recycled aggregate was reached.
- It is possible to say that recycled aggregate concrete is possible to be used in the construction with low requirements for compressive strength and frost resistance.
- It is necessary to optimize a concrete mixture with respects to deteriorated properties. The deterioration of properties is not possible to compensate for the increased amount of cement.

ACKNOWLEDGEMENT

The research was funded by SGS13/109/OHK1/2T/11 Additional constructions for light-weight concrete frame systems made from natural and recycled materials.

REFERENCES

[1] ČSN EN 1097 - 6 (72 1194). *Zkoušení mechanických a fyzikálních vlastností kameniva - Část 1: Stanovení objemové hmotnosti a nasákavosti*. Česká republika: Český normalizační institut, 2001.

[2] CHEN, H. L. T. YEN T. and CHEN K.H. Use of building rubbles as recycled aggregates. In: *Cement and Concrete Research.* 2003, str. 125 – 132.

[3] LEVY, S. M. a HELENE P. Durability of recycled aggregates concrete. In: *Cement and Concrete Research*. 2004, str. 1975 - 1980.

[4] TOPCU, I.B. a SENGEL S. Properties of concretes produced with waste concrete aggregate. In: *Cement and Concrete Research*. 2004, str. 1307 - 1314.

[5] TOPCU, I.B. Physical and mechanical properties of concretes produced with waste concrete. In: *Cement and concrete research*. 1997, str. 1817 - 1823.

[6] ČSN EN 12390 - 7. *Zkoušení ztvrdlého betonu - Část 7: Objemová hmotnost ztvrdlého betonu*. Česká republika: Ústav pro technickou normalizaci, metrologii a státní zkušebnictví, 2009.

[7] ČSN EN 12390-3 (731302). *Zkoušení ztvrdlého betonu - Část 3: Pevnost v tlaku zkušebních těles.* Česká republika: Úřad pro technickou normalizaci, metrologii a státní zkušebnictví, 2009.

[8] ČSN EN 12390-3 (731302). *Zkoušení ztvrdlého betonu - Část 3: Pevnost v tlaku zkušebních těles.* Česká republika: Úřad pro technickou normalizaci, metrologii a státní zkušebnictví, 2009.

[9] UNČÍK, Stanislav a ŠEVČÍK, Patrik. Modul pružnosti betónu. In: *Beton Racio* [online]. 2008 [cit. 2014-07-05]. Available from: http://www.betonracio.sk/betonracio/downloads/modul_pruznosti.pdf

FORCE ANALYSES OF A DOVETAIL JOINT

Karel ŠOBRA[1], **Jorge M. BRANCO**[2], **Petr FAJMAN**[3]

***Abstract**: Two basic approaches of an analytical solution of the response of the dovetail joint to the monotonic loading are discussed in this paper. Force distribution to the monotonic compression and tension of the joint and an effect of positive and negative bending moments are solved using various simplifying assumptions and using principle of virtual work. In the solved examples, the material characteristics obtained from the experimental campaign performed at the University of Minho, Portugal, are used.*

***Keywords**: dovetail joint, analytical equations, principle of virtual work*

INTRODUCTION

Due to neglected maintenance, influence of wood-rotting fungus and wood-destroying insects, mechanical damage, etc., wooden trusses, which are basically ones of the oldest structures in the world, degrades and need to be repaired. Since historical trusses frequently belong to buildings of the Cultural Heritage, their reconstruction is usually under supervision of Monument Care Department of Ministry of Culture of the Czech Republic. Therefore all interventions must preserve the originality of the construction. Due to this, traditional carpentry, usually all wooden, joints have to be used.

All interventions have to be supported by an accurate diagnosis and analysis to decide if an inspected element can be reinforced or needs to be substituted. In this analysis phase, the assessment of the behaviour of the carpentry joints is crucial. Joints play an important role in the stress distribution within the structure as they represent the key elements in terms of strength and ductility [1].

In spite of that historical joints are constructed in the same way during the ages, just by routine, there are not many studies, nowadays, focused on historical joints [2-11].

[1] Ing. Karel Šobra, Department of Mechanics, Faculty of Civil Engineering, Czech Technical University in Prague, Thákurova 7; 166 29, Prague 6 – Dejvice; CZ, e-mail: karel.sobra@fsv.cvut.cz

[2] Prof. Jorge M. Branco, Department of Civil Engineering, School of Engineering, University of Minho, Campus de Azurém 4800-058 Guimarães; Portugal, e-mail: jbranco@civil.uminho.pt

[3] Doc. Ing. Petr Fajman, CSc., Department of Mechanics, Faculty of Civil Engineering, Czech Technical University in Prague, Thákurova 7; 166 29, Prague 6 – Dejvice; CZ, e-mail: fajman@fsv.cvut.cz

Work presented in this paper aims to contribute to need of analysis of carpentry joints by presenting an analytical evaluation of one of the most wide spread carpentry joints, the dovetail.

DOVETAIL JOINT

During Gothic and Baroque periods high roof with angle more than 50° were used. Collar beam truss (seen in *Fig. 1*) is an evolution of a construction, which can be used to resist higher wind load which is caused by bigger inclination of a roof. Utilization of the collar beam in the construction of the truss minimizes rafters span and in the same time increases stiffness of the truss as a whole. Due to this the collar beam truss was one of the most commonly used truss construction during Gothic and Baroque periods.

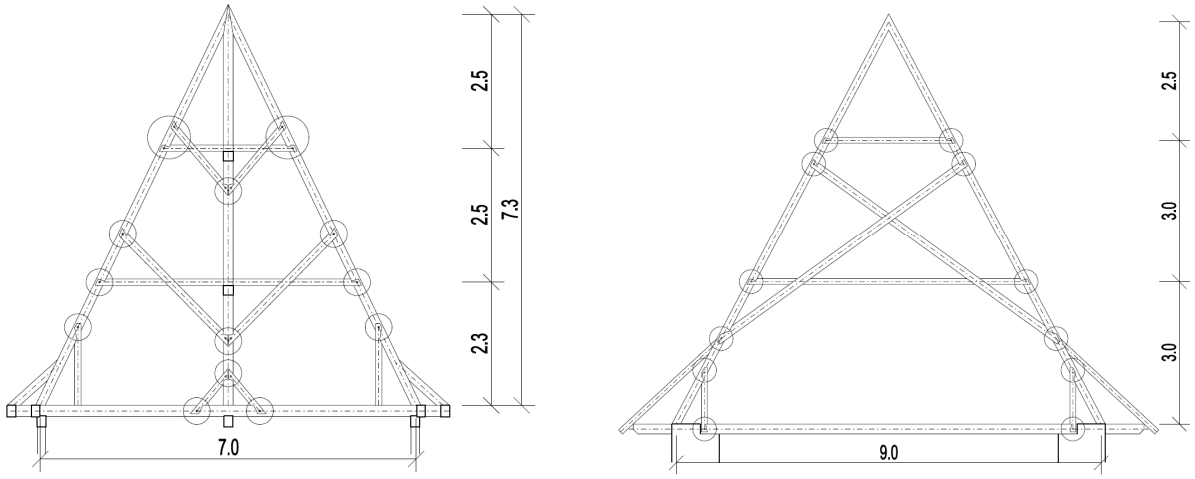

Fig. 1 Collar beam truss: chapel in Kozojedy (Jičín, Czech Republic) on the left and truss of Church of Saint Anna in Prague (Czech Republic) on the right – the dovetail joints are in circles

The dovetail joint is the most commonly used traditional carpentry joint, which can be found in collar beam trusses. It is complete wooden joint which connects two elements in a general angle. In the joint, both elements are weakened of 1/3 of the width of thinner one to fit together and whole joint is held together by the key.

Forces in the joint are transferred through the direct contact of the contact surfaces (further called compressive areas). Even the highly deformed key can still hold whole joint together, but due to gaps which appear in the joint, compressive areas are smaller and local stresses increase. For different types of loading different compressive areas are involved to the force transfer as can be seen in *Fig. 2*.

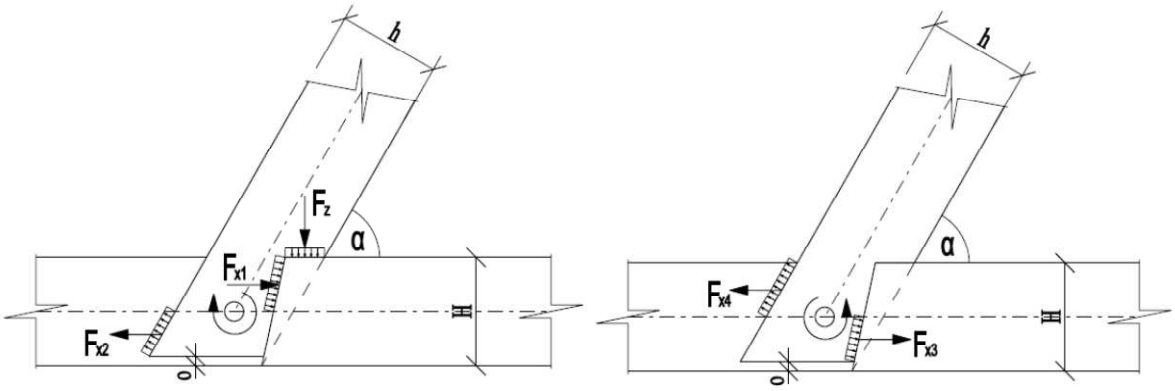

a) *b)*

Fig. 2 Compressive areas of the joint for a) clockwise bending moment and b) anticlockwise bending moment

Since the forces which the joint is able to transfer are depended on the compressive areas, it is possible solve the joint's equilibrium from the geometry of the joint. It is obvious that α angle has main influence on the compressive areas size. With the rising angle α, the size of the compressive areas is lover, what causes bigger stresses in the joint and lower bearing capacity of the joint as a whole. Relationship between the compressive areas size and α angle can be seen in *Fig. 3*. Elements with cross sections b= 0.12 m × h= 0.16 m and B= 0.12 m × H= 0.2 m were used for *Fig. 3*. Influence of the offset o was neglected during the size of compressive areas calculations. Labelling of the areas corresponds with the labelling of the forces at *Fig. 2*.

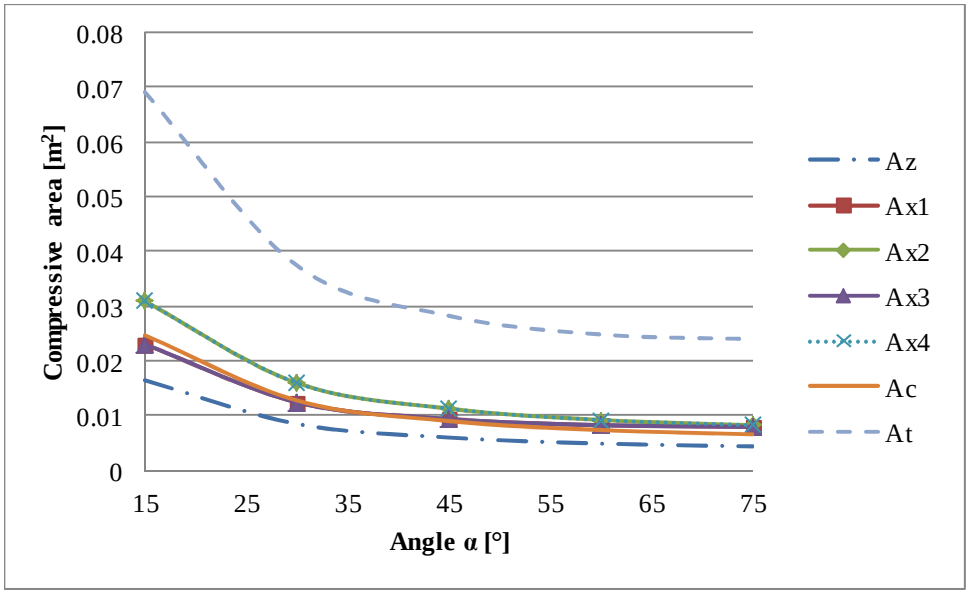

Fig. 3 Angle - compressive areas size diagram

At *Fig. 3* A_z is the compressive responsible for transfer of the force F_z from *Fig. 2*. Other compressive areas shown at *Fig. 3* show the same relationship between a compressive area and a force from *Fig. 2* as was mentioned for compressive area A_z and force F_z.

Force distribution in a dovetail joint

Despite the full theoretical utilization of the compressive areas is not possible due to manufacturing errors, method mentioned above is useful only for homogeneous materials. Properties of wood are different in different directions and depended on the angle of loading. Due to this it is necessary connect material characteristics (strength depended on the loading angle, stiffness, …) and the geometry of the joint

Since different compressive areas are used during different types of loading, it is useful to solve that loading types separately. At the beginning it is important to describe joint's behaviour to the basic types of loading – compression and tension of the joint and influence of positive (anticlockwise) and negative (clockwise) bending moment.

When the joint is under influence of tension, the compressive areas (bold and with arrows) shown at *Fig. 4b)* are used for load transfer. As it was mentioned above, forces are transferred by direct contact what causes deformation of those areas. Maximal force which can be transferred by a compressive area is possible to establish according to *(1)*.

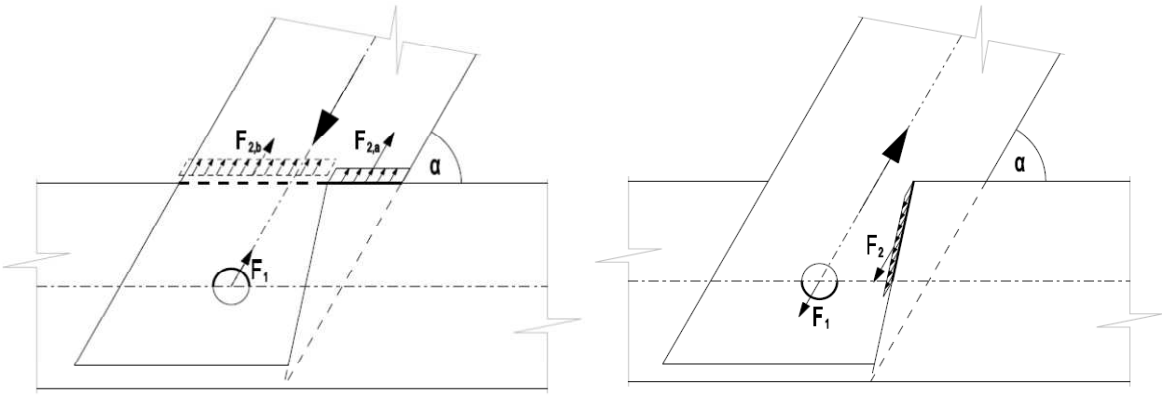

a) *b)*

Fig. 4 Compressive areas of the joint a) for compression of the joint and b) for the tension in the joint

$$F_{u,i} = A_i f_{c,\beta} \qquad (1)$$

In *(1)* A_i is a compressive area and $f_{c,\beta}$ is compressive strength of wood depended on the lading angle to the grain in the place of the compressive area.

For further analysis it is important to establish some assumptions. For certain simplification it is assumed, that parts of the joint which can be deformed in some direction, have the same deformation in this direction. If the elastic bearing capacity of the joint is assumed, the joint is strong as its weakest part. And the last one assumes uniform stress distribution on a compressive area. From the second assumption, using equation *(2)*, it is possible to calculate the deformation of the weakest part of the joint.

$$r_i = k_\beta^{-1} f_{c,\beta} \tag{2}$$

In *(2)* r_i is deformation of a compressive area and $k_{i,\beta}^{-1}$ is reciprocal value of the stiffness of wood according to the loading angle.

Based on the assumption of the same deformation, it is possible to calculate force, which is transferred by other (not the weakest) compressive areas on limit deformation. Then, overall bearing capacity of the joint is calculated as sum of the forces on all compressive areas during limit deformation. Deformation and force distribution on the compressive areas are possible to obtain using this approach what is used for the calculation of the joint response to the loading.

Stiffness of the material is used during calculation of the deformation of a compressive area as is possible to see in *(2)*. Usually it is difficult to find stiffness of wood and its calculation from other material characteristics is not possible. Due to this an experimental campaign performed at University of Minho, Portugal, Guimarães, was made. Some material characteristics including the stiffness of chosen wood species were established during the campaign. The following wood species were studied during the compression tests: Scots pine (*Pinus silvestrys*), Silver fir (*Abies alba*), Maritime pine (*Pinus pinaster*) and chestnut (*Castanea sativa*). The first two are ones of the most widespread wood species in the Czech Republic while the others two are common in Portugal. In the model calculations shown later, material characteristics obtained during the experimental campaign are used. More about the campaign can be found in [12].

Bearing capacity of the joint to the compression was established according to *(3)*. Values of transferred forces to the loading of *N*= 25 kN can be found in *Tab. 1*. Since the key element, especially a compressive area which transfers loading to/from the key should be the weaker part of the construction, results of the force analyses to the tension is almost the same as in compression. Bearing capacity to the tension of the joint is shown in equation *(4)*.

$$\begin{aligned} T_{R,c} &= f_{c,0}A_1 + f_{c,\alpha}A_{2a} + f_{c,\alpha}A_{2b} = f_{c,0}\left(\frac{\pi d}{2}\frac{2}{3}b\right)\gamma_1 + \\ &+ f_{c,\alpha}\left(\frac{h}{3\sin\alpha}\frac{2}{3}b\right)\gamma_{2a} + f_{c,\alpha}\left(\frac{2h}{3\sin\alpha}\frac{1}{3}b\right)\gamma_{2b} \end{aligned} \tag{3}$$

$$T_{R,c} = f_{c,0}A_1 + f_{c,\alpha}A_2 = f_{c,0}\left(\frac{\pi d}{2}\frac{2}{3}b\right)\gamma_1 + f_{c,\alpha}\left(k_{H0}\frac{2}{3}b\right)\gamma_2 \tag{4}$$

Symbols used in *(3)* and *(4)* are described in *Fig. 5*. A_i is a compressive area, $f_{c,0,i}$ is the compressive strength parallel with the grain, $f_{c,\alpha,\mathrm{i}}$ is the compressive strength angled to the grain in

the angle α, z_i and x_i are arms of the forces to the key, what is the point of rotation, γ_i is coefficient of area (how many percent of the compressive area is used from theoretical maximum compressive area) and *b* is the width of the skew element.

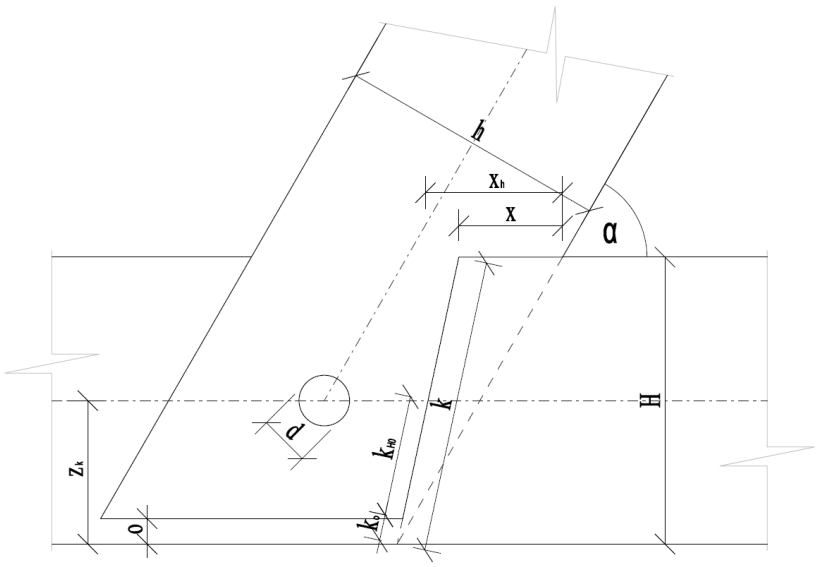

Fig. 5 Symbols used in equations (3) – (6)

The same approach is possible to use to determine response of the joint to the bending moment. During action of positive (counter clockwise) bending moment two compressive areas act in force transfer as is possible to see at *Fig. 2b)*, what is captured in *(5)*. When negative (clockwise) bending moments acts, three compressive areas according to *Fig. 2a)* are used for force transfer. Bearing capacity to negative bending moment can be calculated by *(6)*.

$$M^{+} = f_{c,\alpha} A_4 z_4 + f_{c,\alpha} A_5 z_5 = f_{c,\alpha} \frac{2}{3} b \left(\frac{H - z_k}{\sin\alpha} \frac{H - z_k}{2} \gamma_4 + \left(\frac{k}{2} - k_o \right) \frac{\frac{k}{2} - k_o}{2} \gamma_5 \right) \tag{5}$$

$$M^{+} = f_{c,90} A_z x_z + f_{c,\alpha} \left(A_2 z_2 + A_3 z_3 \right) = f_{c,90} \left[\frac{h}{3\sin\alpha} \frac{2}{3} b \gamma_z \left(\frac{H - z_k}{tg\alpha} + \frac{h}{3\sin\alpha} \right) \right] + \\ + f_{c,\alpha} \left(\frac{k}{2} \frac{2}{3} b \gamma_1 \frac{H - z_k}{2} + \frac{z_k - o}{\sin\alpha} \frac{2}{3} b \gamma_2 \frac{z_k - o}{2} \right) \tag{6}$$

Symbols used in equations *(5)* and *(6)* are the same as was used in equations *(3)* and *(4)*.

Since forces are transferred by direct contact of the elements, it is assumed that deformations measured during experiments on those compressive areas can be influenced by decline of local stiffness. The same behaviour was observed during the compressive test in the experimental campaign,

where two different stiffnesses were obtained. The lower one, called "local", was measured in the places where material in direct contact with support and force actuator (those places showed higher deformation than specimen as a whole) was used for calculation of the deformation of the compressive areas. Other option is to calculate alternative stiffness according to *(7)* where two springs, represented two material with different stiffnesses, are connected in series.

$$K = \frac{k_g k_l}{k_g + k_l} \tag{7}$$

In *(7)* k_g is the "global" stiffness and k_l is the "local" stiffness. Approaches of using different stiffness, mentioned above were used to calculate forces from *Tab. 1*, where comparison of calculated forces according to used type of stiffness and according to the angle α between elements is shown.

Tab. 1 Forces transferred during compression of the dovetail joint

	Skew angle of the joint α								
Force	30°			45°			60°		
[kN]	k_g	k_l	K	k_g	k_l	K	k_g	k_l	K
$F_{N,1}$	23.4	18.1	18.9	24.1	20.3	21.0	24.4	21.4	22.0
$F_{N,2}$	1.6	6.9	6.1	0.9	4.7	4.1	0.6	3.6	3.0

Principle of virtual work

If an analysis of the joint should be more detailed, influence of friction forces is assumed or influence of the key on the geometry of the key should be known, the approach mentioned above cannot be used. It is necessary to made new model for the force equilibrium. More complex equilibrium to the compression is shown at *Fig. 6a)*.

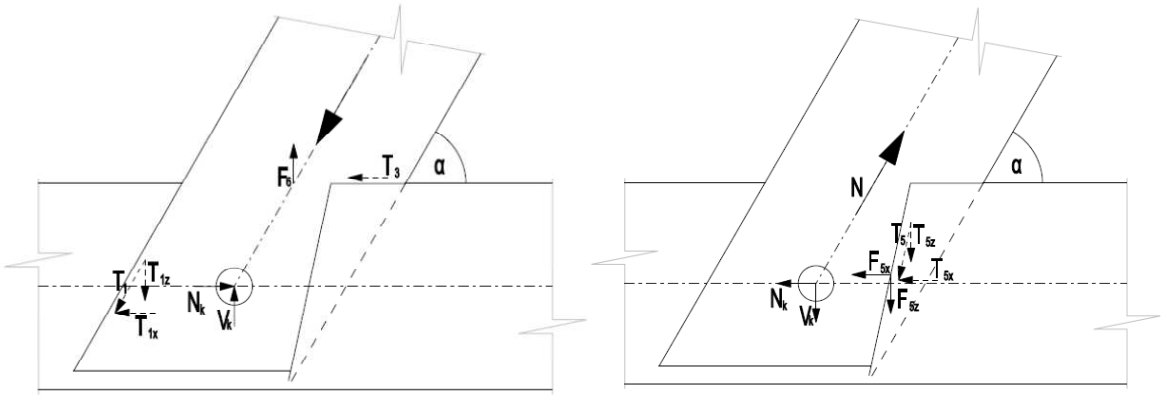

a) *b)*

Fig. 6 Forces in the joint during a) compression and b) tension

For the joint it is possible to set equations of equilibrium, three basic equations are available; equations of equilibrium in horizontal and vertical direction and one moment equation of equilibrium. In general, there are more than three unknown forces in the joint. To solve this problem, principle of virtual work [13] can be used. Thanks to the knowledge of the stiffness of wood materials it is possible to use both the virtual forces and the virtual displacements. Remaining conditions of equilibrium, which are necessary for finding the solution of equilibrium, can be replaced using principle of virtual work. For final virtual work solution *(9)*, displacement solved using approach mentioned above can be used.

In *(8)*, equations used for the joint loaded by compression force are shown. Friction forces T_i can be calculated using coefficient of friction as $T = \mu N$, where μ is the coefficient of friction and N is the compressive force acts to the friction area. Since in the joint there are only three unknown forces according to the *(8)*, it is possible to calculate equilibrium only using *(8)*.

$$\begin{aligned} &M+: F_{x6} \cdot x_{F6} - T_3 \cdot z_{T3} - T_{1z} \cdot x_{T1} - T_{1x} \cdot z_{T1} = 0 \\ &\rightarrow: -N_2 + N_k + T_{1x} + T_3 = 0 \\ &\uparrow: -V_2 + V_k + F_6 + T_{1z} = 0 \end{aligned} \qquad (8)$$

As is shown at *Fig. 6b)*, during the tension there are four unknown forces in the joint. Force which will be later calculated using the principle of virtual work is horizontal force F_{5x}. At the beginning the equilibrium is created on the essential system – joint without the F_{5x} force. In the next step force distribution on the essential system is calculated. Than the joint is loaded by non-dimensional virtual force X - usually chosen as "1". Force distribution is calculated with the virtual force. From those two states, the equilibrium of displacements according to *(9)* will be created and unknown force F_{5x} can be calculated. Force F_{5x} is equal to X_j from *(9)*.

$$\boldsymbol{\delta}_{ij} \cdot \boldsymbol{X}_j + \boldsymbol{\delta}_{i0} = \overline{\boldsymbol{\delta}} \qquad (9)$$

In *(9)* δ_{ij} is displacement in the place *i* in the direction of acting virtual force X_j, X_j is virtual force in the direction *j*, both those quantities are calculated on the joint with acting virtual force, δ_{i0} is displacement in the essential system in the place *i* and direction of *j*, $\overline{\delta}$ is displacement known from the previous chapter *"Force distribution in a dovetail joint"* in the place where X acts in its direction.

Tab. 2 Forces transferred during tension of the dovetail joint calculated based on the principle of virtual work

	Skew angle in the joint α			
Force [kN]	15°	30°	45°	60°
F_{5x}	0.9	4.6	7.9	8.3
F_{5z}	0	0	0	0
N_k	23.3	17.1	9.8	4.2
V_k	6.5	12.5	17.7	21.7

The same approach can be used for calculating force distribution for both bending moments, where even more unknown forces appear. For the positive bending moment there are six unknowns and for the negative bending moment there are seven unknowns.

CONCLUSION

Two different ways of solving the force distribution in the dovetail joint loaded by solitary forces or moments were shown. Those two approaches are possible combine to obtain more detailed solution.

It has to be pointed, that with higher inclination of the angle α between the elements, loading of the key element, which can by the weakest part of the joint, especially when wooden key is used, rises. In the analytical solution, the mechanical properties obtained from the experimental campaign performed at University of Minho were used.

Nowadays experimental test of the joint loaded by solitary forces and moments are made. Those experiments should prove theoretical behaviour shown in this paper. If the analytical solution will be in the match with the experiments, analytical solution will be extended for the combination of the forces. Behaviour of the joint, described with analytical formulas should be used for verification of results of a numerical model created in TNO Diana FEM software.

ACKNOWLEDGEMENT

The financial support by the Faculty of Civil Engineering, Czech Technical University in Prague (SGS project No. SGS14/029/OHK1/1T/11) and financial support of experimental campaign by STSM COST project FP1101 (COST-STSM-FP1101-16790) is gratefully acknowledged.

REFERENCES

[1] BRANCO, J., *et al.*, "Modelling of timber joints in traditional structures," In *International Workshop on "Earthquake Engineering on Timber Structures*, Coimbra, Portugal, 2006, pp. 1 - 15.

[2] BRANCO, J., *et al.*, "Experimental analysis of original and strengthened traditional timber connections," In *9th World Conference on Timber Engineering 2006, WCTE 2006*, Portland, OR, 2006, pp. 1314-1321, ISBN: 9781622762859.

[3] FAJMAN, P. (2013), Rozložení sil v plátovém spoji od ohybového momentu. *Stavební obzor 2013(04)*.

[4] FAJMAN, P., "A scarf joint for reconstructions of historical structures," *Advanced Material Research of Trans Tech Publications*, 2014.

[5] JASIENKO, J., *et al.*, "Study of strains and stresses in historical carpentry joints," In *Structural Analysis of Historical Constructions*, New Delhi, 2006, pp. 375-384, ISBN: 972-8692-27-7.

[6] PARISI, M. A. and CORDIÉ, C., "Mechanical behavior of double-step timber joints," *Construction and Building Materials*, vol. 24, pp. 1364-1371, 2010, ISSN: 0950-0618.

[7] PARISI, M. A. and PIAZZA, M., "Mechanics of Plain and Retrofitted Traditional Timber Connections," *Journal of Structural Engineering*, vol. 126, p. 1395, 2000, ISSN: 07339445.

[8] SANGREE, R. H. and SCHAFER, B. W., "Experimental and numerical analysis of a stop-splayed traditional timber scarf joint with key," *Construction and Building Materials*, vol. 23, pp. 376-385, 2009, ISSN: 0950-0618.

[9] SANGREE, R. H. and SCHAFER, B. W., "Experimental and numerical analysis of a halved and tabled traditional timber scarf joint," *Construction and Building Materials*, vol. 23, pp. 615-624, 2009, ISSN: 0950-0618.

[10] VILLAR, J. R., *et al.*, "Analysis of the Stress State at the Cogging Joint in Timber Structures," *Biosystems Engineering*, vol. 96, pp. 79-90, 2007, ISSN: 1537-5110.

[11] CHANG, W.-S. and HSU, M.-F., "Rotational performance of traditional Nuki joints with gap II: the behavior of butted Nuki joint and its comparison with continuous Nuki joint," *Journal of Wood Science*, vol. 53, pp. 401-407, 2007/10/01 2007, ISSN: 1435-0211.

[12] ŠOBRA, K., "Experimental and numerical analyses of dovetail joint," STSM of COST action FP1101, Guimarães2014.

[13] BITTNAR, Z. and ŠEJNOHA, J., *Numerical Methods in Structural Mechanics*: ASCE Press, 1996, ISBN: 9780727725554.

INFLUENCE OF PVA-CEMENT COMPOSITE CURING CONDITIONS ON ITS MECHANICAL PROPERTIES

Jaroslav TOPIČ[1], Zdeněk PROŠEK[2], Tomáš PLACHÝ[3], Michael SOMR[4], Václav NEŽERKA[5], Pavel TESÁREK[6]

***Abstract**: Main goal of the presented study was to investigate the influence of different curing conditions on mechanical properties of cement-PVA composite pastes. Most of the cement composites are cured in water but thanks to the instability of PVA the results can be affected. Therefore, the samples having the same composition were exposed to different curing conditions in our study to see and evaluate the effect. The first set of samples was stored in water after their removal from molds, while the second set was stored exposed to air at a constant temperature and relative humidity. To determine the influence of curing conditions on mechanical properties, the hardened specimens were subjected to destructive testing of compressive and bending strength.*

***Keywords**: Cement, PVA, mechanical properties, curing conditions*

INTRODUCTION

One of the numerous possibilities to alter the properties of cement-based materials is the addition of polymer that bonds to the cement matrix. PVA, easily soluble in water, is commonly used for such purpose [1, 2]. The properties of concrete and other cement-based materials are also significantly influenced by the curing conditions, especially at the early ages, since presence of water is responsible for the cement hydration process and material hardening [3, 4]. The purpose of this paper is to

[1] Ing. Jaroslav Topič, Czech Technical University in Prague, Faculty of Civil Engineering; Thákurova 7, 166 29 Prague 6 – Dejvice, Czech Republic, jaroslav.topic@fsv.cvut.cz

[2] Ing. Zdeněk Prošek, Czech Technical University in Prague, Faculty of Civil Engineering; Thákurova 7, 166 29 Prague 6 – Dejvice, Czech Republic, tesarek@fsv.cvut.cz

[3] Ing. Tomáš Plachý, Ph.D., Czech Technical University in Prague, Faculty of Civil Engineering; Thákurova 7, 166 29 Prague 6 – Dejvice, Czech Republic, plachy@fsv.cvut.cz

[4] Ing. Michael Somr, Czech Technical University in Prague, Faculty of Civil Engineering; Thákurova 7, 166 29 Prague 6 – Dejvice, Czech Republic, michael.somr@fsv.cvut.cz

[5] Ing. Václav Nežerka, Czech Technical University in Prague, Faculty of Civil Engineering; Thákurova 7, 166 29 Prague 6 – Dejvice, Czech Republic, vaclav.nezerka@fsv.cvut.cz

[6] Ing. Pavel Tesárek, Ph.D., Czech Technical University in Prague, Faculty of Civil Engineering; Thákurova 7, 166 29 Prague 6 – Dejvice, Czech Republic, tesarek@fsv.cvut.cz

investigate the influence of the curing conditions during the first 28 days of hardening on the mechanical properties of PVA-cement pastes.

EXPERIEMNTAL METHODS AND SAMPLES

The destructive testing was performed using standard procedures. The flexural and compressive strengths were determined on the 28 days old samples using the LabTest 4.100SP1 device. The testing was displacement controlled at a constant rate of 0.1 mm/s in the case of three-point bending and 0.3 mm/s in compression. The flexural test was accomplished on prismatic 20 × 20 × 100 mm specimens and consequently the compression was applied to the halves of the broken specimens, with the effective area of 20 × 40 mm.

Each set contained 6 samples to be tested in bending and twice as much in compression. The samples were made of Portland cement CEM I 42.5 R (Radotín, CZ) and modified using 16% PVA solution SLOVIOL® R (Fortischem, CZ). Water / cement ratio was constant, equal to 0.35. Composition of the tested specimens is summarized in Tab. 1. One half of the samples were placed into a water bath immediately after their removal from molds (24 hours after they were cast) while the other was kept at common laboratory conditions at constant temperature and humidity exposed to air.

Tab. 1 Composition of the tested samples

Set	Curing conditions	PVA [wt. %]	Cement [g]	w/c = 0.35	
				Water [g]	PVA solution [g]
CEM	dry/wet	0.0	1000	350.0	0.0
PVA 1.4	dry/wet	1.4	1000	232.5	87.5
PVA 4.0	dry/wet	4.0	1000	100.0	250.0

EXPERIEMNTAL RESULTS

The experimental results are provided in Figs. 1-3. The compressive strength of PVA-enriched cement pastes was significantly reduced and almost constant with respect to the PVA content, see Fig. 1. The drop in strength was probably caused by an increase of porosity, responsible for the effective area reduction and stress concentration near large pores. The strength reduction was more pronounced in the case of samples cured exposed to air (dry).

The flexural strength is proportional to the amount of PVA in the cement paste as clearly demonstrated in Fig. 2. When compared to the reference cement paste samples, the PVA modification clearly contributed to the higher values of flexural strength. The results presented in Fig. 3 demonstrate the influence of PVA on the values of Young's modulus, which is reduced in the early stages of hardening in the case of the PVA-modified pastes, compared to the reference samples.

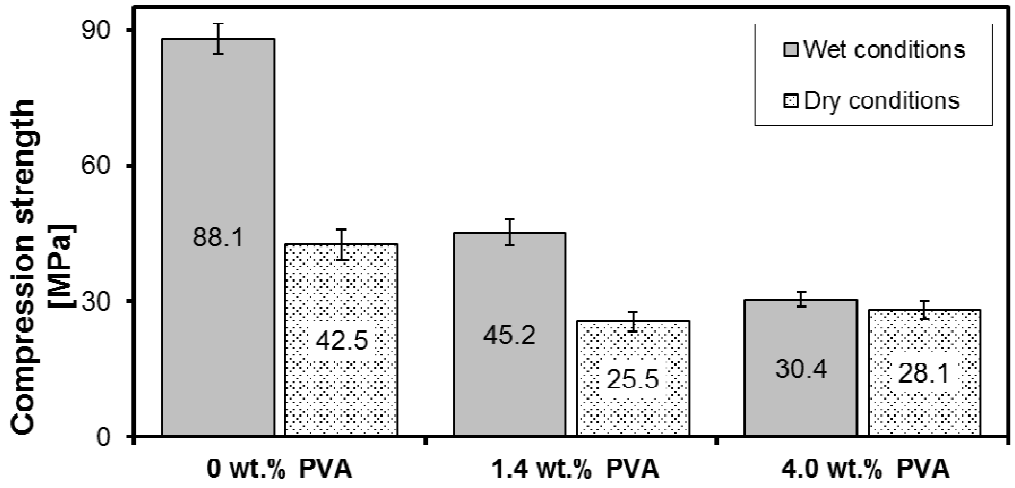

Fig. 1 Dependence of the compressive strength on the amount of PVA in cement pastes after 28 days.

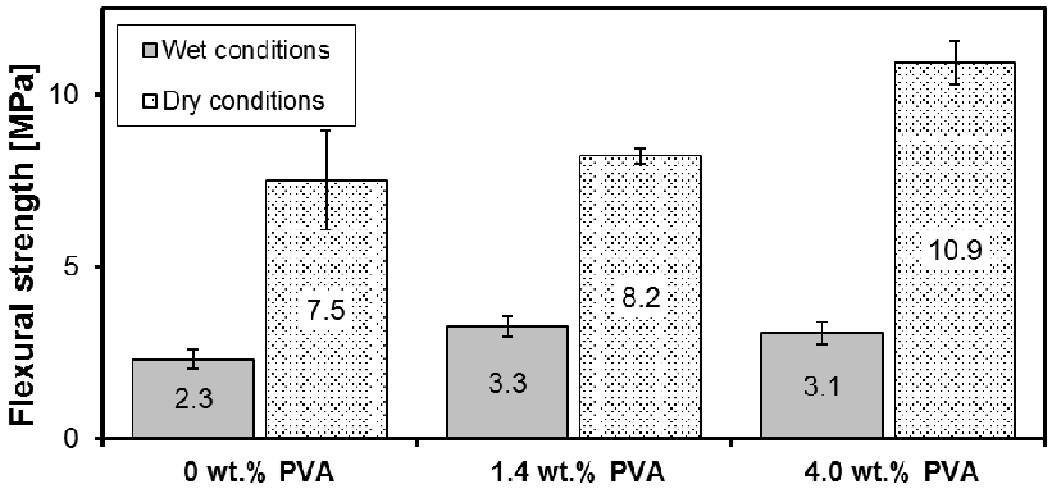

Fig. 2 Dependence of the flexural strength on the amount of PVA in cement pastes after 28 days.

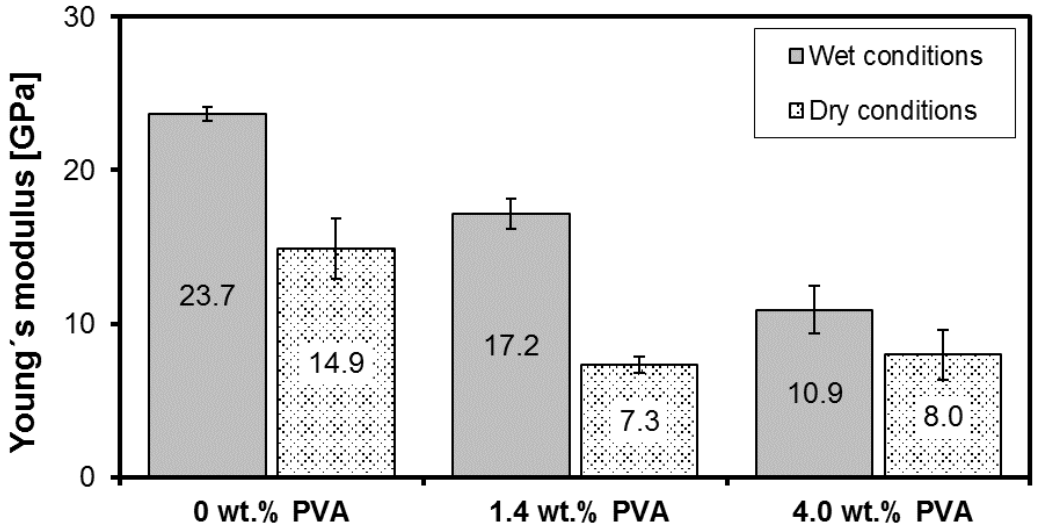

Fig. 3 Dependence of the Young's modulus on the amount of PVA in cement pastes after 28 days.

Based on the presented results it is obvious that the PVA additions to a cement paste contribute to the reduction of compressive strength and values of Young's modulus. On the other hand, the PVA-modified pastes exhibited higher flexural strength. The curing conditions have even more significant impact on the mechanical performance of cement pastes – making the cement pastes less resistant to tensile stresses during three-point bending and stronger with respect to compressive loading. The non-destructive testing appears to be a suitable tool for monitoring of mechanical properties in time to accurately capture the hardening mechanism in different curing conditions [5, 6].

CONCLUSION

The addition of a suitable amount of PVA to the cement-based composites can favorably modify their properties, such as mechanical strength parameters. A maximum amount of 4 % of the cement mass is usually pursued. The PVA additions result in the reduction of the material stiffness and compressive strength, but the ability of the composite to withstand tensile stresses is supported.

ACKNOWLEDGEMENT

The financial support of this experiment by the Faculty of Civil Engineering, Czech Technical University in Prague (SGS project No. SGS14/122/OHK1/2T/11 and SGS14/029/OHK1/1T/11) and Technology Agency of the Czech Republic – Competence Centers under No. TE01020168 Centre for Effective and Sustainable Transport Infrastructure (CESTI) are gratefully acknowledged. Thanks also belong to the Center for Nanotechnology in Civil Engineering at FCE CTU in Prague and Joint Laboratory of Polymer Nanofiber Technologies of Institute of Physics Academy of Science of Czech Republic and FCE CTU in Prague.

REFERENCES

[1] SING, N. B., RAI, S. Effect of polyvinyl alcohol on the hydration of cement with rice husk ash. In: *Cement and Concrete Research*, vol. 31, 2001, p. 239-243. ISSN 0008-8846.

[2] MORLAT, R. et al. Reinforcement of hydrated Portland cement with high molecular mass water-soluble polymers. In: *Journal of Materials Science*, vol. 42, 2007, p. 4858-4869. ISSN 1573-4803.

[3] BENSTED, J. and BARNES, P. *Structure and Performance of Cements*. London, Spon Press, 2002, pp. 1-108, ISBN 0-203-47778-2.

[4] ZONGJIN LI. *Advanced Concrete Technology*. New Jersey, John Wiley & Sons, Inc., 2011, pp. 23-320, ISBN 978-0-470-43743-8.

[5] PADEVĚT, P., TESÁREK, P., PLACHÝ, T. Evolution of Mechanical Properties of Gypsum in Time, In: *International Journal of Mechanics*. 2011 (1) 1-9.

[6] ŤOUPEK, R., PLACHÝ, T., POLÁK, M., TESÁREK, P. Vývoj hodnot mechanických vlastností sádry v průběhu jejího tvrdnutí, In: *The 10th International Conference on New Trends in Statics and Dynamics of Buildings*, Bratislava, 2012, pp. 171-174.

COMPARISON OF DYNAMIC AND STATIC STIFFNESS VALUES IN TIME EVOLUTION: MECHANICAL PROPERTIES OF GYPSUM SAMPLES

Richard ŤOUPEK[1], Jaroslav TOPIČ[2], Zdeněk PROŠEK[3], Pavel TESÁREK[4], Tomáš SVOBODA[5], Tomáš PLACHÝ[6]

***Abstract**: The paper presents monitoring of mechanical properties of the gypsum samples. Especially, the stiffness evolution in time is investigated. It is monitored using destructive (stress test) and non-destructive (resonance method) methods. The stiffness was determined non-destructively at first and then destructively. The results gave us the time dependent changes of the gypsum stiffness. From the comparison of the stiffness values determined non-destructively and destructively, it is evident that results from non-destructive testing are about 30 % higher.*

***Keywords**: stiffness, dynamic method, static method, gypsum, mechanical properties*

INTRODUCTION

For testing of mechanical properties of porous building materials there are usually used destructive methods at present. The samples are irreversibly damaged during these tests and test cannot be repeated on the same sample [1, 2]. This state can be seen also in Czech standards which deal with determination of the mechanical properties because the mention of non-destructive tests occurs mostly only for determination of the frost resistance of the materials.[3].

[1] Ing. Richard Ťoupek, Czech Technical University in Prague, Faculty of Civil Engineering; Thákurova 7, 166 29 Prague 6 – Dejvice, Czech Republic, richard.toupek@fsv.cvut.cz

[2] Ing. Jaroslav Topič, Czech Technical University in Prague, Faculty of Civil Engineering; Thákurova 7, 166 29 Prague 6 – Dejvice, Czech Republic, zdenek.prosek@fsv.cvut.cz

[3] Ing. Zdeněk Prošek, Czech Technical University in Prague, Faculty of Civil Engineering; Thákurova 7, 166 29 Prague 6 – Dejvice, Czech Republic, zdenek.prosek@fsv.cvut.cz

[4] Ing. Pavel Tesárek, Ph.D., Czech Technical University in Prague, Faculty of Civil Engineering; Thákurova 7, 166 29 Prague 6 – Dejvice, Czech Republic, tesarek@fsv.cvut.cz

[5] Bc. Tomáš Svoboda., Czech Technical University in Prague, Faculty of Civil Engineering; Thákurova 7, 166 29 Prague 6 – Dejvice, Czech Republic, tomas.svoboda.1@fsv.cvut.cz

[6] Ing. Tomáš Plachý, Ph.D., Czech Technical University in Prague, Faculty of Civil Engineering; Thákurova 7, 166 29 Prague 6 – Dejvice, Czech Republic, plachy@fsv.cvut.cz

The most widely used non-destructive methods, which can be used for testing of mechanical properties of materials, are ultrasound and impulse excitation methods [4, 5].

TESTED SAMPLES AND USED METHODS

Tested samples were made from the grey gypsum binder (Gypstrend, Ltd. Czech Republic) with the water/gypsum ratio 0.71. The samples have the standard dimensions 40 × 40 × 160 mm. The samples were unmolded after 30 minutes and stored freely in the laboratory conditions with the average temperature 20 °C and relative humidity 50 %.

At first, the impulse excitation method was used for determination of the dynamic Young's modulus on each of the specimen. The specimen was supported in the middle of its span - the fundamental longitudinal nodal position. The acceleration transducer was placed at the centre of one of the end faces of the gypsum specimen. The opposite end face was struck by the impact hammer. Both signals, the excitation force and the acceleration, were recorded and transformed using Fast Fourier Transform (FFT) to the frequency domain, and the Frequency Response Function (FRF) was evaluated from these signals using the vibration control station Bruel&Kjaer Front-end 3560-B-120 and program PULSE 14.1. The test was repeated five times for each gypsum specimen and resultant readings were averaged. From an averaged FRF, the fundamental longitudinal resonant frequency was determined for each specimen.

Based on the equation for longitudinal vibration of the beam with continuously distributed mass with free-free boundary condition, the dynamic Young's modulus E_{dl} can be determined using the relation

$$E_{dl} = \frac{4lmf_l^2}{bt} \qquad (1)$$

where l is the length of the specimen [m], m is the mass of the specimen [kg], f_l is the fundamental longitudinal resonant frequency of the specimen [Hz], b is the width of the specimen [m] and t is the thickness of the specimen [m].

After non-destructive testing, the specimens were tested destructively in three-point bending test and in standard stress test.

EXPERIMENTAL RESULTS

From the results on the Fig. 1 it is evident that there are differences in mechanical properties – in this case stiffness. The difference between maximal and minimal value is about 30 %. The maximal value was achieved at the time of three days from the specimen creation. The comparison of the stiffness from the non-destructive and destructive measurements is mentioned in the Fig. 2. The values of the stiffness were calculated as an average of three measurements, the maximal standard deviation

was 10 %. From the Fig. 2 it can be seen that the difference between non-destructive and desteructive testing decreases in time which could be caused by the decrease of the water content in specimens.

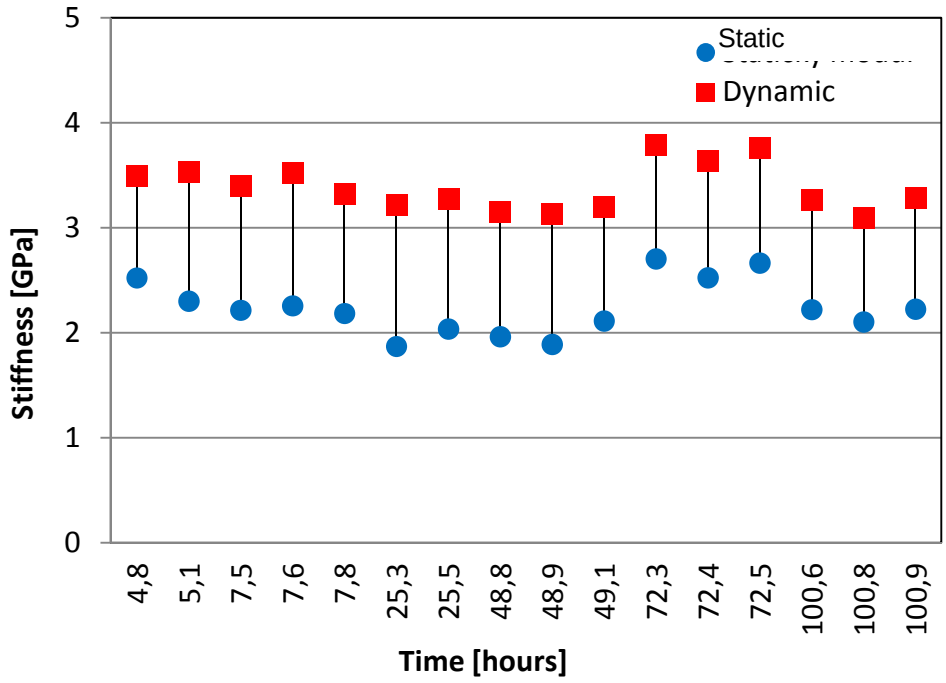

Fig. 1 Time evolution of static and dynamic stiffness

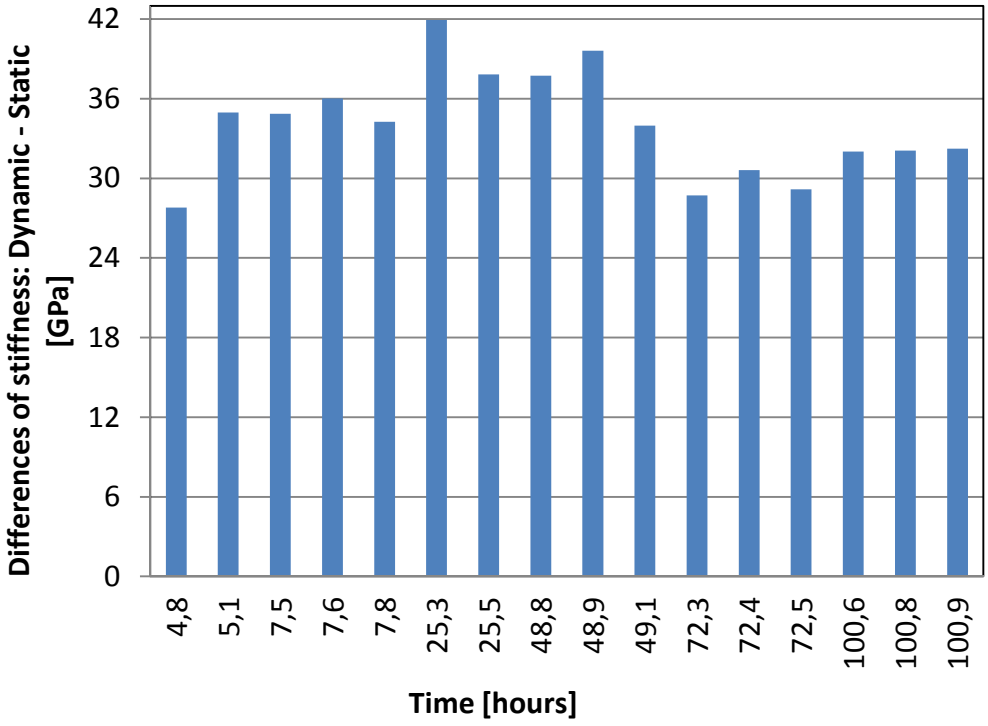

Fig. 2 Differences between dynamic and static stiffnesses – time dependence.

CONCLUSION

The time evolution of the stiffness of the gypsum specimens was determined using two different methods in the initial phase of development of a solid structure after hardening of the gypsum slurry. It is evident from the obtained results that the results from both methods are comparable with respect to the time dependence and both methods can be used.

Especially, it is suitable to use non-destructive tests when the mechanical behavior is needed to determine in time or environment dependence because these methods eliminate disadvantages of destructive methods.

ACKNOWLEDGEMENT

The financial support of this experiment by the Faculty of Civil Engineering, Czech Technical University in Prague (SGS project No. SGS14/122/OHK1/2T/11) is gratefully acknowledged. Special thanks belong to the Center for Nanotechnology in Civil Engineering at Faculty of Civil Engineering CTU in Prague.

REFERENCES

[1] PADEVĚT, P., TESÁREK, P. and PLACHÝ, T. Evolution of mechanical properties of gypsum in time, *International Journal of Mechanics*, 2011, 5, 1-9. ISSN: 1998-4448

[2] NĚMCOVÁ, H. et al. Influence of Moisture to Mechanical Properties of Materials, In*: Engineering Mechanics 2011*, Praha: Ústav termomechaniky AV ČR, 2011, p. 411-414. ISBN 978-80-87012-33-8.

[3] ŤOUPEK, R. et al. Changes of the Dynamic Modulus of Elasticity in Dependence on the Number of the Freeze-Thaw Cycles, In: *Proceedings of the 4th Conference Nano & Macro Mechanics*. Praha: Czech Technical University in Prague, 2013, p. 211-214. ISBN 978-80-01-05332-4.

[4] PLACHÝ, T. et al. Monitoring of Mechanical Properties Evolution of the Cast Gypsum, *Procedia Engineering*, 2012, **48**, 562-567. ISSN 1877-7058.

[5] ŤOUPEK, R. et al. Monitoring of Mechanical Properties of Gypsum Using the Impulse Excitation Method, In: *Recent Advances in Mechanical Engineering and Automatic Control*. Athens: WSEAS Press, 2012, p. 163-167. ISBN 978-1-61804-142-5.

[6] ŤOUPEK, R., PLACHÝ, T. and TESÁREK, P. Development of Mechanical Properties of Gypsum During its Hardening, In: *Proceedings of the 3rd Conference Nano and Macro Mechanics NMM 2012*. Praha: Czech Technical University in Prague, Faculty of Civil Engineering, 2012, p. 253-258. ISBN 978-80-01-05097-2.

EXPERIMENTAL ANALYSIS OF VIBRATION GRANDSTANDS CAUSED BY CROWD OF SPECTATORS

Martin Verner[1]

***Abstract**: The paper describes a research in experimental measurement of vibration of sport stadium grandstands superstructure caused by the behavior of fans during sporting matches. The arrangement of the experiment and the process of gathering the results are described in the first part of the paper. The second part presents the results obtained during two specific football matches – AC Sparta Praha vs. FK Teplice (November 2nd 2014) and AC Sparta Praha vs. FK Mladá Boleslav (November 24th 2014). Natural frequencies of the superstructure were experimentally determined. Furthermore, the maximum levels and the dominant frequencies of the forced vibration caused by intense cheering of the crowd were identified.*

***Keywords**: Grandstands, natural frequency, stadium Letna, FFT, dynamic experiment*

INTRODUCTION

The behavior of supporters has changed significantly during last years. They are not passive more but they support actively their teams. Together with this change, structural changes of stadiums are introduced. The main goal is the capacity. Because the biggest challenge is the overall urban development, architects are projecting multi-floor grandstands with a long cantilever beam. This combination leads to the point that the most interesting thing is dynamic load. Today, dynamic load is not fully described in any standard. There are running experiments during matches and music concerts to compute this load. This article is about measurement done during two football matches.

THE FOOTBALL STADIUM LETNA

The experiment was done during a match on the Letna stadium. This is the home stadium of AC Sparta Prague (Sparta). This stadium was chosen because of two major points: the supporters are one of the most active on today's football scene and secondly, the stadium is constructed using a long steel-concrete cantilever beam. Combination of these factors leads to the maximum dynamic response of the construction.

History

The stadium has been used since 1917. In year 1934 it was decided to rebuild it for a capacity of 45 000 people, but in the same year the main grandstand was burned down. So in year 1937, new iron-

[1] Ing. Martin Verner, Department of Mechanics, Faculty of Civil Engineering, Czech Technical University in Prague, martin.verner@fsv.cvut.cz

concrete one was opened. Between years 1967 and 1969 all other grandstands were replaced by new from iron and concrete with the steel cantilever beam. Outer grandstand, which is pointed to the "Letenska plan" was used by communist functionaries during celebration of the 1st May, army shows etc. On the 9th of September 1994 was the stadium completely modernized, only seated places remain and the stadium meets all standards. From 2002, the stadium has heated grass. [1, 2]

Fig. 1 Grandstand Letna [3]

Fans placement and their behavior during match

Most active fans are called "Ultras" or "Banner-carriers". This group is well organized and lead by one guy. "Ultras" are located in a small piece of the stadium. This part is called "Kotel". "Kotel" is most of the time responsible for atmosphere, leading all fans, performing chores (visual supporting). But they are responsible also for the biggest problems on stadiums. The biggest problems are the fun pyrotechnic during matches, interrupting the match or even stopping the match at all by their fights.

In the last years (since 2004), new supporting method was introduced in Czech sports - jumping. Fans are dragged more in the match and new shouts like "Jump, if you are Spartan!" started. Leaded by "Kotel", usually the whole stadium starts too. Passive fans become active and the active even more active. The passive fans are not a big risk during this type of supporting, but the "Kotel" is well organized and is really fast synchronized to the rhythm of the shout.

At the beginning of century, "Kotel" of Spartans made big problems. It was located just next the gate at the east side of the stadium. Management of Sparta tried to get these fans out of the stadium. The tickets were sold only on name and the police patrols were usually there. The result of all these things was just that the "Kotel" moved from the ground floor to the first floor of the stadium. It is located now at the end of balcony grandstand which is causing the biggest effects.

Fig. 2 View of the "Kotel" [4]

Fig. 4 Experiment set up - location of sensors [5]

EXPERIMENT

The experiment began few days before the first match. After the grandstand was investigated, places which will have the biggest dynamical response in vertical direction were chosen. Horizontal direction was not measured during this experiment. Piezoelectric sensors Delta Tron, type 4507 B005 were used. Dimensions of this sensor are: 10 mm × 10 mm × 10 mm, weight: 5 g. They were attached to the construction using magnets. Under the "Kotel" part of the grandstand, four steel cantilever beams were located. We found a microphone on one of these beams. Even the stadium owners didn't know the purpose of this microphone and we were using strong magnets, so this beam was refused from the experiment. Sensors were put at the end of each remaining beams. Sensors were connected via cables to the measurement infrastructure, which was located next to the "Kotel" part of the grandstand. This leads sometimes to the situation where the infrastructure was affected by the smoke from pyrotechnic (smoke bombs and flares).

EVALUATION PRINCIPLE

The experiment was evaluated by software, which was developed by prof. Polák, and it is called Program Material Damping. Evaluation was carried out that each record was transformed from the time domain to the frequency domain using the Fast Fourier Averaging's Transformation (AFFT). Averaging was conducted over 2^n samples using Hanning window weighting. The frequency that the fans were able to induce was compared to the natural frequency of the grandstands. For better evaluation and reducing compute claims, matches were not recorded continuously but were divided into several sections.

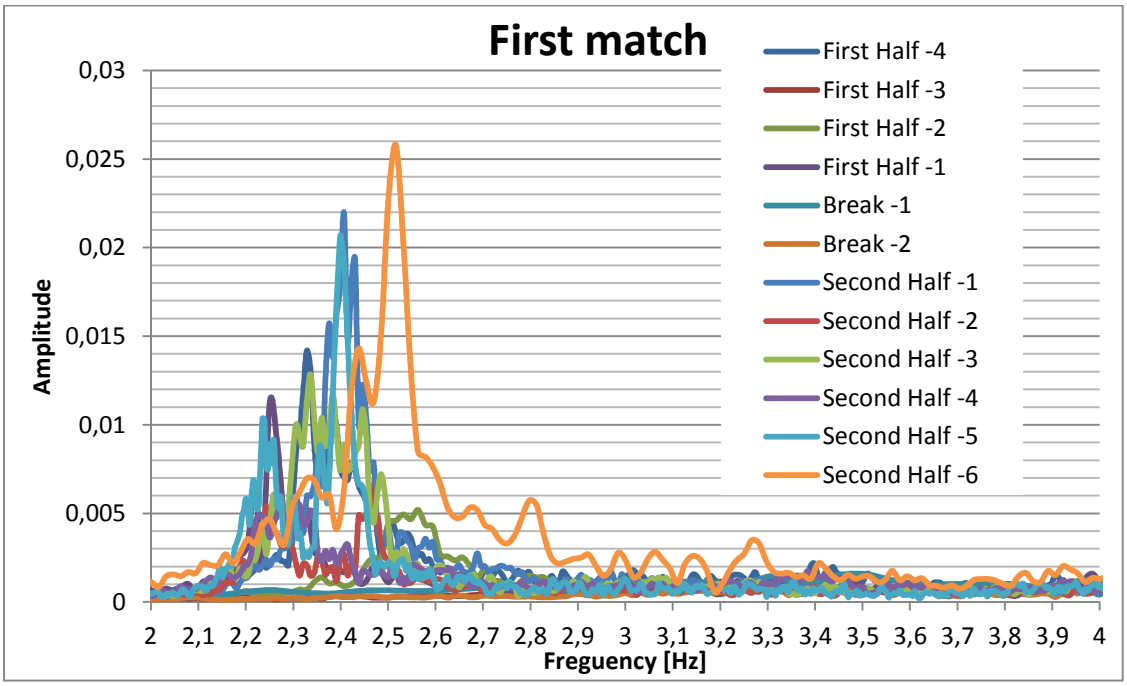

Fig. 5 Frequency level of the first match (area: 2-4Hz)

Subsequent evaluation was performed by using the software Microsoft Excel. Only values of frequencies under 4 Hz were processed. First, the frequencies induced by viewers during its encouragement were determined. Then, the natural frequencies of the grandstands were determined. For better illustration the individual records were graphically plotted into one record. The graphical illustration allows us to observe the changing of the frequency of spectators during the match.

EXPERIMENT EVALUATION

Match Sparta – FK Teplice (2. 11. 2013)

Short description: Match Sparta - FK Teplice was played in the 13th round of Gambrinus 's League. The result of the match was 2:0 for Sparta. Goals for Sparta were scored by Brabec (45 +1 min) and Costa (81min). The greatest dynamic response was recorded during the experiment at this time. .

The graph shows: Viewers caused the most dynamic response during the celebration of goals scored (2.40 Hz) Maximum response was achieved when the fans thanked his team at the end of the match (2.52 Hz).

Match Sparta – FK Mladá Boleslav (23. 11. 2013)

Short description: Match Sparta - FK Mladá Boleslav played in the 15th round of Gambrinus ’s League. The result of the match was 4:1 for Sparta. Goals for Sparta were scored by Krejčí (43 min), Hušbauer (67min), Costa (81min) and Bednář (90min). The greatest dynamic response was recorded during the experiment at this time.

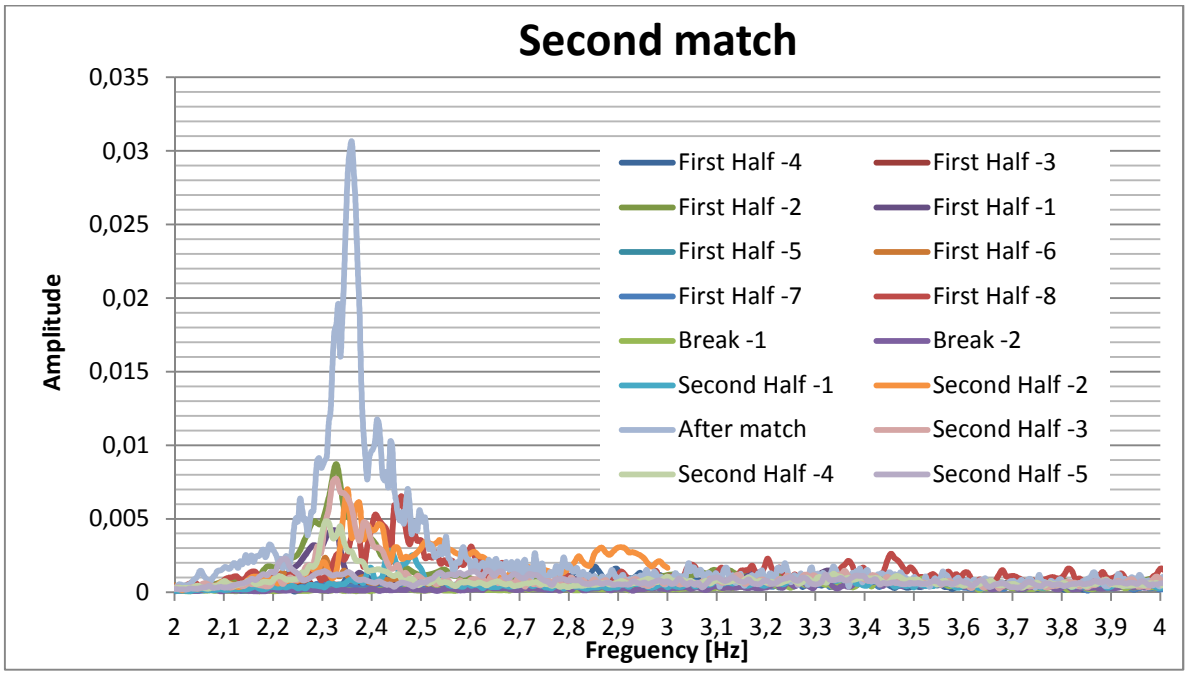

Fig. 6 Frequency level of the second match (area: 2-4Hz)

The graph shows: Viewers caused the most dynamic response during the celebration of goals scored (2.33 Hz). Maximum response was achieved when the fans thanked his team at the end of the match (2.34 Hz). This fully corresponds with the results that were achieved in the first match. This was the last match during the autumn part of the Gambrinus ’s League, after the match the fans performed the popular choreo that caused the greatest dynamic response during the experiments.

Graph also show that the biggest dynamical response was recorded during goals scored by Costa and Bednar, as they are the favorite players of the crowd.

Natural frequency of the grandstand

The natural frequencies of the grandstand were also determined during the experiment. Based on the evaluation of the two matches the frequencies of the grandstand are defined as follows:

Tab. 1 Natural frequencies of the grandstand

Frequency number	Frequency value [Hz]
1	2.66
2	2.89
3	2.98
4	3.06
5	3.27
6	3.45
7	3.83

Other frequencies were not evaluated.

The experiment cannot determine at which frequency the beams vibrate by them self and when the grandstand vibrates as whole. To determine these quantities, it would be necessary perform other experiment. This experiment is planned in the future.

CONCLUSION

The experiment deals with frequencies which fans produce during sports events. The results had shown that fans are most active in the times when the team scores a goal and then after the matches are over and fans give thanks to players for the enjoying the match. Fans are able to cause the frequency close to the natural frequency of the grandstand Letna. In the future there will be performed several experiments (eg Holešovice sport hall, stadium U Nisa), which will confirm the validity of the experiment results from the grandstand Letna.

ACKNOWLEDGEMENT

The financial support of this experiment by the Faculty of Civil Engineering, Czech Technical University in Prague (SGS project No.14 /122/OHK1/2T/11) is gratefully acknowledged.

REFERENCES

[1] *Stadion Sparty na Letne* [online]. [cited 2014-07-14]. Available from: http://cs.wikipedia.org/wiki/Stadion_Sparty_na_Letn%C3%A9

[2] *Generali Arena* [online]. [cited 2014-07-14]. Available from: http://www.sparta.cz/cs/klub/generali-arena.shtml

[3] *Fotbalový stadion zboří! Místo něj vyroste jiný! Národní!* [online]. [cited 2014-07-14]. Available from: http://www.ahaonline.cz/clanek/musite-vedet/1912/fotbalovy-stadion-sparty-zbori-misto-nej-vyroste-jiny-narodni.html

[4] *Foto Report: AC Sprat Praha – FC Slovan Liberec* [online]. [cited 2014-07-14]. Available from: http://www.supporters.cz/clanek/fotoreport-ac-sparta-praha-fc-slovan-liberec/5961.html

[5] *Na Špionáži: Ac Sparta Praha – FK Jablonec* [online]. [cited 2014-07-14]. Available from: http://www.supporters.cz/clanek/na-spionazi-ac-sparta-praha-fk-jablonec/4805.html

FROST RESISTANCE OF CEMENT-FLY ASH COMPOSITES

Ondřej ZOBAL[1], Pavel PADEVĚT[2], Tereza OTCOVSKÁ[3]

***Abstract**: One of the main indicators of the durability of building construction or building material is the frost resistance. This paper deals with the frost resistance of the binder in concrete, namely cement-fly ash composites. Mixtures with fly ash were compared with the reference cement paste. Substitution of fly ash was 40 and 50% by weight of cement. The specimens were subjected successively 50, 100 and 150 freeze-thaw cycles. It was a destructive type of a test for frost resistance, where the endpoint was the change in weight of specimens and their waste during freeze-thaw cycles.*

***Keywords**: cement, fly ash, freeze-thaw resistance*

INTRODUCTION

Durability of building structures and materials is currently under construction one of the most important factors. The proof is the inclusion of the durability of in the European Union in CPR (Construction Products Regulation) between the basic requirements for building construction and materials [1]. The basic indicator of the durability of building material is frost resistance. Frost resistance of binder is essential especially for the concrete. This experiment is concretely focused on cement-fly ash binder. When substitution of clinker with fly ash is carried, it has an impact on the material and mechanical properties of the resulting mixture [2]. As shown in the literature, the use of fly ash in concrete binder by over unwarranted negative opinions should not be a problem for resistance to alternation freezing and thawing [3]. Example from practice is construction of the body dam Orlik, where was replaced from nearly 30 % cement with fly ash in the design of concrete mixtures. This concrete even after more than 50 years in operation exhibits excellent mechanical and material properties [4]. During the construction, the frost resistance was checked, among many other parameters, when the decrease in tensile strength and compressive strength after 150 freeze-thaw cycles against not frozen samples [5] was measured. For elimination of distrust in this issue, it is important to carry out further experiments. The experiments would be especially long term. This paper compares the frost resistance of the cement paste and the cement-fly ash mixture with the substituting

[1]Ing. Ondřej Zobal, Faculty of Civil Engineering, Czech Technical University, ondrej.zobal@fsv.cvut.cz

[2]Ing. Pavel Padevět, Ph.D., Faculty of Civil Engineering, Czech Technical University, pavel.padevet@fsv.cvut.cz

[3]Ing. Tereza Otcovská, Faculty of Civil Engineering, Czech Technical University, tereza.otcovska@fsv.cvut.cz

clinker 40 and 50%. The specimens were 17 and 32 months old. Frost resistance was measured by a destructive method. The specimens were subjected to 50, 100 and 150 freeze cycles. It has been intended to change weights of samples and waste.

POSSIBILITIES OF MEASURING FROST RESISTANCE

The frost resistance can be determined in various ways. The most frequently used procedure according to ČSN 73 1322 - Determination of frost resistance of concrete (1969) [6]. Specimens must be in the form of the beams with dimensions 100 x 100 x 400 mm and must be saturated. The samples are exposed during the test cycles freezing at -15 to -20°C for 2 hours and thawing at +15 to +22°C for 4 hours. The number of cycles is as needed 50, 100 or 150. The monitored parameters are - weight loss, change in tensile strength for bending and compressive strength. Coefficient of frost resistance is derived from the ratio of the tensile strength of frozen and not frozen samples. Although it is the most frequently used approach, so major disadvantage associated with modern cements is that the tensile strength in bending can increase in concrete during freeze-thaw cycles and thus the coefficient of the frost resistance can be greater than 1 [7]. An alternative to destructive testing frost resistance is the standard ČSN 73 1326 - Resistance of cement concrete surface to water and defrosting chemicals (1985) [8]. The main difference is that the test specimens are stored in NaCl. The weight of the waste is measured during freeze-thaw cycles. .The standard ČSN 73 1380 - Testing the freeze-thaw resistance of concrete - Internal structural damage (2007) [9] describes the non-destructive test method of the frost resistance. But this approach is not yet used too. The principle is to determine the relative change in the dynamic modulus of elasticity of specimens after freeze-thaw cycles based on the transit time of ultrasonic pulses or a transverse frequency. The disadvantage, however, is the absence of the evaluation criteria and the length of the freezing cycle of 12 hours [1].

COMPOSITION OF THE MIXTURE AND SPECIMENS

For the measurement of the frost resistance, there were used specimens made from a mixture of the following composition. As a reference mixture has served "pure" cement paste -100% cement and 0% fly ash (designation CFA 1000). The other two mixtures were made by substitution of cement with fly ash - 40 and 50% (designation CFA 6040 CFA and CFA 5050). The ratio of water and binder was 0.4 for all mixtures. For the production of mixtures there were used Portland cement CEM I 42.5 R (Radotín) and fly ash from the power plant Mělník (conforming to ČSN EN 450-1 - fly ash in concrete).

The specimens had the beam shape of dimensions 40 × 40 × 160 mm. The samples were 17 and 32 months old (designation new and old).Six groups of specimens (3 different mixes, 2 different ages) were used for measurements. Three specimens made of each mixture (total of 18 test specimens) were used. All specimens were stored all the time of ripening in a water bath. Specimens were fully

saturated. Standard for testing the frost resistance requires fully saturated specimens. Before the measurements, all specimens were measured and the initial weights were recorded. .The volume density was calculated from the measured dimensions and weights. The age of specimens does not affect the volume density (maximum difference 1.6%). The expected effect of the volume density has substitution of cement with fly ash. The reference mixture has a value of volume density 1980 kg/m^3, at 40% substitution of cement there was a decrease by 6.6 % (1850 kg/m^3) and substitution of 50% by weight of cement, it was 9.6 % (1790 kg/m^3). Tab. 1 summarizes the composition of the mixture and volume density.

Tab. 1 Composition and designation of test mixtures and their volume density

Designation	Mixture		w/b	Age	ø Volume density
-	cement [%]	fly ash [%]	-	[months]	[kg/m^3]
CFA 1000 new	100	0	0.4	17	1990
CFA 1000 old	100	0	0.4	32	1962
CFA 6040 new	60	40	0.4	17	1844
CFA 6040 old	60	40	0.4	32	1856
CFA 5050 new	50	50	0.4	17	1780
CFA 5050 old	50	50	0.4	32	1806

METHODOLOGY FOR MEASUREMENT

The methodology for measurement is based on standard ČSN 73 1322. The specimens were successively subjected to 50, 100 and 150 the freeze cycles. The climatic chamber firm Weiss WKL 100 (Fig. 1) was used for the measurement. Each cycle consists of two phases. The first phase is freezing - temperature -20°C, duration of 4 hours. The second phase is thawing - temperature +20°C, duration 2 hours. The monitored parameter is the change in weight of each of specimens and possibly also the weight of the waste after each set of cycles.

Fig. 1 Climatic chamber Weiss WKL 100

EVALUATION OF MEASUREMENT

The results of the measurement of frost resistance for each mixture were summarized in the following tables 2-4. There is always the designation of the mixture, the number of freeze-thaw cycles and change in weight for younger and older specimens. Weight is then converted to percentages.It can be seen that the trend is very similar for all mixtures.After the maximum number of freeze-thaw cycles (150 cycles) Minimal weight loss (up 1.6% compared to not frozen specimens) is after the maximum number of freeze-thaw cycles (150 cycles). There was not identified any waste. Tables are complemented by a graphical representation of the results. The comparison of the trend of weight changes of younger and older specimens can be seen in Figures 2-4.

Tab. 2 Weight after freeze-thaw cycles for cement binder without fly ash

	cycles	m [g] - new	[%]	m [g] - old	[%]
CFA 1000	0	481	100.00	501	100
	50	480	99.79	500	99.80
	100	479	99.58	499	99.60
	150	474	98.54	496	99.00

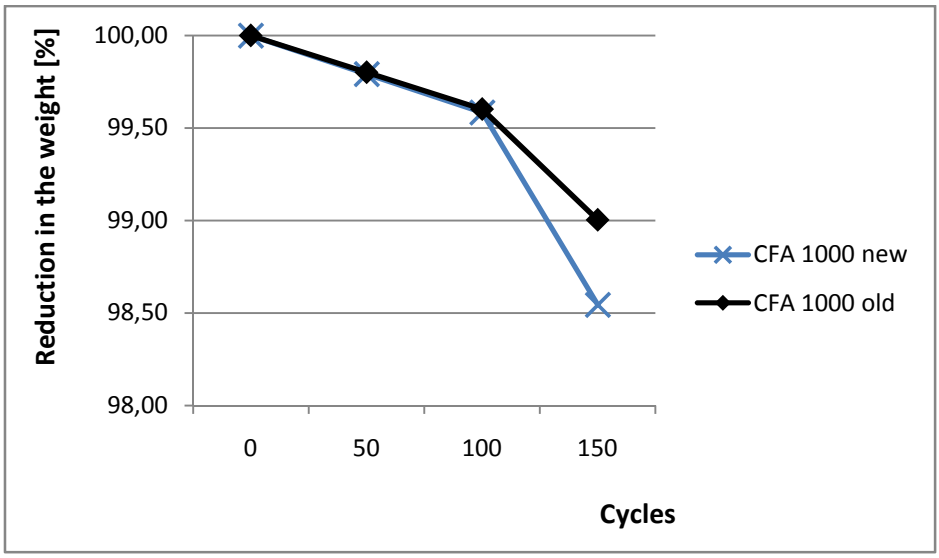

Fig. 2 Trend of weight loss cement paste without fly ash at different ages in percentages

Tab. 3 Weight after freeze-thaw cycles for cement binder with 40 % fly ash

	cycles	m [g] - new	[%]	m [g] - old	[%]
CFA 6040	0	465	100	448	100
	50	463	99.57	447	99.78
	100	462	99.35	446	99.55
	150	459	98.71	442	98.66

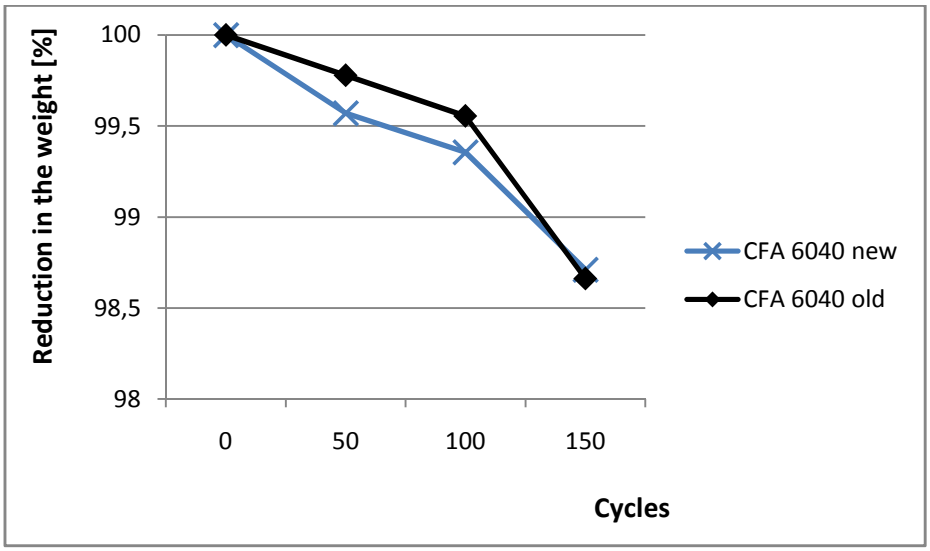

Fig. 3 Trend of weight loss cement paste with 40 % fly ash at different ages in percentages

Tab. 4 Weight after freeze-thaw cycles for cement binder with 50 % fly ash

	cycles	m [g] - new	[%]	m [g] - old	[%]
CFA 5050	0	456	100	434	100
	50	455	99.78	433	99.77
	100	454	99.56	432	99.54
	150	451	98.90	429	98.85

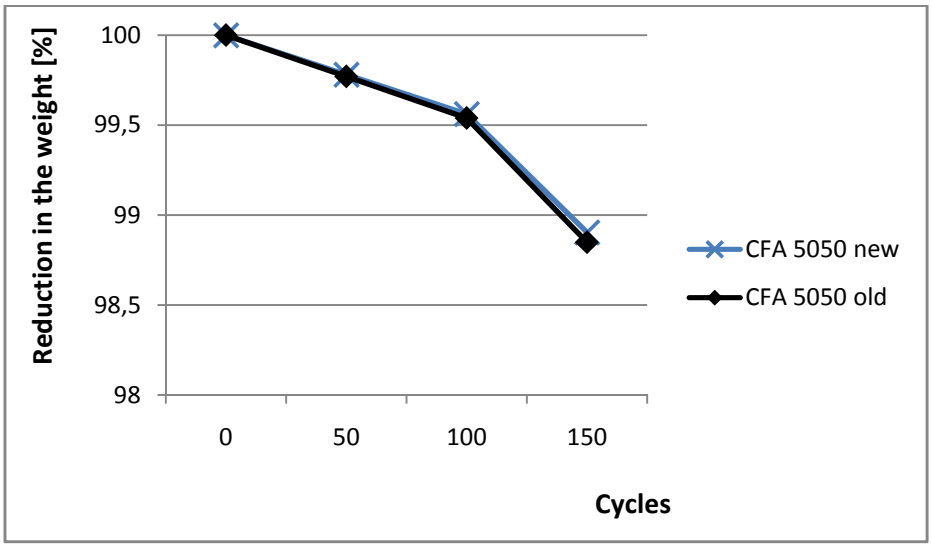

Fig. 4 Trend of weight loss cement paste with 50 % fly ash at different ages in percentages

CONCLUSION

In the design and projects of building construction, there is often neglected the important factor of material resistance to alternating cycles of freezing and heat. Therefore, this issue should be given more attention. Long-term experiments should also serve for this. For the binder in concrete, wherein the cement is replaced with fly ash, it is a particularly important aspect. Fly ash due to his belated

pozzolanic activity enters into process of hydration in the course of time. This paper describes the destructive testing frost resistance of cement binder specimens with different substitution of clinker. Specimens with substitution of 0, 40 and 50% of fly ash by weight of cement were subjected successively to 50, 100 and 150 of the freeze cycles. From the performed measurements there can be seen that the weight loss after freezing cycles is minimal. The substitution of clinker with fly ash did not affect the results. Age of specimens also had not effect to the frost resistance. It can be deduced from this initial measurement durability cement binder mixtures with fly ash, that fly ash should not adversely affect the frost resistance. The goal of further work is confirm this assertion. It will be tested for tensile strength. Then the frost resistance coefficient will be determined. We would like to made comparison of frost resistance using non-destructive methods. Furthermore, we perform a test of the frost resistance of concrete samples from the body of the Orlík dam after more than 50 years in operation. If the results of the further planned measurements will end positively, we believe it will help to alleviate the skepticism concerning to the greater use of fly ash in cement and concrete.

ACKNOWLEDGEMENT

This paper has been supported by the Faculty of Civil Engineering, Czech Technical University in Prague (SGS project No. SGS14/122/OHK1/2T/11) and by the European Union, OP RDI project No. CZ.1.05/2.1.00/03.0091 – University Centre for Energy Efficient Buildings.

REFERENCES

[1] CIRKLE, P. and POSPÍCHAL, O. *Nový způsob stanovení mrazuvzdornosti betonu s využitím metod pro sledování poruch struktur*. In: Beton – technologie, konstrukce, sanace, 03/2011, pp. 56-61. ISSN 1213-3116 (in Czech)

[2] NEVILLE, A., M. *Properties of concrete*. 2009. New York. pp. 503-661. ISBN 0-582-23070-5

[3] BERG, W. et al. *Příručka – Popílek v betonu – základy výroby a použití*. ČEZ Energetické produkty, s.r.o., 2013, pp. 82-86, ISBN 978-80-260-4226-6 (in Czech)

[4] ZOBAL, O. et al. *Analýza betonu z tělesa přehrady Orlík po padesáti letech*. In: Beton – technologie, konstrukce, sanace, 02/2014, pp. 19-25. ISSN 1213-3116 (in Czech)

[5] KEIL, J. et al. *Výstavba vodního díla Orlík – sborník statí*, Národní podnik vodní stavby, 1966, pp 365-366 (in Czech)

[6] ČSN 73 1322: *Stanovení mrazuvzdornosti betonu*, Praha, 1969 (in Czech)

[7] DOHNÁLEK, J. *Vliv mrazuvzdornosti betonu na jeho povrchové úpravy*. In: Beton – technologie, konstrukce, sanace, 03/2012, pp. 44-47. ISSN 1213-3116 (in Czech)

[8] ČSN 73 1326: *Stanovení odolnosti povrchu cementového betonu proti působení vody a chemických rozmrazovacích látek*, Praha, 1985 (in Czech)

[9] ČSN 73 1380: *Zkoušení odolnosti betonu proti zmrazování a rozmrazování - Porušení vnitřní struktury*, Praha, 2007 (in Czech)

ARTIFICIAL NEURAL NETWORK IN PREDICTION OF SOLUTION FOR ESHELBY'S INCLUSION PROBLEM

Lukáš ZRŮBEK[1], Jan NOVÁK[2], Anna KUČEROVÁ[3]

Abstract: *In this contribution we present our approach to estimate mechanical fields (strain, stress or displacement) inside isotropic infinite body with isotropic inhomogeneities. For isotropic ellipsoidal inclusion domains the precise analytical solution has been given by J. D. Eshelby. By changing the size of the semi-axes of the ellipsoid, several shapes of inclusions can be obtained, for example spheres, coin-like ellipsoids or even infinite cylinders. But for other special shapes like short cylinders, there is no analytical solution. Therefore we are creating a model to be able to train Artificial Neural Network (ANN) and with its use then predict mechanical response around these special shapes. At this state Eshelby's solution serves as a source of cheaply obtained results to create the model and test its properties.*

Keywords: *micromechanics, isotropic inhomogeneities, isotropic ellipsoidal inclusions, Eshelby's solution, artificial neural network*

INTRODUCTION

Nowadays, composite materials form an integral part of the world around. Whether it's a well-known material or material being just developed, we want to know the most about its properties and its behaviour at the macro or micro level. In this paper, we focus on the micro level behaviour of composite non-dilute material consisting of inhomogeneities or inclusions and isotropic infinite matrix. Our main interest is the evaluation of micromechanical fields (strain, stress or displacement) on this type of materials.

In 1957 J. D. Eshelby [1] presented in his fundamental work that there is analytical solution for isotropic inhomogeneity with domain that can be described by equation of ellipsoid (1). The x, y and

[1] Ing. Lukáš Zrůbek, Department of Mechanics, Faculty of Civil Engineering, Czech Technical University in Prague, lukas.zrubek@fsv.cvut.cz

[2] Ing. Jan Novák, Ph.D., Department of Mechanics, Faculty of Civil Engineering, Czech Technical University in Prague and Institute of Structural Mechanics, Faculty of Civil Engineering, Brno University of Technology, novakj@cml.fsv.cvut.cz

[3] Ing. Anna Kučerová, Ph.D., Department of Mechanics, Faculty of Civil Engineering, Czech Technical University in Prague, anicka@cml.fsv.cvut.cz

z symbols represent coordinates of a point and the a_1, a_2 and a_3 are the semi-axes of ellipsoid in x, y and z directions, respectively. If we change the dimensions of ellipsoid semi-axes we can describe many different shapes of inhomogeneities, like spheres, oblate spheroids, prolate spheroids, flat ellipsoids, coin-like ellipsoids or if we assign an infinite value to one of the semi-axes we obtain cylinder or elliptical cylinder.

$$\frac{x^2}{a_1^2} + \frac{y^2}{a_2^2} + \frac{z^2}{a_3^2} \leq 1 \qquad (1)$$

But for other special shapes of inhomogeneities which may occur in the macro or micro structure of materials, there is no analytical solution. As an example we can mention short cylinders, suitable for description of steel fiber reinforcements of concrete. The aim of our work is to create model that uses artificial neural network (ANN) to predict the mechanical response around these special shapes of inhomogeneities. So far the Eshelby's solution for ellipsoidal inclusions serves us as a cheap testing example to train the ANN and to investigate its properties.

SINGLE INHOMOGENEITY PROBLEM

In a simplified form, the principle of the solution of mechanical fields in an isotropic infinite medium containing single isotropic inhomogeneity is illustrated in Fig. 1. Solution given by J. D. Eshelby shows that problem of single inhomogeneity can be decomposed into exactly two tasks of a known solution and then assembled back by making use of the superposition principle. The solution of a single inhomogeneity problem is therefore given as the sum of homogeneous infinite body problem and homogeneous inclusion problem, so called perturbation part of mechanical fields [1, 2].

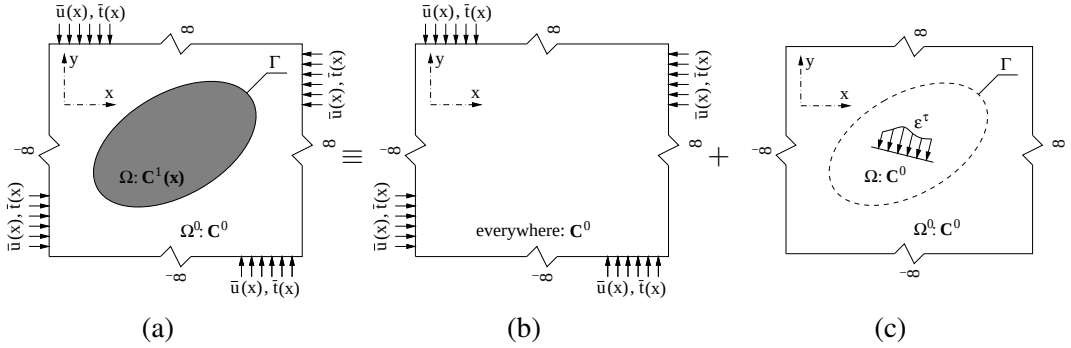

Fig. 1 Principle of Equivalent Inclusion Method: a) inhomogeneity problem, b) problem of infinite homogeneous body, c) homogeneous inclusion problem

In case of multiple inhomogeneities (see Fig. 2) the solution of mechanical field within a body with N inclusions is obtained as the sum of N single inclusion tasks scaled by a multiplier associated with each inclusion so as to fulfil self-equilibrium as presented in paper [3].

Using these solutions and computer programming the μMECH library [4, 5] was created for solving micromechanical fields in materials with single or multiple inclusions.

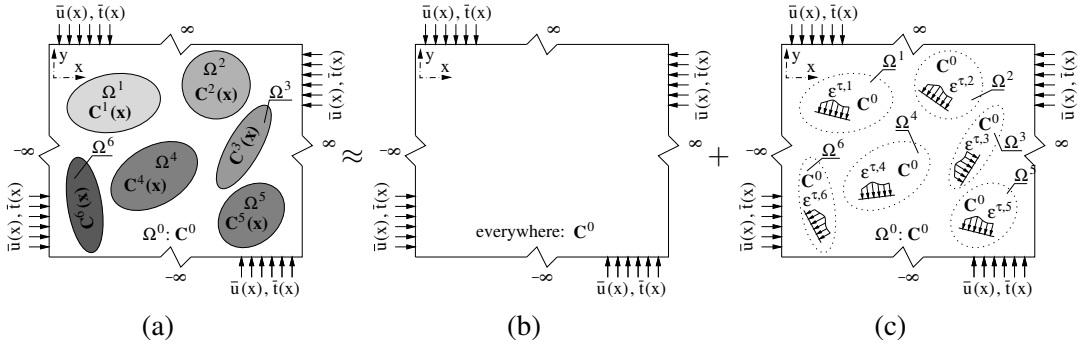

Fig. 2 Principle of Equivalent Inclusion Method: a) multiple inhomogeneity problem, b) infinite homogeneous body, c) multiple homogeneous inclusion problem

ARTIFICIAL NEURAL NETWORK

Artificial Neural Networks are computational models based on central nervous systems, especially on brain [6, 7]. These models are capable of machine learning and recognizing of patterns in given data. ANN consists of many simple processing nodes – so called neurons – interconnected into systems that can change their structure during the training (learning) phase. To each connection between two neurons is assigned an adaptive value representing synaptic weight of this connection. Based on given data and respective results used as an external information flowing through the system, these weights are balanced in a way that the output of ANN corresponds to the actual results.

There are numerous types of ANNs from single-directional systems to complicated multi-directional systems of neurons with many inputs and nested loops. One specific type of ANN is the feed-forward neural network. In this system, neurons are organized into layers where connections among neurons are placed only between adjacent layers, as shown in Fig. 3. There are no loops, cycles or feed-back connections.

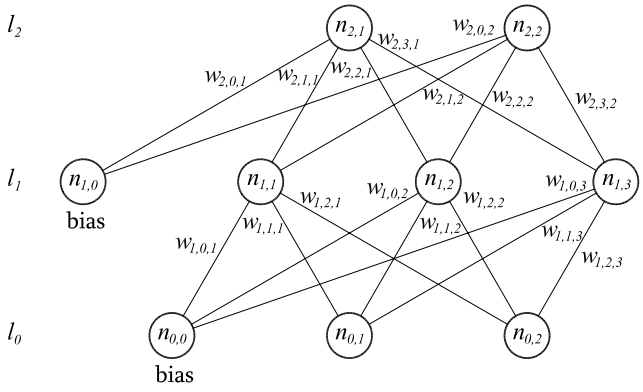

Fig. 3 Architecture of multi-layer perceptron

The most widely used example is the multi-layer perceptron (MLP) with the sigmoid transfer function and the gradient descent method of training – so called backpropagation learning algorithm. The power of MLPs lies in their ability to approximate nonlinear relations which corresponds to our problem, so

when speaking about ANN in the following text, the MLP is considered.

UTILIZATION OF ESHELBY'S SOLUTION

As described in section SINGLE INHOMOGENEITY PROBLEM, the solution for materials with multiple inclusions is decomposed into separate solutions, each for every inclusion. Therefore, we assume here only single ellipsoidal inclusion in the infinite isotropic body. But even so, the solution of mechanical fields depends on many input variables, such as type of load, Young's modulus and Poisson's ratio of the inclusion and matrix, dimensions and rotation (Euler angles) of the inclusion in space, coordinates of the inclusion centre and coordinates of a point where we want to evaluate mechanical response.

Simple model and samples generation

For maximum simplification, we decided to start with the simplest model where the only variable is x coordinate of a given point. The y and z coordinates are set to zero as well as Euler angles and all other variables are constants ($a_1 = 0.15$, $a_2 = 0.1$, $a_3 = 0.05$, $E_{inc} = 10$, $\nu_{inc} = 0.25$, $E_{mat} = 1$, $\nu_{mat} = 0.25$). In such a case when inclusion is not rotated ($\alpha = \beta = \gamma = 0$), the coordinate system of the inclusion coincides with the coordinate system of the applied load and we can limit the range of x to only positive numbers. That is because in this case the mechanical fields around inclusion are symmetrical to planes defined by semi-axes of inclusion and the centre of the inclusion matches the centre of a used coordinate system. Furthermore, because we are trying to predict only mechanical fields around the inclusion we introduced new variable r which is equal to the distance from inclusion surface, i.e. $r = x - a_1$. It should be noted that the solution for a point lying directly on the surface of the inclusion is not defined, therefore we work only with $r > 0$.

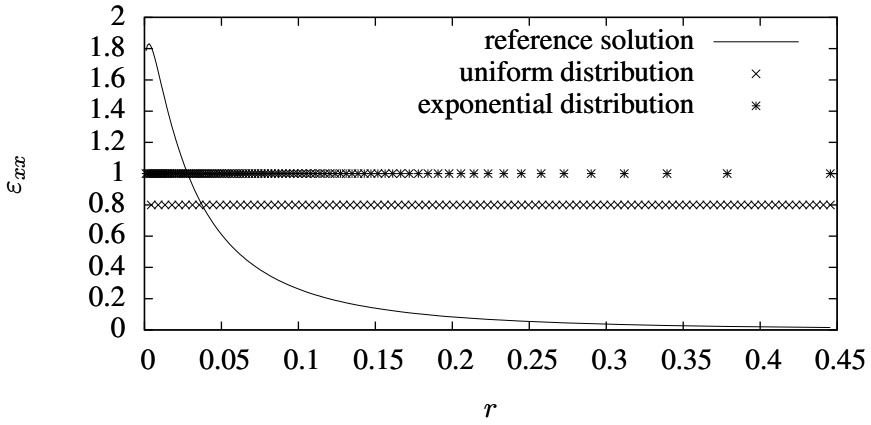

Fig. 4 Reference solution for model

To create input samples for r we generate uniformly distributed values in range $\langle 0; \ell \rangle$ where ℓ is distance from inclusion surface with mechanical response equal to zero. For this, we can safely con-

sider $\ell = 3 \cdot a_1$. But as can be seen on Fig. 4, the mechanical response is changing rapidly with the distance from the surface of the inclusions. With uniformly distributed values of r we get only small amount of samples describing sufficiently the mechanical response near the inclusion. To increase that amount we transform 100 uniformly distributed samples to exponentially distributed samples, i.e.

$$f(q) = \begin{cases} \frac{1}{b-a} & \text{for } a \leq q \leq b, \\ 0 & \text{for } q < a \text{ or } q > b, \end{cases} \Rightarrow f(r) = \begin{cases} \lambda e^{-\lambda r} & \text{for } r \geq 0, \\ 0 & \text{for } r < 0, \end{cases} \tag{2}$$

where the parameters of the uniform distribution are set to $a = 0$ and $b = 1$, the cumulative distribution function of exponential distribution is

$$F(r;\lambda) = \begin{cases} 1 - e^{-\lambda r} & \text{for } r \geq 0, \\ 0 & \text{for } r < 0, \end{cases} \tag{3}$$

and can be used as mapping from r to q

$$q = 1 - e^{-\lambda r} \tag{4}$$

as well as from q to r

$$r = \frac{-1}{\lambda} \ln(1-q), \quad \text{for } q < 1. \tag{5}$$

The resulting range of $r = (0; r_{max}\rangle$ is also influenced by λ

$$\lambda = \frac{-1}{r_{max}} \ln(1-q_{max}), \quad \text{for } q_{max} < 1. \tag{6}$$

ANN training

For the ANN training phase the reference results are needed. We used the above-mentioned μMECH library and solve the perturbations for 100 points given by $[r(q) + a_1, y = 0, z = 0]$ coordinates where $r(q) = (0; \ell\rangle$ and $\ell = 3 \cdot a_1 = 0.45$. As a result we get displacements vector, 6 independent components of strain tensor and 6 independent components of stress tensor for each sample. But in order to keep the model simple we decided to predict only one element from the results, the perturbation strain ε_{xx}.

To create and train the ANN we used software called RegNeN 2012 (Regression by Neural Network) [8] which is a software package for computing a regression for given data using artificial neural network. During the training phase the neural system itself is created. It is composed from input neurons in the first layer, n neurons in the second, so called hidden layer, and one output neuron in the third layer. Number of neurons in the first and hidden layer depends on the number of inputs and the self validating process for which the software uses so called cross-validation method. In this method the samples are

divided into m parts from which $m-1$ parts are used to calibrate the weights between neurons and the remaining part is used for validation. Then one neuron is added into hidden layer, the process of calibrating is repeated with different $m-1$ parts and for validation is used the currently remaining part. This is repeated m-times and finally the ANN with smallest error is saved.

As an input data for the ANN training phase, we used q values and corresponding results $\varepsilon_{xx}(r(q))$. The reason to use q values is that we can express r in dependence of q and the uniformly distributed values of q are more suitable inputs for ANN training phase.

Model verification

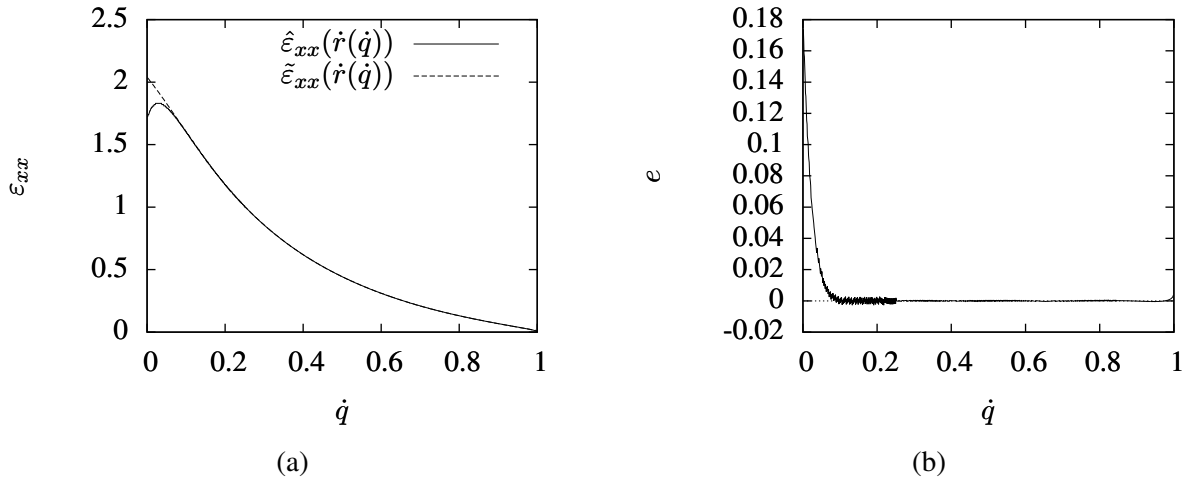

Fig. 5 Simple model verification: a) Comparison of the reference solution and the prediction, b) Error distribution

To verify our simple model we use new set of 1000 samples $\dot{r}(\dot{q})$ also in the range $\langle 0; 0.45\rangle$ created by transformation from uniformly distributed values $\dot{q}$ in range $(0; 1)$. Then using the ANN trained in the preceding step on the reference samples, we predict results $\tilde{\varepsilon}_{xx}(\dot{r}(\dot{q}))$ for the $\dot{q}$ values. These predicted results we compared with the corresponding exact Eshelby's solution $\hat{\varepsilon}_{xx}(\dot{r}(\dot{q}))$ which we obtain by the μMECH library (see Fig. 5a) and the error e (7) is plotted on the Fig. 5b.

$$e \;=\; \tilde{\varepsilon}_{xx}(\dot{r}(\dot{q})) \;-\; \hat{\varepsilon}_{xx}(\dot{r}(\dot{q})) \tag{7}$$

SUMMARY AND LATEST RESULTS

As can be seen from the data in Fig. 5, the ANN can accurately predict desired results. But the closer the points are at the surface of the inclusion then less accurate the prediction is. This is due to a short increase of values of ε_{xx} close to the surface of inclusions after which the values are dropping rapidly towards zero. Such abrupt changes of curvature cannot the ANN adequately capture during the training phase and the predicted results are therefore a kind of smoothed approximation.

At this stage when we are able to predict the results influenced by one input variable (r), we are extending the model by other input parameter φ (8) which is the ratio of the Young's modulus of inclusion E_{inc} and Young's modulus of the matrix E_{mat}. We keep value of $E_{mat} = 1$ and change only E_{inc} by raising it to the power of k i.e.

$$\varphi = \frac{{E_{inc}}^k}{E_{mat}}. \tag{8}$$

To this moment we run only few tests, where 100 training samples were generated in the software called SPERM 2.0 [9] as optimized Latin Hypercube Sampling (LHS). One of the generated variables was $q = (0; 1)$ from which we create exponentially distributed distance from inclusion surface $r = (0; 0.45\rangle$ and the second variable was the exponent k uniformly distributed on range $\langle -5; 5\rangle$.

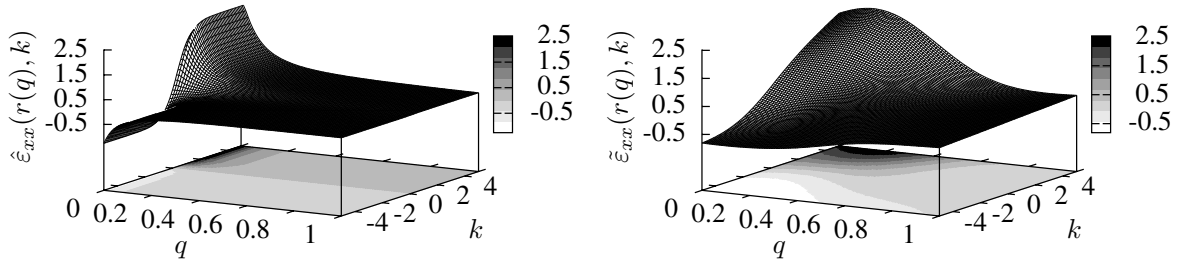

(a) (b)

Fig. 6 a) Reference solution $\hat{\varepsilon}_{xx}(r(q), k)$ dependent on two input variables, b) Prediction of $\tilde{\varepsilon}_{xx}(r(q), k)$ dependent on two input variables.

For the verification process we created 10201 samples on regular grid constructed within the prescribed bounds of $r(q)$ and k. On the Fig. 6a can bee seen how the reference solution $\hat{\varepsilon}_{xx}(r(q), k)$ changes depending on the input variables $r(q), k$ and on the Fig. 6b the predicted values $\tilde{\varepsilon}_{xx}(r(q), k)$.

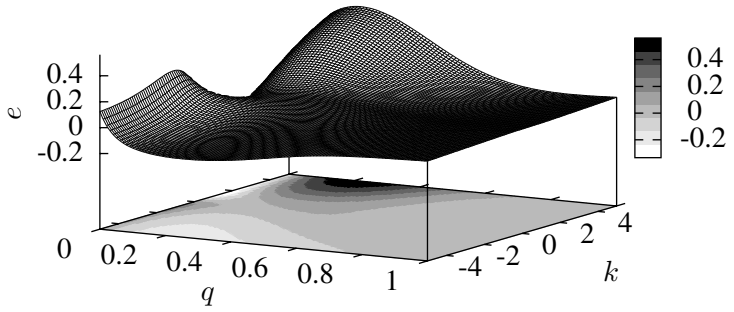

Fig. 7 Error distribution for two input variable model.

Solely by visual comparison of Figure 6a and 6b is clearly visible that the predicted values do not match the reference solution. Exact error values according to equation (7) is plotted in Fig. 7. This is most likely due to the small amount of samples used for training the ANN and therefore in the next step of our work we will focus on creating a sufficient number of input samples and better trained artificial neural network.

ACKNOWLEDGEMENT

This work was supported by the Czech Science Foundation, through projects No. P105/11/P370 (A. Kučerová), No. P105/12/0331 (J. Novák, L. Zrůbek) and by the Grant Agency of Czech Technical University in Prague through project No. SGS14/028/OHK1/1T/11 (L. Zrůbek, A. Kučerová).

REFERENCES

[1] ESHELBY, J. D. The Determination of the Elastic Field of an Ellipsoidal Inclusion, and Related Problems. *Proceedings of the Royal Society A: Mathematical, Physical and Engineering Sciences*. 1957-08-20, vol. 241, issue 1226, p. 376-396. Available from: doi: 10.1098/rspa.1957.0133

[2] MURA, Toshio. *Micromechanics of Defects in Solids*. 2nd rev. ed. Dordrecht: Kluwer Academic Publishers, 1991, 587 p. ISBN 90-247-3256-5.

[3] NOVÁK, Jan. Calculation of Elastic Stresses and Strains inside a Medium with Multiple Isolated Inclusions. *Proceedings of the Sixth International Conference on Engineering Computational Technology (Stirlingshire, UK)* M. Papadrakakis and B.H.V. Topping, eds. 2008, Paper 127, p. 16 pp. Available from: doi: 10.4203/ccp.89.127

[4] NOVÁK, Jan, et al. A micromechanics-enhanced finite element formulation for modelling heterogeneous materials. *Computer Methods in Applied Mechanics and Engineering*, 2012, 201-204, p. 53-64. Available from: doi: 10.1016/j.cma.2011.09.003

[5] OBERRECHT, S. P., NOVÁK, J. and KRYSL, P. B-bar FEMs for anisotropic elasticity. *International Journal for Numerical Methods in Engineering*. 2014-04-13, vol. 98, issue 2, p. 92-104. Available from: doi: 10.1002/nme.4621

[6] GURNEY, Kevin. *An introduction to neural networks*. Boca Raton: CRC Press, 1997, xi, 234 p. ISBN 978-1-85728-503-4.

[7] HAYKIN, Simon S., et al. *Neural networks and learning machines.* 3rd ed. Upper Saddle River, N.J.: Pearson, 2009, 934 p. ISBN 01-312-9376-1.

[8] MAREŠ, T. and KUČEROVÁ, A. RegNeN 2012 [online]. Faculty of Civil Engineering, Czech Technical University in Prague, 2012 [cited 2014-09-01] Available from: http://klobouk.fsv.cvut.cz/ anicka/regnen/regnen.html

[9] NOVÁK, J. Generator of optimal LHS designs SPERM v. 2.0. Centre for Integrated Design of Advanced Structures (CIDEAS), Czech Technical University in Prague, 2011.